

# **Some Topics in Interfacial and Solution Thermodynamics**

by

Hikmat Binyaminov

A thesis submitted in partial fulfillment of the requirements for the degree of

Doctor of Philosophy

in

Chemical Engineering

Department of Chemical and Materials Engineering

University of Alberta

© Hikmat Binyaminov, 2024

# Abstract

Elements from Gibbsian composite-system thermodynamics, classical nucleation theory, combinatorics, and statistical mechanics were used to provide insights into and develop models for some equilibrium systems of practical importance. This thesis consists of two parts. In part one, three problems were considered in which complex interfacial geometries dictate the stability of configurations and phase change properties of the system: (i) interacting drop–drop and drop–bubble systems in an immiscible medium, (ii) vapor nucleation from a liquid–gas solution inside a cylindrical nanopore, and (iii) solid nucleation from a pure liquid inside and out of cylindrical nanopores. Regarding the first problem, contributions were made to the calculation of equilibrium configurations and system behavior at the nanoscale. Regarding the second problem, a nonideal model was derived for liquid–vapor equilibrium across an arbitrarily curved interface, and its predictive capability was demonstrated when used with a constant-value line tension correction. Regarding the third problem, equilibrium shapes of the new-phase nucleus near a liquid meniscus and equilibrium shapes for the growth of the new phase out of a collection of cylindrical pores were analyzed; the roles of these calculated geometries on the ease of nucleation and growth were quantified. In part two of this thesis, contributions were made to the development and application of the multisolute osmotic virial equation and its combining rules. It was shown that a similar model to that which was proposed by Elliott *et al.* earlier using the regular solution model can be derived in a more general solution theory framework with less restrictive assumptions. The derived model has a corrected combining rule for the cubic terms and new combining rules for higher order terms. This model

was then extended to dissociating solutes by utilizing a previously used technique and was then applied to predict freezing points of ternary salt solutions yielding accurate predictions using binary data only as the input. Overall, the findings of this thesis can help further our understanding of the role of interfacial geometry in small systems and of multisolute mixtures, valuable in applications such as atmospheric physics, nanoscience, biology, and energy storage, among others.

## Preface

Chapters 2 to 6 of this thesis have been published or submitted for publication. I performed all the research under the direct supervision of J. A. W. Elliott.

Chapter 2 of this thesis has been published, with minor changes, as H. Binyaminov, F. Abdullah, L. Zargarzadeh, and J. A. W. Elliott, *Thermodynamic Investigation of Droplet–Droplet and Bubble–Droplet Equilibrium in an Immiscible Medium*, *J. Phys. Chem. B* **125**, 8636 (2021). <https://doi.org/10.1021/acs.jpcc.1c02877> © 2021 American Chemical Society. J. A. W. Elliott proposed the original problem. F. Abdullah calculated the results given in Table 2-2 as part of an undergraduate project under the supervision of J. A. W. Elliott with the input of L. Zargarzadeh. I reproduced the results in Table 2-2 with a different method, completed the rest of the research, and wrote the first draft of the manuscript under the supervision of J. A. W. Elliott.

Chapter 3 and Appendix A of this thesis have been published, with minor changes, as H. Binyaminov and J. A. W. Elliott, *Quantifying the Effects of Dissolved Nitrogen and Carbon Dioxide on Drying Pressure of Hydrophobic Nanopores*, *J. Chem. Phys.* **158**, 204710 (2023). <https://doi.org/10.1063/5.0146952> © 2023 American Institute of Physics. I proposed the original problem, performed the research, and wrote the first draft of the manuscript. J. A. W. Elliott revised some of my ideas, provided feedback, and edited the manuscript.

Chapter 4 and Appendix B of this thesis, with minor changes, have been submitted for publication as H. Binyaminov and J. A. W. Elliott, *The Role of Geometry on the Ease of Solidification Inside and Out of Cylindrical Nanopores*. I proposed the original problem, performed the research, and wrote the first draft of the manuscript. J. A. W. Elliott revised some of my ideas, provided feedback, and edited the manuscript.

Chapter 5 and Appendix C of this thesis have been published, with minor changes, as H. Binyaminov and J. A. W. Elliott, *Multicomponent Solutions: Combining Rules for Multisolute Osmotic Virial Coefficients*, *J. Chem. Phys.* **159**, 164116 (2023). <https://doi.org/10.1063/>

[5.0166482](#) © 2023 American Institute of Physics. I proposed the original problem, performed the research, and wrote the first draft of the manuscript. J. A. W. Elliott revised some of my ideas, provided feedback, and edited the manuscript.

Chapter 6 and Appendix D of this thesis have been published, with minor changes, as H. Binyaminov, H. Sun, and J. A. W. Elliott, *Predicting Freezing Points of Ternary Salt Solutions with the Multisolute Osmotic Virial Equation*, *J. Chem. Phys.* **159**, 244502 (2023). <https://doi.org/10.1063/5.0169047> © 2023 American Institute of Physics. J. A. W. Elliott proposed the problem and wrote the background about the previous version of the model in the introduction section (3rd paragraph in the introduction). As part of an undergraduate project, H. Sun did the unit conversions in Appendix D for the Gibbard *et al.* [60–62] data and made predictions for the Gibbard *et al.* [60–62] ternary data using the molality-based model with a different fitting criterion under the supervision of J. A. W. Elliott. I completed the rest of the research and wrote the first draft of the manuscript under the supervision of J. A. W. Elliott.

*to my family*

# Acknowledgements

To Dr. Janet Elliott, thank you for believing in me and giving me complete academic freedom in my research. This thesis would not have been possible without your careful guidance and feedback. Your passion for research, teaching, and mentoring is truly inspiring.

To Drs. Anthony Yeung and Hongbo Zeng, thank you for your help as members of my supervisory committee.

To Drs. William McCaffrey, Vinay Prasad, and Joelle Frechette, thank you for your willingness to be on my examining committee and your time in reading my work.

To all the past and present members of both Elliott groups that I have had the pleasure to get to know, thank you for your stimulating discussions and advice.

To my family and friends back home, especially Nazrin, Rufat, Eybulla, and Seymour, thank you for always being there for me.

To all my friends in Edmonton, especially Sagar, thank you for making this city feel like a second home.

To the Natural Sciences and Engineering Research Council of Canada, Alberta Innovates, and the University of Alberta, thank you for your financial support.

# Table of Contents

<b>Chapter 1 Introduction .....</b>	<b>1</b>
1.1 Gibbsian composite-system thermodynamics .....	3
1.2 Literature overview.....	6
1.2.1 Equilibrium configurations of two-phase drops .....	6
1.2.2 Phase change in confinement.....	7
1.2.3 Multicomponent solutions .....	8
1.3 Thesis scope.....	9
1.3.1 Part I: Interplay of geometry and thermodynamics in three applications .....	10
1.3.2 Part II: Multicomponent solutions .....	11
<b>Part I: Interplay of Geometry and Thermodynamics in Three Applications .....</b>	<b>12</b>
<b>Chapter 2 Thermodynamic Investigation of Droplet–Droplet and Bubble–Droplet Equilibrium in an Immiscible Medium .....</b>	<b>13</b>
2.1 Introduction.....	14
2.2 System definition and governing equations.....	17
2.2.1 System definition .....	17
2.2.2 Derivation of conditions for equilibrium .....	18
2.2.3 On the possibility of the attached configuration .....	25
2.2.4 Derivation of the free-energy equation .....	28
2.2.5 On the stability of the equilibrium states .....	31
2.2.5.1 Explicit forms of the free-energy equations as functions of geometry around equilibrium.....	31



2.2.5.2 Reference configuration and full encapsulation cases viewed as the limits of the attached configuration.....	32
2.2.6 On the contributions of the first and the last terms in Equation (2-75) .....	34
2.3 Results and discussion .....	34
2.3.1 Effects of system parameters on free energy and geometry of equilibrium configurations .....	39
2.3.1.1 Effects of the initial volume of the air bubble .....	39
2.3.1.2 Effects of interfacial tensions.....	42
2.3.1.3 Effects of scale.....	46
2.4 Conclusion .....	48
<b>Chapter 3 Quantifying the Effects of Dissolved Nitrogen and Carbon Dioxide on Drying Pressure of Hydrophobic Nanopores .....</b>	<b>50</b>
3.1 Introduction.....	51
3.2 System definition and free energy .....	54
3.3 Nonideal multicomponent liquid–vapor equilibrium across a curved interface.....	59
3.4 Estimating free-energy barrier from experiments.....	63
3.5 Shape of the critical nucleus .....	64
3.6 Results.....	69
3.6.1 Comparison of free-energy profiles .....	69
3.6.2 Importance of mixture nonideality.....	73
3.6.3 Extrusion pressures and effect of line tension .....	75
3.6.4 Required gas concentration to empty the pore at fixed liquid pressure.....	78
3.6.5 On the oversolubility and distribution of gas in confinement.....	79
3.7 Comparison with available experimental data.....	80
3.8 Conclusion .....	83
<b>Chapter 4 The Role of Geometry on the Ease of Solidification Inside and Out of Cylindrical Nanopores .....</b>	<b>86</b>

4.1 Introduction.....	87
4.2 System definition and free energy .....	91
4.2.1 Solid nucleation at the meniscus.....	92
4.2.2 Bridging of the pores .....	94
4.3 Methods .....	96
4.4 Results: Geometry.....	99
4.4.1 Geometry of nuclei at the meniscus.....	99
4.4.1.1 Symmetric nucleus.....	101
4.4.1.2 Type-1 asymmetric nucleus .....	103
4.4.1.3 Type-2 asymmetric nucleus .....	105
4.4.2 Geometry of bridges .....	107
4.5 Results: Free-energy analysis and energy barriers .....	109
4.5.1 Free-energy analysis for nucleation at the meniscus .....	110
4.5.1.1 Free energy of symmetric nucleation.....	110
4.5.1.2 Free energy of asymmetric nucleation.....	112
4.5.1.3 Comparison of the energy barriers for nucleation .....	115
4.5.2 Free energy of bridging.....	116
4.5.2.1 Comparison of the energy barriers for bridging .....	118
4.6 Conclusion .....	120
<b>Part II: Multicomponent solutions.....</b>	<b>123</b>
<b>Chapter 5 Multicomponent Solutions: Combining Rules for Multisolute Osmotic Virial Coefficients .....</b>	<b>124</b>
5.1 Introduction.....	125
5.2 The model .....	127
5.2.1 Assumptions of the model .....	127

5.2.2 Nonconfigurational Gibbs free energy of random mixing.....	128
5.2.3 Chemical potential .....	132
5.3 Solvent-dominant mixtures.....	133
5.3.1 Asymmetric form of Equation (5-18) for the solvent .....	133
5.3.2 Derivation of combining rules .....	137
5.4 Discussion.....	142
5.4.1 Connection to the original single-solute osmotic virial coefficients.....	142
5.4.2 On the size of $n$ .....	145
5.5 Conclusion .....	146
<b>Chapter 6 Predicting Freezing Points of Ternary Salt Solutions with the Multisolute Osmotic Virial Equation.....</b>	<b>148</b>
6.1 Introduction.....	149
6.2 Methods .....	152
6.2.1 Virial expansion and the original combining rules .....	152
6.2.2 New combining rules for the third- and higher-order coefficients .....	154
6.2.3 Determination of the osmotic virial coefficients.....	156
6.3 Results.....	158
6.3.1 Tabulation of osmotic virial coefficients .....	158
6.3.2 Predictions using the mole-fraction-based new MSOVE .....	162
6.4 Comparison of the new and original combining rules.....	167
6.5 Conclusion .....	173
<b>Chapter 7 Conclusions.....</b>	<b>175</b>
<b>References.....</b>	<b>179</b>
<b>Appendices.....</b>	<b>199</b>

# List of Appendices

<b>Appendix A</b>	<b>Supplementary Information for Chapter 3</b>	<b>200</b>
A.1	Description of the thermodynamic model	200
A.1.1	NRTL activity model	200
A.1.2	Peng–Robinson EOS	200
A.1.3	Calculating $\phi_{1,\text{sat}}$ , $H_{12}$ , $\bar{v}_{2,\infty}^L$ , $P_{1,\text{sat}}$ , and $v_{1,\text{sat}}^L$	202
A.1.4	Validation of the thermodynamic model	205
A.2	Solution procedure for the system of equations	206
A.3	Analytical solution of the symmetric nucleus profile	208
A.4	Pore size distribution data from Li <i>et al.</i> [26]	208
<b>Appendix B</b>	<b>Supplementary Information for Chapter 4</b>	<b>210</b>
B.1	Surface Evolver calculation details	210
B.1.1	Calculating the asymmetric nucleus shape	212
B.1.2	Calculating the bridge geometries	213
<b>Appendix C</b>	<b>Supplementary Information for Chapter 5</b>	<b>216</b>
C.1	Detailed steps between Equations (5-21) and (5-22) and Equations (5-22) and (5-23)	216
C.2	Detailed steps between Equations (5-28) and (5-29)	221
C.3	Detailed steps to arrive at Equation (5-31) using Equations (5-24) and (5-29)	222
C.4	Detailed steps between Equations (5-48) and (5-50) and Equations (5-49) and (5-51)	224
<b>Appendix D</b>	<b>Supplementary Information for Chapter 6</b>	<b>226</b>

D.1 Discussion of binary data reported in the references used for ternary data .....	226
D.2 Graphical representations of binary fits .....	229
D.3 Data sources and unit conversions .....	232
D.3.1 Gibbard <i>et al.</i> .....	232
D.3.2 Haghighi <i>et al.</i> .....	233
D.3.3 Hall <i>et al.</i> .....	234
D.3.4 Khitrova .....	234
D.3.5 Mun and Darer .....	234
D.3.6 Oakes <i>et al.</i> .....	235
D.3.7 Vilcu <i>et al.</i> .....	235
D.4 Estimation of uncertainties in MSOVS coefficients .....	235
D.5 Numerical values of constants .....	236
<b>References .....</b>	<b>237</b>

## List of Tables

Table 2-1. Input parameters used to solve for equilibrium configurations in Table 2-2. $\gamma^{ow}$ and $\gamma^{oa}$ are from reference [65], and $\gamma^{aw}$ is from reference [229]. .....	35
Table 2-2. Solutions of the systems of equations for each configuration with given parameters as specified in Table 2-1 with diagrams to scale. ....	36
Table 4-1. Summary of all cases considered for nucleation at the meinscus. ....	99
Table 4-2. Summary of all cases studied for bridging of pores. ....	107
Table 6-1. Mole-fraction-based binary fit coefficients and related data. The coefficients were obtained by fitting to data after converting molality to mole fraction and FPD to osmole fraction. The data used for fitting are mainly from the CRC handbook [230] except where indicated by a superscript letter, in which case the data are obtained from: (a) Oakes <i>et al.</i> [154]; (b) Gibbard and Gossmann [62]; (c) Haghghi <i>et al.</i> [74]. ....	159
Table 6-2. Molality-based binary fit coefficients and related data. The coefficients were obtained by fitting to data after converting all concentration units to molality and FPD to osmolality. The data used for fitting are mainly from the CRC handbook [230] except where indicated by a superscript letter, in which case the data are obtained from: (a) Oakes <i>et al.</i> [154]; (b) Gibbard and Gossmann [62]; (c) Haghghi <i>et al.</i> [74]. ....	160
Table 6-3. Summary of ternary experimental data from the literature and RMSEs for each subsystem of prediction of the mole-fraction-based new MSOVE. The RMSEs are colored from green (lowest) to red (highest). The all-system RMSE was calculated by considering all data points as one system (total 371 data points). ....	163
Table 6-4. Numerical summary of the performance of the models in terms of all-system RMSEs, MAEs, and MBs. All measures were calculated by considering all data points as one system (total of 371 data points). Each column is separately colored from green (lowest absolute value) to red (highest absolute value). ....	173
Table A-1. Parameters for P–R EOS calculations [25]. ....	202
Table D-1. The numerical values of the required constants for calculations [48]. ....	236

## List of Figures

Figure 2-1. Schematics for (a) the reference state and (b) possible final states, where (I) is the attached configuration, (II) is the full encapsulation of phase 1 by phase 2 and (III) is the full encapsulation of phase 2 by phase 1. For all three configurations, the radii of curvature of the three interfaces are:  $R^{13}$ —the radius of curvature of the interface between phase 1 and phase 3;  $R^{23}$ —the radius of curvature of the interface between phase 2 and phase 3; and  $R^{12}$ —the radius of curvature of the interface between phase 1 and phase 2. For the attached configuration, the contact angles of these interfaces are given by  $\alpha$ ,  $\beta$ , and  $\varphi$ —all defined with respect to the three-phase plane (vertical dashed line). ..... 18

Figure 2-2. 3D free-energy plots and contour maps as functions of two variables,  $\alpha + \beta$  and  $\varphi$ , for (a) a system with the system parameters given in Table 2-1; (b) the same system as in (a) except with  $\gamma^{ow} = 100 \text{ mN/m} > \gamma^{aw} + \gamma^{oa} = 72.4 + 25.3 = 97.7 \text{ mN/m}$ ; (c) the same system as in (a) except with  $\gamma^{aw} = 100 \text{ mN/m} > \gamma^{ow} + \gamma^{oa} = 53.7 + 25.3 = 79 \text{ mN/m}$ ; and (d) the same system as in (a) except with  $\gamma^{oa} = 130 \text{ mN/m} > \gamma^{ow} + \gamma^{aw} = 53.7 + 72.4 = 126.1 \text{ mN/m}$ . The plot in (a) shows a stable equilibrium (a global minimum) at  $\alpha + \beta = 164.3^\circ$  ( $\alpha = 63^\circ$  and  $\beta = 101.3^\circ$ ) and  $\varphi = 66.3^\circ$  indicated by the blue lines corresponding to the attached configuration. The bold, red lines on all figures represent the limiting configurations. Namely, the line at  $\varphi = 180^\circ$  represents the oil-encapsulating-air configuration, the line at  $\varphi = -180^\circ$  represents the air-encapsulating-oil configuration, and the line at  $\alpha + \beta = 0^\circ$  represents the reference configuration. .... 38

Figure 2-3. Effect of the ratio of the initial volumes of air phase to oil phase on: (a) the free energy with respect to the reference state; (b) the radius of the oil–air interface,  $R^{oa}$ , for the attached configuration; and (c) the contact angles  $\alpha$ ,  $\beta$ , and  $\varphi$ , for the attached configuration. Three example schematics from the attached configuration are shown with (from left to right): positively curved interface ( $V_r^a/V^o = 0.01$ ); flat interface ( $V_r^a/V^o \approx 27$ ); and negatively curved interface ( $V_r^a/V^o = 100$ ). The volume of the oil phase,  $V^o = 100 \times 10^{-9} \text{ m}^3$ , is kept constant. The remaining system parameters are fixed as given in Table 2-1. The vertical dashed line indicates the volume ratio where the flat oil–air interface occurs. Note that, in (a), each  $x$ -axis value represents a different system, and therefore, extrema on these plots do not have a stability meaning. .... 41

Figure 2-4. Effects of individually varying  $\gamma^{ow}$ ,  $\gamma^{oa}$ , and  $\gamma^{aw}$  on: (a) the free-energy difference between each final configuration and the reference state; (b) the radius of the oil–air interface,  $R^{oa}$ , for the attached configuration; and (c) the contact angles  $\alpha$ ,  $\beta$ , and  $\varphi$  for the attached configuration. When varying each interfacial tension, the remaining parameters are fixed as given in Table 2-1. Note that the attached configuration is only possible in certain ranges, where the triangle inequalities for the interfacial tensions are satisfied. These limits and the flat

interfaces (when possible) are indicated by vertical dashed lines. Three example schematics are given for each of the varied interfacial tensions. .... 43

Figure 2-5. Contours of constant contact angle  $\varphi$  plotted for constant oil volume,  $V^o = 100 \times 10^{-9} \text{ m}^3$ , and three different initial volumes of the air bubble: (a)  $V_r^a = 75 \times 10^{-9} \text{ m}^3$ ; (b)  $V_r^a = 10 \times 10^{-9} \text{ m}^3$ ; and (c)  $V_r^a = 1000 \times 10^{-9} \text{ m}^3$  as functions of the ratios of interfacial tensions,  $\gamma^{ow}/\gamma^{aw}$  and  $\gamma^{oa}/\gamma^{aw}$ . The air–water interfacial tension,  $\gamma^{aw} = 72.4 \times 10^{-3} \text{ N/m}$ , is fixed. Conventionally, the angle,  $\varphi$ , is chosen to be positive when the interface is convex (red-shaded areas), and negative when it is concave (blue-shaded areas) towards the oil phase. The domains are bounded by the straight lines:  $\gamma^{oa}/\gamma^{aw} = \gamma^{ow}/\gamma^{aw} + 1$ ;  $\gamma^{oa}/\gamma^{aw} = \gamma^{ow}/\gamma^{aw} - 1$ ; and  $\gamma^{oa}/\gamma^{aw} = 1 - \gamma^{ow}/\gamma^{aw}$ . Outside of the domain boundaries, the attached configuration is not possible, so a representative schematic of the most stable configuration is drawn for each of the triangular regions. .... 45

Figure 2-6. Contributions of the interfacial ( $\Delta B_{\text{int}}$ ), pressure ( $\Delta B_p$ ), and chemical potential ( $\Delta B_\mu$ ) terms to the total free energy ( $\Delta B_{\text{total}}$ ) of each configuration at two different size scales. The top row corresponds to a system at the millimeter scale ( $V^o = 100 \times 10^{-9} \text{ m}^3$ ), where the free-energy contributions due to pressure and chemical potential cancel each other leaving the total the free energies with respect to the reference equal to the interfacial free-energy contributions ( $\Delta B_{\text{total}} = \Delta B_{\text{int}}$ ). The bottom row corresponds to a system at the nanometer scale ( $V^o = 100 \times 10^{-24} \text{ m}^3$ ), where these contributions do not cancel. The remaining system parameters of both systems are fixed as given in Table 2-1. Note that each  $x$ -axis value on these plots represents a different system, and therefore, extrema on these plots do not have a stability meaning. .... 47

Figure 2-7. Effect of the ratio of the initial volumes of the air phase to the oil phase on the free energy with respect to the reference state at the nanoscale. The thick lines represent the total free energy, whereas the thin gray lines represent the free energy only due to the interfacial terms. The volume of the oil phase,  $V^o = 100 \times 10^{-24} \text{ m}^3$ , is kept constant, and the remaining system parameters are fixed as given in Table 2-1. Note that each  $x$ -axis value on this plot represents a different system, and therefore, extrema on this plot do not have a stability meaning. .... 48

Figure 3-1. Schematic description of drying of a cylindrical nanopore immersed in a liquid–gas solution. The metastable reference state is shown in panel (a) with a solution-filled cylinder of radius  $R_p$  and length  $l_p$ . After a short waiting time, a new vapor phase forms and pushes the solution out of the pore following a nucleation event. A snapshot of the process after the nucleation is shown in panel (b), where two disjoint spherical caps are moving in opposite directions. The final equilibrium state with the vapor-filled pore and a pinned liquid–vapor interface covering the pore mouth at the end of this process is depicted in panel (c). In this panel, the light blue, purple, and black lines indicate example positions of the interface, depending on the pressure difference,  $P^V - P^L$ . The liquid–gas solution is indicated by the letter “L” and the vapor is indicated by the letter “V”. The liquid has an equilibrium contact angle of  $\theta_{\text{eq}}$  with the solid. While the interface is in motion, the contact angle,  $\theta_r$ , in general, is assumed to be different than  $\theta_{\text{eq}}$ . Note that  $\theta_r$  does not appear in our calculations because we are only concerned with equilibrium states in this work. Schematics of possible critical



nuclei geometries considered in this work are depicted in panels (d) (localized nucleus) and (e) (symmetric nucleus)..... 56

Figure 3-2. Nondimensional geometrical quantities for the critical nuclei and the corresponding energy plots as functions of nondimensional curvature for three different contact angles: blue for  $\theta_{eq} = 110^\circ$ , orange for  $\theta_{eq} = 120^\circ$ , and yellow for  $\theta_{eq} = 130^\circ$ . The solid lines are for the localized nuclei and the dotted dashed lines are for the symmetric nuclei. Panels (a), (b), and (c) show the plots of volume, liquid–vapor interfacial area, and solid–vapor interfacial area, respectively. Panel (d) shows the plots of energy barrier as calculated using Equation (3-2). The inset shows a zoom-in of the curvature range where the symmetric nuclei have slightly lower energy. Here, the energy curves for the localized nuclei are shown in black to highlight the transition points..... 67

Figure 3-3. Examples of localized and symmetric nuclei. As calculated using Surface Evolver, the three-dimensional views of the liquid–vapor interfaces for the localized nuclei are shown in panels (a) and (b), which have constant curvatures of  $k_c R_p = 0.83$  and  $k_c R_p = 0.21$ , respectively. For clear views of these shapes, only the contours of the cylinders are shown at the ends of the bounding boxes. The three-phase contact lines are shown in red. In panel (c), the two-dimensional view of three symmetric nuclei on an axial plane are shown. The three-dimensional surfaces are obtained by rotating these profiles around the cylinder axis (blue dotted dashed line). These surfaces have constant curvatures of  $k_c R_p = -0.8$  (dotted line),  $-0.87$  (dashed line), and  $-0.94$  (solid line)..... 68

Figure 3-4. Free-energy plots for  $\theta_{eq} = 110^\circ$  at different pore radii, liquid pressures, and saturation ratios. The temperature is fixed at  $T = 323.15$  K. The green lines are for pure water, the light blue lines are for water with dissolved carbon dioxide, and the orange lines are for water with dissolved nitrogen. Each row of subplots is for a different pore radius, while the columns are for different liquid pressures. The solid lines are for  $S = 1$ , the dashed lines are for  $S = 2$ , and the dotted dashed lines are for  $S = 0.5$ . The horizontal solid black lines represent  $\Delta B = 35 k_B T$  for visual reference. All curves are highlighted in red around the critical volume and the corresponding free-energy barrier..... 71

Figure 3-5. Free-energy plots for  $\theta_{eq} = 120^\circ$  at different pore radii, liquid pressures, and saturation ratios. The temperature is fixed at  $T = 323.15$  K. The green lines are for pure water, the light blue lines are for water with dissolved carbon dioxide, and the orange lines are for water with dissolved nitrogen. Each row of subplots is for a different pore radius, while the columns are for different liquid pressures. The solid lines are for  $S = 1$ , the dashed lines are for  $S = 2$ , and the dotted dashed lines are for  $S = 0.5$ . The horizontal solid black lines represent  $\Delta B = 35 k_B T$  for visual reference. All curves are highlighted in red around the critical volume and the corresponding free-energy barrier..... 72

Figure 3-6. Free-energy plots for  $\theta_{eq} = 130^\circ$  at different pore radii, liquid pressures, and saturation ratios. The temperature is fixed at  $T = 323.15$  K. The green lines are for pure water, the light blue lines are for water with dissolved carbon dioxide, and the orange lines are for water with dissolved nitrogen. Each row of subplots is for a different pore radius, while the columns are for different liquid pressures. The solid lines are for  $S = 1$ , the dashed lines are

for  $S = 2$ , and the dotted dashed lines are for  $S = 0.5$ . The horizontal solid black lines represent  $\Delta B = 35 k_B T$  for visual reference. All curves are highlighted in red around the critical volume and the corresponding free-energy barrier..... 73

Figure 3-7. Comparison of free-energy barriers as functions of liquid pressure for ideal and nonideal solution models for three different pore sizes: (a)  $R_p = 1$  nm, (b)  $R_p = 1.5$  nm, and (c)  $R_p = 2$  nm. The orange lines are for nitrogen–water and the light blue lines are for carbon dioxide–water. The solid lines correspond to the nonideal model while the dashed lines correspond to the ideal model. The concentration of the gas in the solution is the saturation value at the intrusion pressure of each pore. The horizontal solid black lines represent  $\Delta B = 35 k_B T$  for visual reference. All calculations were done for  $\theta_a = \theta_{eq} = 120^\circ$ ,  $T = 323.15$  K, and  $\sigma^{LV} = 0.068$  J/m<sup>2</sup>. ..... 74

Figure 3-8. Various pressures of interest as functions of pore radius for different values of line tension: (a) and (d)  $\tau = 0$  J/m, (b) and (e)  $\tau = -1.5 \times 10^{-11}$  J/m, and (c) and (f)  $\tau = -3 \times 10^{-11}$  J/m. The black lines on panels (a)–(c) indicate the intrusion pressures for a dry pore. On these panels, the extrusion pressures are shown in green for pure water, in orange for water with dissolved nitrogen, and in light blue for water with dissolved carbon dioxide. The solid lines are for  $S = 1$  and the dashed lines are for  $S = 1.5$ . On panels (d)–(f), the required pressure difference for nucleation,  $P^V - P_{ext}$  (red lines), and the maximum pressure difference where the vapor phase stays confined in the pore after nucleation,  $\Delta P^* = 2\sigma^{LV} \sin\theta_{eq}/R_p$  (blue curves), are shown. All calculations were done for  $\theta_a = \theta_{eq} = 120^\circ$ ,  $T = 323.15$  K,  $\sigma^{LV} = 0.068$  J/m<sup>2</sup>, and  $\Delta B_c = 35k_B T$ . ..... 76

Figure 3-9. The minimum required gas concentrations in the solution,  $x_2$ , to empty the pore in typical experimental times as functions of pore radius at two different extrusion pressures: (a)  $P_{ext} = 1$  atm and (b)  $P_{ext} = P_{int}$  and for three different values of line tension. The bold solid lines are for  $\tau = 0$  J/m, the dashed lines are for  $\tau = -1.5 \times 10^{-11}$  J/m, and the dotted lines are for  $\tau = -3 \times 10^{-11}$  J/m. The light blue lines are for carbon dioxide in water and the orange lines are for nitrogen in water. For reference, the thin, solid blue and red lines show the saturation concentrations of gases in water at  $P_{ext}$  for carbon dioxide and nitrogen, respectively. The thin vertical black dashed lines indicate the metastability limit of pure water. All calculations were done for  $\theta_a = \theta_{eq} = 120^\circ$ ,  $T = 323.15$  K,  $\sigma^{LV} = 0.068$  J/m<sup>2</sup>, and  $\Delta B_c = 35k_B T$ . ..... 79

Figure 3-10. Summary of the simulated experiments based on data from Li *et al.* [121]. (a) simulated intrusion–extrusion cycles where the  $x$ -axis is the magnitude of the normalized volume change of the system,  $\Delta V/\Delta V_{max}$ . The black line is the intrusion curve, the green line is the extrusion curve for pure water, and the orange lines are the extrusion curves for water with dissolved nitrogen at the recalculated experimental gas concentrations. Note that air was used in the experiments, which is modeled here with nitrogen. The solid orange line is for  $x_2 = 1.518 \times 10^{-3}$ , the dashed orange line is for  $x_2 = 1.055 \times 10^{-3}$ , and the dotted orange line is for  $x_2 = 7.695 \times 10^{-4}$ . The vertical black dashed line shows the maximum intruded volume at peak pressure (0.92). The horizontal black dashed line shows the minimum extrusion pressure in the experiments (1 atm). (b) comparison of recovered nanopore volume at the end of the experiments when the pressure was brought to 1 atm (green square: pure water, orange

squares: water with dissolved air) with the simulated results (blue line). All calculations were done for  $\theta_a = \theta_{eq} = 120^\circ$ ,  $T = 298.15$  K,  $\tau = -4.4 \times 10^{-11}$  J/m,  $\sigma^{LV} = 0.072$  J/m<sup>2</sup>, and  $\Delta B_c = 35k_B T$ . See the main text and Appendix A for more details. .... 83

Figure 4-1. Descriptions of the systems and processes of interest in this work: (a) schematic depiction for the pore condensation and solidification process, (b) system definition for the solid nucleation at the liquid–vapor meniscus, and (c) system definition for the solid bridging of the pores. See the text for more details. .... 92

Figure 4-2. 2D schematic of the symmetric nucleus profile at the three-phase contact line in a cylinder of radius 1. The red line represents the meniscus sphere, and the blue line represents the profile of the solid–liquid interface. .... 97

Figure 4-3. Examples of the symmetric nuclei at the meniscus. (a) 2D views of some symmetric nuclei solutions. (b) Energy vs. curvature plot. (c) Energy vs. volume plot. (d) Volume vs. curvature plot. All calculations are for  $\alpha = 30^\circ$ ,  $\beta = 90^\circ$ , and  $\varphi = 45^\circ$ . In panel (a), the vapor meniscus is shown in red, and the solid nuclei are shown with the colored areas. The colored points on the plots in the bottom panels correspond to the nuclei shapes shown in panel (a). .... 103

Figure 4-4. Example of type-1 asymmetric solid nuclei at the vapor meniscus. (a) The first three panels: 3D views of the type-1 asymmetric nuclei; the last panel: an example where  $\tilde{V}_{nuc}^{S*} = 3 > \tilde{V}_{nuc,max}^S$ . The meniscus is shown by the red mesh, and the solid–liquid interface of the nucleus is shown in transparent grey. The contact line of the shape with the pore wall is shown in green. (b) Energy vs. curvature plot. (c) Energy vs. volume plot. (d) Volume vs. curvature plot. All calculations are for  $\alpha = 30^\circ$ ,  $\beta = 90^\circ$ , and  $\varphi = 90^\circ$ . The plots in panels (b), (c), and (d) are up to  $\tilde{V}_{nuc,max}^S$ . .... 105

Figure 4-5. Example of type-2 asymmetric nuclei at the meniscus. (a) The first three panels: 3D views of the type-2 asymmetric nuclei; the last panel: an example where  $\tilde{V}_{nuc}^{S*} = 4 > \tilde{V}_{nuc,max}^S$ . The meniscus is shown by the red mesh, and the solid–liquid interface of the nucleus is shown in transparent grey. The contact line of the shape with the pore wall is shown in green. (b) Energy vs. curvature plot. (c) Energy vs. volume plot. (d) Volume vs. curvature plot. All calculations are for  $\alpha = 30^\circ$ ,  $\beta = 135^\circ$ , and  $\varphi = 135^\circ$ . The plots in panels (b), (c), and (d) are up to  $\tilde{V}_{nuc,max}^S$ . .... 107

Figure 4-6. Examples of bridging of pores. (a) 3D geometries for the bridging of two pores. (b) 3D geometries for the bridging of three pores. (c) Energy vs. curvature plots. (d) Energy vs. volume plots. (e) Volume vs. curvature plots. In panels (a) and (b), the shapes are highlighted in red, blue, and green where they are pinned at the pore mouths and highlighted in yellow where they meet the flat surface at the angle  $\theta$ . All calculations are for  $\theta = 90^\circ$  and  $\tilde{l} = 8/3$ . .... 109

Figure 4-7. Symmetric nucleation at the meniscus. (a) Example free-energy plots for symmetric nuclei for  $\alpha = 30^\circ$ ,  $\beta = 90^\circ$ , and  $\varphi = 45^\circ$  (solid lines), and the corresponding spherical-cap geometries (dashed lines of the same color). (b) The free energy vs. the distance

of the solid–liquid–vapor contact line of the symmetric nucleus from the pore wall. In panels (a) and (b), the vertical dashed lines represent the transition volume. (c) Schematic of the expected nucleation path for symmetric nucleation..... 112

Figure 4-8. Asymmetric nucleation at the meniscus. (a) Example free-energy plots for the type-1 asymmetric nuclei for  $\alpha = 30^\circ$ ,  $\beta = 90^\circ$ , and  $\varphi = 90^\circ$  (solid lines), and the corresponding spherical-cap geometries (dashed lines of the same color). (b) Example free-energy plots for type-2 asymmetric nuclei for  $\alpha = 30^\circ$ ,  $\beta = 135^\circ$ , and  $\varphi = 135^\circ$  (solid lines), and the corresponding spherical-cap geometries (dashed lines of the same color). The vertical dashed lines represents the transition volume. (c) Schematic of the expected nucleation path for the type-1 asymmetric case. (d) Schematic of the expected nucleation path for the type-2 asymmetric case..... 114

Figure 4-9. Comparison of energy barriers for nucleation at the vapor meniscus as a function of solid nucleus curvature. Each row corresponds to a different  $\beta$ , and each column corresponds to a different  $\varphi$ . Colors in each panel correspond to a different  $\alpha$ , as indicated in the first panel..... 116

Figure 4-10. Bridging of pores. (a) Example free-energy plots for the bridging of the pores for  $n = 2$ ,  $\theta = 90^\circ$ , and  $\tilde{l} = 8/3$  (solid lines), and the corresponding profiles calculated for the growth of  $n$  number of spherical caps (dotted lines pinned; dashed lines not pinned). The vertical dashed line represents the transition volume. (b) Schematic of the expected bridging path..... 118

Figure 4-11. Comparison of free-energy barriers for bridging of pores (solid and dashed lines) as well as growth of a cap from a single isolated pore as a function of curvature (dotted lines). Each row corresponds to a different number of pores  $n$ , and each column corresponds to a different pore spacing  $\tilde{l}$ . Colors in each panel corresponds to different contact angle  $\theta$  as indicated in the first panel. Note that the dotted lines are the same in all panels since the growth from a single pore does not depend on  $n$  or  $\tilde{l}$ . ..... 120

Figure 6-1. Comparison of experimental data ( $\circ$ ) with the predictions of the mole-fraction-based new MSOVE for aqueous ternary electrolyte solutions from the following sources: (a) Oakes *et al.* [154]; (b) Hall *et al.* [77]; (c) and (d) Mun and Darer [147]; (e) and (f) Khitrova [105]; and (g)–(j) three papers by Gibbard *et al.* [60–62]. In the title of each panel,  $\alpha$  indicates the connecting feature of each isopleth in that panel. Note that the  $\pi$  axes are linear but the  $\Delta T_m$  axes are slightly nonlinear due to the nonlinearity of Equation (6-2)..... 166

Figure 6-2. Comparison of experimental data ( $\circ$ ) from the given reference with the predictions of the mole-fraction-based new MSOVE for aqueous ternary electrolyte solutions from the following sources: (a)–(e) three papers by Vilcu *et al.* [197–199]; and (f)–(i) Haghghi *et al.* [74]. In the title of each panel,  $\alpha$  indicates the connecting feature of each isopleth in that panel. Note that the  $\pi$  axes are linear but the  $\Delta T_m$  axes are slightly nonlinear due to the nonlinearity of Equation (6-2). ..... 167

Figure 6-3. RMSE values of predictions for every ternary system (separated based on the source) obtained using four versions of the MSOVE. The letters in square brackets are for the

references given in blue in the legend: (a) [198]; (b) [60]; (c) [197]; (d) [62]; (e) [74]; (f) [147]; (g) [61]; (h) [197–199]; (i) [77]; (j) [154]; (k) [105]. Notice that the data from the same source are grouped so that they appear sequentially. The numbers in parentheses in red at the end of each  $x$ -axis label are the numbers of experimental data points for each system..... 169

Figure 6-4. Graphical representation of the performance and residuals of the mole-fraction-based models. The top panels are for the mole-fraction-based new MSOVE, and the bottom panels are for the mole-fraction-based E-MSOVE. On the left panels, the predictions are plotted against the measurements with solid black lines representing perfect prediction. In the panels on the right, the residuals are plotted against the total concentration for each model with a histogram to the right of the panel showing the frequency distribution of the errors. Note that the histograms are given on a log scale. .... 171

Figure 6-5. Graphical representation of the performance and residuals of the molality-based models. The top panels are for the molality-based new MSOVE, and the bottom panels are for the molality-based E-MSOVE. On the left panels, the predictions are plotted against the measurements with solid black lines representing perfect prediction. In the panels on the right, the residuals are plotted against the total concentration for each model with a histogram to the right of the panel showing the frequency distribution of the errors. Note that the histograms are given on a log scale..... 172

Figure A-1. Plots of molar volumes as functions of pressure at three different temperatures:  $T = 323.15$  K (solid lines),  $T = 348.15$  K (dashed lines), and  $T = 373.15$  K (dotted lines). Panel (a) shows the plots of pure liquid water molar volume,  $v_1^L$ , and panel (b) shows the plots of infinite dilution partial molar volume,  $\bar{v}_{2,\infty}^L$ , for nitrogen in water (red lines) and for carbon dioxide in water (blue lines). .... 204

Figure A-2. Mutual solubilities of nitrogen and water as functions of pressure at three different temperatures: (a)  $T = 323.15$  K, (b)  $T = 348.15$  K, and (c)  $T = 373.15$  K. The orange lines show the mole fraction of water in vapor phase,  $y_1$ , and light blue lines show the mole fraction of nitrogen in the liquid phase,  $x_2$ , as calculated from the model described in this work. The green markers are the experimental data points for the water concentration in the vapor phase and violet markers are the experimental data points for the gas concentration in the liquid phase from the literature [6,33,34,46] as compiled in reference [1]. .... 205

Figure A-3. Mutual solubilities of carbon dioxide and water as functions of pressure at three different temperatures: (a)  $T = 323.15$  K, (b)  $T = 348.15$  K, and (c)  $T = 373.15$  K. The orange lines show the mole fraction of water in the vapor phase,  $y_1$ , and the light blue lines show the mole fraction of carbon dioxide in the liquid phase,  $x_2$ , as calculated from the model described in this work. The green markers are the experimental data points for the water concentration in the vapor phase and the violet markers are the experimental data points for the gas concentration in the liquid phase from the literature [2,5,7–9,15,21,27,35,40,44,45] as compiled in reference [38]. .... 206

Figure A-4. Pore size distribution data from the work of Li *et al.* [26]. (a) Volume density data as originally reported but normalized. (b) Transformed number density data with hydrophobic

layer thickness subtracted (red) and fitted with a continuous distribution curve (black line). All curves (both data curves and the fitted curve) are normalized in the data range to unity. ... 209

Figure B-1. Different views of an example asymmetric nucleus geometry at the meniscus before (top row) and after (bottom row) the evolution with SE. The cylinder wall and the edges on the meniscus are not shown after the evolution for clarity. The radius of the cylinder is  $R_p = 1$  and the volume of the nucleus was set to  $\tilde{V}_{nuc}^{S*} = 0.2$ . The meniscus–nucleus contact angle is  $\beta = 90^\circ$  and the contact line is highlighted in red. The cylinder–nucleus contact angle is also  $\varphi = 90^\circ$  and the contact line is highlighted in green. The meniscus angle is  $\alpha = 5^\circ$ . Note that the initial shape is not required to have the correct, prescribed volume..... 213

Figure B-2. Different views of an example bridge geometry connecting two pores before (top row) and after (bottom row) the evolution in SE. The shape is pinned at the pore mouths (circles) but makes  $\theta = 135^\circ$  angle with the flat surface between the pores (the portions of the yellow lines connecting the circles). The radii of the circles are  $R_p = 1$  and the distance between the centers of the circles is  $\tilde{l} = 8/3$ . The volume of the shape is  $\tilde{V}_{bri}^{S*} = 5$ . Note that the initial shape is not required to have the correct, prescribed volume..... 214

Figure B-3. Different views of an example bridge geometry connecting three pores before (top row) and after (bottom row) the evolution with SE. The shape is pinned at the pore mouths (circles) but makes  $\theta = 90^\circ$  angle with the flat surface between the pores (the portions of the yellow lines connecting the circles). The radii of the circles are  $R_p = 1$  and the distance between the centers of the circles is  $\tilde{l} = 10/3$ . The volume of the shape is  $\tilde{V}_{bri}^{S*} = 6$ . Note that the initial shape is not required to have the correct, prescribed volume..... 214

Figure D-1. Comparison of some of the mole-fraction-based binary fits [black lines; (a), (b), and (d) fit to CRC [47], (c) fit to Oakes *et al.* [29], and (e) fit to Gibbard and Gossmann [14]], used in this work to make predictions, with reported binary data from the sources from which the ternary data were obtained [Hall *et al.* [17] in panels (a) and (b); Vilcu *et al.* [41] in panel (a); Mun and Darer [28] in panels (a), (b), and (e); Haghighi *et al.* [16] in panels (b), (c), and (e); Oakes *et al.* [29] in panel (b); Khitrova [22] in panels (b) and (d); Gibbard and Gossmann [14] in panel (b); Gibbard and Fong [13] in panel (c)]. Dashed lines represent extrapolation of the fitted curves. None of these data points were used for fitting in this work. In particular, note that the binary data points from Haghighi *et al.* [16] and Khitrova [22] are poorly described by the curves resulting from fitting to other data or their extrapolations [panels (b), (c), and (d)]. Additionally, note the discrepancy between the experimental data available and the extrapolated polynomial for KCl which was used for the high-concentration prediction region (panel a). Because of the high number of data points in the NaCl plot [panel (b)], black arrows are used to indicate the points that have the highest deviation from the curve. .... 228

Figure D-2. Mole-fraction-based fits to binary solution data plotted as osmole fraction vs. mole fraction. Markers indicate the experimental data points, and solid lines of the same color indicate the best fit based on the mixed criterion described in the main text. The shaded region of the same color indicates the area where all coefficients are within their 95% CIs. The polynomial degree of each fit is given in the legend with the  $R_{RTO,adj}^2$  values in parentheses. .... 230

Figure D-3. Molality-based fits to binary solution data plotted as osmolality vs. molality. Markers indicate the experimental data points, and solid lines of the same color indicate the best fit based on the mixed criterion described in the main text. The shaded region of the same color indicates the area where all coefficients are within their 95% CIs. The polynomial degree of each fit is given in the legend with the  $R_{\text{RTO,adj}}^2$  values in parentheses. The units of osmolality are osmoles/kg, and the units of molality are (moles of solute)/(kg of solvent) on these plots..... 231

# List of Symbols

## Acronyms

CI	Confidence interval
E-MSOVE	Elliott <i>et al.</i> version of multisolute osmotic virial equation
MAE	Mean absolute error
MB	Mean bias
MSOVE	Multisolute osmotic virial equation
NRTL	Nonrandom two-liquid
P–R EOS	Peng–Robinson equation of state
RMSE	Root-mean-square error
RTO	Regression through the origin
SC	Spreading coefficient

## Greek symbols

$\alpha$	Function in the definition of $a^{\text{PR}}$
$\alpha_{12}, \alpha_{21}$	NRTL nonrandomness parameters
$\alpha, \beta, \varphi$	Geometrical angles
$\beta$	Vector of regression coefficients
$\beta_i$	$i$ th element of $\beta$
$\gamma^{jk}$	Interfacial tension of interface $jk$
$\gamma_i$	Activity coefficient of component $i$ in a liquid mixture
$\gamma_i^*$	Infinite dilution activity coefficient of component $i$ in a liquid mixture
$\epsilon$	Vector of model prediction errors
$\zeta$	Function representing the combined criterion to determine optimal degree of a polynomial fit
$\eta$	Parameter in the combined criterion
$\eta_1, \eta_2$	Auxiliary functions in phase-equilibrium equations



$\theta, \theta_{\text{eq}}, \theta_{\text{a}}, \theta_{\text{r}}$	Contact angle, equilibrium, advancing, and receding contact angles
$\kappa_{\text{T},1}$	Isothermal compressibility of a solvent
$\lambda_{\text{c}}$	Length of the three-phase contact line of an equilibrium nucleus
$\mu_i^j, \mu_i^{jk}$	Chemical potential of component $i$ in bulk phase $j$ or in interface $jk$
$\mu_j$	Chemical potential per particle of type $j$ in a mixture
$\mu_j^\circ$	Chemical potential per particle of pure substance $j$
$\mu_j^{\text{ex}}$	Excess chemical potential per particle of type $j$ in a mixture
$\nu$	Microscopic frequency scale
$\xi_{j \mathbf{A}_\ell}$	Multiplicity of element $j$ in multiset $\mathbf{A}_\ell$
$\pi$	Osmolality
$\pi^+$	Osmole fraction
$\rho_1$	Mass density of a solvent
$\sigma^2$	Model variance
$\sigma^{jk}$	Interfacial tension of interface $jk$
$\tau$	Line tension
$\tau_{12}, \tau_{21}$	NRTL interaction parameters
$\phi_i^{\text{V}}$	Fugacity coefficient of pure component $i$
$\hat{\phi}_i^{\text{V}}$	Fugacity coefficient of component $i$ in a vapor mixture
$\omega$	Acentric factor
$\omega_i$	Gibbs free energy change of formation of a particle group in the exact treatment
$\omega_i^{\text{nc}}$	Nonconfigurational part of $\omega_i$

## Latin symbols

$\Delta$	Change in a quantity; quantity with respect to a reference value
$\Delta S_{\text{f}}^\circ$	Standard molar entropy change of fusion of a solvent
$\delta_{ij}$	Kronecker delta
$\ell$	Index used to uniquely identify elements of $\mathbf{A}$
$\mathcal{P}_{\mathbf{A}_\ell}$	Probability of formation of an $n$ -tuple of composition $\mathbf{A}_\ell$
$Z$	Barrier transmission coefficient (Zeldovich factor)
$z_n$	Number of $n$ -tuples sharing each particle

<b>A</b>	Set of all multisets each corresponding to a unique $n$ -tuple composition
$\mathbf{A}_\ell$	Element of <b>A</b> uniquely identified by its index $\ell$ ; a multiset
$A^{jk}$	Area of interface $jk$
$A^{\text{PR}}, B^{\text{PR}}$	Alternative parameters in transformed P–R EOS
$\tilde{A}$	Nondimensional area
$a, b$	Energy and co-volume parameters of pure components
$a^{\text{PR}}, b^{\text{PR}}$	Energy and co-volume parameters in P–R EOS
$a_1$	Relative activity of a solvent
$B$	Free energy
$B_i, B_{ij}, C_i, C_{ijk}$	Second and third osmotic virial coefficients of used with molality as the variable
$B_i^+, B_{ij}^+, C_i^+, C_{ijk}^+$	Second and third osmotic virial coefficients used with mole fraction as the variable
$\tilde{B}$	Nondimensional free energy
$B, \partial B$	Arbitrary three-dimensional body and its boundary surface
$b$	Microscopic length scale
$C_1, C_2, C_3$	Auxiliary angles defined from $\alpha, \beta$ , and $\varphi$
$C_i$	$i$ th order pure osmotic virial coefficient in the exact treatment
$c$	Lower bound of integration
$c_1, c_2$	Arbitrary constants
$d$	Diameter
$d(r)$	Distance to the liquid–vapor interface from a circle of radius $r$
<b>F</b>	Matrix of regressors
$F(\varphi)$	Ratio of volumes
$F^j, F^{jk}$	Helmholtz free energy of bulk phase $j$ or interface $jk$
$f$	Equation of the profile representing the solid–liquid interface or arbitrary function
$f_i^{\text{L}}, f_i^{\text{V}}$	Fugacity of pure component $i$ as a liquid or vapor
$\hat{f}_i^{\text{L}}, \hat{f}_i^{\text{V}}$	Fugacity of component $i$ in a liquid or vapor mixture
$G$	Gibbs free energy of a solution
$G^{\text{c}}$	Configurational Gibbs free energy of a solution
$G^{\text{nc}}$	Nonconfigurational Gibbs free energy of a solution

$G^j$	Gibbs free energy of bulk phase $j$
$g$	Auxiliary function
$g_{\mathbf{A}_\ell}$	Nonconfigurational Gibbs free energy of a particle group denoted by $\mathbf{A}_\ell$ averaged over all spatial configurations
$H_{12}$	Henry's law constant
$i, j, m, k, t$	Dummy indices
$\{i_1, i_2 \dots i_n\}$	Set of dummy indices used in repeated sums
$i_j$	Element of $\{i_1, i_2 \dots i_n\}$
$\vec{i}, \vec{j}, \vec{k}$	Unit vectors in Cartesian coordinates
$J$	Nucleation rate
$k_B$	Boltzmann constant
$k_c, k^*$	Twice the mean curvature of an equilibrium surface
$k_i$	Empirical dissociation constant of solute $i$ used with molality as the variable
$k_i^+$	Empirical dissociation constant of solute $i$ used with mole fraction as the variable
$k_{ij}$	P–R EOS binary interaction parameter
$(k_d)_j$	Empirical dissociation constant of solute $j$
$\tilde{k}^*$	Nondimensional twice the mean curvature of an equilibrium surface
$l$	Distance between the centers of two adjacent pores
$l_p$	Pore length
$\tilde{l}$	Nondimensional distance between two adjacent pores
$M$	Molar mass
$m$	Total number of components in a bulk phase or molality
$m', x_i'$	Equivalent concentration and equivalent fraction
$N$	Total number of particles in a two-component solution
$N_{\mathbf{A}_\ell}$	Number of $n$ -tuples of composition $\mathbf{A}_\ell$
$N_i^j, N_i^{jk}$	Number of moles of component $i$ in bulk phase $j$ or surface excess of number of moles of component $i$ in interface $jk$
$N_j$	Number of particles of type $j$
$\vec{N}$	Unit normal vector

$n$	Total number of components in an interface, number of pores participating in bridging, number of particles in an $n$ -tuple, or number of data points used in a fit
$P$	Pressure
$p^j$	Pressure of bulk phase $j$
$P_c, T_c$	Critical pressure and temperature
$p$	Degree of a polynomial
$p_0, p_1, p_2, p_3$	Empirical functions for calculating $\phi_{1,\text{sat}}$
$Q_j^{n,m}$	$m$ th order pure coefficient of the excess chemical potential expression of solute $j$
$\hat{Q}_j^{n,m}$	$m$ th order pure osmotic virial coefficient of component $j$
$R^{jk}$	Radius of curvature of interface $jk$
$R_{1,c}, R_{2,c}$	Principal radii of curvature of an equilibrium interface
$R_{\text{cap}}$	Radius of a spherical cap
$R_p$	Pore radius
$R_{\text{RTO,adj}}^2$	RTO-adjusted R-squared value
$R_s$	Radius of the vapor meniscus sphere
$\bar{R}$	Universal gas constant
$r$	Total number of components in a mixture
<b>S</b>	Covariance matrix
$S$	Saturation ratio
$S, \partial S$	Arbitrary surface and its boundary line
$S^C$	Total entropy of a composite system
$S^j, S^{jk}$	Entropy of bulk phase $j$ or surface excess entropy of interface $jk$
$S_{ii}$	$i$ th diagonal element of <b>S</b>
$s$	Molar entropy or total salinity
$T$	Absolute temperature of a solution
$T^j, T^{jk}$	Absolute temperature of bulk phase $j$ or interface $jk$
$T_0$	Temperature parameter
$T_m$	Freezing point of a solution
$T_m^\circ$	Freezing point of a pure solvent
$T_r, \bar{T}$	Reduced temperature

$t$	Experimental time
$t_{\frac{\alpha}{2}, n-p}$	$\alpha$ th percentile of Student's $t$ -distribution for $n - p$ number of degrees of freedom
$U^j, U^{jk}$	Internal energy of bulk phase $j$ or surface excess internal energy of interface $jk$
$u, v, z$	Arbitrary independent variables
$V^j$	Volume of bulk phase $j$
$\tilde{V}$	Nondimensional volume
$v$	Molar volume
$v^{\text{PR}}$	P-R EOS molar volume
$v_1^{\text{L}}$	Molar volume of a pure liquid solvent
$\tilde{v}_{2,\infty}^{\text{L}}$	Infinite dilution partial molar volume of a gas in a solution
$w_2, w_3$	Weight percentages of salts
$w_{\mathbf{A}_\ell}$	Nonconfigurational Gibbs free energy change of formation of an $n$ -tuple of composition $\mathbf{A}_\ell$
$\bar{w}$	Weight ratio of salts
$\vec{w}, \vec{v}$	Arbitrary vector fields
$x$	Arbitrary variable
$x_0$	Radius of the intersection circle of the meniscus and the solid-liquid interface
$x_i, y_i$	Liquid- or vapor-phase mole fraction of component $i$
$x_j$	Mole fraction of particles of type $j$
$y$	Vector of calculated osmolalities or osmole fractions
$y_i$	$i$ th data point
$y_s$	Equation of the circle representing the liquid-vapor meniscus
$\bar{y}_i$	Model prediction at the $i$ th data point
$Z$	Compressibility factor
$z_i$	Charge of species $i$

# Chapter 1

## Introduction

In the broadest sense, the physical world is classically described in terms of two concepts: the concept of matter and the concept of forces. The competition between different forces causes a collection of matter to exhibit distinct and easily observable qualitative behavior, historically referred to as being a solid, liquid, or gas. There exist other, more exotic phases of matter (*e.g.*, plasma, Bose–Einstein condensate, neutron-degenerate matter), but these three are the most common in everyday life. Importantly, if the balance of the competing forces is changed (for example, by heating), the same collection of matter can go from being in one phase to another through a process known as phase transition. A phase can be further categorized as being single-component (pure) or multicomponent (mixture), depending on whether all its constituents, such as its molecules or atoms, are of the same type or not. Although pure phases have many applications in engineering and science, they are typically artificially made with almost all naturally occurring phases belonging to the multicomponent category.

When a system contains more than one phase, it is referred to as a multiphase system. If two bulk phases are brought into contact, they will share a region of space—a two-phase contact area—through which they can interact, and this is known as an interface. Similarly, three phases (or equivalently, three interfaces) can meet at what is called a three-phase contact line. These interfaces and contact lines can be made using all combinations of the three phases of matter (except when there is more than one gas phase), and they can be made between phases consisting of the same component(s), different components, or sharing some components. Although intuitively recognized throughout history, it was not until the 19th century that the importance of interfaces was firmly established through deliberate studies, which, with intensive research over the subsequent years, led to the development of a field known today as interfacial science. While many important phenomena happen directly at these boundaries such

as evaporation, adsorption, catalysis, and corrosion, interfaces can also influence the properties of the bulk phases that they separate.

The extent to which an interface affects the properties of a phase typically depends on system's size. For example, water will take the shape of a glass it is poured into with no apparent interfacial effects, whereas a small rain drop on a flat surface can be observed being a spherical cap. If we were to measure the angle this cap makes with the surface at the solid–liquid–gas contact line, we would find that it is a constant for different volumes of the drop. This observation was first qualitatively elucidated in 1805 by Thomas Young who assigned energy to each interface and further used this concept to explain liquid rise in a capillary [212]. Another piece of the puzzle was found a year later by Pierre-Simon Laplace, who, with mathematical arguments, showed that capillary action is related to the radius of the meniscus [115]. Later, mathematician Carl Friedrich Gauss unified the ideas from both works and gave a differential equation relating the mean curvature and energy of an interface to the difference in pressures in the phases it separates [56]. It turns out that the pressure inside a spherical liquid drop (gas bubble) suspended in a gas (liquid) is larger than the pressure of the gas (liquid) by an amount proportional to the energy of the interface and inversely proportional to its radius. Consequently, the effects of phase boundaries on the behavior of a system become increasingly important as either one or more of the phases it contains are made smaller.

In natural processes and in engineering, many small domains of phases (solid, liquid, or gas) with curved interfaces often exist in the same system. For example, microscopic drops of water (pure or with solutes) interact with drops of organic matter and various types of solid particles in the atmosphere. Unlike liquids, solid particles come in different shapes and sizes, some with smooth surfaces, some with rough surfaces, and some containing pores. These features of solids are essential and often control phase transitions in a cloud, such as condensation of liquids or solid formation from liquid or vapor. The collective behavior of the aerosols determines characteristics of a cloud, ultimately affecting precipitation patterns and climate [165]. Another example is a process known as froth floatation used for recovery of bitumen from oil sands. One of the crucial steps in froth floatation involves encapsulation of air bubbles by the oil phase [180]. For the effectiveness of this process, it is important to know the energy required to separate these phases, or alternatively, how stable are the distinct spatial configurations of the phases. Interface-dominated systems can also be engineered for specific

purposes. For example, lab-made porous particles with tunable features such as the pore size and shape have gained popularity in recent years owing to their numerous applications in fluid separation, energy storage, and biology. These pores can contain liquids with down to a nanoscale spatial dimension in either one direction (liquid in a slit pore) or more directions (liquid in a cylindrical pore) creating a system with a small volume but large interfacial area. The phase-change and transport properties of liquids in such confinements are of particular interest in nanoscience.

Besides being prevalent, small-scale multiphase systems typically contain at least one multicomponent phase. Following the above examples, in the atmosphere, water drops can be pure, or they may dissolve salts and/or other compounds, while the surrounding air is a mixture of mainly nitrogen, oxygen, and water vapor, with trace amounts of other gases. Bitumen in froth flotation is a blend of various types of hydrocarbons. In applications utilizing porous materials, the properties of liquids in the pores can be altered by adding solutes.

While simple multiphase systems, such as a drop on a flat surface, a liquid with one solute, or a pure liquid in an isolated pore, have been extensively studied, our knowledge of equally important but more complicated systems, such as interacting drops and bubbles, a liquid with multiple solutes, a solution in a pore, or a pure liquid in a collection of pores, is not complete. This thesis seeks to answer some questions pertaining to these problems in the framework of thermodynamics—a branch of physics that quantitatively studies properties of matter, energy, and their relations to each other.

## **1.1 Gibbsian composite-system thermodynamics**

As a scientific discipline, the history of thermodynamics began in the mid-1600s with the discovery that the temperature, pressure, and volume of a contained gas are related. The next two centuries saw the development of the field with contributions from many esteemed scientists, especially during the industrial revolution with the need to design powerful and efficient heat engines. This eventually led to two fundamental ideas: the conservation-of-energy and increase-of-entropy principles—known today, respectively, as the first and second laws of thermodynamics. Later, in his two-part seminal paper [63], Josiah Willard Gibbs presented a complete mathematical framework of thermodynamics with a list of a few



necessary postulates from which all previously known results could be derived. In the same paper, he also introduced several new concepts such as chemical potential.

To apply thermodynamics in Gibbs's framework, the first step is to define the system. A *system* is any collection of matter (single-phase, multiphase, single component, multicomponent, with or without interfaces, and so on) that is being investigated. A system is often in contact with a *reservoir* with which it can exchange matter, volume, or energy. With respect to its relation to the reservoir, a system can be *open*—if both matter and energy exchange are allowed, *closed*—if only energy and/or volume exchange are allowed, or *isolated*—if no matter, volume, or energy exchange are allowed. One important contribution of Gibbs is that systems can also be categorized as being simple or composite. A *simple* system is a system whose macroscopic thermodynamic properties, such as its temperature, pressure, and chemical potential are uniform throughout, and which is not affected by fields (*e.g.*, gravity) or charged. A *composite* system is a group of systems where each constituent can be described as a simple system. All macroscopic properties of a simple system can be put into two categories: An *intensive* property, such as temperature and pressure, does not change with the amount of matter in the system. An *extensive* property, such as energy and volume, depends on the amount of matter in the system.

Another concept is that of a thermodynamic state. A thermodynamic *state* of a system refers to a set of values of macroscopic properties that uniquely identifies the system. Specifically, thermodynamics is the study of equilibrium states. Much like mechanical equilibrium, an *equilibrium* state in thermodynamics is a state corresponding to a stationary point in the energy landscape, *i.e.*, at equilibrium states there exists no driving force in any direction for the system to change its macroscopic state. If an equilibrium state represents a global minimum, it is called a *stable* equilibrium state. If an equilibrium represents a local minimum, it is called a *metastable* equilibrium state. In all other extremum cases (local and global maxima, inflection points), it is called an *unstable* equilibrium state.

Gibbs's work is also noted for its treatment of interfaces. From a molecular standpoint, an interface is a region where the density of particles changes smoothly as one moves from one bulk phase to the other. Gibbs represented this region with a mathematical surface having area but no volume. To account for the density variation in a real system, he introduced surface excess quantities, which can be negative or positive. With these definitions, an interface can

be treated as another phase and assigned properties. One important property of an interface is its interfacial tension—the analog of pressure for a two-dimensional surface. Still, a choice needs to be made regarding the placement of the mathematical surface with respect to the bulk phases. Gibbs gave two choices: For a flat interface, the surface is placed such that the surface excess moles of one of the components is zero. This uniquely placed surface is known as the *Gibbs dividing surface*. For a curved interface, the surface is placed such that the interfacial tension is not a function of the curvature of the surface. This uniquely placed surface is known as the *Gibbs surface of tension*.

At the center of the Gibbsian composite-system thermodynamics approach is the so-called fundamental equation relating different properties of each simple subsystem. For a bulk phase denoted by  $j$ , the differential form of the fundamental equation in the entropy representation is given as [25]

$$dS^j = \frac{1}{T^j} dU^j + \frac{P^j}{T^j} dV^j - \sum_i \frac{\mu_i^j}{T^j} dN_i^j \quad (1-1)$$

where the extensive quantities  $S$ ,  $U$ , and  $V$  are the entropy, internal energy, and volume of the phase, respectively. The intensive quantities  $T$  and  $P$  are the temperature and pressure of the phase, respectively.  $\mu_i$  (intensive) and  $N_i$  (extensive) are the chemical potential and number of moles of each species  $i$  present in the phase, respectively. Equation (1-1) can also be written for the reservoir.

For an interface separating bulk phases  $j$  and  $k$ , the fundamental equation takes the following form [25]:

$$dS^{jk} = \frac{1}{T^{jk}} dU^{jk} - \frac{\sigma^{jk}}{T^{jk}} dA^{jk} - \sum_i \frac{\mu_i^{jk}}{T^{jk}} dN_i^{jk} \quad (1-2)$$

where  $\sigma$  is the interfacial tension, and  $A$  is the area of either the Gibbs dividing surface (when the interface is flat) or the Gibbs surface of tension (when the interface is curved). All the other variables in Equation (1-2) are the same as in Equation (1-1), except that the extensive variables here ( $S$ ,  $U$ , and  $N_i$ ) represent the surface excesses of these quantities.

Once the system to be examined is defined, its entropy is written as the sum of the entropies of its constituents using Equations (1-1) and (1-2). At equilibrium states, the entropy of an isolated system must be an extremum, so the derivative of the total entropy of the system,

including the reservoir, can be set to zero. Combining this condition with the constraints of the system (*e.g.*, conservation of energy, conservation of the number of moles, conservation of volume, *etc.*), a set of equations can be derived that must hold at equilibrium. These conditions for equilibrium can then be combined with equations of state for each phase (*e.g.*, the ideal gas law for a gas or an empirical equation for the tension of an interface) yielding useful equations involving observables.

While the above method identifies the equilibrium states and produces the conditions for equilibrium, it does not contain information about the stability of the equilibrium states. For that, the free energy (equivalently, thermodynamic potential) of the system should be identified. The equation acting as the free energy of the system can be found by requiring the overall change in the entropy of the entire system be nonnegative, subject to constraints. Usually, its first-order approximation with respect to extensive variables is used, which is only valid at the equilibrium states, but nevertheless, has the correct convexity at the equilibrium states allowing the states to be sorted. The equilibrium states of a system with one or two independent variables in the free-energy equation can be visually sorted by plotting the free-energy equation *vs.* these variables. When there are more independent variables, the Hessian matrix can be constructed and analyzed or, if this is not feasible, the free-energy landscape can be discretized to numerically compare the equilibrium points with their neighborhood.

## **1.2 Literature overview**

This section provides a brief background on the problems investigated in this thesis. In order to avoid having an excessive overlap, a more comprehensive literature review is reserved for the introduction of each chapter.

### ***1.2.1 Equilibrium configurations of two-phase drops***

The interaction between two small fluid domains surrounded by another fluid has applications in microfluidics, atmospheric physics, soft photonics, and oil recovery, among others. Often, qualitative methods, such as spreading coefficient, are used to sort the resulting equilibrium configurations. However, these simple methods do not provide enough detail to calculate the exact geometries and energies of the configurations. Furthermore, their applicability to drop–bubble systems needs to be checked, especially at small scales where the compressibility of the gas becomes important.

Drop–drop and drop–bubble systems at the macroscopic scale have been previously investigated, and the effects of interfacial tensions are well established. For example, Mori [144,145] gave the conditions for stability of millimeter-sized drop–bubble systems using the same free-energy equation used for drop–drop systems. In the same work, comparison with experiments verified the deduced criteria for two-phase drops. Zhang *et al.* [222] provided a method for tuning the configurations of oil–air two-phase drops in water by adding cellulosic particles. These particles were absorbed at the interfaces resulting in changes in interfacial tensions. However, only drop–drop systems have been investigated at the small scale. For example, Zarzar *et al.* [220] and Nagelberg *et al.* [148] used surfactants to adjust the interfacial tensions of micrometer-sized drop–drop systems to achieve full encapsulation or lens configurations with highly tunable and predictable behavior. In another study, Qiu and Molinero [167] studied the morphologies of atmospherically relevant water–organic liquid systems in vapor, both from thermodynamic free-energy perspective and molecular simulations. Their findings suggest that, when the system’s size is larger than  $\sim 100$  nm, the interfacial tensions between the phases can be used to accurately calculate the resulting geometries. In smaller systems, the inclusion of a line-tension term in the free-energy equation was necessary for quantitative agreement.

While there are studies dedicated to the morphology of multiphase systems, configurations and free energy of drop–bubble systems at small scales have not been thoroughly investigated. This gap in the literature is addressed in this thesis.

### ***1.2.2 Phase change in confinement***

When a liquid is confined in nanoscopic pores, the phase-change behavior of this liquid can significantly differ from its bulk behavior, and understanding the role of this confinement is one of the goals of nanoscience. Specifically, the effects of added solutes, such as dissolved gases, and the effects of the geometry of a porous medium, such as sharp corners, are not well understood.

Regarding the influence of gases, liquid-to-vapor transition in nanopores has been previously studied using equilibrium density functional theory [174], molecular dynamics simulations [12,26,120,123,129,166], and experiments [121,122,166,206]. For example, the calculations of Roth *et al.* [174] showed that a small amount of xenon gas in a hydrophobic

channel can significantly decrease its probability of being in dry state. In molecular dynamics simulations by Camisasca *et al.* [26], a single atom of argon was able to cause the drying of a water-filled pore in simulation time. Attempts were made [121] to predict the drying pressure of nanopores in the presence of a gas using the ideal solution model, but the ideality assumption is questionable in extreme confinement.

When it comes to the influence of geometry of porous media, there is a particular interest in the liquid-to-solid phase transition in confinement because this process is believed to be responsible for atmospheric ice nucleation in certain conditions. Simulations [13,30,175] and experiments [27,28,200] show that sharp features of a material (pits, cracks, corners) can be efficient nucleation sites for the initial solid formation. However, the eventual growth of the solid to form a macroscopic phase seems to be limited by the geometry of pore openings as well as the proximity of neighboring pores [27,37,38]. For example, simulations [38] and later experiments [37] of David *et al.* showed that the condensation of vapor in nanopores, then freezing of liquid in individual pores, and finally, bridging of neighboring pores was responsible for ice nucleation in undersaturated conditions. There is also some evidence that free liquid–vapor interface can further promote solid nucleation [2,75,95,100,187].

With simulation studies being time-consuming and often having limited spatial and temporal resolution (small pores, short simulation times), there is an opportunity to use Gibbsian composite-system thermodynamics to investigate the phase-change behavior of liquids in pores. To that end, one chapter of this thesis is dedicated to the calculation of the effects of a dissolved gas on the drying pressure of nanopores. In another chapter, the role of the liquid–vapor meniscus inside a pore and the role of pore proximity of the material on the ease of solid formation from a liquid are investigated.

### ***1.2.3 Multicomponent solutions***

One of the important problems of thermodynamics is the determination of the chemical potential of a mixture. Consequently, there are numerous predictive models varying in application type, complexity, and accuracy. The simplest solution model is the ideal solution model where only the entropy of mixing is considered [69]. Therefore, it is only applicable to dilute solutions. The regular solution model [69,70] adds pairwise interactions to the ideal solution model, which allows more accurate predictions to be made when the solution is no

longer dilute. However, in order to apply the regular solution model, the binary interaction parameters need to be determined. The nonrandomness of the entropy of mixing is addressed in the quasi-chemical family of models [69,82] with interactions in particle groups of varying sizes. Although the quasi-chemical approach may provide good accuracy, these models can be quite complicated to apply in practice requiring multiple input parameters. Finally, there are the so-called exact models (*e.g.*, McMillan and Mayer solution theory) [83,84,140] with minimum number of assumptions, but their application can be difficult and computationally expensive.

One easy-to-use but accurate multicomponent model was proposed by Elliott *et al.* [42], which has combining rules to make predictions for the chemical potential of a solvent with multiple solutes. This polynomial model was derived based on the regular-solution assumption but its application to different types of solutions, some of which are not expected to be regular, showed surprisingly good agreement with experimental measurements [42,163,223,224,226, 227]. The combining rules of Elliott *et al.* [42] take the form of arithmetic average for quadratic terms and geometric average for cubic terms. Additionally, this model was empirically extended to dissociating solutes by including a single fitting parameter for each solute [163].

In this thesis, a generalized polynomial model [102,179] for the Gibbs free energy of mixing of a solution (with less restrictive assumptions) is explored to derive an equation for the solvent chemical potential and update the combining rules. Furthermore, the connection between the studied model and the above-mentioned solution theories is discussed. Then, the revised model is empirically extended to dissociating solutes in the same fashion as the Elliott *et al.* version and successfully applied.

### **1.3 Thesis scope**

The objectives of this thesis are (i) to provide insights into the behavior of multiphase systems in confinement and (ii) to develop a simple predictive model for the chemical potential of multicomponent solutions. Accordingly, the thesis consists of two independent parts titled “Part I: Interplay of geometry and thermodynamics in three applications” and “Part II: Multicomponent solutions”.

### ***1.3.1 Part I: Interplay of geometry and thermodynamics in three applications***

Part I combines geometry and equilibrium thermodynamics in three different applications where the phases exist as small domains, such as drops, or a liquid confined in a nanopore, and their behavior differs from that of their bulk counterparts.

In Chapter 2 (*Thermodynamic Investigation of Droplet–Droplet and Bubble–Droplet Equilibrium in an Immiscible Medium*), equilibrium morphologies of drop–bubble and drop–drop systems are rigorously analyzed in the framework of Gibbsian composite-system thermodynamics. For exactly calculating the geometry of each configuration and computing the corresponding free energies, a set of equations are derived and solved. Additionally, by varying the fluid volumes and interfacial tensions, stability diagrams for these systems are constructed showing the regions of stability of each configuration. The importance of the correct free-energy equation for drop–bubble systems at small sizes is also highlighted.

In Chapter 3 (*Quantifying the Effects of Dissolved Nitrogen and Carbon Dioxide on Drying Pressure of Hydrophobic Nanopores*), the effects of a dissolved gas on drying pressure of hydrophobic cylindrical nanopores (emptying of liquid-filled pores) are investigated. To that end, an equation is derived that relates the nonideal chemical equilibrium of the components to the geometry of the liquid–vapor interface. This interface takes a nontrivial shape, which is calculated using an open-source finite-element tool, Surface Evolver, and the interface geometry is essential for the behavior of the liquid in the pore. Furthermore, line-tension effects are discussed, the incorporation of which shows satisfactory agreement between the available experimental data and the developed model.

In Chapter 4 (*The Role of Geometry on the Ease of Solidification Inside and Out of Cylindrical Nanopores*), solidification inside and out of nanopores is investigated from the free-energy perspective. First, the nucleation of a solid inside the pore, near the three-phase contact line, where the liquid, vapor, and the pore wall meet, is studied. Different nucleus geometries are identified depending on the internal angles of the solid and the angle of the corner generated by the liquid meniscus in the pore. Second, the bridging of neighboring pores on the porous particle surface is discussed. By considering the different number of pores participating, distance between the pores, and solid–particle contact angles, free-energy barriers are calculated. In this chapter too, the nontrivial shapes of the nuclei and bridges are

mainly calculated numerically, except for certain cases for which an analytical solution could be developed.

Overall, Part I of this thesis gives valuable insights into the behavior of three practically important systems by combining equilibrium thermodynamics with geometry.

### ***1.3.2 Part II: Multicomponent solutions***

Part II focuses on the development and application of an improved solvent chemical potential model.

The first chapter of Part II, Chapter 5 (*Multicomponent Solutions: Combining Rules for Multisolute Osmotic Virial Coefficients*), is dedicated to a theoretical exploration of a particular multicomponent solution theory, which results in a polynomial equation for the chemical potential of the solvent with multiple solutes. Additionally, combining rules are derived for this model, which allows predictions to be made for a multicomponent system based on binary data alone (data for each solute with the solvent). Furthermore, the connection between the derived model and well-known exact solution theories is elucidated.

In Chapter 6 (*Predicting Freezing Points of Ternary Salt Solutions with the Multisolute Osmotic Virial Equation*), the developed model is empirically extended to dissociating solutes and then applied to ternary salt solutions of water. This application requires the binary data to be fitted with polynomials, the degrees of which are determined using a newly proposed criterion. Moreover, a comparison with similar models used previously by our group is given.

To summarize, Part II of this thesis derives an easy-to-use polynomial model for multicomponent solutions and then illustrates its practical application to obtain accurate predictions.

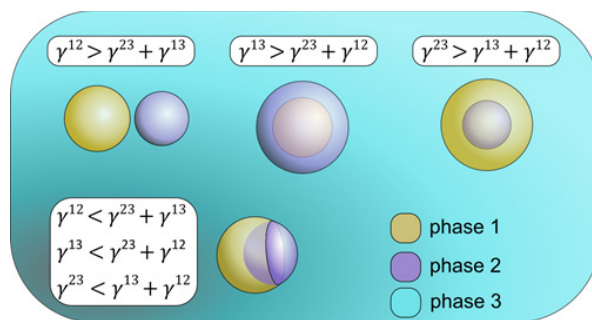
The main outcomes of this thesis are summarized in Chapter 7.



**Part I: Interplay of Geometry and Thermodynamics  
in Three Applications**

## Chapter 2

# Thermodynamic Investigation of Droplet–Droplet and Bubble–Droplet Equilibrium in an Immiscible Medium<sup>1</sup>



### Chapter summary

In the absence of external fields, interfacial tensions between different phases dictate the equilibrium morphology of a multiphase system. Depending on the relative magnitudes of these interfacial tensions, a composite system made up of immiscible fluids in contact with one another can exhibit contrasting behavior: formation of lenses in one case, complete encapsulation in another. Relatively simple concepts such as spreading coefficient (SC) have been extensively used by many researchers to make predictions. However, these qualitative methods are limited to determining the nature of the equilibrium states and do not provide enough information to calculate the exact equilibrium geometries. Moreover, due to the assumptions made, their validity is questionable at smaller scales where pressure forces due to curvature of the interfaces become significant or in systems where a compressible gas phase is

<sup>1</sup> Reproduced, with minor changes, with permission from H. Binyaminov, F. Abdullah, L. Zargarzadeh, and J. A. W. Elliott. *Thermodynamic Investigation of Droplet–Droplet and Bubble–Droplet Equilibrium in an Immiscible Medium*, J. Phys. Chem. B **125**, 8636 (2021). <https://doi.org/10.1021/acs.jpcc.1c02877> © 2021 American Chemical Society.

present. Here, we investigated equilibrium configurations of two fluid drops suspended in another fluid, which can be seen as a simple building block of more complicated systems. We used Gibbsian composite-system thermodynamics to derive equilibrium conditions and the equation acting as the free energy (thermodynamic potential) for this system. These equations were then numerically solved for an example system consisting of a dodecane drop and an air bubble surrounded by water, and the relative stability of distinct equilibrium shapes was investigated based on free-energy comparisons. Quantitative effects of system parameters such as interfacial tensions, volumes, and the scale of the system on geometry and stability were further explored. Multiphase systems similar to the ones analyzed here have broad applications in microfluidics, atmospheric physics, soft photonics, froth flotation, oil recovery, and some biological phenomena.

## 2.1 Introduction

Bubble–droplet or droplet–droplet systems, which involve attachment of two nonmixing fluids surrounded by another mutually immiscible medium (*e.g.*, an air bubble and an oil drop in water; a phase separated aerosol drop in the atmosphere, *etc.*), have been investigated by many researchers due to their importance in both natural and industrial processes. Although there exist methods to estimate the nature of the interactions and resulting geometries [6,24,78,116,144,145,167,192,220,222], increasing interest in the applications of these systems in recent years has made it necessary to study them in a more detailed framework in order to make better predictions [19,98,108,116]. For applications such as froth flotation there is a growing interest in particular properties of configurations involving bubbles. During the froth flotation used for the recovery of bitumen from oil sands, for example, the air bubbles are encapsulated by the bitumen in the conditioning step [180]. In this process, it is important to identify critical parameters of the system that result in the most stable configuration. In another example, in dissolved air flotation, microbubbles (40–70  $\mu\text{m}$ ) are used for removing impurities in water and wastewater treatment facilities. In this application, it is desirable to know the carrying capacity of bubbles of various sizes from an energy-difference perspective for the efficiency of the operation [136,189]. In the atmosphere, phase-separated aerosols have a strong impact on a number of physical and chemical processes. Their morphology determines the characteristics of absorption and reflection of solar radiation, facilitates certain chemical

reactions, creates nucleation sites for condensation or freezing in clouds, and affects the uptake of important atmospheric gases such as  $\text{N}_2\text{O}_5$  [79,138,167,214,228].

In microfluidics, encapsulation of one phase by another immiscible fluid is required for some applications. For instance, in microreactors, each pH-sensitive reaction must be carried out separately in its own environment. For this reason, compartmental hydrogels, where one phase encapsulates the other with each phase being a compartment, are used [194]. Additionally, the study of the dynamics of encapsulation and decapsulation by fluids can help give explanations for a number of biological phenomena, including fecundation, pinocytosis, and phagocytosis with eventual utilization for advancing cancer treatment through selective encapsulation of cancer cells [196]. Configurations resembling encapsulation or decapsulation and effects of shape in biological systems have been previously considered to a great extent in references [98] and [96].

Recently, special particles known as “Janus particles” with two opposite sides exhibiting dissimilar chemical and physical properties have drawn significant interest for their promising applications [57,73,116,192,220]. For these particles, it is important to be able to design and alter their morphologies to achieve certain characteristics. For example, for the perfect Janus state, the particle as a whole is required to be a perfect sphere [73]. In addition to this, increasing curiosity in soft photonics as a result of attempts to mimic nature by the use of deformable, reconfigurable materials has created an extra need for the making of virtually infinitely adjustable multiphase arrangements such as those for liquid–liquid multidrop lenses [108,148,150].

Microemulsion science is another area where understanding of interactions of immiscible fluids from the stability perspective is needed [20,57,113,177,220]. Depending on the mole fractions of components and the size of individual drops, microemulsion systems can be made stable and coalescence-free over a long period of time. For ternary, surfactant-free systems, this is usually captured in a triangular phase diagram where each side of the triangle represents the fraction of one component. A comprehensive study of single drop–drop or drop–bubble systems as presented in this chapter, can give new insights into the behavior of microemulsion systems, especially those in the presence of gas phase(s) as we provide a novel free-energy equation for drop–bubble systems. Furthermore, in the future, the effects of surfactants can be studied by building upon the framework provided in this work.

Overall, previously these bubble–droplet or droplet–droplet systems have been mostly studied in the context of spreading coefficient (SC) [19,78,132,146,153,173,210], which, by definition, is restricted only to limiting cases of the emerging shapes, and even then, their validity is questionable at the scales where other effects (*e.g.*, effects of the pressure forces due to curvature of the interface) become significant alongside the interfacial forces. The concept of spreading coefficient was first formalized in 1865 by Carlo Marangoni [133,134] (similar results were later published by other authors independently [78,98,173]). The spreading coefficient is defined as [196]

$$SC = \gamma^{13} - \gamma^{23} - \gamma^{12} \quad (2-1)$$

where  $\gamma^{13}$  is the interfacial tension between the base fluid and the surrounding medium,  $\gamma^{23}$  is the interfacial tension between the spreading fluid and the surrounding medium, and  $\gamma^{12}$  is the interfacial tension between the base fluid and the spreading fluid. The study of spreading behavior and spreading coefficient is highly focused on the spreading of aliphatic hydrocarbons on a bulk water phase, primarily due to its relevance in enhanced oil recovery from reservoirs. This is because a positive spreading coefficient ( $SC > 0$ ) means the oil phase would spread on the water phase instead of forming a lens of static oil, thereby improving oil recovery [51,132,178,180,222].

The result of the calculation in Equation (2-1) is usually used in a qualitative fashion, in that, its sign is used to determine whether a fluid will exhibit spreading behavior or form a lens. This criterion alone does not provide enough information about the geometry of the configurations, such as radii of curvature or contact angles of the interfaces of the lenses. Therefore, it is desirable to explore these systems in a more detailed framework to make better predictions about their observed behavior, and consequently, have the knowledge to design, produce, and control their geometry as required.

In this chapter, we use Gibbsian surface thermodynamics [45,63], which is one of the most powerful tools to study interfacial thermodynamics of composite systems, as previously shown by many works that have made use of it with great success [41,45,49,125,183–185,203,215–217]. Briefly, the fundamental Gibbsian thermodynamics approach is first, to develop a system of equations for the equilibrium states based on the equilibrium conditions, then combine these equations with the equations of state to calculate equilibrium geometry (possibly, more than one), and finally, derive the free energy acting for the system and analyze

the free energy to determine whether specific equilibrium states are stable, metastable, or unstable.

## 2.2 System definition and governing equations

### 2.2.1 System definition

Here, we investigate configurations of three-phase systems with interfacial curvature and determine their relative stability from the perspective of the thermodynamic free energy (thermodynamic potential). More specifically, we focus on two immiscible drops (or a drop and a bubble) in another mutually immiscible bulk medium with all interfaces considered throughout this chapter having constant curvature, as would be the case in the absence of field effects. Figure 2-1 shows reference and possible final configurations for such a system. In the reference state, there are two immiscible fluid drops (or a drop and a bubble) denoted by phase 1 and phase 2 that are not touching each other in another mutually immiscible bulk fluid denoted by phase 3 that is placed in a container sealed with a moveable, massless piston. Through its walls, the container is in contact with a reservoir denoted by superscript R, which, by definition, has fixed pressure,  $P^R$ , and temperature,  $T^R$  [25]. The reservoir and the container are only allowed to exchange volume and energy but not mass with each other, and together they make up an isolated system. After the phases are brought into contact, three final equilibrium configurations are possible (not including the reference configuration itself): (I) attached configuration where one phase partially enters the other; (II) full encapsulation of phase 1 by phase 2; and (III) full encapsulation of phase 2 by phase 1. It should be noted that these three configurations presented here are hypothetical at this point as we will need to perform free-energy analysis for a given system and for a set of system parameters to decide which configuration is more favorable compared to the reference state, if any.

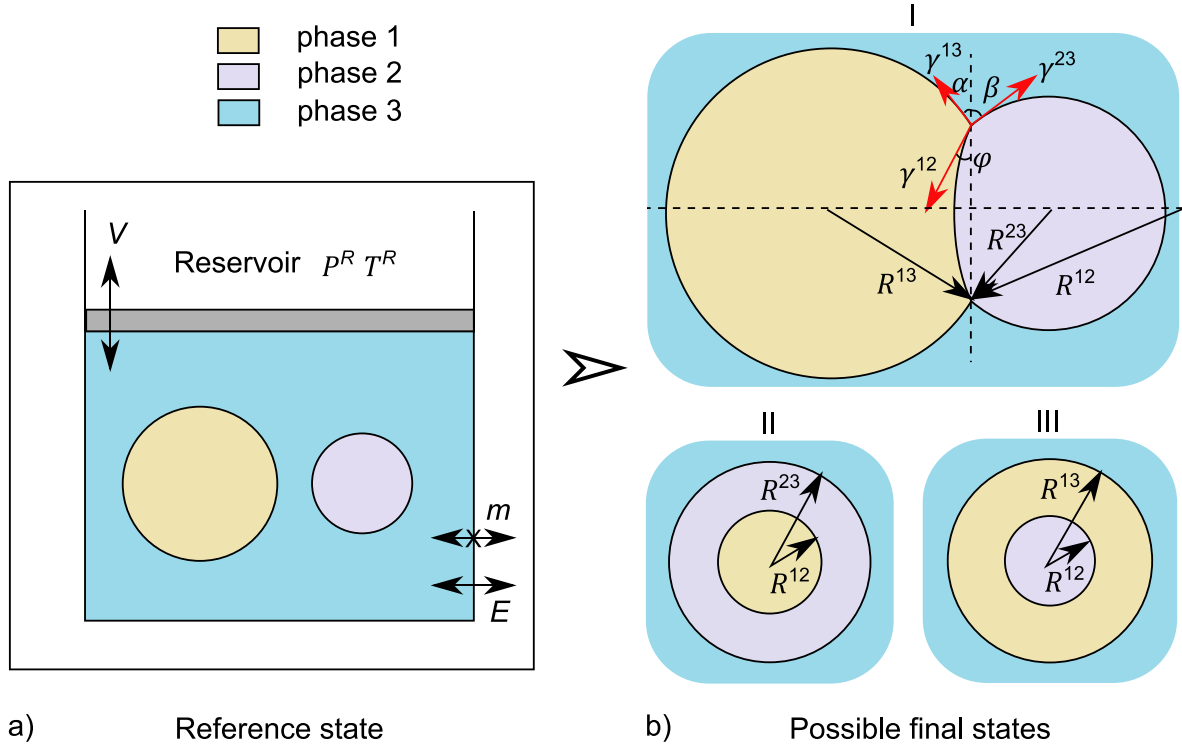


Figure 2-1. Schematics for (a) the reference state and (b) possible final states, where (I) is the attached configuration, (II) is the full encapsulation of phase 1 by phase 2 and (III) is the full encapsulation of phase 2 by phase 1. For all three configurations, the radii of curvature of the three interfaces are:  $R^{13}$ —the radius of curvature of the interface between phase 1 and phase 3;  $R^{23}$ —the radius of curvature of the interface between phase 2 and phase 3; and  $R^{12}$ —the radius of curvature of the interface between phase 1 and phase 2. For the attached configuration, the contact angles of these interfaces are given by  $\alpha$ ,  $\beta$ , and  $\varphi$ —all defined with respect to the three-phase plane (vertical dashed line).

### 2.2.2 Derivation of conditions for equilibrium

In the framework of Gibbsian composite-system interfacial thermodynamics, one finds conditions for equilibrium of a system by equating its total variation of entropy about equilibrium to zero, subject to constraints. The entropy of a composite system can be expressed as the sum of the entropies of its constituent subsystems [25]. For the most general case of our problem (the attached configuration with three maximum possible interfaces) we can write

$$dS^C = dS^R + dS^1 + dS^2 + dS^3 + dS^{12} + dS^{13} + dS^{23} = 0 \quad (2-2)$$

where  $dS^C$  represents an infinitesimal change in total entropy of the composite system,  $dS^R$ ,  $dS^1$ ,  $dS^2$ , and  $dS^3$  represent entropy changes of the reservoir and corresponding bulk phases, and finally,  $dS^{12}$ ,  $dS^{13}$ , and  $dS^{23}$  represent entropy changes of the corresponding interfaces,

all about equilibrium. Each of the terms in Equation (2-2) can be expressed in the entropy representation of the fundamental equation of thermodynamics. For the reservoir and each of the three bulk phases, the differential form of the fundamental equation is given as

$$dS^j = \frac{1}{T^j} dU^j + \frac{P^j}{T^j} dV^j - \sum_{i=1}^m \frac{\mu_i^j}{T^j} dN_i^j \quad (2-3)$$

where  $T^j$ ,  $U^j$ ,  $P^j$ ,  $V^j$  are temperature, internal energy, pressure, and volume respectively, for  $j = R$  or 1, 2, or 3.  $\mu_i^j$  and  $N_i^j$  are chemical potential and number of moles, respectively, of component  $i$  in phase  $j$ .  $m$  is the number of components in the bulk phase. Since we only consider single-component bulk fluids throughout this chapter,  $m = 1$ . For each of the interfaces, the fundamental equation can be written as

$$dS^{jk} = \frac{1}{T^{jk}} dU^{jk} - \frac{\gamma^{jk}}{T^{jk}} dA^{jk} - \sum_{i=1}^n \frac{\mu_i^{jk}}{T^{jk}} dN_i^{jk} \quad (2-4)$$

where  $\gamma^{jk}$  represents interfacial tension between phases  $j$  and phase  $k$  with an interfacial area of  $A^{jk}$ , and  $n$  stands for the number of components present at that interface. There are always two components at any given interface (between the bulk phases, each bulk phase considered to be made of a different pure component), as a result of using Gibbs surface of tension [63] to define the location of the dividing surface for curved interfaces,  $n = 2$ .

Next, constraints of the system must be specified. These constraints are given below:

- (i) the system together with the reservoir are isolated, and their energy is conserved:

$$dU^R + dU^1 + dU^2 + dU^3 + dU^{12} + dU^{13} + dU^{23} = 0 \quad (2-5)$$

- (ii) there is no mass transfer between the system and the reservoir:

$$dN_1^1 + dN_1^{12} + dN_1^{13} = 0 \quad (2-6)$$

$$dN_2^2 + dN_2^{12} + dN_2^{23} = 0 \quad (2-7)$$

$$dN_3^3 + dN_3^{13} + dN_3^{23} = 0 \quad (2-8)$$

$$dN^R = 0 \quad (2-9)$$

- (iii) there is volume exchange between the system and the reservoir:

$$dV^R + dV^1 + dV^2 + dV^3 = 0 \quad (2-10)$$



By definition, the reservoir is large enough that its intensive parameters ( $T^R$ ,  $P^R$ ) stay constant and are equal to their initially set values [25]. We assume that the values of interfacial tensions ( $\gamma^{12}$ ,  $\gamma^{13}$ , and  $\gamma^{23}$ ) do not vary for the types of interactions we investigate if the temperature is fixed.

Due to the existence of derivatives of volumes of bulk phases in Equation (2-3), as well as of interfacial areas in Equation (2-4), we must list geometric relations. These relations are stated below for the attached configuration and full encapsulation cases separately. To describe the geometries conveniently, we consider the symmetry plane (the plane of the paper) that passes through the centers of both spheres and define everything two-dimensionally on this plane. For the attached configuration [Figure 2-1 (b), case (I)] the geometric relations are:

$$V^1 = \frac{\pi(R^{13})^3}{3} [2 + \cos \alpha (2 + \sin^2 \alpha)] - \frac{\pi(R^{12})^3}{3} [2 - \cos \varphi (2 + \sin^2 \varphi)] \quad (2-11)$$

$$V^2 = \frac{\pi(R^{23})^3}{3} [2 + \cos \beta (2 + \sin^2 \beta)] + \frac{\pi(R^{12})^3}{3} [2 - \cos \varphi (2 + \sin^2 \varphi)] \quad (2-12)$$

$$A^{13} = 2\pi(R^{13})^2(1 + \cos \alpha) \quad (2-13)$$

$$A^{23} = 2\pi(R^{23})^2(1 + \cos \beta) \quad (2-14)$$

$$A^{12} = 2\pi(R^{12})^2(1 - \cos \varphi) \quad (2-15)$$

$$R^{13} = \frac{R^{12} \sin \varphi}{\sin \alpha} \quad (2-16)$$

$$R^{23} = \frac{R^{12} \sin \varphi}{\sin \beta} \quad (2-17)$$

For encapsulation of phase 1 by phase 2 [Figure 2-1 (b), case (II)] the geometric relations are:

$$V^1 = \frac{4\pi}{3} (R^{12})^3 \quad (2-18)$$

$$V^2 = \frac{4\pi}{3} [(R^{23})^3 - (R^{12})^3] \quad (2-19)$$

$$A^{12} = 4\pi(R^{12})^2 \quad (2-20)$$

$$A^{23} = 4\pi(R^{23})^2 \quad (2-21)$$

For encapsulation of phase 2 by phase 1 [Figure 2-1 (b), case (III)] the geometric relations are:

$$V^2 = \frac{4\pi}{3}(R^{12})^3 \quad (2-22)$$

$$V^1 = \frac{4\pi}{3}[(R^{13})^3 - (R^{12})^3] \quad (2-23)$$

$$A^{12} = 4\pi(R^{12})^2 \quad (2-24)$$

$$A^{13} = 4\pi(R^{13})^2 \quad (2-25)$$

To continue further, for each configuration separately, we need to differentiate the respective volumes and areas with respect to each independent variable of that configuration and obtain the total derivatives. For the attached configuration, because of the geometric relations given in Equations (2-16) and (2-17), only four of the six variables ( $\alpha$ ,  $\beta$ ,  $\varphi$ ,  $R^{13}$ ,  $R^{23}$ , and  $R^{12}$ ) are independent. The choice of the set of four variables is arbitrary. However, in order to completely describe the geometry, this set must include at least one variable from each variable pair describing each interface:  $\{\alpha, R^{13}\}$ ,  $\{\beta, R^{23}\}$ , and  $\{\varphi, R^{12}\}$ . For example, the set  $\{\alpha, R^{13}, \beta, \varphi\}$  is a valid choice of variables, but the set  $\{\alpha, R^{13}, \beta, R^{23}\}$  is not a valid choice of variables since it does not contain a variable from the last pair. Here, we choose  $\{\alpha, \beta, \varphi, R^{12}\}$  as our set of independent variables and rewrite Equations (2-11) to (2-15) in terms of these four variables. Both the contact angle of the interface between phase 1 and phase 2,  $\varphi$ , and the radius of curvature of this interface,  $R^{12}$ , are allowed to take positive and negative values, depending on whether the interface is convex or concave, respectively, towards phase 1 (e.g., in Figure 2-1 (b), case (I), since the interface between phase 1 and phase 2 is arbitrarily given as convex towards phase 1, both  $\varphi$  and  $R^{12}$  are positive). Additionally, angles  $\alpha$  and  $\beta$  are taken to be positive. Overall, we have the domains of the independent variables as given below:

$$\begin{cases} R^{12} \in (-\infty, \infty) \\ \alpha, \beta \in (0^\circ, 360^\circ) \\ \varphi \in (-180^\circ, 180^\circ) \end{cases} \quad (2-26)$$

with the condition that  $R^{12}$  and  $\varphi$  have the same signs. These are just the conventions that we adopt throughout this chapter, and the results are unaffected if different conventions are chosen.

For the case where phase 1 fully encapsulates phase 2, it is easy to see that the two radii of the spheres,  $R^{13}$  and  $R^{12}$ , completely describe the geometry and that they are the only independent variables. Likewise, when phase 2 fully encapsulates phase 1, the final configuration is completely described by  $R^{23}$  and  $R^{12}$ .

After differentiating the volume and area equations, the resulting derivatives are substituted into Equations (2-10) and (2-3) for volumes, and into Equation (2-4) for areas, together with constraints given in Equations (2-5) to (2-9) for each bulk phase and interface respectively. Note that the volume of phase 3 is arbitrary—it is not a function of the set of the variables used, and its derivative must be kept as  $dV^3$  throughout the derivation. After some algebraic manipulation, the results are substituted into Equation (2-2), which yields

$$\begin{aligned}
& \left(\frac{1}{T^1} - \frac{1}{T^R}\right) dU^1 + \left(\frac{1}{T^2} - \frac{1}{T^R}\right) dU^2 + \left(\frac{1}{T^3} - \frac{1}{T^R}\right) dU^3 + \left(\frac{1}{T^{12}} - \frac{1}{T^R}\right) dU^{12} \\
& + \left(\frac{1}{T^{13}} - \frac{1}{T^R}\right) dU^{13} + \left(\frac{1}{T^{23}} - \frac{1}{T^R}\right) dU^{23} \\
& + \left\{ \pi(R^{12})^2 \left(\frac{P^1}{T^1} - \frac{P^R}{T^R}\right) \left[ \frac{\sin^3 \varphi}{\sin^3 \alpha} (2 + 3 \cos \alpha - \cos^3 \alpha) - 2 \right. \right. \\
& \left. \left. + 3 \cos \varphi - \cos^3 \varphi \right] \right. \\
& + \pi(R^{12})^2 \left(\frac{P^2}{T^2} - \frac{P^R}{T^R}\right) \left[ \frac{\sin^3 \varphi}{\sin^3 \beta} (2 + 3 \cos \beta - \cos^3 \beta) + 2 \right. \\
& \left. - 3 \cos \varphi + \cos^3 \varphi \right] - \frac{4\pi R^{12} \gamma^{12} (1 - \cos \varphi)}{T^{12}} - \frac{4\pi R^{12} \gamma^{13} \sin^2 \varphi}{T^{13} (1 - \cos \alpha)} \\
& \left. - \frac{4\pi R^{12} \gamma^{23} \sin^2 \varphi}{T^{23} (1 - \cos \beta)} \right\} dR^{12} \\
& - \left[ \left(\frac{P^1}{T^1} - \frac{P^R}{T^R}\right) \frac{\pi(R^{12})^3 \sin^3 \varphi}{4 \sin^4 \frac{\alpha}{2}} - \frac{8\pi(R^{12})^2 \gamma^{13} \sin^2 \varphi \cos^4 \frac{\alpha}{2}}{T^{13} \sin^3 \alpha} \right] d\alpha \\
& - \left[ \left(\frac{P^2}{T^2} - \frac{P^R}{T^R}\right) \frac{\pi(R^{12})^3 \sin^3 \varphi}{4 \sin^4 \frac{\beta}{2}} - \frac{8\pi(R^{12})^2 \gamma^{23} \sin^2 \varphi \cos^4 \frac{\beta}{2}}{T^{23} \sin^3 \beta} \right] d\beta \quad (2-27) \\
& + \left\{ \pi(R^{12})^3 \left(\frac{P^1}{T^1} - \frac{P^R}{T^R}\right) \left[ \frac{\sin^2 \varphi \cos \varphi}{\sin^3 \alpha} (2 + 3 \cos \alpha - \cos^3 \alpha) \right. \right. \\
& \left. \left. + \sin \varphi (\cos \varphi - 1)^2 \right] \right. \\
& + \pi(R^{12})^3 \left(\frac{P^2}{T^2} - \frac{P^R}{T^R}\right) \left[ \frac{\sin^2 \varphi \cos \varphi}{\sin^3 \beta} (2 + 3 \cos \beta - \cos^3 \beta) \right. \\
& \left. - \sin \varphi (\cos \varphi - 1)^2 \right] - \frac{2\pi(R^{12})^2 \gamma^{12} \sin \varphi}{T^{12}} \\
& \left. - \frac{2\pi(R^{12})^2 \gamma^{13} \sin 2\varphi}{T^{13} (1 - \cos \alpha)} - \frac{2\pi(R^{12})^2 \gamma^{23} \sin 2\varphi}{T^{23} (1 - \cos \beta)} \right\} d\varphi \\
& + \left(\frac{P^3}{T^1} - \frac{P^R}{T^R}\right) dV^3 + \left(\frac{\mu_1^1}{T^1} - \frac{\mu_1^{12}}{T^{12}}\right) dN_1^{12} + \left(\frac{\mu_1^1}{T^1} - \frac{\mu_1^{13}}{T^{13}}\right) dN_1^{13} \\
& + \left(\frac{\mu_2^2}{T^2} - \frac{\mu_2^{12}}{T^{12}}\right) dN_2^{12} + \left(\frac{\mu_2^2}{T^2} - \frac{\mu_2^{23}}{T^{23}}\right) dN_2^{23} + \left(\frac{\mu_3^3}{T^3} - \frac{\mu_3^{13}}{T^{13}}\right) dN_3^{13} \\
& + \left(\frac{\mu_3^3}{T^3} - \frac{\mu_3^{23}}{T^{23}}\right) dN_3^{23} = 0
\end{aligned}$$

Because Equation (2-27) must hold valid for any arbitrary displacement about equilibrium, we may equate each coefficient of every independent variation to zero. The resulting system of 17 equations (one equation per each independent variation) is then solved

with the help of some algebraic manipulation and using trigonometric identities, which yields the conditions for equilibrium for the attached configuration:

$$T^1 = T^2 = T^3 = T^{12} = T^{13} = T^{23} = T^R \quad (2-28)$$

$$\mu_1^1 = \mu_1^{12} = \mu_1^{13} \quad (2-29)$$

$$\mu_2^2 = \mu_2^{12} = \mu_2^{23} \quad (2-30)$$

$$\mu_3^3 = \mu_3^{13} = \mu_3^{23} \quad (2-31)$$

$$\gamma^{13} \cos \alpha + \gamma^{23} \cos \beta - \gamma^{12} \cos \varphi = 0 \quad (2-32)$$

$$\gamma^{13} \sin \alpha + \gamma^{12} \sin \varphi - \gamma^{23} \sin \beta = 0 \quad (2-33)$$

$$P^1 - P^3 = \frac{2\gamma^{13}}{R^{13}} \quad (2-34)$$

$$P^2 - P^1 = \frac{2\gamma^{12}}{R^{12}} \quad (2-35)$$

$$P^2 - P^3 = \frac{2\gamma^{23}}{R^{23}} \quad (2-36)$$

$$P^3 = P^R \quad (2-37)$$

Note that Equation (2-35) does not directly result from Equation (2-27). It is obtained by inserting Equations (2-16) and (2-17) into Equations (2-34) and (2-36), respectively, subtracting Equation (2-34) from Equation (2-36) and then combining the result with Equation (2-33). For this reason, there are 18 equilibrium conditions in Equations (2-28) to (2-37) compared to 17 independent variations in Equation (2-27).

Following the same procedure highlighted for the attached configuration but instead using the geometry of the full encapsulation cases, the corresponding conditions for equilibrium are obtained. For encapsulation of phase 1 by phase 2, these conditions are found to be:

$$T^1 = T^2 = T^3 = T^{12} = T^{23} = T^R \quad (2-38)$$

$$\mu_1^1 = \mu_1^{12} \quad (2-39)$$

$$\mu_2^2 = \mu_2^{12} = \mu_2^{23} \quad (2-40)$$

$$\mu_3^3 = \mu_3^{23} \quad (2-41)$$

$$p^1 - p^2 = \frac{2\gamma^{12}}{R^{12}} \quad (2-42)$$

$$p^2 - p^3 = \frac{2\gamma^{23}}{R^{23}} \quad (2-43)$$

$$p^3 = p^R \quad (2-44)$$

Similarly, the conditions for equilibrium for encapsulation of phase 2 by phase 1 are:

$$T^1 = T^2 = T^3 = T^{12} = T^{13} = T^R \quad (2-45)$$

$$\mu_1^1 = \mu_1^{12} = \mu_1^{13} \quad (2-46)$$

$$\mu_2^2 = \mu_2^{12} \quad (2-47)$$

$$\mu_3^3 = \mu_3^{13} \quad (2-48)$$

$$p^2 - p^1 = \frac{2\gamma^{12}}{R^{12}} \quad (2-49)$$

$$p^1 - p^3 = \frac{2\gamma^{13}}{R^{13}} \quad (2-50)$$

$$p^3 = p^R \quad (2-51)$$

Equations (2-28), (2-38), and (2-45) indicate that temperatures in equilibrium states must be equal across all bulk phases and interfaces. Equations (2-29) to (2-31), (2-39) to (2-41), and (2-46) to (2-48) indicate equality of chemical potentials of component  $j$  in the subsystems in contact. Equations (2-32) and (2-33) are interfacial mechanical force balance equations in the vertical and horizontal planes, respectively, which are also known as the Young equations. Equations (2-34) to (2-36), (2-42), (2-43), (2-49), and (2-50) are additional mechanical equilibrium equations—the Young–Laplace equations for the corresponding interfaces. Note that the Young–Laplace equations for the attached configuration [Equations (2-34) to (2-36)] are given in more familiar forms in terms of the radii of curvature of the corresponding interfaces  $R^{12}$ ,  $R^{13}$ , and  $R^{23}$  instead of in terms of the set of independent variables  $\{\alpha, \beta, \varphi, R^{12}\}$ .

### 2.2.3 On the possibility of the attached configuration

Observe that Equations (2-32) and (2-33) impose limits on the range of possible values of  $\gamma^{13}$ ,  $\gamma^{23}$ , and  $\gamma^{12}$  for which an attached configuration is at all possible (*i.e.*, possibility to

find angles that satisfy these equations for given  $\gamma^{13}$ ,  $\gamma^{23}$ , and  $\gamma^{12}$ ). To investigate this, we construct a new system of three equations (clearly, only any two of the new equations are linearly independent as in the original two equations) by multiplying Equation (2-32) by  $\cos \alpha \neq 0$ , multiplying Equation (2-33) by  $\sin \alpha \neq 0$ , linearly combining them together, and then repeating for  $\beta$  and  $\varphi$ . Noting that  $\sin^2 x + \cos^2 x = 1$  we get

$$\begin{aligned} \gamma^{13} + \gamma^{23}(\cos \beta \cos \alpha - \sin \beta \sin \alpha) - \gamma^{12}(\cos \varphi \cos \alpha - \sin \varphi \sin \alpha) \\ = 0 \end{aligned} \quad (2-52a)$$

$$\begin{aligned} \gamma^{13}(\cos \beta \cos \alpha - \sin \beta \sin \alpha) + \gamma^{23} \\ - \gamma^{12}(\cos \varphi \cos \beta + \sin \varphi \sin \beta) = 0 \end{aligned} \quad (2-52b)$$

$$\begin{aligned} \gamma^{13}(\cos \varphi \cos \alpha - \sin \varphi \sin \alpha) + \gamma^{23}(\cos \varphi \cos \beta + \sin \varphi \sin \beta) \\ - \gamma^{12} = 0 \end{aligned} \quad (2-52c)$$

Further simplifying using the trigonometric identity  $\cos x \cos y - \sin x \sin y = \cos(x + y)$ , we obtain

$$\gamma^{13} + \gamma^{23} \cos(\alpha + \beta) - \gamma^{12} \cos(\varphi + \alpha) = 0 \quad (2-53a)$$

$$\gamma^{13} \cos(\alpha + \beta) + \gamma^{23} - \gamma^{12} \cos(\beta - \varphi) = 0 \quad (2-53b)$$

$$\gamma^{13} \cos(\varphi + \alpha) + \gamma^{23} \cos(\beta - \varphi) - \gamma^{12} = 0 \quad (2-53c)$$

Solving for  $\cos(\alpha + \beta)$ ,  $\cos(\varphi + \alpha)$ , and  $\cos(\beta - \varphi)$  we get

$$\cos(C_1) = \frac{(\gamma^{12})^2 + (\gamma^{23})^2 - (\gamma^{13})^2}{2\gamma^{12}\gamma^{23}} \quad (2-54a)$$

$$\cos(C_2) = \frac{(\gamma^{12})^2 - (\gamma^{13})^2 - (\gamma^{23})^2}{2\gamma^{13}\gamma^{23}} \quad (2-54b)$$

$$\cos(C_3) = \frac{(\gamma^{12})^2 + (\gamma^{13})^2 - (\gamma^{23})^2}{2\gamma^{12}\gamma^{13}} \quad (2-54c)$$

where  $C_1 = \beta - \varphi$ ,  $C_2 = \alpha + \beta$ , and  $C_3 = \varphi + \alpha$  are constants that only depend on the interfacial tensions,  $\gamma^{12}$ ,  $\gamma^{13}$ , and  $\gamma^{23}$ , and they satisfy the equality  $C_2 = C_1 + C_3$ . Ignoring the differences in the signs of some terms, the Equations (2-54a) to (2-54c) together are generally known as the law of cosines. The sign differences arise because we have defined: (i)  $\beta$  in the opposite direction of  $\alpha$ , and (ii)  $\varphi$  in the opposite direction with a  $180^\circ$  shift compared to the direction of  $\alpha$ . Since  $-1 \leq \cos x \leq 1$  for all real values of  $x$  and  $\gamma^{12}$ ,  $\gamma^{13}$ ,  $\gamma^{23} > 0$ , we finally have

$$\gamma^{13} + \gamma^{23} > \gamma^{12} \quad (2-55a)$$

$$\gamma^{12} + \gamma^{23} > \gamma^{13} \quad (2-55b)$$

$$\gamma^{12} + \gamma^{13} > \gamma^{23} \quad (2-55c)$$

as the necessary conditions for the attached configuration. Equalities are ignored as they correspond to the degenerate cases (*i.e.*, full encapsulation and the reference configurations). These inequalities are sometimes referred to as the triangle inequalities.

Using the definition of the inverse cosine function, bounds can be put on the angles appearing in Equations (2-54a) to (2-54c) as follows:

$$0^\circ < C_1 < 180^\circ \quad (2-56a)$$

$$0^\circ < C_2 < 180^\circ \quad (2-56b)$$

$$0^\circ < C_3 < 180^\circ \quad (2-56c)$$

Since the cosine function is continuous and one-to-one (bijective) in  $[0^\circ, 180^\circ]$ ,  $C_1$ ,  $C_2$ , and  $C_3$  exist and are unique for any given  $\gamma^{12}$ ,  $\gamma^{13}$ , and  $\gamma^{23}$  satisfying the triangle inequalities. Combining Equations (2-56a) to (2-56c) with the previously defined domains of variables  $\alpha$  and  $\beta$ , given in Equation (2-26), we additionally have

$$-C_1 < \varphi < C_3 \quad (2-57)$$

Now, we want to show that these inequalities are also the sufficient conditions to guarantee the existence of the attached configuration. First, notice that the conditions given by Equations (2-34) to (2-36) do not impose any restrictions on the solution, so we can ignore them for our analysis here. Next, we take the ratio of the volumes given by Equations (2-11) and (2-12), substitute Equations (2-16) and (2-17), and use the identity  $\sin^2 x + \cos^2 x = 1$  to get

$$\begin{aligned} F(\varphi) &= \frac{V^1}{V^2} \\ &= \frac{\frac{2 + 3 \cos(C_3 - \varphi) - \cos^3(C_3 - \varphi)}{\sin^3(C_3 - \varphi)} - \frac{2 - 3 \cos \varphi + \cos^3 \varphi}{\sin^3 \varphi}}{\frac{2 + 3 \cos(\varphi + C_1) - \cos^3(\varphi + C_1)}{\sin^3(\varphi + C_1)} + \frac{2 - 3 \cos \varphi + \cos^3 \varphi}{\sin^3 \varphi}} \end{aligned} \quad (2-58)$$

as a function of the single variable  $\varphi$  [because  $C_1$  and  $C_3$  are constants when the interfacial tensions are fixed, see equations (2-54a) to (2-54c)]. There are three special points (points of



discontinuity) of  $F(\varphi)$ :  $\varphi = -C_1$ ,  $\varphi = 0$  and  $\varphi = C_3$ . It is easy to see that  $\lim_{\varphi \rightarrow -C_1^+} F(\varphi) = 0$  and  $\lim_{\varphi \rightarrow C_3^-} F(\varphi) = +\infty$  by substitution. For the case where  $\varphi = 0$ , by applying l'Hôpital's rule for indeterminate limits to Equation (2-58) [from the quotient rule for limits, we can apply the limit operator in the numerator and denominator of  $F(\varphi)$  as they are nonzero], we have

$$\begin{aligned} \lim_{\varphi \rightarrow 0} \frac{2 - 3\cos \varphi + \cos^3 \varphi}{\sin^3 \varphi} &= \lim_{\varphi \rightarrow 0} \frac{(2 - 3\cos \varphi + \cos^3 \varphi)'}{(\sin^3 \varphi)'} = \lim_{\varphi \rightarrow 0} \frac{\sin \varphi}{\cos \varphi} \\ &= 0 \end{aligned} \quad (2-59)$$

Hence,  $\varphi = 0$  is a removable discontinuity, and we have

$$\lim_{\varphi \rightarrow 0} F(\varphi) = \frac{\frac{2 + 3\cos C_3 - \cos^3 C_3}{\sin^3 C_3}}{\frac{2 + 3\cos C_1 - \cos^3 C_1}{\sin^3 C_1}} \quad (2-60)$$

As  $F(\varphi)$  approaches 0 and  $+\infty$  in  $\varphi \in (-C_1, C_3)$ , from the intermediate value theorem for continuous functions, we conclude that  $F(\varphi)$  takes all positive values for  $\varphi \in (-C_1, C_3)$ , proving that a solution always exists for any final volumes. From another perspective, all values of  $\varphi$ , including  $\varphi = 0$ —given by Equation (2-60)—can be achieved by tuning the ratio of the volumes in a system. Furthermore, we will assume that the solution set is unique for a given set of system parameters provided that the triangle inequalities are satisfied (*i.e.*, only one attached configuration is possible).

#### 2.2.4 Derivation of the free-energy equation

One of the most fundamental laws of nature, as we know it today, is the second law of thermodynamics. It states that the entropy of a system, together with its surroundings, should always increase towards equilibrium and stay constant at that equilibrium—the state of maximum entropy—for any spontaneously evolving processes. The free energy (also known as the thermodynamic potential) of any system can be calculated by combining this law with constraints imposed on the system following procedures developed previously [25,45,63,203]. Since the reservoir, has constant intensive parameters, the change in its internal energy can be written as

$$\Delta U^R = T^R \Delta S^R - P^R \Delta V^R + \mu_R^R \Delta N_R^R \quad (2-61)$$

Rearranging and substituting the difference forms of Equations (2-5), (2-9), and (2-10), as well as Equations (2-28) and (2-37) into Equation (2-61), we get

$$\begin{aligned} -T\Delta S^R = & \Delta U^3 + \Delta U^1 + \Delta U^2 + \Delta U^{12} + \Delta U^{13} + \Delta U^{23} + P^3\Delta V^1 \\ & + P^3\Delta V^2 + P^3\Delta V^3 \end{aligned} \quad (2-62)$$

The increase-of-entropy principle can be expressed as

$$\Delta S^R + \Delta S^3 + \Delta S^1 + \Delta S^2 + \Delta S^{12} + \Delta S^{13} + \Delta S^{23} \geq 0 \quad (2-63)$$

After multiplying Equation (2-63) by  $-T$  and substituting Equation (2-62) for  $-T\Delta S^R$ , we have

$$\Delta \left[ \begin{aligned} & (U^3 - TS^3 + P^3V^3) + (U^1 - TS^1) + (U^2 - TS^2) + (U^{12} - TS^{12}) \\ & + (U^{13} - TS^{13}) + (U^{23} - TS^{23}) + P^3V^1 + P^3V^2 \end{aligned} \right] \leq 0 \quad (2-64)$$

identifying the free energy as the terms inside the square brackets. Finally, using the definitions of auxiliary thermodynamic functions, we obtain the equation acting as the thermodynamic potential of the system as

$$B = G^3 + F^1 + F^2 + F^{12} + F^{13} + F^{23} + P^3V^1 + P^3V^2 \quad (2-65)$$

which includes the Gibbs free energy,  $G$ , of phase 3, the Helmholtz free energy,  $F$ , of the remaining bulk phases as well as the interfaces, and additional terms,  $P^3V^1$  and  $P^3V^2$ . The free energy of a system must be computed with respect to a reference state. As shown in Figure 2-1 (a), for convenience, we choose our reference state to be the state before the contact, where phase 1 and phase 2 are separate in phase 3. (It should be noted that any equilibrium state can be taken to be the reference state, and the results will be equivalent). To quantify free energy, we rewrite Equation (2-64) using the Euler relations [25,63] for bulk phases and interfaces respectively:

$$U^j = T^j S^j - P^j V^j + \sum_{i=1}^m \mu_i^j N_i^j \quad (2-66)$$

$$U^{jk} = T^{jk} S^{jk} + \gamma^{jk} A^{jk} + \sum_{i=1}^n \mu_i^{jk} N_i^{jk} \quad (2-67)$$

which, when substituted into Equation (2-64), gives

$$\begin{aligned}
B = & \mu_3^3 N_3^3 + (-P^1 V^1 + \mu_1^1 N_1^1) + (-P^2 V^2 + \mu_2^2 N_2^2) \\
& + (\gamma^{12} A^{12} + \mu_1^{12} N_1^{12} + \mu_2^{12} N_2^{12}) \\
& + (\gamma^{13} A^{13} + \mu_1^{13} N_1^{13} + \mu_3^{13} N_3^{13}) \\
& + (\gamma^{23} A^{23} + \mu_2^{23} N_2^{23} + \mu_3^{23} N_3^{23}) + P^3 V^1 + P^3 V^2
\end{aligned} \tag{2-68}$$

for the system free energy and

$$\begin{aligned}
B_r = & \mu_{3,r}^3 N_{3,r}^3 + (-P_r^1 V_r^1 + \mu_{1,r}^1 N_{1,r}^1) + (-P_r^2 V_r^2 + \mu_{2,r}^2 N_{2,r}^2) \\
& + (\gamma^{13} A_r^{13} + \mu_{1,r}^{13} N_{1,r}^{13} + \mu_{3,r}^{13} N_{3,r}^{13}) \\
& + (\gamma^{23} A_r^{23} + \mu_{2,r}^{23} N_{2,r}^{23} + \mu_{3,r}^{23} N_{3,r}^{23}) + P_r^3 V_r^1 + P_r^3 V_r^2
\end{aligned} \tag{2-69}$$

for the free energy of the reference state (in the absence of a phase 1–phase 2 interface), where the subscript “r” indicates the reference state. Next, to calculate  $\Delta B = B - B_r$ , we assume that both the reference and the system states are equilibrium states (*i.e.*, that conditions for equilibrium apply). As a consequence of the homogenous first-order property of the fundamental equation, the variation in chemical potential of a single-component, simple system is a function of the variations in pressure and temperature, and it can be computed according to the Gibbs–Duhem relation [25]. Since we keep both  $T^R$  and  $P^R$  constant, from Equations (2-28) and (2-37),  $T^3$  and  $P^3$  are also constant. Hence, we obtain

$$\mu_3^3 = \mu_{3,r}^3 \tag{2-70}$$

To continue further, it is necessary to specify the equations of state and the relations for the chemical potentials for the remaining phases. Note that, as there is no notion of a gas–gas interface (*i.e.*, they always mix), there are three distinct possibilities depending on the physical phases of the sub-systems to fit in our framework: (i) two liquid drops surrounded by another liquid; (ii) a liquid drop and a gas bubble surrounded by a liquid; and, (iii) two liquid drops surrounded by a gas. From here on, we will assign the superscript “2” to the gas bubble in the discussions of the second scenario.

Using the Gibbs–Duhem relation and assuming incompressibility, for the chemical potential and volume of any liquid phase, we can write [25,45]

$$\mu(T, P) = \mu_r(T, P_r) + v(P - P_r) \tag{2-71}$$

$$V = V_r \tag{2-72}$$

respectively, where  $v$  denotes molar volume of liquid. Equivalently, assuming ideality, for the chemical potential and the volume of any gas phase in the system, we have [25,45]

$$\mu(T, P) = \mu_r(T, P_r) + \bar{R}T \ln \frac{P}{P_r} \quad (2-73)$$

$$PV = P_r V_r \quad (2-74)$$

respectively, where  $\bar{R}$  is the universal gas constant.

Additionally, we assume that the numbers of absorbed molecules at the interfaces are negligible compared to the numbers of molecules in the bulk phases. Finally, subtracting Equation (2-69) from Equation (2-68), substituting appropriate forms of Equations (2-71) to (2-74) and conserving the number of molecules in bulk phases yields the free-energy equation for the case when phase 2 is a gas (subscript “g”):

$$\begin{aligned} \Delta B_g = & P^3(V^2 - V_r^2) + \gamma^{13}(A^{13} - A_r^{13}) + \gamma^{23}(A^{23} - A_r^{23}) + \gamma^{12}A^{12} \\ & - P_r^2 V_r^2 \ln \frac{P_r}{P^2} \end{aligned} \quad (2-75)$$

and when both phase 1 and 2 are liquids (subscript “l”):

$$\Delta B_l = \gamma^{13}(A^{13} - A_r^{13}) + \gamma^{23}(A^{23} - A_r^{23}) + \gamma^{12}A^{12} \quad (2-76)$$

The first term in Equation (2-75) represents the energy contribution related to the volume change of phase 2, and it is not cancelled by the last term, which is due to the chemical potential change. These two contributions cancel each other when both phases (phase 1 and phase 2) are liquids as seen in Equation (2-76).

Note that the free-energy equations are derived for the attached configuration as the general case but are also applied to the other two cases by simply taking  $A^{13} = 0$  when phase 2 encapsulates phase 1, and  $A^{23} = 0$  when phase 1 encapsulates phase 2. As we did not need to specify whether phase 3 is liquid or gas for the purposes of derivation of Equation (2-76), it is valid when two immiscible liquid drops are surrounded by either a liquid or a gas.

## ***2.2.5 On the stability of the equilibrium states***

### ***2.2.5.1 Explicit forms of the free-energy equations as functions of geometry around equilibrium***

Equilibrium states can be stable, metastable, or unstable depending on whether the function acting as the free energy of the system attains a global minimum, a local minimum,

or a maximum (or an inflection point, or a saddle point if there is more than one degree of freedom), respectively, at the equilibrium point. Therefore, it is sufficient to investigate the free energy in the neighborhood of the equilibrium to identify the nature of that equilibrium. For arbitrary small variations in the vicinity of an equilibrium state, higher order terms in the expansion of the equations of the intensive parameters of the system can be neglected retaining only the first order terms. Therefore, intensive parameters can be assumed to be constant and equal to their equilibrium values around equilibrium [203]. Additionally, the volume of the gaseous phase at equilibrium,  $V^2$ , is constant for small changes around equilibrium as it is a function of the pressure of the gas, given by the ideal gas law.

After inserting Equations (2-13) to (2-15) into Equations (2-75) and (2-76), we obtain

$$\begin{aligned} \Delta B_g = \pi(R^{12})^2 \left[ \frac{\gamma^{13} \sin^2 \varphi}{1 - \cos \alpha} + \frac{\gamma^{23} \sin^2 \varphi}{1 - \cos \beta} + \gamma^{12}(1 - \cos \varphi) \right] - \gamma^{13} A_r^{13} \\ - \gamma^{23} A_r^{23} + P^3(V^2 - V_r^2) - P_r^2 V_r^2 \ln \frac{P_r^2}{P^2} \end{aligned} \quad (2-77)$$

$$\begin{aligned} \Delta B_l = \pi(R^{12})^2 \left[ \frac{\gamma^{13} \sin^2 \varphi}{1 - \cos \alpha} + \frac{\gamma^{23} \sin^2 \varphi}{1 - \cos \beta} + \gamma^{12}(1 - \cos \varphi) \right] - \gamma^{13} A_r^{13} \\ - \gamma^{23} A_r^{23} \end{aligned} \quad (2-78)$$

as functions of geometry. Note that  $V^2$  and  $P^2$  in Equation (2-77) are not functions of geometry in the neighborhood of an equilibrium state, and they take different values at different equilibrium states.

### ***2.2.5.2 Reference configuration and full encapsulation cases viewed as the limits of the attached configuration***

From Equations (2-13) to (2-15), we notice that as  $\alpha \rightarrow 0^\circ$  and  $\varphi \rightarrow 180^\circ$ , the attached configuration approaches the phase-1-encapsulating-phase-2 case, and  $\beta$  becomes undefined. Similarly, as  $\beta \rightarrow 0^\circ$  and  $\varphi \rightarrow -180^\circ$ , the attached configuration approaches the case where phase 2 encapsulates phase 1, and  $\alpha$  becomes undefined. Additionally, as  $\alpha \rightarrow 0^\circ$  and  $\beta \rightarrow 0^\circ$ , the configuration corresponds to two phases being separate (the reference state), where  $\varphi$  is undefined. Of course, these values cannot be directly substituted into the equations describing the attached configuration as the system would not be well-defined; instead, a simpler, more intuitive approach can be used to investigate the stability of these cases due to their simpler geometry. Without loss of generality, we take a drop and a bubble that are in the reference state

(i.e., separate in phase 3) and analyze what happens when they just touch each other and create a small drop–bubble interfacial area denoted by  $dA^{12}$ . Because this area is small, it can be approximated by a flat disk with diameter

$$d = \sqrt{\frac{4dA^{12}}{\pi}} \quad (2-79)$$

From geometry, angles  $\alpha$  and  $\beta$  are given by the following relations:

$$\alpha = \sin^{-1} \frac{d}{2R_r^{13}} \quad (2-80)$$

$$\beta = \sin^{-1} \frac{d}{2R_r^{23}} \quad (2-81)$$

where  $R_r^{13}$  and  $R_r^{23}$  indicate the radii of the drop and the bubble, respectively, and  $\sin^{-1}$  is the inverse sine function. Using Equations (2-13) and (2-14), corresponding changes in the areas of the remaining interfaces would be

$$\begin{aligned} dA^{13} &= A^{13} - A_r^{13} = 2\pi(R_r^{13})^2 \left[ 1 + \cos \left( \sin^{-1} \frac{d}{2R_r^{13}} \right) \right] - 4\pi(R_r^{13})^2 \\ &= 2\pi(R_r^{13})^2 \left( 1 + \sqrt{1 - \left( \frac{d}{2R_r^{13}} \right)^2} \right) - 4\pi(R_r^{13})^2 \\ &= 2\pi(R_r^{13})^2 \left( 1 + \sqrt{1 - \frac{dA^{12}}{\pi(R_r^{13})^2}} \right) - 4\pi(R_r^{13})^2 \\ &= 2\pi(R_r^{13})^2 \left[ 2 - \frac{dA^{12}}{2\pi(R_r^{13})^2} \right] - 4\pi(R_r^{13})^2 = -dA^{12} \end{aligned} \quad (2-82)$$

and

$$dA^{23} = A^{23} - A_r^{23} = -dA^{12} \quad (2-83)$$

In Equations (2-82) and (2-83), we have used the approximation  $\sqrt{1-x} \approx 1-x/2$  because the higher order terms are negligible when  $x$  is sufficiently small. Substituting Equations (2-82) and (2-83) back into Equation (2-75) and noting that  $P^2$  and  $V^2$  do not change around equilibrium, we have

$$dB_g = (\gamma^{12} - \gamma^{13} - \gamma^{23})dA^{12} \quad (2-84)$$

Notice that the reference configuration is unstable (*i.e.*, the change in free energy is negative) when  $\gamma^{12} < \gamma^{13} + \gamma^{23}$ . With similar arguments, it can be shown that the case where phase 1 encapsulates phase 2 is unstable when  $\gamma^{23} < \gamma^{12} + \gamma^{13}$ , and that the case where phase 2 encapsulates phase 1 is unstable when  $\gamma^{13} < \gamma^{12} + \gamma^{23}$ . Furthermore, note that when all three of these configurations are unstable (*i.e.*, when the triangle inequalities are satisfied), the physical interpretation is that the attached configuration must be stable. Additionally, it is easy to check that only one configuration out of four (including the reference configuration) discussed in this chapter can be stable for given  $\gamma^{12}$ ,  $\gamma^{13}$ , and  $\gamma^{23}$ . These results are in full agreement with the predictions of the spreading coefficient concept and can be seen as the generalization of it to systems of all scales that may have a gas phase present.

### ***2.2.6 On the contributions of the first and the last terms in Equation (2-75)***

In the case of a liquid drop and a gas bubble surrounded by a liquid, depending on the size of the bubble or the magnitude of the external pressure, if the Laplace pressure is small compared to the external pressure ( $P^R \gg P^{\text{Laplace}}$ ) we have:  $P^3 \approx P^2 \approx P_r^2$ . Using the Taylor series expansion of  $\ln x$  at  $x = 1$  we have

$$\ln \frac{P_r^2}{P^2} \approx \frac{P_r^2}{P^2} - 1 \quad (2-85)$$

Substituting Equation (2-85) into Equation (2-75), the first and the last terms cancel out leaving only the interfacial terms [*i.e.*, Equation (2-75) reduces to Equation (2-76)]. Intuitively, this means that, when the pressure caused by a curved interface is small compared to the external pressure, the compression of the gas can be neglected and the free energy is the same as that for the liquid case.

On the other hand, if the Laplace pressure is much higher than the bulk pressure ( $P^R \ll P^{\text{Laplace}}$ ) (*e.g.*, a nanoscale system), we note that the contribution of the last term in Equation (2-75) would be significantly larger compared to the first term. This is because the last term is of order of magnitude of  $\sim P_r^2 V_r^2$ , whereas the first term is of order of magnitude of  $\sim P^3 V_r^2$ , where  $P^3 \ll P_r^2$ .

## **2.3 Results and discussion**

In this section, the equilibrium of an air bubble with a dodecane drop (referred to as “oil” hereafter) in water is considered for analysis as an example (for clarity, superscripts are

changed: “1” to “o” for oil, “2” to “a” for air and “3” to “w” for water). For simplicity, solubilities of these substances in one another are ignored and they are treated as completely immiscible. To solve for equilibrium, the required system parameters are given in Table 2-1. Temperature,  $T^R = 22$  °C, is only given for reference for which the values of the interfacial tensions were selected, and it is not directly used in the calculations. We first use the parameters from Table 2-1 to obtain solutions for each equilibrium configuration and compare free energies, then explore how varying some of these parameters individually or, in some cases, systematically may affect the resulting geometries. Lastly, the effects of the system scale are investigated.

Table 2-1. Input parameters used to solve for equilibrium configurations in Table 2-2.  $\gamma^{ow}$  and  $\gamma^{oa}$  are from reference [65], and  $\gamma^{aw}$  is from reference [229].

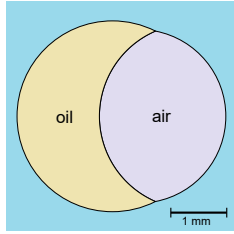
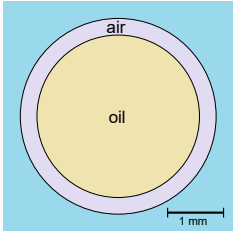
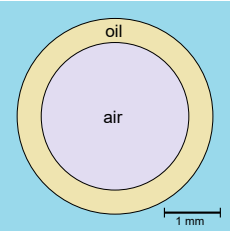
Parameter	Value	Units
$T^R$	22	°C
$P^R$	101325.0	Pa
$V^o$	$100 \times 10^{-9}$	m <sup>3</sup>
$V_r^a$	$75 \times 10^{-9}$	m <sup>3</sup>
$\gamma^{ow}$	53.7	mN/m
$\gamma^{aw}$	72.4	mN/m
$\gamma^{oa}$	25.3	mN/m

Due to the complexity and nonlinear nature of the equations, an analytical solution could not be developed. Instead, the numerical solver *vpasolve()* from MATLAB (v.2020b, Natick, MA, USA) was successfully adopted to solve for equilibrium configurations. First, we calculate the radius of the air bubble in the reference state,  $R_r^{aw}$ , using the equation for the volume of a sphere and the corresponding reference pressure of air  $P_r^a$  from the Laplace equation written for the reference radius of curvature  $R_r^{aw}$ . Then we simultaneously solve: (i) Equations (2-11), (2-12), (2-16), (2-17), (2-32) to (2-34), (2-36), and (2-74) for unknowns  $V^a$ ,  $R^{aw}$ ,  $R^{ow}$ ,  $P^o$ ,  $P^a$ ,  $R^{oa}$ ,  $\alpha$ ,  $\beta$ ,  $\varphi$  for the attached configuration, (ii) Equations (2-18), (2-19), (2-42), (2-43), and (2-74) for unknowns  $V^a$ ,  $R^{aw}$ ,  $P^o$ ,  $P^a$ ,  $R^{oa}$  for the configuration where air encapsulates oil, and (iii) Equations (2-22), (2-23), (2-49), (2-50), and (2-74) for unknowns  $V^a$ ,  $R^{ow}$ ,  $P^o$ ,  $P^a$ ,  $R^{oa}$  for the configuration where oil encapsulates air. Therefore, we obtain the



values describing the geometry and the states of the bulk phases of final configurations. Free energies are then calculated for each configuration by substituting these results into Equation (2-75). Results are given in Table 2-2 with diagrams drawn to scale.

Table 2-2. Solutions of the systems of equations for each configuration with given parameters as specified in Table 2-1 with diagrams to scale.

Configuration:	(I)	(II)	(III)	Units
Figures to scale				
$V^a$	$75.006 \times 10^{-9}$	$75.01 \times 10^{-9}$	$75.004 \times 10^{-9}$	$\text{m}^3$
$R_r^a$	0.002616	0.002616	0.002616	m
$P_r^a$	101380.4	101380.4	101380.4	Pa
$R^{aw}$	0.003070	0.003470	N/A	m
$R^{ow}$	0.003379	N/A	0.003470	m
$P^o$	101356.8	101384.3	101356.0	Pa
$P^a$	101372.2	101366.7	101375.3	Pa
$R^{oa}$	0.003287	0.002879	0.002616	m
$\alpha$	63.009	N/A	N/A	$^\circ$
$\beta$	101.317	N/A	N/A	$^\circ$
$\varphi$	66.326	N/A	N/A	$^\circ$
$B - B_r$	$-1.75 \times 10^{-6}$	$1.77 \times 10^{-6}$	$-1.52 \times 10^{-6}$	J

In this particular example, because the interfacial tensions,  $\gamma^{ow}$ ,  $\gamma^{aw}$ , and  $\gamma^{oa}$  satisfy the triangle inequalities, the reference configuration and the two full encapsulation configurations are unstable, while the attached configuration is stable. To visualize this, a 3D free-energy plot is given in Figure 2-2 (a). It is plotted using Equation (2-77) with two volume constraints given by Equations (2-11) and (2-12) with geometry Equations (2-16) and (2-17)

substituted in. The  $x$ - and  $y$ -axes represent  $\alpha + \beta$  and  $\varphi$ , respectively. Note that this selection of variables to plot against is arbitrary and setting both  $\alpha + \beta$  and  $\varphi$  fixes both  $\alpha$  and  $\beta$  as the system effectively only has two degrees of freedom (four variables,  $\alpha$ ,  $\beta$ ,  $\varphi$ ,  $R^{12}$ , and two constraints). However, this selection results in the best visual representation of the free-energy surface and all three of the limiting cases appear as straight lines since one of  $\alpha$ ,  $\beta$ , or  $\varphi$  is undefined at those limits as noted earlier. These straight lines are shown in red on all panels of Figure 2-2 at  $\varphi = 180^\circ$  (representing the oil-encapsulating-air configuration),  $\varphi = -180^\circ$  (representing the air-encapsulating-oil configuration), and  $\alpha + \beta = 0^\circ$  (representing the reference configuration; notice that the free energy is zero for the reference configuration). Figure 2-2 (a) shows that for the parameters in Table 2-1 only one minimum (a global minimum) is observed at the point corresponding to the stable equilibrium being the attached configuration with  $\alpha = 63^\circ$ ,  $\beta = 101.3^\circ$ , and  $\varphi = 66.3^\circ$  [indicated by the blue lines on Figure 2-2 (a)]. It is clear from this plot that the limiting cases are unstable meaning that, as soon as the three-phase contact line is created, the system will evolve towards the stable attached configuration.

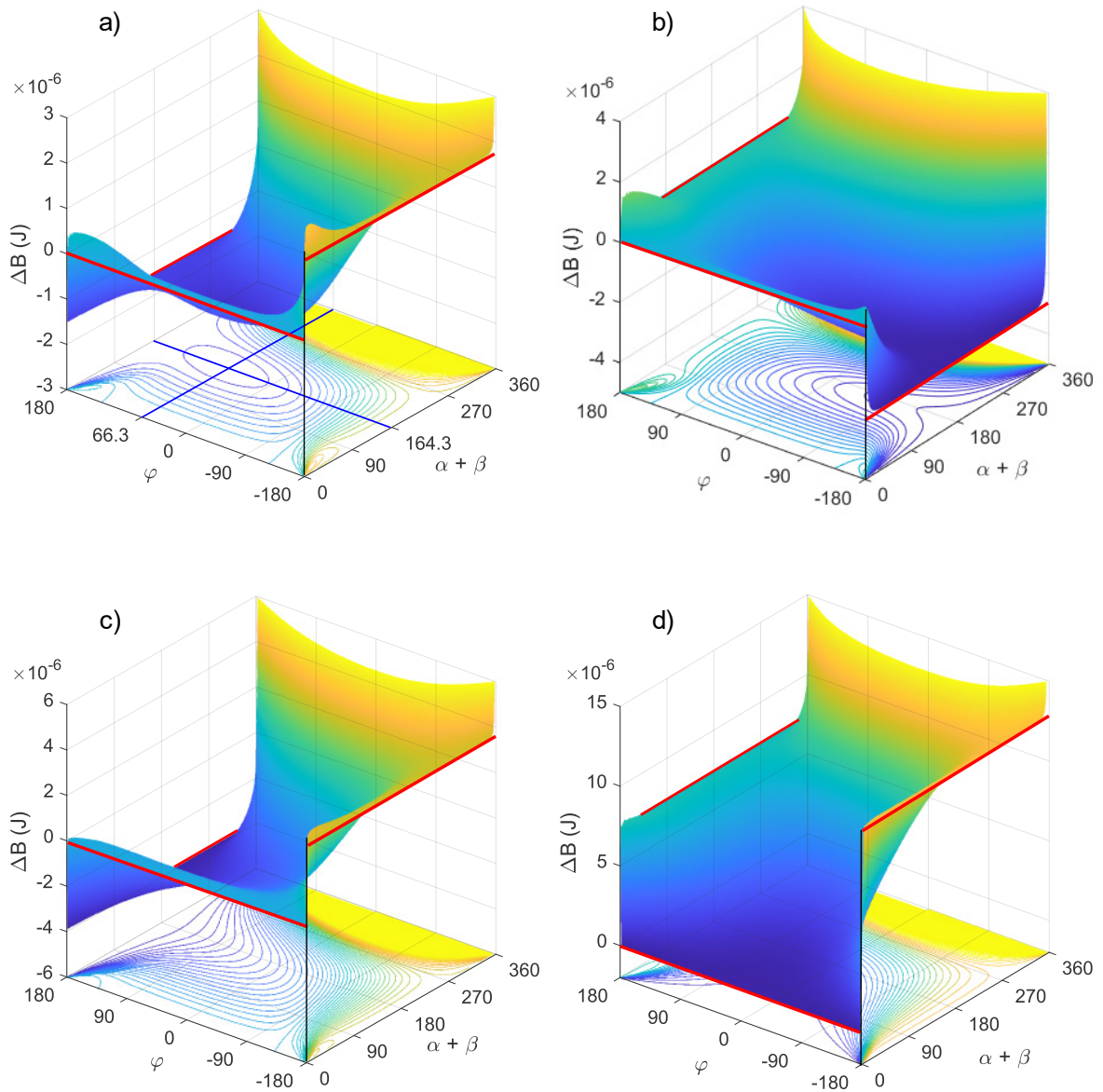


Figure 2-2. 3D free-energy plots and contour maps as functions of two variables,  $\alpha + \beta$  and  $\varphi$ , for (a) a system with the system parameters given in Table 2-1; (b) the same system as in (a) except with  $\gamma^{ow} = 100 \text{ mN/m} > \gamma^{aw} + \gamma^{oa} = 72.4 + 25.3 = 97.7 \text{ mN/m}$ ; (c) the same system as in (a) except with  $\gamma^{aw} = 100 \text{ mN/m} > \gamma^{ow} + \gamma^{oa} = 53.7 + 25.3 = 79 \text{ mN/m}$ ; and (d) the same system as in (a) except with  $\gamma^{oa} = 130 \text{ mN/m} > \gamma^{ow} + \gamma^{aw} = 53.7 + 72.4 = 126.1 \text{ mN/m}$ . The plot in (a) shows a stable equilibrium (a global minimum) at  $\alpha + \beta = 164.3^\circ$  ( $\alpha = 63^\circ$  and  $\beta = 101.3^\circ$ ) and  $\varphi = 66.3^\circ$  indicated by the blue lines corresponding to the attached configuration. The bold, red lines on all figures represent the limiting configurations. Namely, the line at  $\varphi = 180^\circ$  represents the oil-encapsulating-air configuration, the line at  $\varphi = -180^\circ$  represents the air-encapsulating-oil configuration, and the line at  $\alpha + \beta = 0^\circ$  represents the reference configuration.

We further explore the plot of the free-energy function by changing values of each individual interfacial tension to values such that the triangle inequalities no longer hold. In each case, this results in a shift to the plot towards one of the limiting cases making its free energy minimum, while the global minimum corresponding to the attached configuration disappears. In Figure 2-2 (b), the oil–water interfacial tension is set to be  $\gamma^{\text{ow}} = 100 \text{ mN/m}$ , while all the remaining system parameters are kept as given in Table 2-1, so that  $\gamma^{\text{ow}} > \gamma^{\text{aw}} + \gamma^{\text{oa}} = 72.4 + 25.3 = 97.7 \text{ mN/m}$  for which the air-encapsulating-oil configuration (represented by the red line at  $\varphi = -180^\circ$ ) is the only stable configuration as shown by its free energy being a global minimum. Similarly, in Figure 2-2 (c), we set  $\gamma^{\text{aw}} = 100 \text{ mN/m} > \gamma^{\text{ow}} + \gamma^{\text{oa}} = 53.7 + 25.3 = 79 \text{ mN/m}$  for which the oil-encapsulating-air configuration (represented by the red line at  $\varphi = 180^\circ$ ) is the only stable configuration as shown by its free energy being a global minimum. And finally, in Figure 2-2 (d), we set  $\gamma^{\text{oa}} = 130 \text{ mN/m} > \gamma^{\text{ow}} + \gamma^{\text{aw}} = 53.7 + 72.4 = 126.1 \text{ mN/m}$  for which the reference configuration (represented by the red line at  $\alpha + \beta = 0^\circ$ ) is the only stable configuration as shown by its free energy being a global minimum.

### ***2.3.1 Effects of system parameters on free energy and geometry of equilibrium configurations***

Next, we look at the effects of the system parameters on the free energy of the equilibrium configurations and geometry of the attached configuration. For brevity, the effects on the geometry of the full encapsulation cases are omitted since they are relatively simple. Because the number of initial parameters that can be individually varied is large ( $T^{\text{R}}$ ,  $P^{\text{R}}$ ,  $V^{\text{o}}$ ,  $V_{\text{r}}^{\text{a}}$ ,  $\gamma^{\text{oa}}$ ,  $\gamma^{\text{ow}}$ , and  $\gamma^{\text{aw}}$ ), it is not practical to analyze their combined effects all at once, instead they are considered individually, and the reservoir pressure,  $P^{\text{R}} = 101.325 \text{ kPa}$ , and the temperature,  $T^{\text{R}} = 22 \text{ }^\circ\text{C}$ , are kept constant throughout for simplicity.

#### ***2.3.1.1 Effects of the initial volume of the air bubble***

For a fixed volume of the oil drop of  $V^{\text{o}} = 100 \times 10^{-9} \text{ m}^3$ , the effects of the ratio of the initial volume of the air phase to the volume of the oil phase,  $V_{\text{r}}^{\text{a}}/V^{\text{o}}$  are shown in Figure 2-3 over a range from 0.001 to 1000. The  $x$ -axis is given in logarithmic scale for clarity. Figure 2-3 (a) shows the free energy with respect to a reference state as a function of relative

air volume for each configuration. As expected, at small volume ratios, the free energy associated with the air-encapsulating-oil configuration is high as this would mean a formation of a thin shell of the air phase around the much bigger oil phase resulting in an increase in the air–water interfacial area. On the other hand, at high volume ratios, the oil-encapsulating-air configuration has much higher free energy as this would mean a formation of a thin shell of oil around the much bigger air phase, hence greatly increasing the oil–water interfacial area and the free energy. In Figure 2-3 (a), note that each  $x$ -axis value represents a different system, and therefore, extrema on this plot do not have a stability meaning. It should be noted that the reference configuration and the two full encapsulation configurations are always unstable, and the attached configuration is always stable (minimum free energy) as expected.

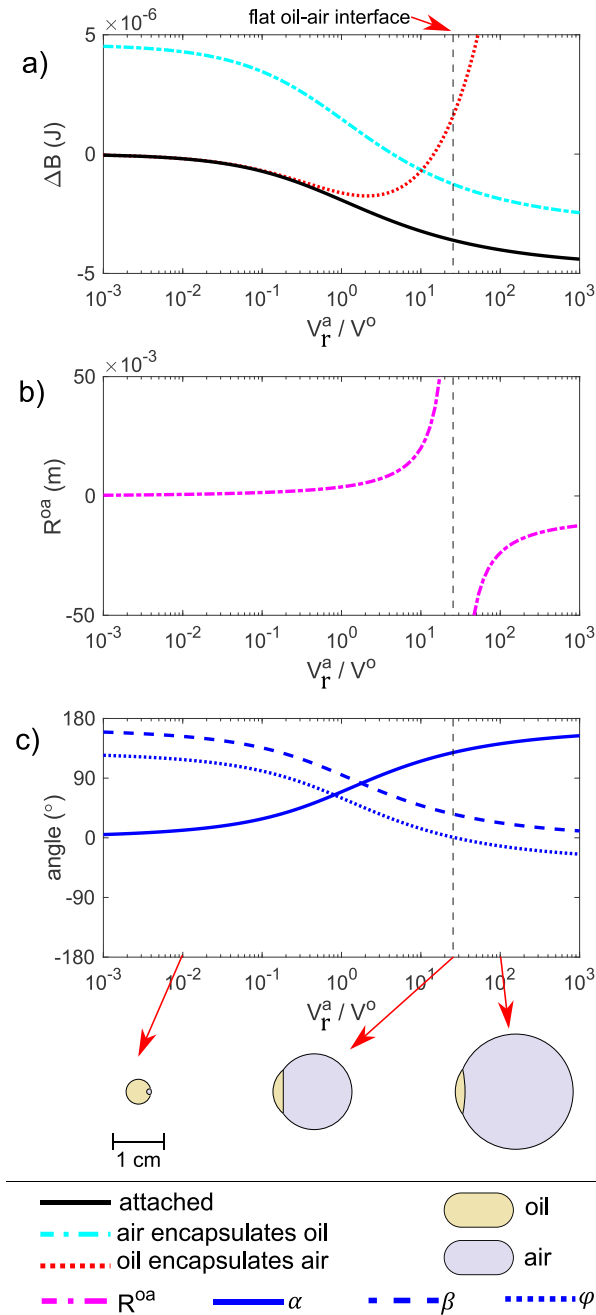


Figure 2-3. Effect of the ratio of the initial volumes of air phase to oil phase on: (a) the free energy with respect to the reference state; (b) the radius of the oil–air interface,  $R^{oa}$ , for the attached configuration; and (c) the contact angles  $\alpha$ ,  $\beta$ , and  $\varphi$ , for the attached configuration. Three example schematics from the attached configuration are shown with (from left to right): positively curved interface ( $V_r^a/V^o = 0.01$ ); flat interface ( $V_r^a/V^o \approx 27$ ); and negatively curved interface ( $V_r^a/V^o = 100$ ). The volume of the oil phase,  $V^o = 100 \times 10^{-9} \text{ m}^3$ , is kept constant. The remaining system parameters are fixed as given in Table 2-1. The vertical dashed line indicates the volume ratio where the flat oil–air interface occurs. Note that, in (a), each x-axis value represents a different system, and therefore, extrema on these plots do not have a stability meaning.

In Figure 2-3, panels (b) and (c) together describe the geometry in terms of the radius of curvature of the oil–air interface,  $R^{oa}$ , and the contact angles  $\alpha$ ,  $\beta$ , and  $\varphi$ , respectively, as the volume of the air phase is varied. In this range, both negative and positive curvatures of the oil–air interface are observed. This interface is flat around  $V_r^a/V^o \approx 27$  for which a schematic is given, together with two additional example schematics at  $V_r^a/V^o = 0.01$  and  $V_r^a/V^o = 100$ , all indicated by the red arrows.

The effects of changing the volume of the oil phase are omitted for brevity as they would be practically the same (but opposite in terms of direction) of changing the volume of the air phase. For example, increasing the volume of the air phase, in some sense, is equivalent to decreasing the volume of the oil phase as long as we are staying in roughly the same size scale.

### ***2.3.1.2 Effects of interfacial tensions***

To investigate the effects of the interfacial tensions,  $\gamma^{ow}$ ,  $\gamma^{oa}$ , and  $\gamma^{aw}$ , we separately vary them while keeping all the other system parameters fixed as given in Table 2-1. Although this may not be achievable in practice (for example, using surfactants or changing temperature will usually affect more than one interfacial tension), doing so gives insight to the problem and combined effects can still be examined later. These effects are summarized in Figure 2-4, where the top row, (a), shows the effects on the free energy with respect to the reference, the second row, (b), shows the effects on the radius of curvature of the oil–air interface,  $R^{oa}$ , and the third row, (c), shows the effects on the contact angles  $\alpha$ ,  $\beta$ , and  $\varphi$ . Every column of figures corresponds to varying one of the interfacial tensions. Three example schematics of the attached configuration are given for each varying interfacial tension below its plot. Note that the attached configuration is only possible in a certain range in each case as the interfacial tensions are varied. As discussed earlier, this happens because of the violation of the triangle inequalities past a certain point when varying the interfacial tensions. These limits are indicated by vertical dashed lines in Figure 2-4 for each of the varying interfacial tensions, with the corresponding triangle inequality limits marked at the top of the figure.

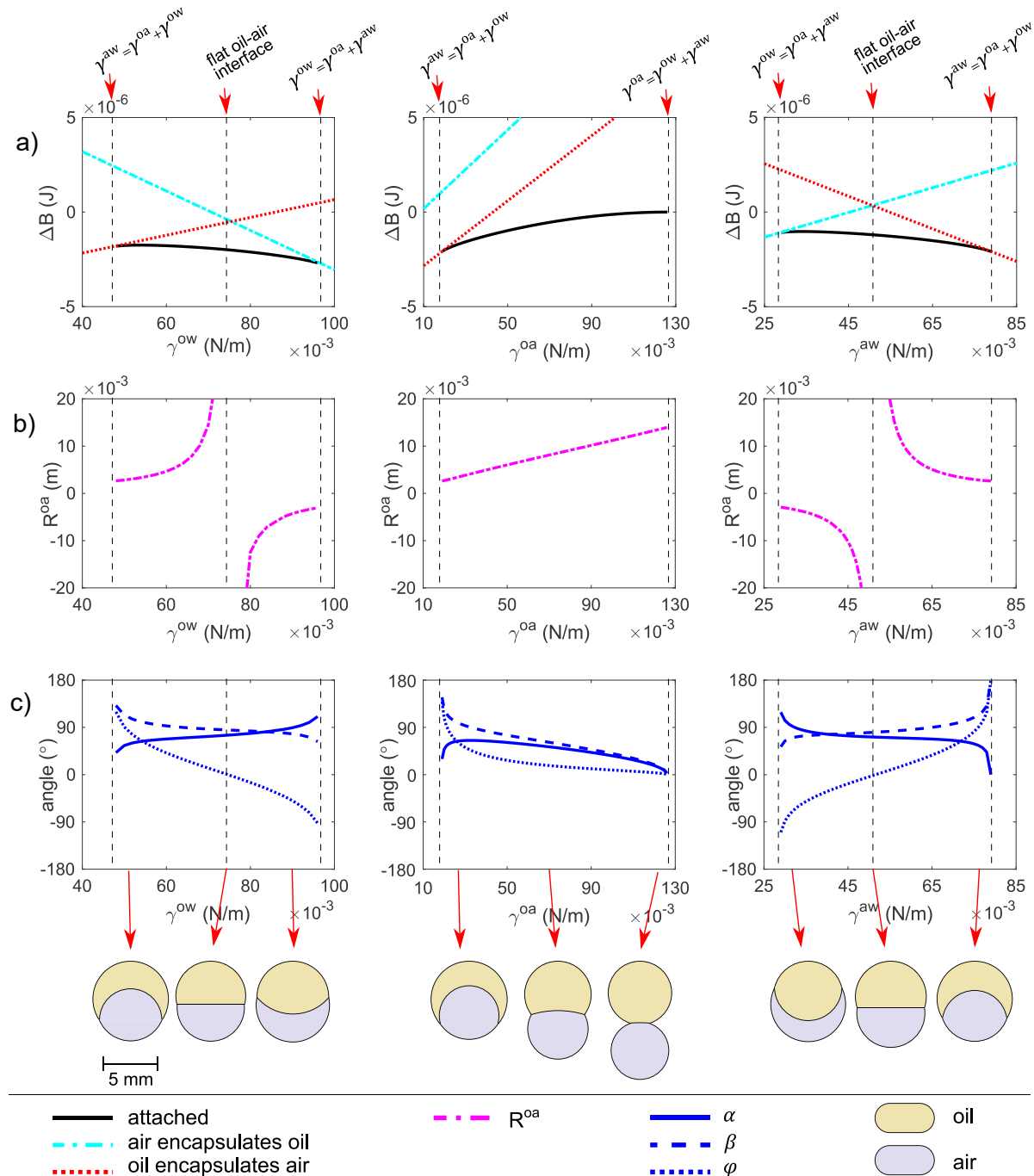


Figure 2-4. Effects of individually varying  $\gamma^{ow}$ ,  $\gamma^{oa}$ , and  $\gamma^{aw}$  on: (a) the free-energy difference between each final configuration and the reference state; (b) the radius of the oil–air interface,  $R^{oa}$ , for the attached configuration; and (c) the contact angles  $\alpha$ ,  $\beta$ , and  $\varphi$  for the attached configuration. When varying each interfacial tension, the remaining parameters are fixed as given in Table 2-1. Note that the attached configuration is only possible in certain ranges, where the triangle inequalities for the interfacial tensions are satisfied. These limits and the flat interfaces (when possible) are indicated by vertical dashed lines. Three example schematics are given for each of the varied interfacial tensions.



Figure 2-5 shows the combined effects of the interfacial tensions on the contact angle of the oil–air interface,  $\varphi$ , for three different volumes of air: (a)  $V_r^a = 75 \times 10^{-9} \text{ m}^3$ ; (b)  $V_r^a = 10 \times 10^{-9} \text{ m}^3$ ; and (c)  $V_r^a = 1000 \times 10^{-9} \text{ m}^3$ . The interfacial tension of the air–water interface,  $\gamma^{aw} = 72.4 \text{ mN/m}$ , is kept constant. The horizontal axes are given by a nondimensional parameter  $\gamma^{ow}/\gamma^{aw}$ , while the vertical axes are similarly given by  $\gamma^{oa}/\gamma^{aw}$ . The shaded rectangular domains are bounded by the straight lines, which represent the limits of the triangle inequalities. Every solid line within these boundaries is a constant-angle contour of the resultant surface. As conventionally defined, the red-shaded areas correspond to positive radii of curvature (convex), while the blue-shaded areas correspond to negative radii of curvature (concave). It should be noted that changing  $\gamma^{aw}$  in a realistic, physical range does not change these plots at this scale since the contributions of pressure due to curvature are small compared to external pressure. This is also true if one chooses to take a different combination of the ratios of interfacial tensions—scaling all interfacial tensions proportionally in a physical range does not affect the geometry noticeably in this example. This is because, at this scale, the volume change of the gas phase due to the change in Laplace pressure (caused by the change in radius of the air–water interface) is negligible. When this is the case, we can factor out any of the interfacial tensions from Equations (2-32) and (2-33), divide both sides by it and only consider the ratios of the remaining interfacial tensions.

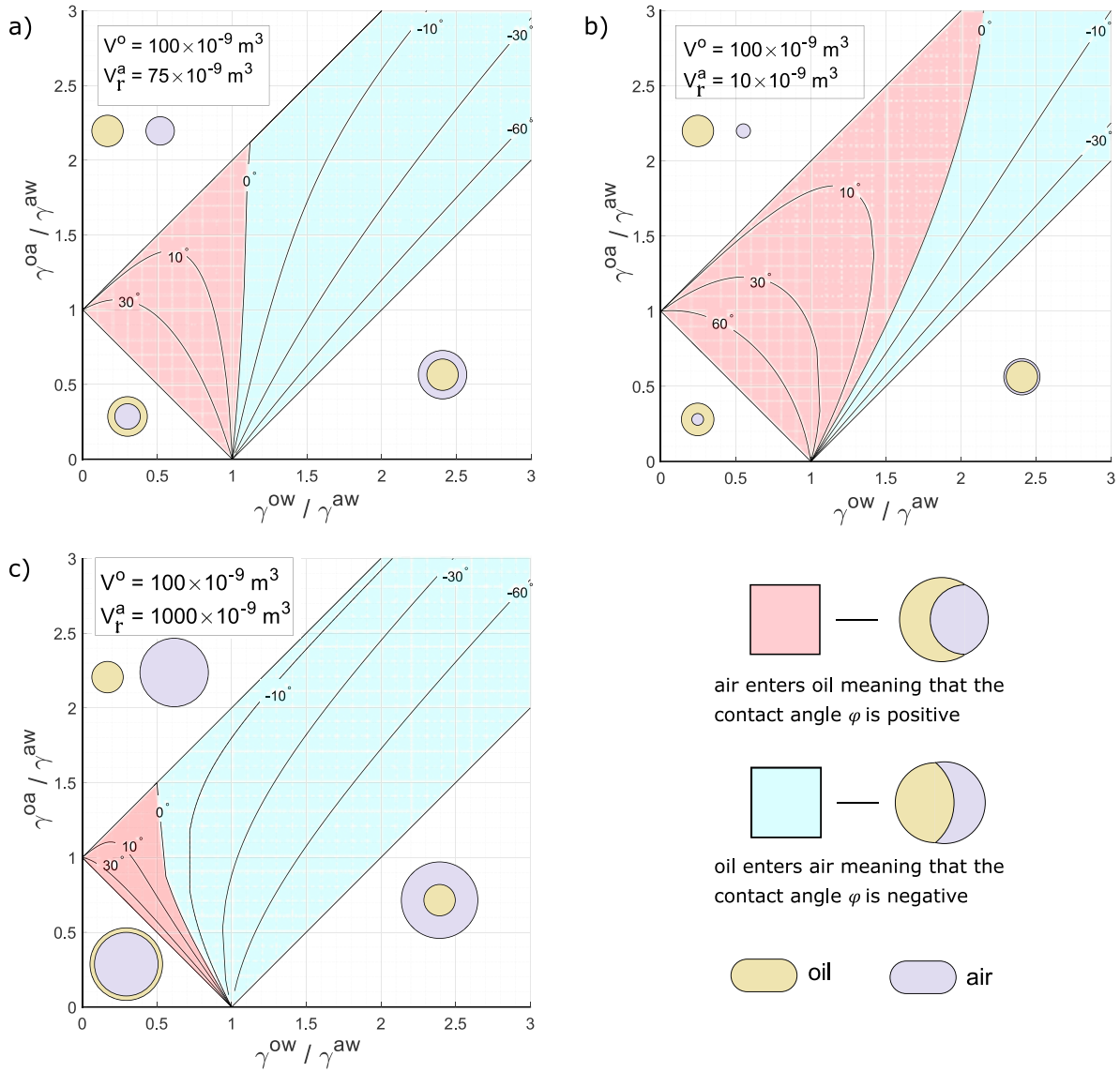


Figure 2-5. Contours of constant contact angle  $\varphi$  plotted for constant oil volume,  $V^o = 100 \times 10^{-9} \text{ m}^3$ , and three different initial volumes of the air bubble: (a)  $V_r^a = 75 \times 10^{-9} \text{ m}^3$ ; (b)  $V_r^a = 10 \times 10^{-9} \text{ m}^3$ ; and (c)  $V_r^a = 1000 \times 10^{-9} \text{ m}^3$  as functions of the ratios of interfacial tensions,  $\gamma^{ow}/\gamma^{aw}$  and  $\gamma^{oa}/\gamma^{aw}$ . The air–water interfacial tension,  $\gamma^{aw} = 72.4 \times 10^{-3} \text{ N/m}$ , is fixed. Conventionally, the angle,  $\varphi$ , is chosen to be positive when the interface is convex (red-shaded areas), and negative when it is concave (blue-shaded areas) towards the oil phase. The domains are bounded by the straight lines:  $\gamma^{oa}/\gamma^{aw} = \gamma^{ow}/\gamma^{aw} + 1$ ;  $\gamma^{oa}/\gamma^{aw} = \gamma^{ow}/\gamma^{aw} - 1$ ; and  $\gamma^{oa}/\gamma^{aw} = 1 - \gamma^{ow}/\gamma^{aw}$ . Outside of the domain boundaries, the attached configuration is not possible, so a representative schematic of the most stable configuration is drawn for each of the triangular regions.

### 2.3.1.3 Effects of scale

In this section, we investigate the effects of the scale by comparing the same system at two different size scales. This is done to highlight the importance of using the correct free-energy equation in a system with a gas phase. We take the original oil–air–water system and look at this system at two different size scales: (i) the millimeter scale, where we fix the volume of the oil phase at  $V^o = 100 \times 10^{-9} \text{ m}^3$  (*i.e.*, the same as all cases studied up to this point in this chapter); and (ii) the nanometer scale, where we fix the volume of the oil phase at  $V^o = 100 \times 10^{-24} \text{ m}^3$ , and vary the volume of the air phase such that the air-to-oil volume ratio is between 0.001 and 1000 in both cases. Doing so, we plot the free-energy contributions of the interfacial terms,  $\Delta B_{\text{int.}}$ :

$$\Delta B_{\text{int.}} = \gamma^{\text{ow}}(A^{\text{ow}} - A_{\text{r}}^{\text{ow}}) + \gamma^{\text{aw}}(A^{\text{aw}} - A_{\text{r}}^{\text{aw}}) + \gamma^{\text{oa}}A^{\text{oa}} \quad (2-86)$$

the pressure term,  $\Delta B_{\text{p}}$ :

$$\Delta B_{\text{p}} = P^{\text{w}}(V^{\text{a}} - V_{\text{r}}^{\text{a}}) \quad (2-87)$$

and the chemical potential term,  $\Delta B_{\mu}$ :

$$\Delta B_{\mu} = -P_{\text{r}}^{\text{a}}V_{\text{r}}^{\text{a}} \ln\left(\frac{P_{\text{r}}^{\text{a}}}{P^{\text{a}}}\right) \quad (2-88)$$

to the total free energy,  $\Delta B_{\text{total}}$ :

$$\Delta B_{\text{total}} = \Delta B_{\text{p}} + \Delta B_{\text{int.}} + \Delta B_{\mu} \quad (2-89)$$

as given by Equation (2-75). This is shown in Figure 2-6 for the attached, the air-encapsulating-oil, and the oil-encapsulating-air configurations separately. The  $x$ -axis (relative air volume) is given in logarithmic scale for clarity. We observe that, when the system is at the millimeter scale, the pressure and the chemical potential terms cancel each other leaving the total free energy equal to the interfacial terms only (the reason explained earlier). This is no longer the case when the system is at a much smaller nanometer scale, where these contributions do not cancel each other, and the total free energy with respect to the reference is different than the interfacial free energy with respect to the reference. Therefore, it is important to take the pressure and chemical potential terms into account when studying systems at small scales. This is further highlighted by superimposing the plots of the total free energy and the interfacial free energy in Figure 2-7 [similar to Figure 2-3 (a)]. We note that, when the chemical potential term is ignored (the pressure term is already negligible; see Figure 2-6 and theoretical discussion on

the contributions of these terms), this results not only in quantitative errors, but also the relative positions of the curves with respect to each other may change. Without these contributions, for some range of  $V_r^a/V^o$  (well-pronounced around  $V_r^a/V^o = 10$ ), the oil-encapsulating-air configuration appears to have less free energy than the attached configuration resulting in a wrong conclusion (*i.e.*, the oil-encapsulating-air configuration is wrongly concluded to be more stable than the attached configuration when only the interfacial free-energy terms are considered). However, when the correct free-energy equation considered [with the pressure and the chemical potential terms as given in Equation (2-75)], we arrive at the correct conclusion that the attached configuration is the most stable configuration at all volume ratios since the triangle inequalities for the interfacial tensions are satisfied.

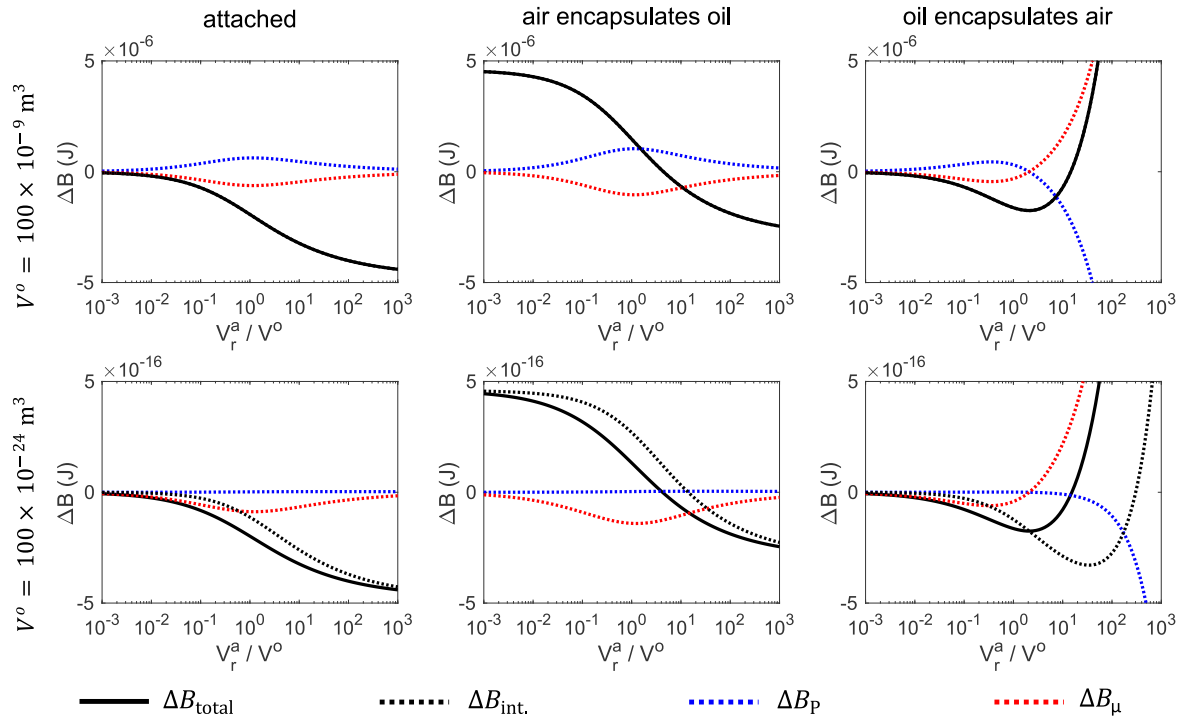


Figure 2-6. Contributions of the interfacial ( $\Delta B_{\text{int.}}$ ), pressure ( $\Delta B_P$ ), and chemical potential ( $\Delta B_\mu$ ) terms to the total free energy ( $\Delta B_{\text{total}}$ ) of each configuration at two different size scales. The top row corresponds to a system at the millimeter scale ( $V^o = 100 \times 10^{-9} \text{ m}^3$ ), where the free-energy contributions due to pressure and chemical potential cancel each other leaving the total the free energies with respect to the reference equal to the interfacial free-energy contributions ( $\Delta B_{\text{total}} = \Delta B_{\text{int.}}$ ). The bottom row corresponds to a system at the nanometer scale ( $V^o = 100 \times 10^{-24} \text{ m}^3$ ), where these contributions do not cancel. The remaining system parameters of both systems are fixed as given in Table 2-1. Note that each  $x$ -axis value on these plots represents a different system, and therefore, extrema on these plots do not have a stability meaning.

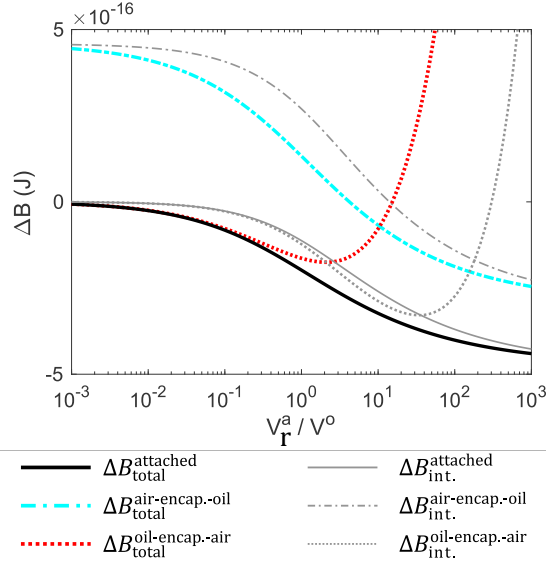


Figure 2-7. Effect of the ratio of the initial volumes of the air phase to the oil phase on the free energy with respect to the reference state at the nanoscale. The thick lines represent the total free energy, whereas the thin gray lines represent the free energy only due to the interfacial terms. The volume of the oil phase,  $V^o = 100 \times 10^{-24} \text{ m}^3$ , is kept constant, and the remaining system parameters are fixed as given in Table 2-1. Note that each  $x$ -axis value on this plot represents a different system, and therefore, extrema on this plot do not have a stability meaning.

## 2.4 Conclusion

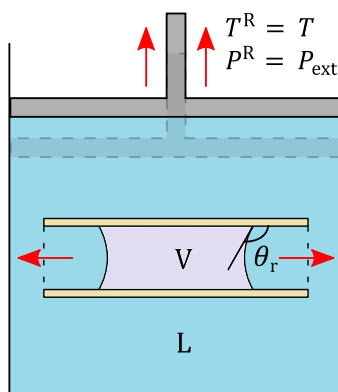
In this chapter, we used Gibbsian composite-system thermodynamics to derive the conditions for equilibrium for a three-phase system with spherical interfaces at constant external pressure and temperature, where all phases are assumed to be immiscible. Effects of any external fields were neglected. We considered liquid-only systems in parallel with systems where a gas phase may be present. The equations for the free energy for these systems were then derived and compared. We rigorously explained the predictions of the spreading coefficient concept from the perspective of free energy and showed that it is valid for liquid–gas systems at any scale as well as liquid–liquid systems. In addition to this, we also provided a method for calculating the exact geometries of the configurations that may arise in these systems such as an attached configuration (*i.e.*, lens formation) or full encapsulation configurations. We used a numerical solver to solve the system of equations describing each equilibrium geometry.

An example system consisting of a dodecane drop and an air bubble surrounded by water was further investigated. Effects of various initial parameters such as initial volume,

interfacial tensions, and overall size scale of the system on the equilibrium geometry and the relative stability of the configurations were explored. Finally, we showed that using the correct form of the free-energy equation is important even for qualitative conclusions.

## Chapter 3

# Quantifying the Effects of Dissolved Nitrogen and Carbon Dioxide on Drying Pressure of Hydrophobic Nanopores<sup>1</sup>



### Chapter summary

The effects of a dissolved gas on the behavior of liquid in cylindrical nanopores were investigated in the framework of Gibbsian composite-system thermodynamics and classical nucleation theory. An equation was derived relating the phase equilibrium of a mixture of a subcritical solvent and a supercritical gas to the curvature of the liquid–vapor interface. Both the liquid and the vapor phases were treated nonideally, which was shown to be important for the accuracy of the predictions in the case of water with dissolved nitrogen or carbon dioxide. The behavior of water in nanoconfinement was found to be only affected when the gas amount is significantly more than the saturation concentration of these gases in atmospheric conditions.

<sup>1</sup> Reproduced (including Appendix A), with minor changes, with permission from H. Binyaminov and J. A. W. Elliott. *Quantifying the Effects of Dissolved Nitrogen and Carbon Dioxide on Drying Pressure of Hydrophobic Nanopores*, J. Chem. Phys. **158**, 204710 (2023). <https://doi.org/10.1063/5.0146952> © 2023 American Institute of Physics.

However, such concentrations can be easily reached at high pressures during intrusion if there is sufficient gas present in the system, especially considering gas oversolubility in confinement. By including an adjustable line tension term in the free-energy equation ( $-44$  pJ/m for all points), the theory can make predictions in line with a few data points available from a recent experimental work. But we note that such a fitted value empirically accounts for multiple effects and should not be interpreted as the energy of the three-phase contact line alone. Compared to molecular dynamics simulations, our method is easy to implement, requires minimal computational resources, and is not limited to small pore sizes and/or short simulation times. It provides an efficient path for first-order estimation of the metastability limit of water–gas solutions in nanopores.

### 3.1 Introduction

The dynamics of intrusion and extrusion of liquids into and out of nanoscale environments has drawn great interest in recent years, owing mainly to the increasing number of technological and industrial applications, such as fluid separation [110], energy dampening and storage [29,48,68,155], porosimetry [81], and DNA sequencing [191], among many others. The interplay of the parameters that dictate the behavior of a liquid in confinement is notoriously difficult to determine leading to poor predictability, controllability, and other design challenges [39,59]. Additionally, understanding of these processes is crucial from the fundamental-science perspective as they are believed to play an important role in many organic phenomena, such as gating in biological channels [11,94,130,168,174].

One of the variables that strongly affects the characteristics of a liquid in confinement is the dissolved gas, such as nitrogen, which is naturally present in the liquid, such as water, if special precautions are not taken to eliminate it [71,72]. The ability of the dissolved gas to promote drying of a liquid-filled pore has implications beyond technological applications. For example, in biology, the anesthetic potency of a gas is known to be related to its solubility [126] (the Meyer–Overton correlation). Although the phenomenon has been known for over a century and many hypotheses have been put forward to explain it since, a scientific consensus has not yet been reached. In recent years, a new idea has been gaining popularity with growing evidence suggesting a mechanism where the gas migrates to the channels of the lipid bilayer, destabilizes the liquid, and creates a vapor bubble that blocks ion transfer [26,130,174].



Previously, equilibrium density functional theory [174] and molecular dynamics simulations [12,26,120,123,129,166] have been utilized to study the effects of a weakly soluble gas on the wet-to-dry transition in nanoconfinement. Roth *et al.* [174] studied gating in a model hydrophobic biological channel. Their calculations show that a small amount of xenon gas dramatically decreases the open probability of a channel with radius in the 0.4–1.2 nm range. In molecular dynamics simulations by Camisasca *et al.* [26], a single atom of argon gas was able to migrate into a water-filled nanopore with radius of 0.7 nm and result in drying of the pore within the simulation time by reducing the free-energy barrier considerably and nucleating a bubble. By means of molecular dynamics simulations, Li *et al.* [123] studied the effect of nitrogen gas on the critical distance between hydrophobic plates in water. They concluded that, by aggregating near the surfaces of the plates, the gas increases the critical distance below which water is unstable in the confinement. In a similar study by Feng *et al.* [53], electric field applied perpendicularly to the plates resulted in enhanced aggregation of the nitrogen molecules in the slit and further increased the critical distance in proportion to the field strength. Leung *et al.* [120] realized that, at atmospheric pressures, the dissolved gases should have no significant effect on drying by performing simulations with water confined in hydrocarbon-like slits. In their simulations, a single nitrogen molecule inserted into the slit reduced the free-energy barrier by  $\sim 2k_B T$ , where  $k_B$  is the Boltzmann constant and  $T$  is absolute temperature. Luzar *et al.* [129] found that the fugacities of nitrogen and carbon dioxide required to trigger expulsion of water from a 1.4 nm hydrophobic slit were  $\sim 40$  bar and  $\sim 2$  bar, respectively.

There have been some experimental attempts [121,122,166,206] to quantify the effects of dissolved gases on the behavior of water in nanoconfinement. Li *et al.* [121,122] used nanoporous material with cylindrical pores of varying sizes mixed with water and conducted experiments with different amounts of air in the system. At the end of the first compression–decompression cycle, depending on the amount of gas, very little, some, or most of the total nanopore volume could be recovered for use in the second cycle. In the works of Xu *et al.* [206] and Qiao *et al.* [166], the researchers performed experiments with cylindrical nanopores open at both ends, and closed at one end, respectively, with trapped gas occupying the pore volume at the beginning of intrusion (*i.e.*, air; the samples were not degassed). Both groups observed that, if the samples were held at high pressures at the end of the infiltration process ( $\sim 3$ –12 hrs

holding time), a significant portion of the usable nanopore volume was lost in the next cycle. On the other hand, if the intrusion and extrusion processes were performed in succession with no holding, all pore volume was recovered allowing practically identical intrusion–extrusion cycles. This was because the trapped gas in the nanopores was not enough to saturate the liquid at the pressure at which the samples were held, and the gas was diffusing into the bulk liquid (a rather slow process) reducing the gas concentration in the pores. No drying was observed in the same experiment of Qiao *et al.* [166] performed with material with larger average pore size, regardless of the presence of the gas or high-pressure holding.

In this chapter, we study the effect of dissolved nitrogen and carbon dioxide on the wet/dry state of a cylindrical nanopore in the framework of Gibbsian composite-system thermodynamics coupled with classical nucleation theory. Previously, using similar methods, our group has explored free-energy landscapes in other geometries such as formation of bubbles in finite cones [217] or stability of surface nanobubbles [218]. In these works, the pressures considered were low so that the ideal-mixture assumptions could be safely made. We have also developed equations for liquid–vapor equilibrium of multicomponent mixtures of condensable components accounting for the effect of interfacial curvature and the liquid-phase nonideality [183,186]. The extension to nonideal vapor phase was mentioned in reference [45] but not applied. Here, to study the stability of water in cylindrical nanopores in the presence of gas, we derive the fully nonideal phase equilibrium equations for a mixture of a condensable solvent and a noncondensable gas with a curved liquid–vapor interface. These equations can be applied to any confinement geometry and interface shape and are accurate for typical pressures of interest in the studies of liquids in nanopores.

Regarding the applicability of the macroscopic thermodynamic equations at extreme confinement and reliability of the predictions, there are many works in the literature supporting their validity under certain circumstances in the 1–4 nm size range [46]. For instance, it has been shown that the macroscopic equation relating the saturation vapor pressure of the liquid to the curvature of the interface—the Kelvin equation—holds for clusters as small as 0.7 nm in radius [50]. In our group’s previous work, the multicomponent version of this equation applied to pores of 2 nm radius gave predictions of composition-dependent dew points of subcritical mixtures in excellent agreement with independent measurements [183]. Another example is the Young–Laplace equation (in fact, it is used in the derivation of the Kelvin

equation), which has been demonstrated to be valid for nanodroplets down to drop radius of 1 nm [131]. In the context of nanopores, this equation is known to predict the intrusion pressures accurately for pore radii 1.3 nm and larger [71,72,118,119]. Additionally, it has been concluded that the properties of water bridges sandwiched between two planar surfaces can be calculated using capillary theory for wall separations of 3 nm and above with no additional corrections [3]. Moreover, classical nucleation theory with the Kelvin equation applied to the nitrogen–ethyl ether mixture was able to accurately predict the homogeneous bubble nucleation rate and correctly capture its pressure and temperature dependencies [54,201].

### 3.2 System definition and free energy

A schematic description of the system is given in Figure 3-1. We consider a piston–cylinder device that is coupled with a constant pressure ( $P^R$ ) and constant temperature ( $T^R$ ) reservoir with which only volume and energy exchanges are allowed. We let the system exist in the absence of external forces, such as gravity. We assume that the container is filled with a liquid with dissolved gas in it, which is denoted by the superscript letter “L” (referred to as “liquid” or “solution”). Sufficient for the analysis here, we consider a single cylindrical pore open at both ends with internal radius of  $R_p$  and length of  $l_p$  placed in the liquid. It is assumed that the pore is made of a solid material with which the liquid would have a macroscopic equilibrium contact angle  $\theta_{eq}$  (measured through the liquid) if placed on a flat surface. The solid is taken to be insoluble, nonvolatile, and infinitely rigid.

After the pore is filled with the liquid, the pressure is suddenly brought to pressure  $P_{ext} = P^R$ , which is referred to as the extrusion pressure. This is the pressure at which the pore empties (or dries) in an experiment in a reasonable time. A schematic of the system immediately after the pressure is brought to  $P_{ext}$  is given in Figure 3-1 (a). As depicted in Figure 3-1 (b), after a short time, the liquid starts to empty the pore while the piston moves up to accommodate for the formation of the new vapor phase in the pore, which is denoted by “V” (referred to as “vapor”). Finally, the system reaches a new equilibrium state where the pore is sealed at both ends with pinned spherical liquid–vapor interfaces as depicted in Figure 3-1 (c). We note that the final pinned equilibrium state is only possible if the difference between the vapor-phase pressure and the liquid-phase pressure,  $\Delta P = P^V - P^L$ , is not larger than the pore mouth geometry can accommodate. This threshold pressure difference is denoted by  $\Delta P^*$ .

Assuming a flat pore mouth surface, it can be calculated as  $\Delta P^* = 2\sigma^{LV} \sin \theta_{eq} / R_p$ , where  $\sigma^{LV}$  is the surface tension of the liquid–vapor interface. This means that the inequality  $\Delta P \leq \Delta P^*$  should be satisfied for the vapor phase to stay confined in the pore.

It has been experimentally confirmed [71,72,118,119] that the capillary pressure required to force the liquid into an initially dry pore (initially, the pressure is zero inside the capillary) is well described by Laplace’s law of capillarity:

$$P_{\text{int}} = -\frac{2\sigma^{LV} \cos \theta_a}{R_p} \quad (3-1)$$

where  $P_{\text{int}}$  is the required intrusion pressure, and  $\theta_a \geq \theta_{eq}$  is the advancing contact angle. Notice that a positive intrusion pressure is required if the solid is nonwetting (*i.e.*, if  $\theta_{eq} > 90^\circ$ ).

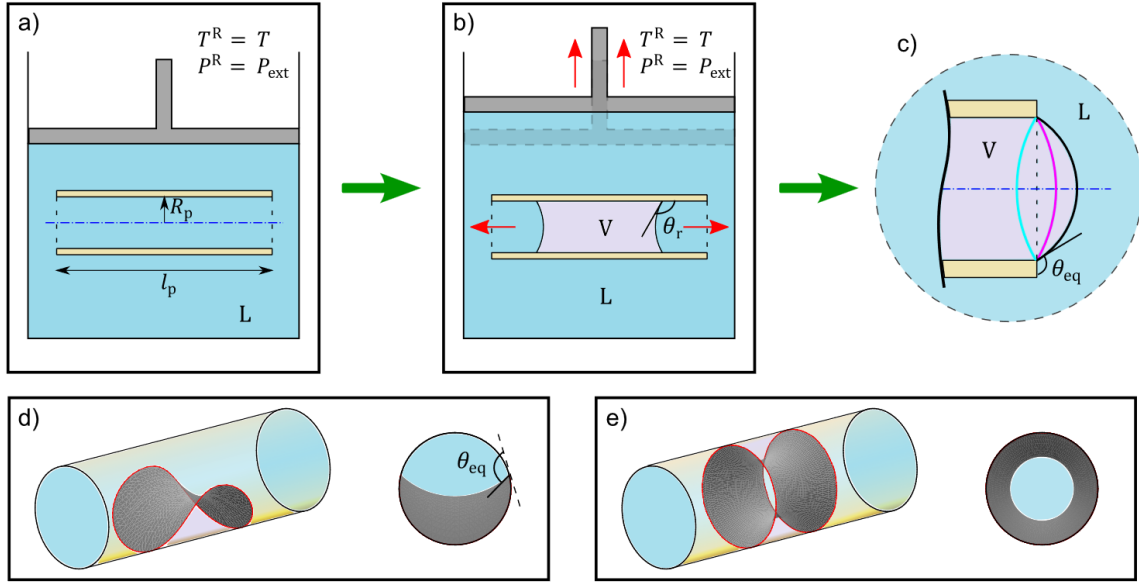


Figure 3-1. Schematic description of drying of a cylindrical nanopore immersed in a liquid–gas solution. The metastable reference state is shown in panel (a) with a solution-filled cylinder of radius  $R_p$  and length  $l_p$ . After a short waiting time, a new vapor phase forms and pushes the solution out of the pore following a nucleation event. A snapshot of the process after the nucleation is shown in panel (b), where two disjoint spherical caps are moving in opposite directions. The final equilibrium state with the vapor-filled pore and a pinned liquid–vapor interface covering the pore mouth at the end of this process is depicted in panel (c). In this panel, the light blue, purple, and black lines indicate example positions of the interface, depending on the pressure difference,  $P^V - P^L$ . The liquid–gas solution is indicated by the letter “L” and the vapor is indicated by the letter “V”. The liquid has an equilibrium contact angle of  $\theta_{eq}$  with the solid. While the interface is in motion, the contact angle,  $\theta_r$ , in general, is assumed to be different than  $\theta_{eq}$ . Note that  $\theta_r$  does not appear in our calculations because we are only concerned with equilibrium states in this work. Schematics of possible critical nuclei geometries considered in this work are depicted in panels (d) (localized nucleus) and (e) (symmetric nucleus).

In our analysis, the intrusion pressure,  $P_{int}$ , only serves as a guide for the concentration of the gas in the liquid, which can be independently set to make the liquid (i) undersaturated, (ii) saturated, or (iii) oversaturated with respect to  $P_{int}$ . The most obvious case would be to assume that the concentration of the gas in the liquid, after the system pressure is brought to  $P_{ext}$ , is equal to the saturation concentration of the gas at  $P_{int}$ . However, other possibilities are also considered to gain insight into the physics of the problem. In practice, undersaturation may happen due to, for example, not having enough gas molecules in the system for saturation, and oversaturation can be the result of the initial pressure being higher than the required (minimum) intrusion pressure,  $P_{int}$ , in abundance of gas. In experiments, one usually deals

with many pores in one system with a certain pore size distribution. As a result, the maximum pressure reached for the complete intrusion of all pores can be significantly higher (typically at least ~30%–50% higher) than the mean intrusion pressure. If the pore studied in this work represents the average pore size in the experiments, it is reasonable to consider oversaturation with respect to the required intrusion pressure. Furthermore, nanopores are known to attract “hydrophobic” dissolved gas resulting in a significant increase in gas concentrations in the pore compared to the bulk concentration [23,86–90,129,158].

In the experiments, the extrusion pressure is often measured to be significantly lower than the required intrusion pressure, while (linearly) increasing with temperature, indicating that there exists a free-energy barrier that needs to be overcome. This energy barrier is associated with the formation of a critical nucleus of vapor (which contains both vapor of the solvent and gas) because of random fluctuations in the liquid, as formulated in the context of classical nucleation theory [103]. This nucleus is in an unstable equilibrium with the liquid, and as a result, smaller nuclei disappear, and larger nuclei grow until a new equilibrium state is reached. It is well known that heterogeneous bubble nucleation (*i.e.*, creation of a nucleus in contact with the pore wall) has a lower energy barrier compared to homogenous bubble nucleation (*i.e.*, creation of nucleus in the bulk liquid inside the pore), especially when  $\theta_{\text{eq}} > 90^\circ$  [103]. Therefore, only the formation of a critical nucleus on the pore wall (inside the pore) is considered. The shape of this nucleus will be discussed later as it may have nontrivial geometry due to the confinement inside the cylinder. The nucleus shape need not be specified for the derivation and qualitative description of the thermodynamic potential of the system (the free-energy equation).

To investigate the nature of equilibrium states, it suffices to study the free-energy equation in the neighborhood of an equilibrium state. Following the standard techniques [41,43,45,201,203,215], the expansion of the free energy in intensive parameters around the equilibrium state can be written. Because the variations around equilibrium can be made arbitrarily small, only the first order terms can be retained, which reduces to [215]

$$\Delta B(V^V) = -V^V \sigma^{\text{LV}} k_c + \sigma^{\text{LV}} A^{\text{LV}} + \sigma^{\text{LV}} A^{\text{SV}} \cos \theta_{\text{eq}} \quad (3-2)$$

where  $B$  is the free-energy function,  $V^V$  is the volume of a nucleus,  $k_c = 1/R_{1,c} + 1/R_{2,c}$  is twice the mean curvature of the liquid–vapor interface of the critical nucleus with  $R_{1,c}$  and  $R_{2,c}$  being the principal radii of curvature of the surface (the surface is oriented with the unit

normals pointing towards the liquid). For brevity, we will refer to  $k_c$  simply as “curvature” in the remainder of this chapter.  $A^{LV}$  and  $A^{SV}$  are the areas of the liquid–vapor and the solid–vapor interfaces, respectively. The reference state is chosen to be the metastable liquid state in the absence of a vapor nucleus [as depicted in Figure 3-1 (a)] and the following conditions for equilibrium have been incorporated:

- (i) uniformity of temperature across all phases

$$T^R = T^j = T^{jk} \quad (3-3)$$

where  $j = L$  or  $V$ , and  $jk = LV, SL$ , or  $SV$  representing bulk phases and interfaces, respectively.

- (ii) equality of chemical potentials of each component in each subsystem

$$\mu_i^j = \mu_i^k = \mu_i^{jk} \quad (3-4)$$

where the subscript denotes the component  $i$ . In this chapter, we use  $i = 1$  for the solvent and  $i = 2$  for the gas.

- (iii) mechanical equilibrium conditions

$$\sigma^{SV} = \sigma^{SL} + \sigma^{LV} \cos \theta_{eq} \quad (3-5)$$

$$P^L = P^R \quad (3-6)$$

$$P^V - P^L = \sigma^{LV} k_c \quad (3-7)$$

$\sigma^{SV}$  and  $\sigma^{SL}$  in Equation (3-5) are the interfacial tensions of the solid–vapor and the solid–liquid interfaces, respectively.

For derivation of Equation (3-2), it is also assumed that the liquid surrounding the critical nucleus is large enough that the temperature and pressure changes due to the formation of the nucleus can be neglected. Additionally, since the number of molecules of various components that go into the creation of the critical nucleus can be shown to be small compared to the number of molecules in the solution, the concentration of the components in the solution can be assumed to be constant. Consequently, the variations in the chemical potentials of components in solution can also be neglected because they are functions of temperature, pressure, and concentration only [201].

### 3.3 Nonideal multicomponent liquid–vapor equilibrium across a curved interface

For heterogenous nucleation of a vapor bubble from a pure liquid, the critical curvature,  $k_c$ , in Equation (3-2) can be found by knowing the vapor pressure of the liquid at the given temperature and using a version of the Kelvin equation [41] generalized to nonspherical liquid–vapor interfaces. In the presence of other components, however, the equations for multicomponent liquid–vapor equilibrium need to be established first, while considering the geometry (*i.e.*, the curvature of the liquid–vapor interface). Since the pressure is not uniform in the system, the applicability of the typical phase equilibrium equations for uniform pressure (*i.e.*,  $P = P^L = P^V$ ) from the literature need to be checked and the necessary modifications should be made. Here, we give a detailed derivation of the liquid–vapor equilibrium equations for the general case where  $P^L \neq P^V$ .

We start by writing the equality of chemical potentials [Equation (3-4)] in liquid and vapor phases for both components:

$$\mu_1^L(T, P^L, x_1) = \mu_1^V(T, P^V, y_1) \quad (3-8)$$

$$\mu_2^L(T, P^L, x_2) = \mu_2^V(T, P^V, y_2) \quad (3-9)$$

where  $x_i$  and  $y_i$  are the mole fractions of the components in liquid and in vapor phases, respectively. Considering the pressures in the systems of interest can be quite high, we do not make ideality assumptions *a priori*. For the solvent, using the definition of fugacity [44], Equation (3-8) can be rewritten as

$$\mu_1^L(T, P^L, x_1 = 1) + \bar{R}T \ln\left(\frac{\hat{f}_1^L}{f_1^L}\right) = \mu_1^V(T, P^V, y_1 = 1) + \bar{R}T \ln\left(\frac{\hat{f}_1^V}{f_1^V}\right) \quad (3-10)$$

where  $f_i^L$  is the fugacity of pure component  $i$  as a liquid at  $T$  and  $P^L$ ,  $\hat{f}_i^L$  is the fugacity of component  $i$  in a liquid mixture (*i.e.*, in the presence of other components) at  $T$  and  $P^L$ ,  $f_i^V$  is the fugacity of pure component  $i$  as a vapor at  $T$  and  $P^V$ ,  $\hat{f}_i^V$  is the fugacity of component  $i$  in a vapor mixture at  $T$  and  $P^V$ , and  $\bar{R}$  is the universal gas constant. In the framework of our problem, the solvent component is always kept subcritical. Hence, for convenience, the state at which the pressure is equal to the saturation pressure of the solvent,  $P_{1,\text{sat}}$ , at temperature  $T$  can be chosen as the reference state. Using the Gibbs–Duhem equation, we can write [25]



$$\begin{aligned} \mu_1^L(T, P_{1,\text{sat}}, x_1 = 1) + \int_{P_{1,\text{sat}}}^{P^L} v_1^L dP + \bar{R}T \ln \left( \frac{\hat{f}_1^L}{f_1^L} \right) \\ = \mu_1^V(T, P_{1,\text{sat}}, y_1 = 1) + \bar{R}T \ln \left( \frac{\hat{f}_1^V}{f_{1,\text{sat}}^V} \right) \end{aligned} \quad (3-11)$$

where  $v_1^L$  is the molar volume of pure liquid solvent. For a component  $i$  in a liquid solution, the activity coefficient is defined as  $\gamma_i = \hat{f}_i^L / x_i f_i^L$ , and the fugacity coefficient is defined as  $\hat{\phi}_i^V = \hat{f}_i^V / y_i P^V$  [44]. Note that the pure component activity coefficient is unity [*i.e.*,  $\lim_{x_i \rightarrow 1} (\gamma_i) = 1$ ]. However, note that the pure gas fugacity coefficient is not necessarily unity:  $\phi_i^V = \lim_{y_i \rightarrow 1} (\hat{\phi}_i^V) = f_i^V / P^V$ . Using these definitions and the equality of chemical potentials of the liquid and vapor of pure solvent at saturation, we can write

$$\hat{\phi}_1^V y_1 P^V = x_1 \gamma_1 \phi_{1,\text{sat}} P_{1,\text{sat}} \eta_1 \quad (3-12)$$

where  $\phi_{1,\text{sat}}$  is the fugacity coefficient of the vapor of pure solvent at saturation, and  $\eta_1$  is defined as

$$\eta_1 = \exp \left( \frac{\int_{P_{1,\text{sat}}}^{P^L} v_1^L dP}{\bar{R}T} \right) \quad (3-13)$$

Equation (3-12) is a practically more useful version of Equation (3-8) for the equality of chemical potential of the solvent between the phases.

Since the typical gas component is usually supercritical at the conditions of interest (*e.g.*, nitrogen or carbon dioxide at 50 °C),  $P_{2,\text{sat}}$  may not be defined at  $T$  and the pure gas component at saturation cannot be chosen as the reference state. Instead, we first consider a state where both vapor and solution are at the pressure  $P^L$  with arbitrary concentrations of gas as  $x'_2$  and  $y'_2$  in the solution and in the vapor phases, respectively. Using Equation (3-9), we write

$$\mu_2^L(T, P^L, x'_2) + \bar{R}T \ln \left( \frac{\hat{f}_2^L}{\hat{f}_2'^L} \right) = \mu_2^V(T, P^L, y'_2) + \bar{R}T \ln \left[ \frac{\hat{f}_2^V}{\hat{f}_2'^V(P^L)} \right] \quad (3-14)$$

For clarity, in the parentheses, we indicate the pressure at which the quantity needs to be evaluated if it is different than what is indicated by the phase descriptor (*i.e.*, the superscript

letter). Using the definitions of the fugacity and activity coefficients and rearranging, Equation (3-14) can be rewritten as

$$\mu_2^V(T, P^L, y_2') - \mu_2^L(T, P^L, x_2') = \bar{R}T \ln \left[ \frac{x_2 \gamma_2 \hat{\phi}_2^V(P^L) y_2' P^L}{x_2' \gamma_2' \hat{\phi}_2^V y_2 P^V} \right] \quad (3-15)$$

Now, we choose  $P_{1,\text{sat}}$  as the reference pressure for the left-hand-side of Equation (3-15) and write

$$\begin{aligned} \mu_2^V(T, P_{1,\text{sat}}, y_2') - \mu_2^L(T, P_{1,\text{sat}}, x_2') + \bar{R}T \ln \left[ \frac{\hat{f}_2^V(P^L)}{\hat{f}_2^V(P_{1,\text{sat}})} \right] - \int_{P_{1,\text{sat}}}^{P^L} \bar{v}_2^L dP \\ = \bar{R}T \ln \left[ \frac{x_2 \gamma_2 \hat{\phi}_2^V(P^L) y_2' P^L}{x_2' \gamma_2' \hat{\phi}_2^V y_2 P^V} \right] \end{aligned} \quad (3-16)$$

where  $\bar{v}_2^L$  is the partial molar volume of the gas component in the solution at  $x_2'$ . By rearranging and taking the limit as  $x_2' \rightarrow 0$  of both sides of Equation (3-16), we can write

$$\begin{aligned} \lim_{x_2' \rightarrow 0} [\mu_2^V(T, P_{1,\text{sat}}, y_2') - \mu_2^L(T, P_{1,\text{sat}}, x_2')] \\ = \lim_{x_2' \rightarrow 0} \left\{ \bar{R}T \ln \left[ \frac{x_2 \gamma_2 \hat{\phi}_2^V(P_{1,\text{sat}}) y_2' P_{1,\text{sat}}}{x_2' \gamma_2' \hat{\phi}_2^V y_2 P^V} \right] + \int_{P_{1,\text{sat}}}^{P^L} \bar{v}_2^L dP \right\} \end{aligned} \quad (3-17)$$

Instead of keeping  $y_2'$  independent, for a small  $x_2'$  chosen arbitrarily close to zero, we choose the equilibrium concentration  $y_2'$  (also close to zero) such that the vapor pressure is equal to  $P_{1,\text{sat}}$  (the vapor is almost entirely component 1), which makes the left-hand side of Equation (3-17) vanish. Additionally, one can make the following definitions at this equilibrium:

- (i) infinite dilution activity coefficient of component 2

$$\gamma_2^* = \lim_{x_2' \rightarrow 0} \left( \frac{\gamma_2}{\gamma_2'} \right) \quad (3-18)$$

Note that  $\lim_{x_2 \rightarrow 0} (\gamma_2^*) = 1$  (*i.e.*,  $\gamma_2^*$  is normalized to unity at  $x_2 \rightarrow 0$ ).

- (ii) partial molar volume of component 2 in solution at infinite dilution

$$\bar{v}_{2,\infty}^L = \lim_{x_2' \rightarrow 0} (\bar{v}_2^L) \quad (3-19)$$

- (iii) the ratio of fugacity in the vapor to the concentration in the liquid of component 2 at infinite dilution

$$H_{12} = \lim_{x_2' \rightarrow 0} \left[ \frac{\hat{\phi}_2'^V(P_{1,\text{sat}}) y_2' P_{1,\text{sat}}}{x_2'} \right] \quad (3-20)$$

which is Henry's law constant by definition [31,188].

Substituting these definitions into Equation (3-17) and rearranging, the liquid–vapor equilibrium for the gas component across a curved interface can be expressed as

$$\hat{\phi}_2^V y_2 P^V = x_2 \gamma_2^* H_{12} \eta_2 \quad (3-21)$$

where  $\eta_2$  is defined as

$$\eta_2 = \exp \left( \frac{\int_{P_{1,\text{sat}}}^{P^L} \bar{v}_{2,\infty}^L dP}{RT} \right) \quad (3-22)$$

Like Equation (3-12), Equation (3-21) is a practically more useful version of Equation (3-9). Equations (3-12) and (3-21) together establish the nonideal liquid–vapor equilibrium for a liquid–gas mixture, which, in general, may have different phase pressures. Note that, by setting  $P = P^V = P^L$  in Equations (3-12) and (3-21), we recover the two-component liquid–vapor equilibrium equations across a flat interface [44].

By combining Equations (3-12) and (3-21) with Equation (3-7) and noting that  $P^V = y_1 P^V + y_2 P^V$ , we can write

$$k_c = \left( \frac{x_1 \gamma_1 \phi_{1,\text{sat}} P_{1,\text{sat}} \eta_1}{\hat{\phi}_1^V} + \frac{x_2 \gamma_2^* H_{12} \eta_2}{\hat{\phi}_2^V} - P^L \right) / \sigma^{\text{LV}} \quad (3-23)$$

Equation (3-23) relates the equilibrium thermodynamic properties of the mixture to the equilibrium geometry. It can be viewed (after some rearranging) as the nonideal Kelvin equation for a liquid–gas mixture, generalized to an arbitrary constant-mean-curvature interface shape.

When dealing with aqueous systems, it is customary to use an activity model for the liquid phase activity coefficients,  $\gamma_1$  and  $\gamma_2^*$ , and to use an equation of state for the vapor phase fugacity coefficients,  $\hat{\phi}_1^V$  and  $\hat{\phi}_2^V$ , to correlate them to other variables and/or known parameters (the so-called  $\gamma$ – $\phi$  approach/model). This method generally produces a more accurate description compared to, for example, using the same equation of state for both liquid and vapor, while still being relatively simple. We use the nonrandom two-liquid model [169] for the activity in solution and the Peng–Robinson cubic equation of state [157] for the vapor phase fugacity. Since the only solvent in this chapter is water, the parameters  $\phi_{1,\text{sat}}$ ,  $P_{1,\text{sat}}$ ,  $v_1^L$ ,  $H_{12}$ ,

and  $\bar{v}_{2,\infty}^L$  in Equations (3-12) and (3-21) can be accurately obtained from the tabulated values and/or functional correlations from the literature. For nitrogen–water and carbon dioxide–water solutions, the model we have chosen provides enough accuracy for pressures up to 100 MPa at moderate temperatures (see Figure A-2 and Figure A-3). This pressure range is sufficient to describe equilibrium across a spherical liquid–vapor interface with the radius of curvature down to  $\sim 1.4$  nm assuming negligible pressure at the low-pressure side (for  $\sigma^{LV} = 0.068$  J/m<sup>2</sup>—the value at  $T = 323.15$  K). For comparison, a critical nucleus (having free-energy barrier of  $\sim 35k_B T$ ; see the next section) for heterogeneous vapor nucleation from liquid water on a hydrophobic flat substrate with contact angle of  $120^\circ$  (*i.e.*, a spherical cap) has a radius of curvature of  $\sim 2$  nm. This presents the worst-case scenario because the critical nuclei corresponding to the same energy barrier in nanoconfinement need not be as curved (mean curvature implied). Note that the liquid-phase pressure is allowed to be negative (*i.e.*, tension), although, there is no experimental data available for this case since most experiments are done at the macroscopic scale having a flat liquid–vapor interface (*i.e.*, uniform pressure; negative pressure is not defined for a gas). The detailed description of the thermodynamic model, the correlations used, and the validation against available experimental data are given in Appendix A.

### 3.4 Estimating free-energy barrier from experiments

We use classical nucleation theory to estimate the free-energy barrier from the nucleation rate, which has been applied to nanopores before in references [71] and [118]. To summarize, the probability of fluctuations in thermodynamic properties of liquid is inversely proportional to the exponential of the reversible work associated with such fluctuations. For the formation of a vapor bubble, this reversible work is the corresponding free-energy barrier. Written in units of expected nucleation events per unit length of the pore,  $l_p$ , per unit time, the nucleation rate is given as [118]

$$J = \frac{\mathcal{Z}v}{b} \exp\left(-\frac{\Delta B_c}{k_B T}\right) \quad (3-24)$$

where  $\mathcal{Z}$  is the barrier transmission coefficient (also known as the Zeldovich factor),  $b$  and  $v$  are the microscopic length and frequency scales, respectively, and  $\Delta B_c$  denotes the free-energy barrier. Note that references [71] and [118] use transition state theory approximation to

extract the nucleation energy barriers, which presumes negligible barrier recrossings (*i.e.*,  $Z = 1$ ). This approximation is questionable because of flat energy profiles and diffusive propagation characteristics of nucleation [139]. Indeed, for capillary drying of water in a hydrocarbon-like slit, the transmission coefficient was found to be  $Z \sim 0.01\text{--}0.1$  [120].

Since  $J$  depends much more strongly on  $\Delta B_c$  than the pre-exponential factor, the dependence of  $\nu$  on pore radius is neglected. The typical values of  $b$  and  $\nu$  for pure water are  $\sim 0.1\text{--}1$  nm and  $\sim 10^{12}\text{--}10^{13}$  Hz, respectively [71,118]. We will assume that these values are also applicable to the liquid–gas solutions considered in this work.

To estimate the free-energy barrier that is low enough for the nucleation event to be observable in typical experimental time,  $t$ , one usually sets  $Jtl_p = 1$ . Using this value, we can invert Equation (3-24) to find the energy barrier:

$$\Delta B_c = k_B T \ln \left( \frac{Z t \nu l_p}{b} \right) \quad (3-25)$$

Typical cylindrical nanopores have lengths of hundreds of nanometers ( $l_p \sim 100\text{--}1000$  nm) [10,111,213] and typical experimental times range from a fraction of a second to a few tens of seconds ( $t \sim 0.1\text{--}100$  s). By substituting the parameters from the listed ranges above in Equation (3-25), one calculates  $\Delta B_c \sim 25k_B T$  as the lowest value, and  $\Delta B_c \sim 44k_B T$  as the highest value with the average being  $\Delta B_c = 35k_B T$ . We use this average as a representative value of the energy barrier, where applicable in the following sections. Since the energy barrier scales with the square of the pore radius, this translates to  $\sim 12\%$  uncertainty for the inference of the pore size. Note that about  $2/3$  of the uncertainty in  $\Delta B_c$  is eliminated with information about the pore length in the experiment and the observation time. For example, for drying of an average-sized pore with length of 500 nm that is observed for 10 seconds, the range becomes  $\Delta B_c \sim 32\text{--}38 k_B T$ .

### 3.5 Shape of the critical nucleus

Once the chemical equilibrium is solved at given conditions, the critical curvature of the liquid–vapor interface,  $k_c$ , is known from Equation (3-23) (see Appendix A for the details of the solution procedure). Next, the goal is to find a nucleus shape inside a cylinder whose liquid–vapor interface has the curvature  $k_c$  and calculate the free-energy barrier corresponding to this shape. If there are more than one nucleus geometries corresponding to  $k_c$ , the one with

the lowest free energy should be chosen as the critical nucleus. Following reference [118], two distinct possibilities are considered for the shape of the critical nucleus confined to a cylinder wall: (i) an annulus shape—a symmetric nucleus with the axis of symmetry being the cylinder axis and with two disjoint three-phase contact lines [Figure 3-1 (e)], and (ii) a saddle shape—a localized nucleus on the wall of the cylinder with one continuous three-phase contact line [Figure 3-1 (d)]. To our knowledge, only the symmetric nucleus has a known analytical solution, details of which can be found in reference [118] (see Appendix A for the main equation written in our notation). To determine the geometry of the localized nucleus we use the Surface Evolver (SE) code [21], which is a specialized software package designed for complex variational problems involving surface forces.

Briefly, SE tries to minimize the energy of a surface subject to constraints, such as fixed volume of the nucleus and fixed walls with surface energy. The surface of the shape to be evolved is approximated by triangles (*i.e.*, the surface is represented as a simplicial complex) that are moved towards an equilibrium (minimum-energy) shape by gradient descent or conjugate gradient methods. The shape usually converges fast, although the accuracy may depend on the mesh size as well as the number of evolution steps. Surface Evolver works in a unitless system (*i.e.*, it only deals with numerical values), in that, the user is free to assign a consistent system of units of measurement to relate the results to real-world applications. The volume of the shape is calculated by evaluating surface integrals (Gauss's theorem), and the solid–vapor interfacial area is calculated by evaluating a line integral over the contact line (Stokes's theorem). This eliminates the need to cover the solid surfaces with otherwise useless facets. More details about Surface Evolver can be found elsewhere [21].

In general, it is not practical to run SE with a prescribed curvature because stability becomes an issue. Instead, we created a series of saddle shaped nuclei in the volume range from 0.1 to 7 (with an increment of 0.05; a total of 139 points) for contact angles 110°, 120°, and 130° in a unit cylinder (radius of 1) and generated look-up tables for the curvature and the area of the liquid–vapor interface, the area of the solid–vapor interface, and the length of the three-phase contact line. This way, after converting the tabulated values to a consistent system of units for a given pore radius, the quantities can be interpolated in the table for the prescribed critical curvature. The free-energy barrier can be calculated using these values directly in

Equation (3-2). Then, the volume and the areas can be varied following the trends around this equilibrium to investigate the stability of the equilibrium.

The summary of nondimensionalized results of geometry calculations is given in Figure 3-2 (a), (b), and (c) for both symmetric (dotted dashed lines) and localized nuclei (solid lines) and for three different values of contact angle. The quantities are plotted against the dimensionless critical curvature,  $k_c R_p$ . The corresponding free-energy barriers are given in Figure 3-2 (d) as calculated using Equation (3-2). It is seen that the symmetric nucleus is only slightly preferred when the prescribed curvature is close to the minimum possible curvature in the pore (*i.e.*,  $k_c R_p \sim 2 \cos \theta_{eq}$ ). This is in complete agreement with previous results [71,118]. Note that there are infinite solutions for the shape of the nucleus when  $k_c R_p = 2 \cos \theta_{eq}$  with different volumes and solid–vapor interfacial areas, which all have the same liquid–vapor interfacial areas and energies. These correspond to the vapor nuclei sealed with two disjoint spherical caps at both ends. The end points of the curves in Figure 3-2 (b) and (d) indicate the transition to the two-disjoint-spherical-caps geometry. For  $k_c R_p < 2 \cos \theta_{eq}$  there are no solutions, meaning that the pore cannot dry at such conditions.

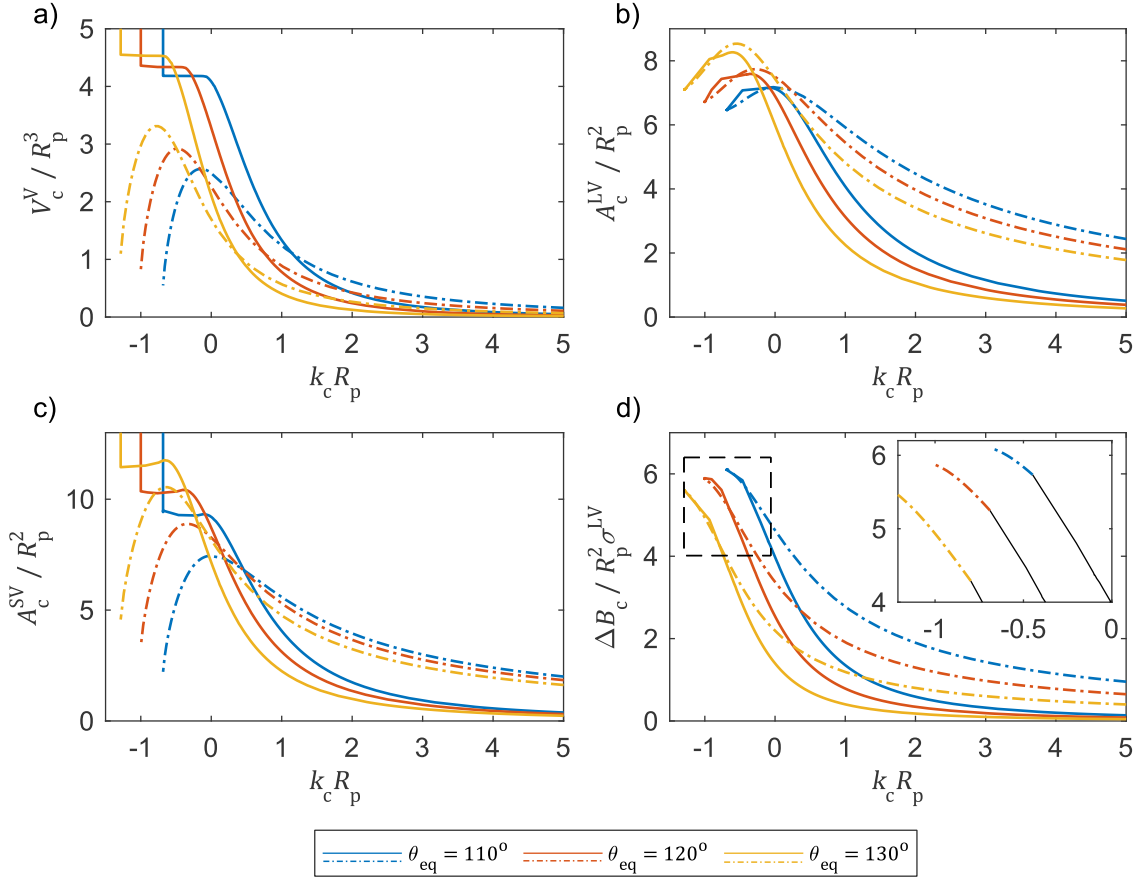


Figure 3-2. Nondimensional geometrical quantities for the critical nuclei and the corresponding energy plots as functions of nondimensional curvature for three different contact angles: blue for  $\theta_{\text{eq}} = 110^\circ$ , orange for  $\theta_{\text{eq}} = 120^\circ$ , and yellow for  $\theta_{\text{eq}} = 130^\circ$ . The solid lines are for the localized nuclei and the dotted dashed lines are for the symmetric nuclei. Panels (a), (b), and (c) show the plots of volume, liquid–vapor interfacial area, and solid–vapor interfacial area, respectively. Panel (d) shows the plots of energy barrier as calculated using Equation (3-2). The inset shows a zoom-in of the curvature range where the symmetric nuclei have slightly lower energy. Here, the energy curves for the localized nuclei are shown in black to highlight the transition points.

Examples of the lowest-energy shapes for the prescribed curvature are given in Figure 3-3 for contact angle  $\theta_{\text{eq}} = 120^\circ$ . These examples are chosen from ranges where they have lower energy compared to the other geometry. The curvatures of the localized nuclei in panels (a) and (b) are  $k_c R_p = 0.83$  and  $k_c R_p = 0.21$ , respectively. In panel (c), the two-dimensional slices of three symmetric nuclei with curvatures  $k_c R_p = -0.8$  (dotted line),  $-0.87$  (dashed line), and  $-0.94$  (solid line) are shown. For the equation used to calculate these profiles, see Appendix A.



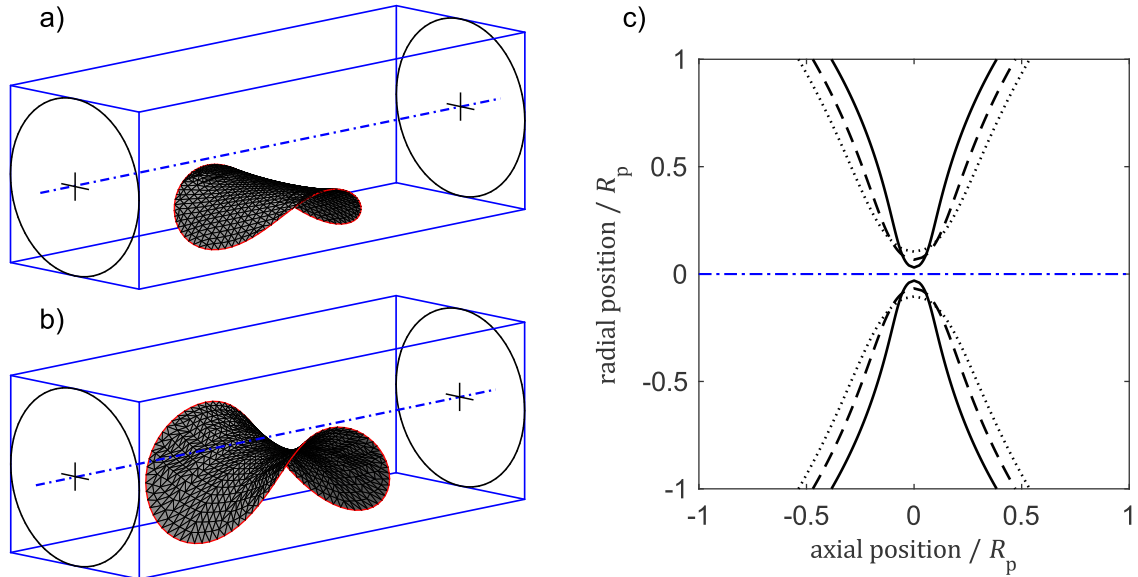


Figure 3-3. Examples of localized and symmetric nuclei. As calculated using Surface Evolver, the three-dimensional views of the liquid–vapor interfaces for the localized nuclei are shown in panels (a) and (b), which have constant curvatures of  $k_c R_p = 0.83$  and  $k_c R_p = 0.21$ , respectively. For clear views of these shapes, only the contours of the cylinders are shown at the ends of the bounding boxes. The three-phase contact lines are shown in red. In panel (c), the two-dimensional view of three symmetric nuclei on an axial plane are shown. The three-dimensional surfaces are obtained by rotating these profiles around the cylinder axis (blue dotted dashed line). These surfaces have constant curvatures of  $k_c R_p = -0.8$  (dotted line),  $-0.87$  (dashed line), and  $-0.94$  (solid line).

It is important to discuss the reasonableness of both nucleus geometries in the context of physical theory, which has not been addressed in previous studies. One of the main assumptions of classical nucleation theory is that the primary dynamic variable of interest (*i.e.*, the reaction coordinate) is the number of molecules in the nucleus and that other variables equilibrate much faster [103,160]. The number of molecules is often well approximated by the volume of the nucleus. From atomistic simulations in nanopores, it has been concluded that, even for a pore with radius  $R_p \sim 1$  nm, the volume of the nucleus alone is a good choice for the reaction coordinate [120]. This means that the shape found by solving the variational problem for a prescribed curvature should also be the minimum-energy shape at that volume to describe a critical nucleus. To test this, the symmetry constraint should be removed since there is no physical basis for this requirement. In other words, a symmetric nucleus should be allowed to transform to a localized nucleus if this transition is energy-minimizing. For a given volume in the volume range where the symmetric nuclei are possible [see Figure 3-2 (a)], there are two

or three solutions, one of which is the localized nucleus. Using their corresponding curvatures on the energy plot [Figure 3-2 (d)], we see that the localized nucleus always has the lowest energy for a given volume up to the maximum volume above which only the disjoint-spherical-caps geometry is possible. We confirmed this using SE by initializing the shapes symmetrically for prescribed volumes, which, upon evolution towards minimum energy, quickly destabilized and transformed into localized nuclei. Therefore, we believe that the formation of the symmetric nuclei (excluding the disjoint-caps geometry) as part of the nucleation path is unlikely in a physical system. In the remainder of this chapter, we only consider either the localized geometry or the two-spherical-caps geometry (at large volumes when a localized nucleus is not possible) as the shape of the critical nucleus. However, it is worth noting that the nucleation barrier is only slightly different in a small range of curvature values [see the inset in Figure 3-2 (d)] depending on the choice of symmetric or localized geometry as the critical nucleus shape in the potential range. Therefore, both our qualitative and quantitative results would not be altered noticeably, even if the symmetric nuclei were physically possible.

As part of the discussion of the nucleus shape, it is instructive to highlight the importance of confinement geometry and its effect on the phase transition. It is due to the shape of the confinement that the nuclei with close to zero and negative (according to our sign convention) curvatures are also energy-minimizing. For pores small enough so that the corresponding free-energy barrier is  $\Delta B_c \sim 35k_B T$ , this means that, even at conditions where  $P^L \gg P^V$ , the liquid-to-vapor transition can happen. Without the confinement geometry of the pore,  $P^L \ll P^V$  is required for phase transition because the energy-minimizing nuclei would necessarily have spherical liquid–vapor interfaces with  $k_c > 0$  while also having to be small to satisfy  $\Delta B_c \sim 35k_B T$ .

## 3.6 Results

### 3.6.1 Comparison of free-energy profiles

Next, we investigate the effects of dissolved nitrogen and carbon dioxide in water on the nucleation free-energy barrier. Here, it is convenient to introduce an auxiliary variable,  $S$ , termed the saturation ratio, defined as the ratio of the concentration of the gas in the liquid phase to the saturation concentration at the intrusion pressure:  $S = x_2/x_{2,\text{sat}}$  with  $x_{2,\text{sat}}$  being

the saturation concentration at  $P_{\text{int}}$ . We consider three pore sizes:  $R_p = 1, 1.5, \text{ and } 2 \text{ nm}$ ; three contact angles:  $\theta_{\text{eq}} = 110, 120, \text{ and } 130^\circ$ . These are the typical sizes of the pores and the typical contact angles of the materials used in the experiments. The advancing contact angle,  $\theta_a$ , used to calculate the intrusion pressure is taken to be equal to the equilibrium contact angle,  $\theta_{\text{eq}}$ . This choice does not affect the results because slight incorrect estimation of the intrusion pressure, which is only needed to estimate the gas concentration, is compensated for by varying the gas concentration independently around this saturation value. The temperature is fixed at  $T = 323.15 \text{ K}$  (to avoid subcriticality and potential error in the phase description of carbon dioxide below its critical temperature of  $304.13 \text{ K}$ ).

The interfacial tension of liquid with vapor is taken to be constant and equal to the surface tension of pure water at  $T = 323.15 \text{ K}$  ( $\sigma^{\text{LV}} = 0.068 \text{ J/m}^2$ ). Studies on the effects of dissolved gas have shown that the water surface tension is lower when the gas is present (as low as  $\sigma^{\text{LV}} = 0.030 \text{ J/m}^2$  for dissolved carbon dioxide at high pressures) [14,127]. The adsorption of the gas at the solid–liquid interface would also decrease the solid–liquid interfacial tension with both changes in  $\sigma^{\text{SL}}$  and  $\sigma^{\text{LV}}$  affecting the contact angle. Assuming these effects are comparable in size, the inclusion of only one of them is expected to give worse predictions compared to if both effects are neglected. Quantifying these effects is beyond the scope of this chapter, with only the former effect being well-documented in the literature [14,127] (and not at the nanoscale), we will assume that, in the presence of the gas, the interfacial tension of the liquid–vapor interface and the contact angle are equal to those of for pure water.

Assuming a localized nucleus, the free-energy plots [calculated using Equation (3-2)] are given in Figure 3-4 for  $\theta_{\text{eq}} = 110^\circ$ , in Figure 3-5 for  $\theta_{\text{eq}} = 120^\circ$ , and in Figure 3-6 for  $\theta_{\text{eq}} = 130^\circ$ . Only the region up to the transition to the two-disjoint-spherical-caps geometry is shown. The intrusion pressures are calculated using Equation (3-1) for each pore size and contact angle combination. In these three figures, each row of plots is for a different pore size, whereas the columns are for different liquid pressures. For each plot, the  $x$ -axis is the volume of the nucleus in  $\text{nm}^3$ , and the  $y$ -axis is the energy in units of  $k_B T$ . The  $\Delta B = 35 k_B T$  limit is shown by the horizontal solid black line on each subplot for visual reference. The green lines correspond to the pure-water case, while the orange lines are for nitrogen dissolved in water,

and the light blue lines are for carbon dioxide dissolved in water. The lines are solid for  $S = 1$ , dashed for  $S = 2$ , and dotted dashed for  $S = 0.5$ . All curves are highlighted in red around the critical volume and the corresponding free-energy barrier, indicating an unstable equilibrium in all cases. Overall, the presence of gas is seen to decrease the free-energy barrier significantly in most cases: the higher the gas concentration the easier it is to nucleate. This is because of the increased vapor pressure in the presence of the gas.

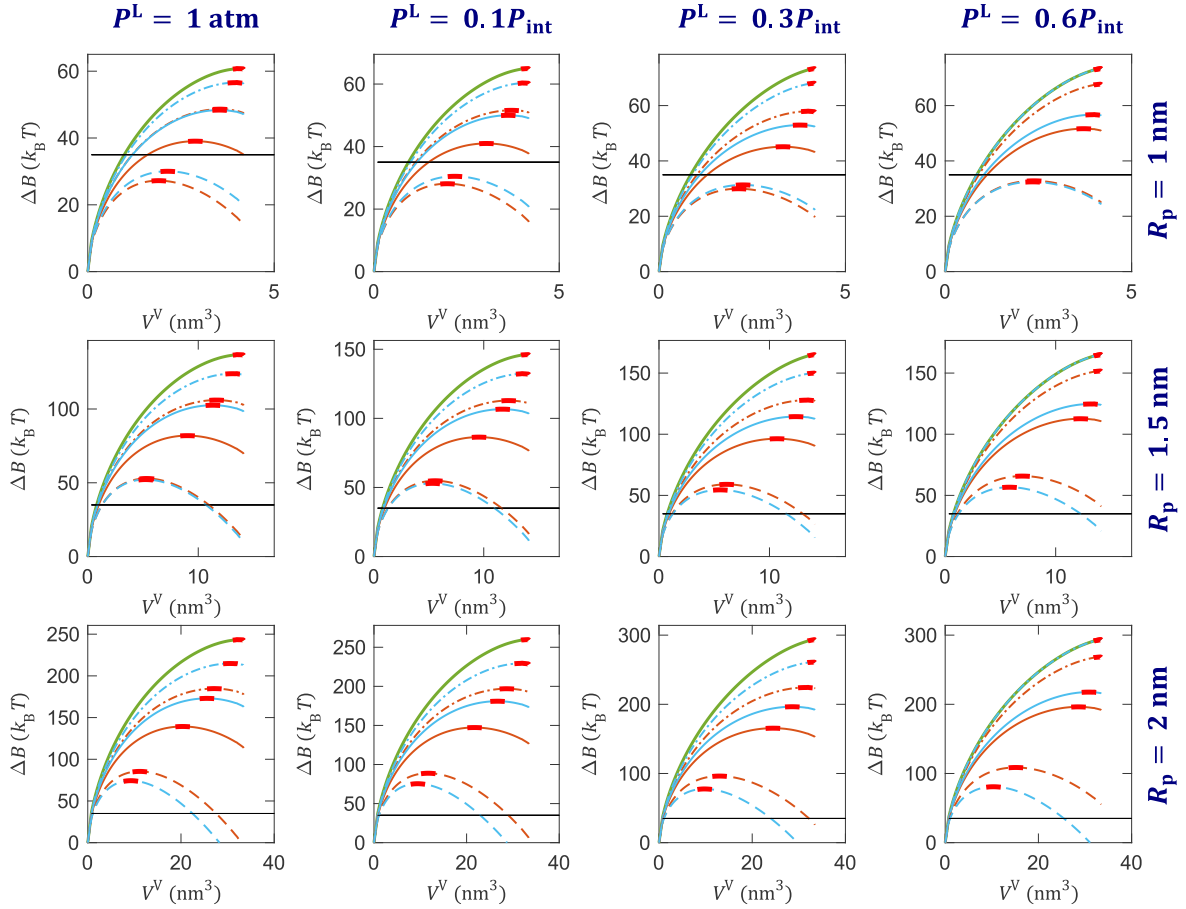


Figure 3-4. Free-energy plots for  $\theta_{eq} = 110^\circ$  at different pore radii, liquid pressures, and saturation ratios. The temperature is fixed at  $T = 323.15$  K. The green lines are for pure water, the light blue lines are for water with dissolved carbon dioxide, and the orange lines are for water with dissolved nitrogen. Each row of subplots is for a different pore radius, while the columns are for different liquid pressures. The solid lines are for  $S = 1$ , the dashed lines are for  $S = 2$ , and the dotted dashed lines are for  $S = 0.5$ . The horizontal solid black lines represent  $\Delta B = 35 k_B T$  for visual reference. All curves are highlighted in red around the critical volume and the corresponding free-energy barrier.

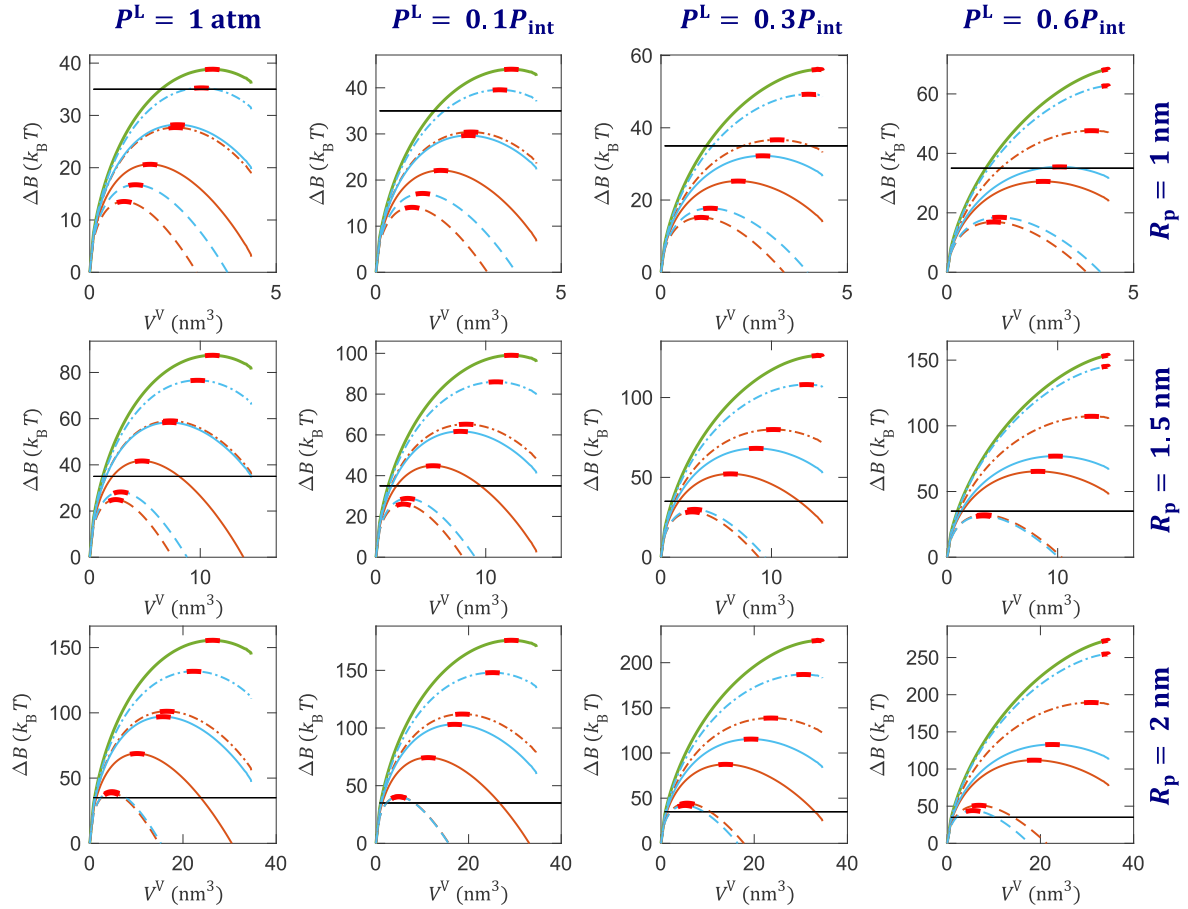


Figure 3-5. Free-energy plots for  $\theta_{\text{eq}} = 120^\circ$  at different pore radii, liquid pressures, and saturation ratios. The temperature is fixed at  $T = 323.15$  K. The green lines are for pure water, the light blue lines are for water with dissolved carbon dioxide, and the orange lines are for water with dissolved nitrogen. Each row of subplots is for a different pore radius, while the columns are for different liquid pressures. The solid lines are for  $S = 1$ , the dashed lines are for  $S = 2$ , and the dotted dashed lines are for  $S = 0.5$ . The horizontal solid black lines represent  $\Delta B = 35 k_B T$  for visual reference. All curves are highlighted in red around the critical volume and the corresponding free-energy barrier.

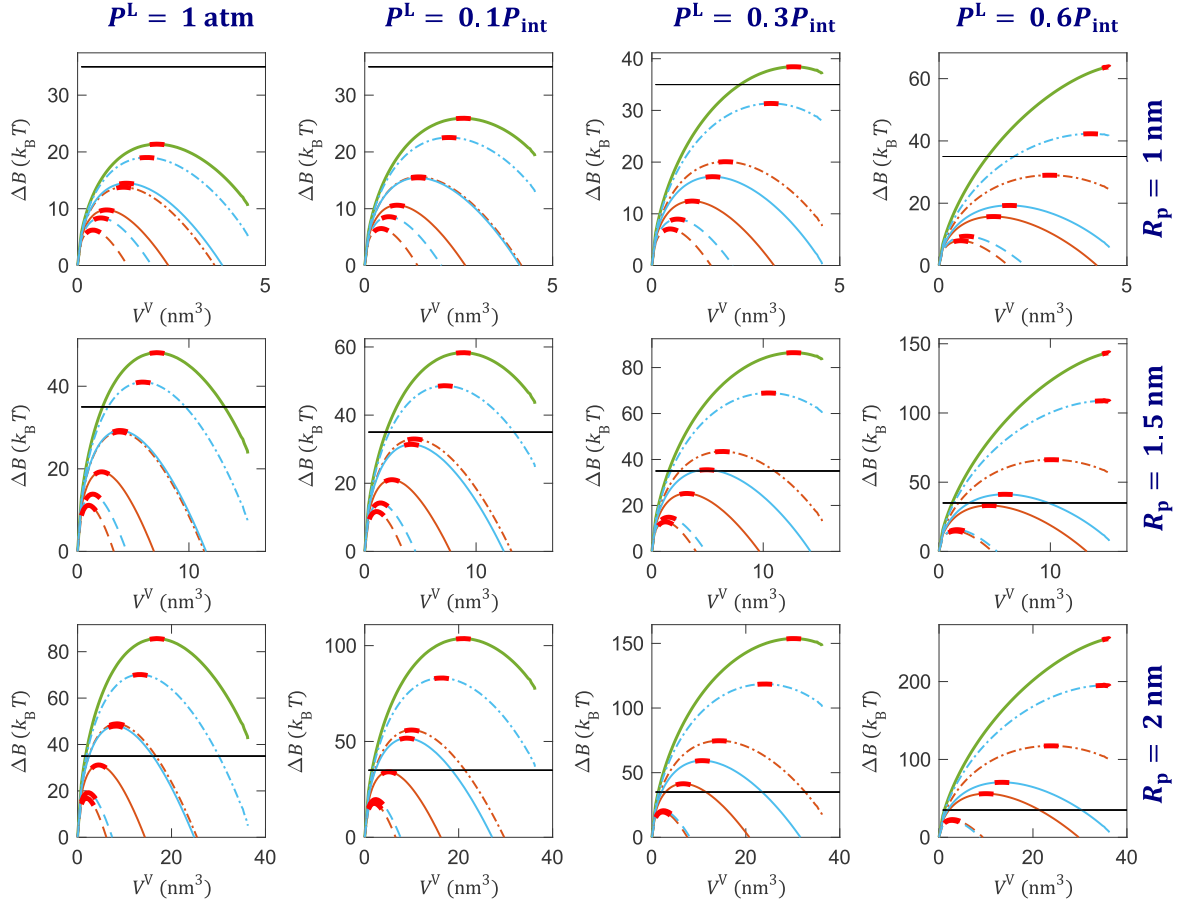


Figure 3-6. Free-energy plots for  $\theta_{\text{eq}} = 130^\circ$  at different pore radii, liquid pressures, and saturation ratios. The temperature is fixed at  $T = 323.15$  K. The green lines are for pure water, the light blue lines are for water with dissolved carbon dioxide, and the orange lines are for water with dissolved nitrogen. Each row of subplots is for a different pore radius, while the columns are for different liquid pressures. The solid lines are for  $S = 1$ , the dashed lines are for  $S = 2$ , and the dotted dashed lines are for  $S = 0.5$ . The horizontal solid black lines represent  $\Delta B = 35 k_B T$  for visual reference. All curves are highlighted in red around the critical volume and the corresponding free-energy barrier.

### 3.6.2 Importance of mixture nonideality

In the literature [121,122,129], the effects of gas on nucleation are often quantified by assuming simple, ideal solution theories such as Henry's or Raoult's laws. For gases that have very low solubility, the error because of this assumption is not expected to be large. By taking  $\gamma_1 = \gamma_2^* = \hat{\phi}_2 = \hat{\phi}_1 = \phi_{1,\text{sat}} = \eta_1 = \eta_2 = 1$ , Equation (3-21) reduces to Henry's law and Equation (3-12) to Raoult's law. Here, the model with these assumptions is referred to as the ideal model. Note that, for nitrogen in water, we already assume  $\gamma_1 = \gamma_2^* = 1$ , even for the nonideal model (see Appendix A). We compare the primary parameter of interest in this

study—the free-energy barrier—of both nonideal and ideal models in Figure 3-7. The orange lines are for the nonideal nitrogen–water system, the light blue lines are for the nonideal carbon dioxide–water system, and the purple dashed lines are for the ideal model. Notice that, for the ideal model, the type of gas is irrelevant because the vapor pressure does not depend on the liquid pressure. We consider three pore sizes (the same pore sizes as above), and the concentration of gas in the liquid is set to be the saturation concentration at the pore intrusion pressure. Since carbon dioxide in water exhibits a highly nonideal behavior at the pressures of interest (see Figure A-3), we see large deviations between the predictions of the two models. The nonideal and ideal curves for the nitrogen–water system follow the same trend while still being noticeably different. For instance, in a 1.5 nm-radius pore, the ideal model overestimates the drying pressure for the carbon dioxide–water mixture by  $\sim 40$  MPa and for the nitrogen–water mixture by  $\sim 20$  MPa [using  $\Delta B_c = 35k_B T$ ; Figure 3-7 (b)]. On all panels of Figure 3-7, the intersection points of the three free-energy curves correspond to the intrusion pressure of the pore. Consequently, the critical nucleus at this point has a liquid–vapor interface with zero (mean) curvature.

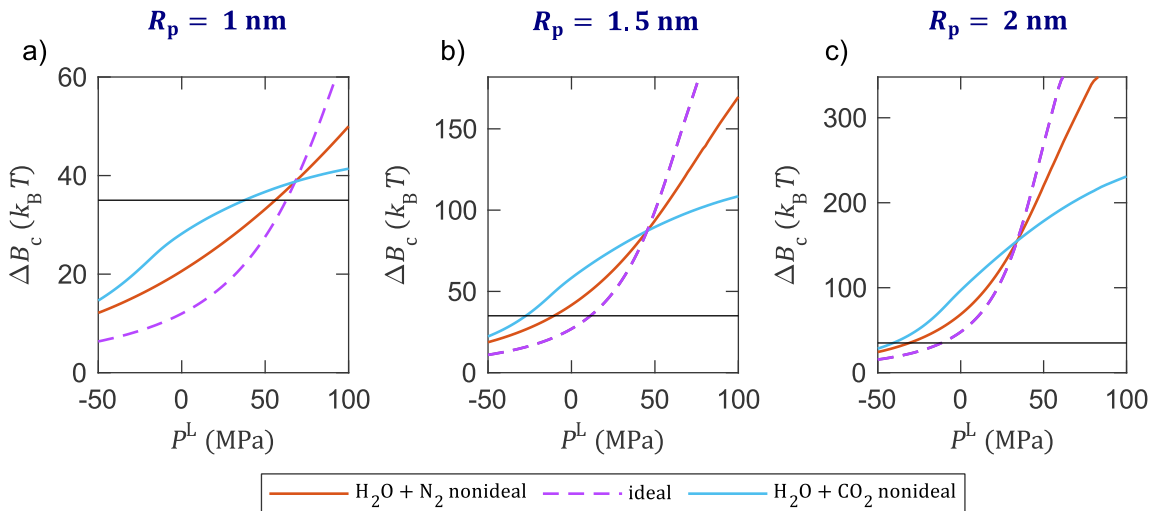


Figure 3-7. Comparison of free-energy barriers as functions of liquid pressure for ideal and nonideal solution models for three different pore sizes: (a)  $R_p = 1$  nm, (b)  $R_p = 1.5$  nm, and (c)  $R_p = 2$  nm. The orange lines are for nitrogen–water and the light blue lines are for carbon dioxide–water. The solid lines correspond to the nonideal model while the dashed lines correspond to the ideal model. The concentration of the gas in the solution is the saturation value at the intrusion pressure of each pore. The horizontal solid black lines represent  $\Delta B = 35 k_B T$  for visual reference. All calculations were done for  $\theta_a = \theta_{eq} = 120^\circ$ ,  $T = 323.15$  K, and  $\sigma^{LV} = 0.068$  J/m<sup>2</sup>.

### 3.6.3 Extrusion pressures and effect of line tension

Previous studies [71,118,195] have found that the free-energy barrier calculated from Equation (3-2) for pure water (see the green curves on Figure 3-4, Figure 3-5, and Figure 3-6) is too high to match with the experiments. Additionally, atomistic simulations in collective variables [195] have shown that, even though the saddle-shaped nucleus is a good approximation, the energy barrier is significantly lower than what is predicted by Equation (3-2). In both cases, it was possible to match the predictions of Equation (3-2) (using the geometry from SE) and the results from the experiments or simulations by adding an energy term to Equation (3-2) proportional to the length of the three-phase contact line. While these may seem like attempts to artificially force classical nucleation theory to agree with the observations, it is often found that an equivalence can be established for the complex physics due to small size by assigning energy to the three-phase contact line (the so-called apparent or effective line tension) [8,33,64,190,193,204,205]. For instance, a good agreement could be achieved between the heterogeneous nucleation experiments and the predictions of classical nucleation theory by including a line tension term in the free-energy equation [149]. Additionally, by preferentially accumulating near the three-phase contact line, dissolved gases in water are reported to act as line-active agents and increase the magnitude of the line tension promoting nucleation [12]. Regardless, we acknowledge that the topic of line tension stays controversial in the scientific community. This is mainly due to difficulties in its direct measurability and a wide range of values reported that vary up to a few orders of magnitude and can be both negative and positive [4]. For pure water in hydrophobic nanopores the reported values are somewhat consistent ranging from  $-10^{-11}$  J/m to  $-6 \times 10^{-11}$  J/m [67,71,118,195].

The inclusion of line tension necessarily modifies the geometry of the critical nucleus. However, by directly calculating the shape, Guillemot *et al.* [71] found that simply calculating the shape without the line tension and then adding an energy term proportional to the length of the three-phase contact line is an excellent approximation, which was first hypothesized by Lefevre *et al.* [118]. Hence, the only modification to the classical model is to add a line energy term,  $\tau\lambda_c$ , to Equation (3-2), where  $\tau$  is the line tension and  $\lambda_c$  is the length of the three-phase contact line of the critical nucleus [160]. We report the theoretical extrusion pressures in Figure 3-8 (a), (b), and (c), for three different values of line tension: (a)  $\tau = 0$  J/m (*i.e.*, no line tension



correction), (b)  $\tau = -1.5 \times 10^{-11}$  J/m, and (c)  $\tau = -3 \times 10^{-11}$  J/m. The orange lines are for the nitrogen–water system, the light blue lines are for the carbon dioxide–water system, and the green lines are for pure water. The required intrusion pressures (the intrusion pressures for a dry pore with no gas or vapor present in the pore) are also shown with black lines as calculated using Equation (3-1). The saturation ratios of gases are  $S = 1$  for the solid curves and  $S = 1.5$  for the dashed curves.

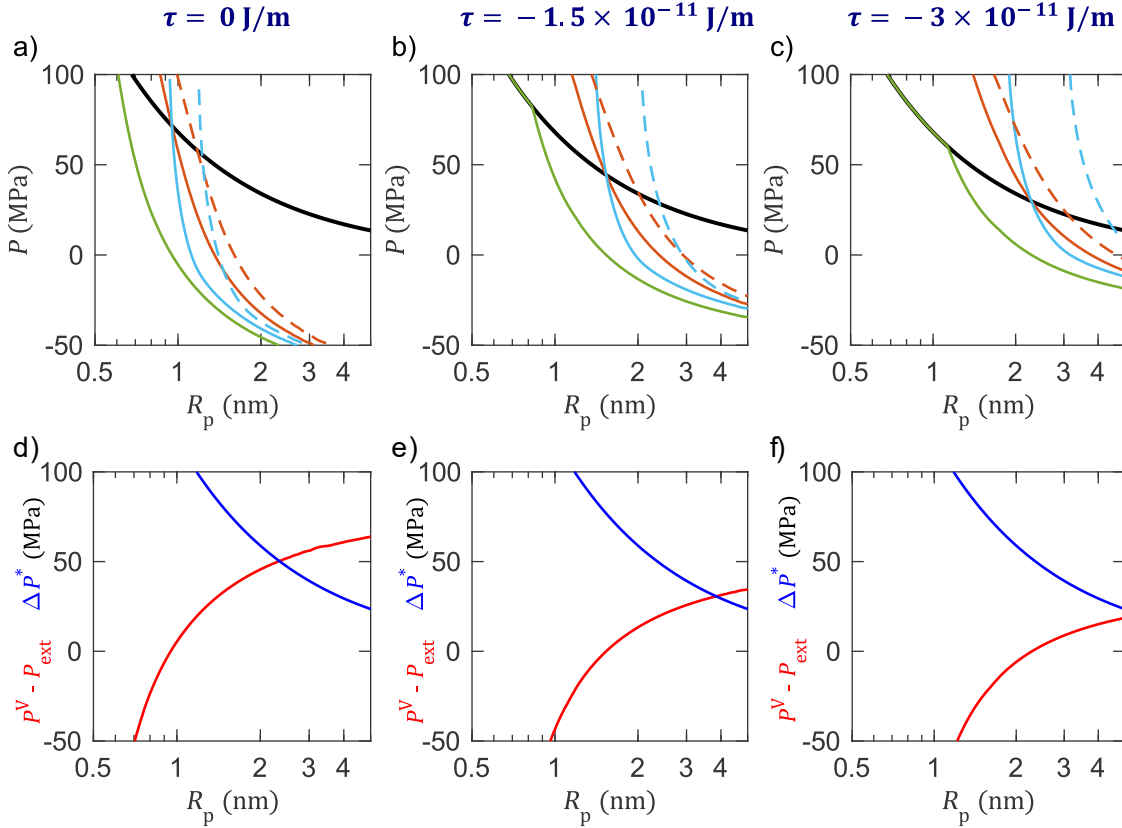


Figure 3-8. Various pressures of interest as functions of pore radius for different values of line tension: (a) and (d)  $\tau = 0$  J/m, (b) and (e)  $\tau = -1.5 \times 10^{-11}$  J/m, and (c) and (f)  $\tau = -3 \times 10^{-11}$  J/m. The black lines on panels (a)–(c) indicate the intrusion pressures for a dry pore. On these panels, the extrusion pressures are shown in green for pure water, in orange for water with dissolved nitrogen, and in light blue for water with dissolved carbon dioxide. The solid lines are for  $S = 1$  and the dashed lines are for  $S = 1.5$ . On panels (d)–(f), the required pressure difference for nucleation,  $P^V - P_{\text{ext}}$  (red lines), and the maximum pressure difference where the vapor phase stays confined in the pore after nucleation,  $\Delta P^* = 2\sigma^{LV} \sin \theta_{\text{eq}} / R_p$  (blue curves), are shown. All calculations were done for  $\theta_a = \theta_{\text{eq}} = 120^\circ$ ,  $T = 323.15$  K,  $\sigma^{LV} = 0.068$  J/m<sup>2</sup>, and  $\Delta B_c = 35k_B T$ .

For all cases in Figure 3-8 (a), (b), and (c), since the amount of dissolved gas decreases as the required intrusion pressure becomes lower with increasing pore size, the effect of the

dissolved gas on the nucleation barrier is negligible for large pores. As the pore size gets smaller, however, the effect becomes more pronounced, and below a certain pore size, a filled pore is unstable even at pressures much higher than the required intrusion pressure. Note that this threshold is independent of the type of gas, if the saturation ratio is  $S = 1$ , but changes with the magnitude of the line tension. This is the pore size where a nucleus with zero curvature ( $P^V = P^L$ ) has energy of  $35k_B T$  meaning that a fluctuation of this size is enough to empty the pore. Clearly, this pore size is independent of the gas type because we assume that water is saturated with gas at  $P_{\text{int}}$  (*i.e.*, the chemical equilibrium is also at  $P^V = P^L = P_{\text{int}}$ ).

It is seen that the stability of pure water in the pore can be controlled by changing the extrusion pressure for all pore sizes, although, the extrusion pressure below a certain pore size becomes at least equal to the intrusion pressure. This is because, at lower temperatures, the pressure of pure water vapor can be taken to be zero because it would be small compared to the pressures of interest in the system. Hence, at pressures higher than the intrusion pressure, a filled pore will be stable because the pressure difference required to form a critical nucleus cannot be accommodated in the pore. Once the extrusion pressure is below the intrusion pressure, however, small pores can always accommodate the required pressure difference for chemical equilibrium, while the corresponding nucleus would have an energy barrier  $\Delta B_c \leq 35k_B T$ , resulting in drying of the pore. For pores larger than a certain size, the extrusion pressure is lower than the intrusion pressure and this gap grows with the pore size. For pure water at high temperatures (but below the critical temperature), water-filled small pores will be unstable even at pressures significantly higher than the intrusion pressure, since water vapor will have high pressures (*i.e.*, comparable to extrusion pressures). However, the extrusion curve in this region will still be parallel to the intrusion curve. The qualitative differences between the pure-water and the water-with-dissolved-gas cases are the result of water being at subcritical conditions while the dissolved gas is supercritical. We also note that, between the two gases, the variation of extrusion pressure with the pore size is smoother for nitrogen compared to carbon dioxide. This is ultimately due to the differences in response of gas solubility to pressure variation [see Figure 3-9 (b), Figure A-2 and Figure A-3].

In Figure 3-8 (d), (e), and (f), we also show the required pressure difference,  $P^V - P_{\text{ext}}$ , in red and the maximum pressure difference a given pore can maintain after nucleation,  $\Delta P^* = 2\sigma^{\text{LV}} \sin \theta_{\text{eq}} / R_p$ , in blue, assuming a flat pore mouth, constant vapor and liquid pressures, and

gas concentration after nucleation. With more negative line-tension value, the required pressure difference is not as high, and pores in a larger size range can maintain the confinement of the vapor phase by pinning the liquid–vapor interface [as depicted in Figure 3-1 (c)].

### ***3.6.4 Required gas concentration to empty the pore at fixed liquid pressure***

Instead of fixing the gas concentration and seeking the required extrusion pressure, the inverse problem can also be solved, which provides more insights. In Figure 3-9, the plots of gas concentration *vs.* pore size are given. In panel (a), the extrusion pressure is set to atmospheric pressure, and in panel (b), it is taken to be equal to the intrusion pressure (varying with pore size). On each panel, for each system (orange curves: nitrogen–water; light blue curves: carbon dioxide–water) three curves are shown representing the three different values of line tension. The solid lines are calculated assuming no line tension, the dashed lines are calculated assuming  $\tau = -1.5 \times 10^{-11}$  J/m, and the dotted lines are calculated assuming  $\tau = -3 \times 10^{-11}$  J/m. All curves start from a certain pore size below which pure water in the pore becomes unstable (*i.e.*,  $x_2 = 0$ ; no gas required). These limits are indicated with the vertical dashed lines. We also show the saturation concentration of gases at  $P_{\text{ext}}$  with the solid red (nitrogen–water) and the solid blue (carbon dioxide–water) curves for visual reference. From panel (a), we see that, at atmospheric pressure, the saturation concentrations of these gases are at least a few orders of magnitude lower than what is required for nucleation. On the other hand, from Figure 3-9 (b) we see that, if the liquid is saturated with the gas at the pore intrusion pressure, there will be a significant shift in what pore sizes can maintain the liquid-filled state. For example, assuming a line tension value of  $\tau = -3 \times 10^{-11}$  J/m, if the liquid is saturated with the gas at the intrusion pressure, the pores  $\sim 2.2$  nm or smaller in size are expected to dry, whereas for pure water this size limit is  $\sim 1.2$  nm [see Figure 3-9 (b) dotted lines and Figure 3-8 (c) solid lines].

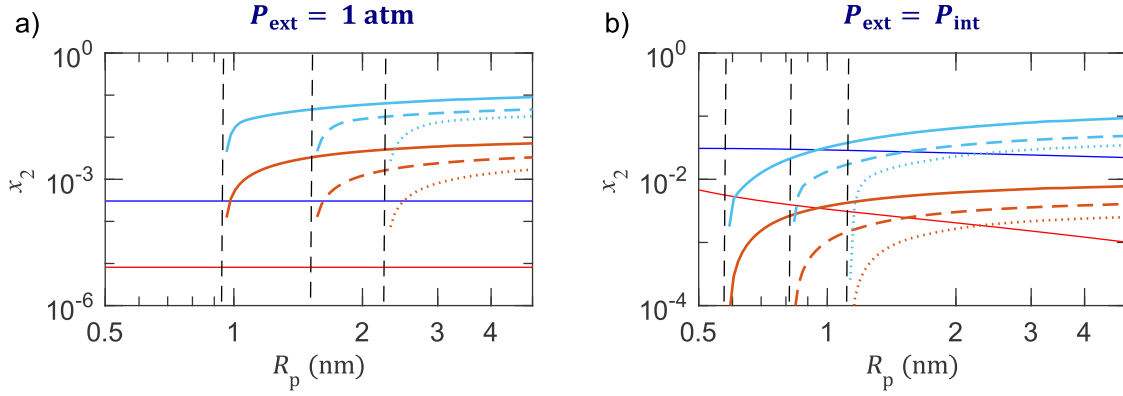


Figure 3-9. The minimum required gas concentrations in the solution,  $x_2$ , to empty the pore in typical experimental times as functions of pore radius at two different extrusion pressures: (a)  $P_{\text{ext}} = 1 \text{ atm}$  and (b)  $P_{\text{ext}} = P_{\text{int}}$  and for three different values of line tension. The bold solid lines are for  $\tau = 0 \text{ J/m}$ , the dashed lines are for  $\tau = -1.5 \times 10^{-11} \text{ J/m}$ , and the dotted lines are for  $\tau = -3 \times 10^{-11} \text{ J/m}$ . The light blue lines are for carbon dioxide in water and the orange lines are for nitrogen in water. For reference, the thin, solid blue and red lines show the saturation concentrations of gases in water at  $P_{\text{ext}}$  for carbon dioxide and nitrogen, respectively. The thin vertical black dashed lines indicate the metastability limit of pure water. All calculations were done for  $\theta_a = \theta_{\text{eq}} = 120^\circ$ ,  $T = 323.15 \text{ K}$ ,  $\sigma^{\text{LV}} = 0.068 \text{ J/m}^2$ , and  $\Delta B_c = 35k_B T$ .

### 3.6.5 On the oversolubility and distribution of gas in confinement

So far, we have assumed that the system is homogeneous in terms of the distribution of the gas in the bulk and in the pores. However, for pore sizes of interest here ( $\sim 1\text{--}5 \text{ nm}$ ), it is well documented [23,86–90,129,158] that the gas tends to migrate into the pores from the bulk resulting in the so-called gas oversolubility due to confinement. For example, from molecular simulations [129], the concentrations of nitrogen and carbon dioxide in water in a pore size of  $R_p = 1.5 \text{ nm}$  have been found to be  $\sim 10$  and  $\sim 5$  times more than the bulk concentration, respectively. Since we consider equilibrium for a vapor nucleus inside the pore and far from the bulk environment, our results are not altered. With oversolubility in mind, when interpreting our results, one should think about the concentrations of gas in the pore and not in the bulk. In practice, this would mean that the amount of gas in the bulk liquid can be an order of magnitude smaller than the saturation concentration (at  $P_{\text{int}}$ ) while still having a significant effect on the extrusion pressure due to oversolubility.

Furthermore, although the distribution of water molecules was found to be bulk-like in the pore, the gas tends to accumulate closer to the walls of the pore [120,123,129,158]. Note that the saturation solubilities of carbon dioxide and nitrogen in water at the conditions

considered are  $\sim 5\%$  and  $\sim 0.5\%$  at most, respectively (mole fraction units; see Figure A-2 and Figure A-3). If the gas was distributed homogeneously inside the pore, it would be unlikely to get a fluctuation that results in a large vapor nucleus containing  $\sim 10$  gas molecules (corresponding to the typical size of the critical nucleus). The highly localized distribution profile of the gas molecules makes these fluctuations more likely. This further suggests that the nucleus should form near the wall of the pore where the gas has significantly higher density.

### 3.7 Comparison with available experimental data

We are aware of only one experimental work with open cylindrical nanopores where a large gas volume was dissolved in water and the drying effects were quantified. In the experiments of Li *et al.* [121], the authors compared intrusion–extrusion cycles of water in cylindrical nanopores with various amounts of dissolved air. They found that, with more gas present, more of the total pore volume could be recovered at the end of the extrusion process. In these experiments, the samples were not held at high pressures at the end of intrusion, and the minimum extrusion pressure was atmospheric. We simulated representative experiments by transforming and fitting to the reported pore size distribution data and calculating the corresponding intrusion–extrusion cycles (for the analysis of the data and the fitted distribution curve, see Appendix A). We used nitrogen for calculations assuming that its effect would be very close to that of air. We fixed the temperature and the contact angle at  $T = 298.15$  K,  $\theta_a = \theta_{eq} = 120^\circ$ , respectively. Note that these values were not reported in reference [121], but the experiments were conducted in lab conditions, and there are other experimental works in the literature [36,71,118] reporting a value of  $\sim 120^\circ$  for the contact angle of pure water with the same grafting/coating material [chloro(dimethyl)octylsilane]. To mimic the experiments, we set the maximum intrusion pressure to 35 MPa. This value corresponds to a minimum intruded pore radius of 2.1 nm, which meant that only  $\sim 92\%$  of the total available pore volume,  $\Delta V_{max}$ , was accessible.

In the experiments of Li *et al.* [121], they had gas-filled pores as well as a controlled volume of gas at the top of the water column at the beginning of the experiments. During the intrusion, the researchers recorded the pressures at which all extra gas dissolved into the liquid, and for the amount of gas they had, this pressure was always lower than the peak pressure reached in the system. From the information about the pore volume, the calculation of gas

concentration in the pore was straight forward. Then, they calculated the gas concentration in the bulk using the ideal Henry's law and added the extra gas concentration to the pore gas concentration. Since the pore volume and the pressure data are reported in reference [121], we could recalculate the extra gas concentration using the nonideal model and determine the gas concentration in the pore more accurately. At the highest gas concentration, we found that our result is  $\sim 16\%$  lower than the reported value calculated with the ideal Henry's law.

The results are summarized in Figure 3-10 for  $10^5$  simulated pores (a large number for smoother curves and reproducibility) sampled from the fitted distribution. In panel (a), the simulated intrusion–extrusion cycles are shown. The  $x$ -axis is the normalized volume change of the system,  $\Delta V/\Delta V_{\max}$ , where  $\Delta V$  is the magnitude of the volume change of the system. The black line is the intrusion curve, the green line is the extrusion curve for pure water, and the orange lines are the extrusion curves for water with dissolved nitrogen. The solid orange line is for  $x_2 = 1.518 \times 10^{-3}$ , the dashed orange line is for  $x_2 = 1.055 \times 10^{-3}$ , and the dotted orange line is for  $x_2 = 7.695 \times 10^{-4}$ . These values are the concentrations of nitrogen in the confinement as recalculated here using the data from reference [121]. In panel (b), the simulated results (blue curve) are compared with the experimental results (green and orange squares) in terms of the percentage of the total intruded pore volume recovered at the end of the extrusion. Note that, in the experiments, the minimum pressure reached at the end of extrusion was atmospheric, which is shown by the horizontal black dashed line in panel (a) (precise value not reported; assumed to be 1 atm). We treated the line tension,  $\tau$ , as an adjustable parameter. A constant value of  $\tau = -4.4 \times 10^{-11}$  J/m was chosen to best fit the experimental data in terms of root-mean-square deviation from the reported data for the portion of the recovered volume. This value of the line tension is reasonable and within the range of the previously published results for pure water in hydrophobic nanopores [67,71,118,195].

In Figure 3-10 (b), it is seen that the simulated line does not exactly go through all experimental points, but it is close and follows a similar trend. One of the reasons for the deviation could be the accuracy of the reported data and the inherent uncertainties due to the lack of experimental detail. Note that the results in reference [121] are given without isolating the volume change purely due to the intrusion and extrusion of solution in and out of the nanopores from other effects, such as the volume change due to the compressibility of the test chamber and the compressibility of the solution itself. That such effects are important is

obvious when the intrusion–extrusion cycles in reference [121] are compared to other works in the literature where the device was calibrated, or the results were numerically corrected like in reference [72] (additionally, see the intrusion–extrusion curves in references [118] and [71]). Consequently, the way the volume change information was inferred from the raw experimental data is ambiguous. Therefore, we believe that the reported data in reference [121] may not exactly reflect the recovered nanopore volume. Clearly, there are other factors and inherent uncertainties, including that the actual macroscopic contact angle could be slightly different than the one we used in the simulations, or the pore size distribution after the hydrophobic coating was applied could be different from the theoretical estimation we made (see Appendix A). The uncertainties in the ambient temperature and pressure at the time of the experiments are also important as these parameters are input to the phase equilibrium equations. The assumption we made of nitrogen exhibiting the same quantitative behavior as air should be reevaluated as well. Additionally, the effects of dissolved gas on the liquid–vapor interfacial tension, the solid–liquid contact angle, and the line tension need to be quantified, which are not considered here. Also note that there are uncertainties in selecting  $35k_{\text{B}}T$  as the height of the activation barrier.

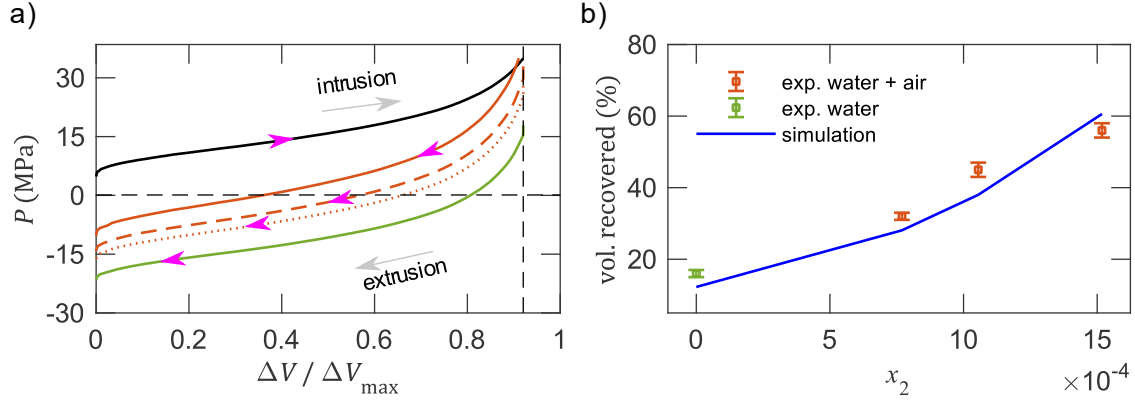


Figure 3-10. Summary of the simulated experiments based on data from Li *et al.* [121]. (a) simulated intrusion–extrusion cycles where the  $x$ -axis is the magnitude of the normalized volume change of the system,  $\Delta V/\Delta V_{\max}$ . The black line is the intrusion curve, the green line is the extrusion curve for pure water, and the orange lines are the extrusion curves for water with dissolved nitrogen at the recalculated experimental gas concentrations. Note that air was used in the experiments, which is modeled here with nitrogen. The solid orange line is for  $x_2 = 1.518 \times 10^{-3}$ , the dashed orange line is for  $x_2 = 1.055 \times 10^{-3}$ , and the dotted orange line is for  $x_2 = 7.695 \times 10^{-4}$ . The vertical black dashed line shows the maximum intruded volume at peak pressure (0.92). The horizontal black dashed line shows the minimum extrusion pressure in the experiments (1 atm). (b) comparison of recovered nanopore volume at the end of the experiments when the pressure was brought to 1 atm (green square: pure water, orange squares: water with dissolved air) with the simulated results (blue line). All calculations were done for  $\theta_a = \theta_{\text{eq}} = 120^\circ$ ,  $T = 298.15$  K,  $\tau = -4.4 \times 10^{-11}$  J/m,  $\sigma^{\text{LV}} = 0.072$  J/m<sup>2</sup>, and  $\Delta B_c = 35k_B T$ . See the main text and Appendix A for more details.

### 3.8 Conclusion

In this chapter, we used Gibbsian composite-system thermodynamics with classical nucleation theory to study the effects of dissolved nitrogen and carbon dioxide on the behavior of water in hydrophobic cylindrical nanopores open at both ends. For this purpose, we derived an equation relating the nonideal chemical equilibrium of a mixture made of a subcritical solvent and a supercritical gas to the curvature of the liquid–vapor interface. The role of the confinement geometry on drying pressure of a nanopore was highlighted. To summarize, in a cylindrical pore, the surface of the energy-minimizing nuclei can be either negatively or positively curved. It is due to this shape that small pores can empty at high liquid pressures. Following previous works, we used Surface Evolver to calculate the nontrivial nucleus geometry. Unlike previous studies, the possibility of symmetric nuclei as part of the nucleation path was ruled out based on physical arguments.



Our findings are in qualitative agreement with the previous molecular dynamics simulations, and experiments; that is, the dissolved gas effects are negligible if water is saturated with the gas in atmospheric conditions. However, if, at intrusion pressure, an ample amount of gas is present in the system to dissolve, it can greatly reduce the vapor nucleation barrier, and as a result, increase the pressure at which the pore dries. This was attributed to increased vapor pressure inside the critical nucleus hence its smaller size and energy compared to the pure-liquid case at the same liquid pressure and temperature. A direct consequence of this is that smaller pores can dry even at pressures much higher than their intrusion pressures (intrusion pressure for an empty pore). Furthermore, it was found that the ideality assumption typically made in the studies of weakly soluble gases may result in significant errors at the conditions of interest.

There is a recent study in the literature where the recovered nanopore volume at the end of extrusion was observed to be proportional to the amount of dissolved air in water. By simulating the experimental intrusion–extrusion cycles and adjusting the line tension, a semi-quantitative agreement could be achieved between the theory and the reported data for water with dissolved air. However, more carefully controlled experiments are needed for a conclusive test of the theory because of the scarcity of available measurements that are directly comparable. Moreover, there are uncertainties in the studied dataset that are difficult to evaluate.

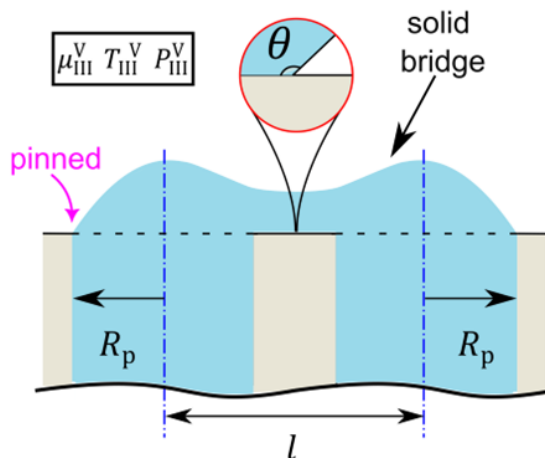
Molecular dynamics simulations might shed light on some of the aspects that are difficult to probe experimentally, such as the concentration of the gas in the pore, shape of the critical nucleus in the presence of the gas, and phase partitioning during nucleation. Simulation of rare events, such as nucleation with traditional methods have been difficult and expensive because of different time scales involved. Up until recently, long waiting times before the onset of nucleation and the fast dynamics near the criticality region have forced researchers to simulate in unrealistic conditions and extrapolate their results. With the development of new, rare-event-specific algorithms and increasing computational power, however, it is becoming feasible to simulate larger systems for longer times obtaining more realistic results.

Finally, we emphasize that what is referred to as line tension in this chapter is merely an adjustable parameter and the corresponding energy term scales linearly with the size of the nucleus. In the previous section, its value is obtained from fitting to the experimental data.

Neither the magnitude nor the sign of this value should be interpreted as the energy of the three-phase contact line as it empirically accounts for other effects. These other effects include the shortcomings of the continuum approach at the relevant scale, experimental uncertainties (*e.g.*, pore size distribution, temperature), model uncertainties (*e.g.*, height of the energy barrier), and the simplifications made by neglecting the interfacial effects of the dissolved gas.

## Chapter 4

# The Role of Geometry on the Ease of Solidification Inside and Out of Cylindrical Nanopores<sup>1</sup>



### Chapter summary

We investigated the role of a nanoporous particle on the formation of macroscopic solid in the framework of equilibrium thermodynamics and from the free-energy perspective. The model particle has cylindrical pores with equidistant circular openings on the particle surface. We focused on two potentially limiting steps: (i) the solid nucleation from liquid inside a single pore and (ii) the bridging of multiple pores on the particle surface *via* vapor deposition. We examined the nucleation near the liquid–vapor meniscus inside a pore by considering different solid–vapor and solid–pore wall contact angles, as well as the liquid–vapor meniscus angles. For bridging, we quantified the effects of the proximity of neighboring pores and the number of participating pores where we considered two or three pores, placed two different distances apart, and three contact angles of the solid with the particle surface. Except in special cases for

---

<sup>1</sup> This chapter and Appendix B of this thesis, with minor changes, have been submitted for publication as H. Binyaminov and J. A. W. Elliott, *The Role of Geometry on the Ease of Solidification Inside and Out of Cylindrical Nanopores*.

which an analytical solution could be developed, we determined the equilibrium nucleus and bridge shapes numerically using the Surface Evolver code. The geometry of these equilibrium shapes was the key for correctly calculating the energy barriers. Our results indicate that the meniscus angle can be an important factor in reducing the barrier for nucleation if the internal angles of the solid nucleus satisfy a certain criterion. For the solid growth out of the pores, we found that the barriers were significantly lower in the presence of multiple, closely packed pores compared to the growth from a single pore. This chapter is deliberately written with no reference to material properties or a specific process to highlight the generality of geometry-controlled barriers. A direct application where our findings can be particularly valuable is the ice formation in clouds, which is the subject of intensive research in atmospheric sciences for its role in influencing precipitation patterns and hence the climate.

## 4.1 Introduction

Solid formation from liquids in confinement has been extensively researched starting with experiments as early as the beginning of the 20th century, followed by an exponential growth in the number of articles over the past few decades, thanks to the ability to now image nanoscopic phenomena, make porous materials of desired characteristics in the lab, and access to advanced computational tools such as atomistic simulations. The interest in these systems stems from their abundance in nature as well as a plethora of technological applications. Consequently, there are many theoretical, experimental, and simulation works in the literature focusing on solid–liquid phase behavior in various confinements. Excellent reviews on this topic can be found in references [58], [34], and [1]. Although the general effects of confinement on phase transition have been well established, the influence of geometrical features of porous media have stayed somewhat elusive. We discuss below some of the more recent articles regarding the role of geometry, which have been the inspiration for our analysis presented in this chapter. With water being, by far, the most studied fluid in literature due to its importance, the majority of works mentioned here deal with water–ice systems.

The molecular simulation work of David *et al.* [38] showed that the pore condensation and freezing process is responsible for ice nucleation in the presence of porous particles and below water saturation. Using model porous particles with cylindrical pores in atmospherically relevant conditions, they concluded that water vapor first condenses in the pores, and then

freezes homogenously. However, the ice in the pores remained confined unless vapor pressure was substantially increased, in which case the neighboring pores bridged and grew into macroscopic ice on the particle surface. The same particle with a single ice-filled pore, or with no pores did not grow bulk ice at the same conditions during the simulation time. Later, experiments of David *et al.* [37] supported the ice nucleation *via* the pore condensation and freezing mechanism and showed the importance of the pore size, water contact angle, and surface functionalization. The researchers also observed solid nucleation above the homogenous nucleation temperature of ice, which they attributed to the presence of so-called active sites and/or to the effect of the surface functionalization. In another study, Campbell *et al.* [27,28] experimentally investigated solid formation from water [27,28] and organic vapors [28] inside and out of mica pockets with sharp wedges. By directly imaging the crystallization within the pockets, they demonstrated that the acute angle of the pocket provides extremely efficient nucleation sites. After the condensation of the liquid, the solid phase first formed along the apex of the wedge and then proceeded to grow out of the pockets, if a threshold vapor pressure was achieved. In the case of ice [27], the limiting step for bulk solid formation was not the nucleation of the solid within the pockets but rather the growth of the solid out of the pockets.

Molecular simulations of Bi *et al.* [13] with a coarse-grained water model revealed that atomically sharp concave wedge geometries made of carbon can promote ice nucleation, with or without a match between the wedge angle and the ice lattice structure. In a different study by the same group, Cao *et al.* [30] observed temperature-dependent simultaneous ice formation in hydrophobic slit pores and sharp wedges. In simulations with the wedges, the formation of ice started at the intersection line of the wedge walls (*i.e.*, at the wedge apex). Roudsari *et al.* [175] performed similar simulations with model AgI pores, but they also used an atomistic model of water in addition to the coarse-grained model. They found that, besides the effect of the confinement, the ice nucleation efficiency of the slit and wedge pores depends on the geometrical match between the slit width, wedge angle, and ice lattice structure. Furthermore, a small amount of ice remained in the wedge apex even above the melting point of ice in their simulations. They also demonstrated the inability of ice to grow out of the slit pores unlike for the wedge shapes. While most of the findings of Roudsari *et al.* [175] were consistent with the conclusions of Bi *et al.* [13] and Cao *et al.* [30], the discrepancies were attributed to the

accuracy levels of the models used and the strong lattice match between AgI and ice compared to that between carbon and ice. Another finding in favor of geometry-dominated heterogeneous ice nucleation was provided by Wang *et al.* [200]. Their experiments with microscopic kaolinite particles—a material whose basal plane has a good lattice-match with ice—showed the emergence of ice crystals from the rough features (pits, cracks) on the particles rather than from the smooth basal planes of the particles.

Experiments have also shown solid-like behavior in a nanomeniscus above the bulk melting point of the solid. For example, Jinesh and Frenken [100] used an atomically sharp tungsten tip with a friction force microscope and scanned over a graphite surface. They found that water condensation between the tip and the surface and the subsequent formation of solid at ambient temperature was responsible for the observed stick-slip motion of the tip during the scanning. Using spherical noble-metal particles in contact with one another, Shin *et al.* [187] demonstrated the existence of ice-like water near the contact points of the spheres in ambient conditions. This behavior seemed to be unaffected by the temperature, material type, particle size, and particle shape. In another study, by high-resolution imaging, Algara-Siller *et al.* [2] reported “square-ice” at room temperature in samples of water trapped between two graphene monolayers. Molecular simulations in the same work indicated that “square-ice” should be present in any water inside hydrophobic nanopores, independent of the exact nature of the confining atoms.

The role of the liquid–vapor interface in the formation of a solid phase has also been the subject of many studies. For example, Haji-Akbari and Debenedetti [75] used a molecular model of water to study the influence of the liquid–vapor interface on ice nucleation in free-standing thin water films (4 nm in thickness). Since the liquid–vapor interfaces were flat, curvature effects were not present. The authors observed seven orders of magnitude increase in the ice nucleation rate compared to the bulk nucleation rate at the same conditions with the ice nuclei starting in the subsurface regions of the film. Interestingly, the opposite trend was observed by the same [76] or different researchers utilizing computationally less expensive coarse-grained water models. For example, molecular simulations by Rosky *et al.* [171] of water bridges confined between two hydrophilic walls with varying separations and well-defined liquid–vapor interfaces showed no preference for the nucleation of ice at the meniscus. In fact, the nuclei avoided the immediate vicinity of the interface and primarily formed near

the walls. The predominant role of the meniscus in this study was to create a negative pressure in the liquid, which facilitated an increase in nucleation rate. Simulations with a coarse-grained water model by Moore *et al.* [143] in hydrophobic, filled cylindrical nanopores and by Solveyra *et al.* [66] in hydrophobic or hydrophilic, partially-filled cylindrical nanopores showed no evidence for heterogenous nucleation. In all cases, ice formed away from the interfaces in the bulk-like regions of the liquid. In a recent study, Hussain and Haji-Akbari [95] used a modified version of the coarse-grained model, which had surface propensity for nucleation. Using this model, they investigated ice nucleation in water films of varying thickness attached to flat solid substrates. They found that when the liquid–vapor interface was close to the substrate (*i.e.*, thin film;  $\sim 1$  nm), the nuclei formed as hourglass shapes connecting the substrate surface and the free surface of the liquid. When the film thickness was larger ( $\sim 3$  nm), however, the nuclei formed on the surface of the substrate as spherical caps. This topological change in the nucleus shape was partially responsible for the observed several orders of magnitude increase in the ice nucleation rate in the thinner films.

Overall, these problems, at least to some extent, seem to be amenable to the framework of classical heterogenous nucleation theory with a single reaction coordinate (nucleus volume). To that end, Bai *et al.* [7] experimentally probed the critical ice nucleus size by including graphene nanoparticles of different sizes in supercooled water droplets. They found that, if the nanoparticles are smaller than a certain, temperature-dependent size, then the pinning of the ice nucleus around the periphery of the particles results in suppression of the nucleation instead of promotion observed for larger particles—consistent with the predictions of classical nucleation theory. Furthermore, formation of a new phase at the three-phase contact lines (*i.e.*, nucleation of a third phase at the intersection line of two phases and the confining wall) or in the corners of a fixed confinement geometry, and even the barrier-limited growth from the confinement into the bulk seem to be generic features of any system capable of criticality. For example, simulations of Sear [181] with a three-spin system (three-state Potts model) in a two-dimensional box showed orders of magnitude increase in the nucleation rate at the three-phase contact line compared to nucleation in the bulk or heterogenous nucleation. In a similar study by Page and Sear [156], the new phase of a two-spin system started in the concave corner of a two-dimensional square well, and the growth of the new phase out of the well required

overcoming a second energy barrier. Based on nucleation theory, the authors argued that these findings equally translate to more complex systems such as ice or protein nucleation.

Our work here aims to provide insights, from the equilibrium thermodynamics perspective, for the role of (i) liquid–vapor meniscus angle on the solid nucleation inside liquid-filled cylindrical nanopores and (ii) the pore numbers and proximity on the ease of growth of the solid out of the pores. Equilibrium thermodynamics has been previously used by our group to investigate similar systems, such as the stability of liquid capillary bridges and three-phase lenses [15,43], new phase formation in various geometries [17,215,217], and stability of surface nanobubbles [218], among others. The first part of this study was motivated by the growing literature providing evidence for the preferential solid nucleation in wedges as well as near the liquid–vapor interface, some of which have been referenced above. The second part of this study was mainly motivated by the simulation work of David *et al.* [38], where the authors argued that pore proximity plays an important role in the formation of bulk solid out of the pores.

## 4.2 System definition and free energy

A schematic description of the pore condensation and solidification process is given in Figure 4-1 (a). Initially, a dry porous particle exists in a vapor environment. The model particle is assumed to contain locally equidistant cylindrical nanopores with the same pore radii,  $R_p$ , that have circular openings on the particle surface. The pore lengths are assumed to be much larger than their radii, hence, they can be assumed to be infinitely long for our purposes. The distance between the central axes of the pores is  $l$ . The particle surface is assumed to be flat in the neighborhood of a collection of a few pores. The mechanism by which the porous particle facilitates bulk solid formation has the following three stages: (I) condensation of liquid into the pores, (II) solidification of the liquid in the pores, and (III) formation of bulk solid. Stage (I) takes place due to the (inverse) Kelvin effect, and it has been thoroughly studied in the literature [85,112,141,209,211]. Stage (II) starts with the nucleation of a solid, which then grows to fill the entire pore. Similarly, in Stage (III), individual solid-filled pores should first bridge—possibly a barrier-limited step, which is then followed by growth. In this chapter, we study, from the free-energy perspective, first, solid nucleation inside a single pore at the liquid–



vapor meniscus, and then, solid bridging of multiple pores. Nonequilibrium growth of the solid in both Stages (II) and (III) is not discussed.

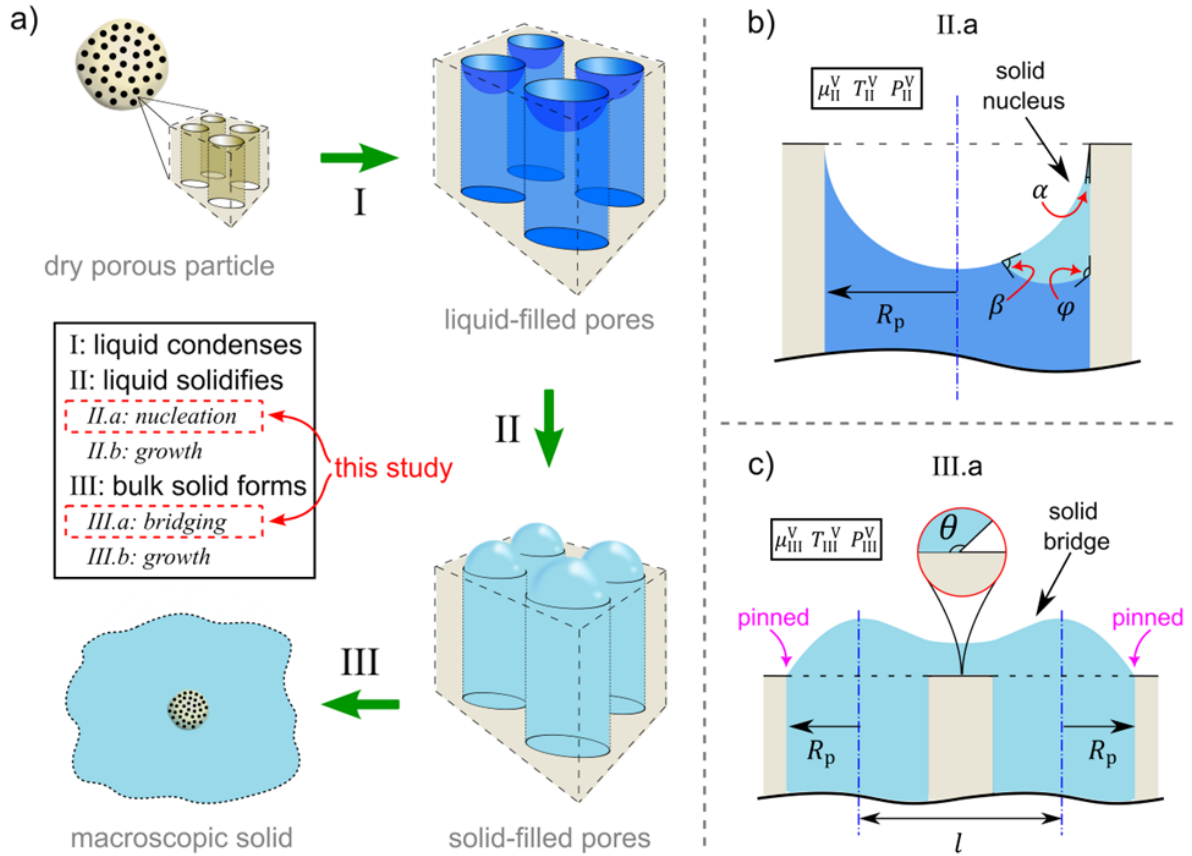


Figure 4-1. Descriptions of the systems and processes of interest in this work: (a) schematic depiction for the pore condensation and solidification process, (b) system definition for the solid nucleation at the liquid–vapor meniscus, and (c) system definition for the solid bridging of the pores. See the text for more details.

#### 4.2.1 Solid nucleation at the meniscus

We consider nucleation of a solid phase in contact with the pore wall and the liquid–vapor interface (meniscus), *i.e.*, at the three-phase contact line. We assume that, because the flux of molecules from the vapor into the solid phase can be shown to be negligible compared to that from the liquid in the pore, the shape of the meniscus does not change upon the formation of the nucleus. In other words, the liquid–vapor interface is treated as fixed during this nucleation, which has been found to be the case for freezing of small domains of liquid water in molecular simulations [93,101,128]. This also means that our findings would equally apply if, instead of vapor, we had a fixed sphere (with potentially different chemistry than the

pore wall) that blocks the pore. We will refer to this phase as vapor and the interface as the meniscus throughout this chapter, although the thermodynamics would be the same if the vapor phase were to be replaced by a fixed immiscible sphere.

The hypothetical equilibrium state of the system is schematically depicted in Figure 4-1 (b). The reference state is chosen to be the liquid-filled pore at equilibrium with the vapor at the end of Stage (I). The system with the nucleus is described by the pore radius,  $R_p$ , the meniscus angle,  $\alpha$ , the solid–liquid–vapor contact angle,  $\beta$ , the solid–liquid–pore wall contact angle,  $\varphi$  (all angles measured through the solid), and the nucleus volume. The pore is assumed to be infinitely rigid and insoluble. The system is allowed to exchange mass, energy, and volume with the vapor phase, which acts as a reservoir; that is, its chemical potential  $\mu_{II}^V$ , temperature  $T_{II}^V$ , and pressure  $P_{II}^V$  stay constant during the nucleation. However, because the nucleus volume is negligible compared to the bulk liquid volume in the pore, the volume change due to the difference in the densities of solid and liquid is assumed to be negligible upon nucleation. This leads to a system in the  $\mu VT$  ensemble for which, following the increase-of-entropy principle for a spontaneous change around equilibrium subject to constraints, the system free energy with respect to the reference state can be found as [15,43,202,215]

$$\Delta B_{\text{nuc}} = -\sigma^{\text{SL}} k_{\text{nuc}}^* V_{\text{nuc}}^{\text{S}} + \sigma^{\text{SL}} A_{\text{nuc}}^{\text{SL}} - \sigma^{\text{SL}} \cos \beta A_{\text{nuc}}^{\text{SV}} - \sigma^{\text{SL}} \cos \varphi A_{\text{nuc}}^{\text{SP}} \quad (4-1)$$

where  $k_{\text{nuc}}^*$  is twice the mean curvature of the solid–liquid interface of the equilibrium nucleus with the unit normals of the surface pointing from the solid to the liquid (simply curvature hereafter).  $\sigma^{\text{SL}}$  is the interfacial tension between the solid and the liquid.  $A_{\text{nuc}}^{\text{SL}}$ ,  $A_{\text{nuc}}^{\text{SV}}$ , and  $A_{\text{nuc}}^{\text{SP}}$  are the areas of solid–liquid, solid–vapor, and solid–pore wall interfaces, respectively. Equation (4-1) can be put in a dimensionless form by dividing both sides by  $R_p^2 \sigma^{\text{SL}}$  yielding

$$\Delta \tilde{B}_{\text{nuc}} = -\tilde{k}_{\text{nuc}}^* \tilde{V}_{\text{nuc}}^{\text{S}} + \tilde{A}_{\text{nuc}}^{\text{SL}} - \cos \beta \tilde{A}_{\text{nuc}}^{\text{SV}} - \cos \varphi \tilde{A}_{\text{nuc}}^{\text{SP}} \quad (4-2)$$

where  $\Delta \tilde{B}_{\text{nuc}} = \Delta B_{\text{nuc}} / R_p^2 \sigma^{\text{SL}}$ ,  $\tilde{V}_{\text{nuc}}^{\text{S}} = V_{\text{nuc}}^{\text{S}} / R_p^3$ ,  $\tilde{k}_{\text{nuc}}^* = k_{\text{nuc}}^* R_p$ ,  $\tilde{A}_{\text{nuc}}^{\text{SL}} = A_{\text{nuc}}^{\text{SL}} / R_p^2$ ,  $\tilde{A}_{\text{nuc}}^{\text{SV}} = A_{\text{nuc}}^{\text{SV}} / R_p^2$ , and  $\tilde{A}_{\text{nuc}}^{\text{SP}} = A_{\text{nuc}}^{\text{SP}} / R_p^2$ . Furthermore, we denote the energy of an equilibrium nucleus by  $\Delta \tilde{B}_{\text{nuc}}^*$ , which is obtained when the volume and areas of an equilibrium nucleus are used in Equation (4-2). In general, we denote the quantities corresponding to an equilibrium state by a superscript asterisk.

For solid–liquid equilibrium, the curvature,  $\tilde{k}_{\text{nuc}}^*$ , is dictated by the well-known Gibbs–Thomson equation [45,46], which relates the degree of undercooling,  $\Delta T$ , to the curvature of the solid–liquid interface:

$$\Delta T = T_m - T_{\text{II}}^{\text{V}} = \frac{\tilde{k}_{\text{nuc}}^* \sigma^{\text{SL}} v^{\text{S}}}{(s^{\text{L}} - s^{\text{S}}) R_{\text{p}}} \quad (4-3)$$

where  $T_m$  is the melting point of the solid at the pressure of the liquid inside the pore,  $v^{\text{S}}$  is the molar volume of the solid, and  $s^{\text{L}}$  and  $s^{\text{S}}$  are the molar entropies of the liquid and the solid, respectively. Equation (4-3) shows that, for a given pore, setting the temperature,  $T_{\text{II}}^{\text{V}}$ , is equivalent to setting  $\tilde{k}_{\text{nuc}}^*$ . Therefore, for a comparative analysis, it is natural to investigate how the dimensionless free-energy barrier depends on the angles,  $\alpha$ ,  $\beta$ , and  $\varphi$  for a fixed  $\tilde{k}_{\text{nuc}}^*$ .

We emphasize that,  $T_m$  in Equation (4-3) depends on the liquid pressure in the pore, which is dictated by the Laplace pressure due to the curvature of the liquid–vapor interface [171]. Consequently, it is a function of the meniscus angle  $\alpha$ . This dependence is complicated mainly because it is determined by the properties of the liquid as well (*e.g.*, the slope of the solid–liquid equilibrium line in the phase diagram). For this reason, we assume that  $T_m$  is independent of  $\alpha$ . This simplification lets us isolate the direct effects of geometry alone on the energy barriers, which is our goal here.

#### 4.2.2 Bridging of the pores

Once sufficient time has passed and all the pores have frozen at the end of Stage (II), the system reaches a new equilibrium state where each pore has a spherical solid cap pinned at the pore mouth. This state can be shown to be metastable or stable. For generality, we assume that the intensive properties of the reservoir may have changed, and that they take the new values of  $\mu_{\text{III}}^{\text{V}}$ ,  $T_{\text{III}}^{\text{V}}$ , and  $P_{\text{III}}^{\text{V}}$ . The curvature of the spherical caps at the pore mouth is dictated by the (complete) Kelvin equation [41], written for the vapor–solid equilibrium:

$$\tilde{k}_{\text{cap}}^* = \frac{R_{\text{p}}}{v^{\text{S}} \sigma^{\text{SV}}} \left[ \bar{R} T_{\text{III}}^{\text{V}} \ln \left( \frac{P_{\text{III}}^{\text{V}}}{P_{\infty}} \right) - v^{\text{S}} (P_{\text{III}}^{\text{V}} - P_{\infty}) \right] \quad (4-4)$$

where  $\tilde{k}_{\text{cap}}^* = 2R_{\text{p}}/R_{\text{cap}}$  is the dimensionless curvature of the equilibrium cap with  $R_{\text{cap}}$  being the radius of the cap,  $\bar{R}$  is the universal gas constant,  $P_{\infty}$  is the saturation vapor pressure with respect to solid across a flat interface at  $T_{\text{III}}^{\text{V}}$ , and  $\sigma^{\text{SV}}$  is the interfacial tension of the solid–vapor interface. We are only interested in scenarios where the vapor properties are such that it

can be in equilibrium with a cap with positive curvature (*i.e.*, convex, protruding into the vapor). This limits the range of  $\tilde{k}_{\text{cap}}^*$  to  $0 < \tilde{k}_{\text{cap}}^* < 2$ , for the following reasons: If the conditions are such that  $\tilde{k}_{\text{cap}}^* < 0$ , the solid–vapor interface is concave (*i.e.*, depressed into the pore) so it cannot grow out of the pores because no negatively curved solid geometry is possible outside of the pore on a flat substrate. If  $\tilde{k}_{\text{cap}}^* > 2$ , the pinned caps are no longer equilibrium shapes so the solid is expected to grow out of the pore spontaneously without a barrier. The latter case will be shown by free-energy analysis in section 4.5.2.

The ease of formation of the bulk solid beyond the pore mouths depends on the growth path and the corresponding free-energy barrier. One often-studied scenario is the growth from a single pore where the barrier is calculated by following a path of a sequence of spherical caps (first pinned, then not pinned). This is a reasonable assumption if the distance between the neighboring pores is large. If, however, the distance between the neighboring pores is comparable to the size of the pores, then the possibility of bridging of the pores should be considered because these shapes might provide energetically more favorable growth pathways. An example schematic of such a bridging scenario is depicted in Figure 4-1 (c). The bridging is characterized by the number of pores participating,  $n$  [in Figure 4-1 (c),  $n = 2$ ]; the radii of the pores,  $R_p$ ; the distance between the pore centers,  $l$ ; the solid–porous particle surface–vapor contact angle,  $\theta$  (measured through the solid); and the volume of the entire shape above the plane of the particle surface.

Similarly to the nucleation at the meniscus, following the increase-of-entropy principle for a spontaneous change around equilibrium subject to constraints, we can arrive at the free energy,  $\Delta B_{\text{bri}}$ , for the bridging of  $n$  pores by the formation of solid from the vapor [15,43,202,215]. In a dimensionless form, the free-energy equation can be written as

$$\Delta \tilde{B}_{\text{bri}} = \Delta B_{\text{bri}}/R_p^2 \sigma^{SV} = -\tilde{k}_{\text{bri}}^* \tilde{V}_{\text{bri}}^S + (\tilde{A}_{\text{bri}}^{SV} - n\pi) - \cos \theta \tilde{A}_{\text{bri}}^{\text{SP}} \quad (4-5)$$

for which the reference state is chosen as the state where  $n$  number of pores are covered with flat disks of solid at the pore mouths at the same conditions (*i.e.*, same chemical potential of the solid). This is a convenient reference state because the volume and solid–pore wall area above the particle surface plane are zero, hence the nondimensional free energy of the reference state is simply  $n\pi$ . Note that the reference state does not need to be an equilibrium state. In Equation (4-5),  $\tilde{k}_{\text{bri}}^* = k_{\text{bri}}^* R_p$  with  $k_{\text{bri}}^*$  being twice the mean curvature of the equilibrium

bridge with the unit normals of the surface pointing from the solid to the vapor (simply curvature hereafter), and since the bridge forms at the same conditions,  $\tilde{k}_{\text{bri}}^* = \tilde{k}_{\text{cap}}^*$ . That is, the curvature of the equilibrium bridge is also dictated by the solid–vapor equilibrium through Equation (4-4).  $\tilde{V}_{\text{bri}}^S = V_{\text{bri}}^S/R_p^3\sigma^{SV}$  is the dimensionless volume of the shape above the plane of the particle surface,  $\tilde{A}_{\text{bri}}^{SV} = A_{\text{bri}}^{SV}/R_p^2\sigma^{SV}$  is the dimensionless area of the solid–vapor interface,  $\tilde{A}_{\text{bri}}^{SP} = A_{\text{bri}}^{SP}/R_p^2\sigma^{SV}$  is the dimensionless area of the solid–particle surface interface (*i.e.*, the flat part of the shape covering the particle surface).

Similarly to the nucleation inside the pore, we denote the dimensionless free energy of an equilibrium bridge by  $\Delta\tilde{B}_{\text{bri}}^*$ , which corresponds to using the volume and areas of an equilibrium bridge in Equation (4-5). We also denote the quantities corresponding to an equilibrium state by a superscript asterisk when studying bridging. Furthermore, we define the dimensionless distance between the pores as  $\tilde{l} = l/R_p$ . Since setting the temperature,  $T_{\text{III}}^V$ , and the vapor pressure,  $P_{\text{III}}^V$ , for a given pore is equivalent to fixing  $\tilde{k}_{\text{bri}}^*$  through Equation (4-4), it is natural to compare the energy barriers for different values of parameters,  $n$ ,  $\tilde{l}$ , and  $\theta$  for a fixed  $\tilde{k}_{\text{bri}}^*$ .

### 4.3 Methods

The volumes and areas in Equations (4-2) and (4-5) need to be quantified to compute the free energies of nuclei and bridges, respectively. To that end, we use the Surface Evolver (SE) code [21,22] to find the nontrivial equilibrium geometries. Surface Evolver is an open-source software designed for complex variational problems involving surface and other forces (*e.g.*, gravity). The surfaces in SE are discretized and represented by a union of triangles, including their edges and vertices. The equilibrium shapes are calculated by first providing a rough mesh of the expected shape (*e.g.*, a cube to represent a sphere), which is then refined and moved towards the minimum-energy shape by the built-in gradient descent or conjugate gradient methods. Constraints can be put on the system such as the conservation of the volume, and fixed boundaries can be used with specified contact angles. For stability and to reduce the computational cost, the portions of the shape to be evolved that lie on the constraints are omitted and replaced by appropriate compensating integrals. The details of SE calculations used in this chapter are given in Appendix B.

While SE is versatile and can be used for all cases of this study, it is possible to develop an analytical solution in certain cases. Namely, when using SE for the nucleation at the meniscus, if the sum of the internal angles of the solid nucleus,  $\alpha + \beta + \varphi$ , is less than  $180^\circ$ , then the nuclei form axisymmetrically covering the entire meniscus–pore wall contact line. Because of this symmetry, it is possible to find an analytical solution for the nucleus shape by solving the variational problem (Euler–Lagrange equation)  $\delta(\Delta\tilde{B}_{\text{nuc}})/\delta f = 0$ , where  $f = y(x)$  is the function for the profile of the nucleus, schematically shown in Figure 4-2. The actual surface is obtained by the revolution of this solid–liquid profile around the  $y$ -axis. We scale the coordinate system by  $1/R_p$  in Figure 4-2 so that the cylinder has a base of a unit circle. Note that a version of this problem without the spherical boundary at the meniscus has been previously solved by Lefevre *et al.* [118] on which our solution here is based.

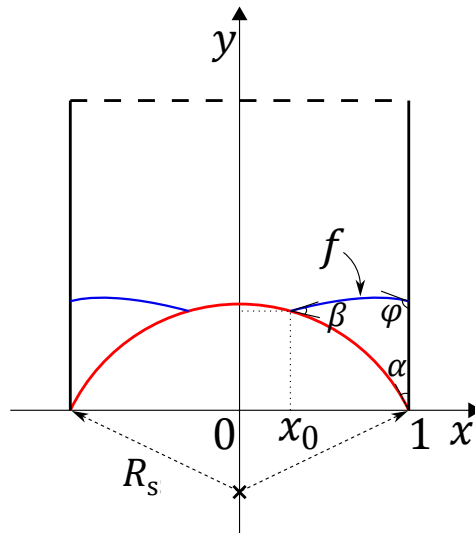


Figure 4-2. 2D schematic of the symmetric nucleus profile at the three-phase contact line in a cylinder of radius 1. The red line represents the meniscus sphere, and the blue line represents the profile of the solid–liquid interface.

Starting with Equation (4-2), we may express the volume and the areas as integrals and write the nondimensional energy as (normalized by  $2\pi$ ):

$$\begin{aligned} \frac{\Delta \tilde{B}_{\text{nuc}}}{2\pi} = & -\tilde{k}_{\text{nuc}}^* \int_{x_0}^1 x(f - y_s) dx + \int_{x_0}^1 x \sqrt{1 + \left(\frac{df}{dx}\right)^2} dx \\ & - \cos \beta \int_{x_0}^1 x \sqrt{1 + \left(\frac{dy_s}{dx}\right)^2} dx - \cos \varphi f(1) \end{aligned} \quad (4-6)$$

where  $y_s$  is the equation of the vapor meniscus circle, which has the following form:

$$y_s = \sqrt{R_s^2 - x^2} - \tan \alpha \quad (4-7)$$

with  $R_s = 1/\cos \alpha$  being the radius of the vapor-meniscus sphere.  $x_0$  is the radius of the intersection circle of the meniscus and the solid–liquid interface.

Taking the functional derivative of Equation (4-6) with respect to  $f$  and setting it equal to zero, we obtain the following:

$$\tilde{k}_{\text{nuc}}^* = -\frac{1}{x} \frac{d}{dx} \left[ \frac{x \frac{df}{dx}}{\sqrt{1 + \left(\frac{df}{dx}\right)^2}} \right] \quad (4-8)$$

Equation (4-8) can be integrated once using the following boundary condition at  $x = 1$ , which is simply the angle-of-intersection requirement at the wall (*i.e.*, contact angle):

$$\frac{\frac{df}{dx}}{\sqrt{1 + \left(\frac{df}{dx}\right)^2}} \Big|_{x=1} = \cos \varphi \quad (4-9)$$

which yields

$$\frac{df}{dx} = \frac{g}{\sqrt{1 - g^2}} \quad (4-10)$$

where

$$g(x) = -\frac{\tilde{k}_{\text{nuc}}^* x}{2} + \frac{2 \cos \varphi + \tilde{k}_{\text{nuc}}^*}{2x} \quad (4-11)$$

The second boundary condition states that the profiles of  $f$  and  $y_s$  should intersect at the point  $(x_0, y_s(x_0))$  and at the angle  $\beta$ . This can be mathematically expressed as

$$\frac{f' - y_s'}{1 + f' y_s'} \Big|_{x=x_0} = \tan \beta \quad (4-12)$$

where  $f' = df/dx$  and  $y'_s = dy_s/dx$ . Substituting Equation (4-10) directly into Equation (4-12) and taking the derivative of Equation (4-7) and then substituting into Equation (4-12), Equation (4-12) can be numerically solved for  $x_0$ . Once  $x_0$  is found,  $y_s(x_0)$  can be found from Equation (4-7), and since  $f(x_0) = y_s(x_0)$ , this leads to

$$f(x) = \int_{x_0}^x \frac{g}{\sqrt{1-g^2}} dx + y_s(x_0) \quad (4-13)$$

Substituting Equation (4-11) into Equation (4-13) and integrating it numerically, we obtain  $f$ . We use MATLAB's (v. 2023a, Natick, MA, USA) built-in symbolic solver `vpasolve()` and integrator `vpaintegral()` for this problem.

The geometries in all the remaining cases (*i.e.*, asymmetric nuclei and all cases of bridges) are calculated numerically with SE.

The rest of the chapter is organized as follows: In section 4.4, we summarize all the cases considered in this work, give examples of the nucleus and bridge shapes, and discuss their features. In section 4.5, using the results of the geometry calculations, we determine the minimum-energy nucleation and bridging paths and calculate the energy barriers for nucleation and bridging. In section 4.6, we summarize the main findings of this study.

## 4.4 Results: Geometry

In this section, we discuss different nucleus and bridge geometries, analyze their features, and give examples.

### 4.4.1 Geometry of nuclei at the meniscus

For the nucleation at the meniscus, we consider three meniscus angles:  $\alpha = 5, 30,$  and  $60^\circ$ , three solid–liquid–vapor contact angles:  $\beta = 45, 90,$  and  $135^\circ$ , and three solid–liquid–pore wall contact angles:  $\varphi = 45, 90,$  and  $135^\circ$ . All cases studied in this work for the nucleus angles are listed in Table 4-1. The remaining columns of Table 4-1 will be discussed later in the chapter.

Table 4-1. Summary of all cases considered for nucleation at the meniscus.

$\alpha$ (°)	$\beta$ (°)	$\varphi$ (°)	Nucleus type	$\tilde{k}_{\text{nuc,max}}^*$	$\tilde{V}_{\text{nuc,max}}^S$	$\tilde{V}_{\text{nuc,tran}}^S$	Notes
5	45	45	sym	−1.2371	1.9647	1.8896	



5	45	90	sym	0.3555	1.3639	1.2989	
5	45	135	asym-1	–	1.45	1.0928	
5	90	45	sym	–0.7045	2.4968	2.3067	
5	90	90	asym-1	–	2.5	1.8154	Figure B-1
5	90	135	asym-2	–	3.15	2.7874	
5	135	45	asym-1	–	4	2.7690	
5	135	90	asym-2	–	3.8	3.0953	
5	135	135	asym-2	–	3.7	3.3814	
30	45	45	sym	–1.2213	1.7451	1.6694	
30	45	90	sym	0.4494	1.1460	1.0804	
30	45	135	asym-1	–	1.55	1.0409	
30	90	45	sym	–0.5858	2.2939	2.0994	Figure 4-3 Figure 4-7
30	90	90	asym-1	–	2.45	1.7602	Figure 4-4 Figure 4-8
30	90	135	asym-2	–	3	2.6237	
30	135	45	asym-1	–	3.9	2.7193	
30	135	90	asym-2	–	3.75	3.0310	
30	135	135	asym-2	–	3.7	3.3685	Figure 4-5 Figure 4-8
60	45	45	sym	–1.1548	1.3858	1.3057	
60	45	90	asym-1	–	1.1	0.7537	
60	45	135	asym-1	–	1.05	0.8975	
60	90	45	asym-1	–	2.45	1.6502	
60	90	90	asym-1	–	2.15	1.6724	
60	90	135	asym-1	–	2.45	2.0708	
60	135	45	asym-1	–	4	2.7367	
60	135	90	asym-1	–	3.4	2.7191	
60	135	135	asym-2	–	3.65	3.3045	

Depending on the angles, three qualitatively different nucleus types were identified:

- (i) symmetric nucleus: if  $\alpha + \beta + \varphi < 180^\circ$

- (ii) asymmetric nucleus of type 1: if  $\alpha + \beta + \varphi > 180^\circ$  and  $\beta + \varphi - \alpha < 180^\circ$
- (iii) asymmetric nucleus of type 2: if  $\alpha + \beta + \varphi > 180^\circ$  and  $\beta + \varphi - \alpha > 180^\circ$

These nucleus types are separately discussed below.

#### 4.4.1.1 Symmetric nucleus

As mentioned, when  $\alpha + \beta + \varphi < 180^\circ$ , the nucleus forms as a symmetric shape around the pore axis at the three-phase contact line, and the nucleus shapes in this case are calculated analytically.

It was found that the analytical method yields one solution when  $-\infty < \tilde{k}_{\text{nuc}}^* < -2 \cos \varphi$  and two solutions when  $-2 \cos \varphi < \tilde{k}_{\text{nuc}}^* < \tilde{k}_{\text{nuc,max}}^*$ , where  $\tilde{k}_{\text{nuc,max}}^*$  is a numerically determined constant (for every given set of angles satisfying  $\alpha + \beta + \varphi < 180^\circ$ ) above which no solution exists. Furthermore, each combination of angles allows a maximum volume of the nucleus, which we denote by  $\tilde{V}_{\text{nuc,max}}^S$ . These constants for the symmetric case are given in Table 4-1. Note that the point of maximum curvature and the point of maximum volume do not coincide.

Example solutions of the symmetric nuclei for angles  $\alpha = 30^\circ$ ,  $\beta = 90^\circ$ , and  $\varphi = 45^\circ$  are given in Figure 4-3. Two-dimensional slices of the nuclei geometry are shown for four different  $\tilde{k}_{\text{nuc}}^*$ 's in Figure 4-3 (a). Here, the small, blue-shaded area in the left-most panel of Figure 4-3 (a) is a solution from the range where only one solution is possible with  $\tilde{k}_{\text{nuc}}^* = -2$ . The orange-shaded areas in the second panel are for  $\tilde{k}_{\text{nuc}}^* = -1.414$  (just above  $-2 \cos \varphi$ ) for which there are two solutions, shown in dark and light orange, respectively. Note that one of these solutions—the larger light orange area—almost represents a spherical cap (deviations are not noticeable in the figure). If  $\tilde{k}_{\text{nuc}}^*$  is exactly  $-2 \cos \varphi$ , one solution would be practically the same as the dark orange region together with infinitely many spherical cap solutions spanning the pore length and all having the same spherical solid–liquid interfacial area but different volumes and solid–pore wall interfacial areas. The areas and volumes of these shapes are easily calculated using the formulae for a spherical cap and will be important in section 4.5. Another set of solutions is given in the third panel in yellow for  $\tilde{k}_{\text{nuc}}^* = -1.0732$ , the larger of which corresponds to the maximum possible nucleus volume,  $\tilde{V}_{\text{nuc,max}}^S$ . Note that in the second and third panels of Figure 4-3 (a), the light-colored areas contain the smaller, dark-colored areas as

well. Finally, the purple-shaded area in the right-most panel represents the two overlapping solutions corresponding to  $\tilde{k}_{\text{nucl,max}}^*$ .

In Figure 4-3 (b) and (c), the energy of the equilibrium shape,  $\Delta\tilde{B}_{\text{nucl}}^*$ , is plotted vs. the curvature,  $\tilde{k}_{\text{nucl}}^*$ , and equilibrium volume,  $\tilde{V}_{\text{nucl}}^{S*}$ , respectively. In Figure 4-3 (d),  $\tilde{k}_{\text{nucl}}^*$  is plotted vs.  $\tilde{V}_{\text{nucl}}^{S*}$ . In panels (b), (c), and (d), the points corresponding to the solutions in Figure 4-3 (a) are shown with the same color. Note that, in these plots, each point corresponds to a different value of  $\tilde{k}_{\text{nucl}}^*$ , hence, different equilibrium. Therefore, the extrema on these plots do not have stability meaning. Other combinations of angles with  $\alpha + \beta + \varphi < 180^\circ$  yield qualitatively similar results to what is illustrated in Figure 4-3.

We note that the analytical method used for calculating the symmetric nucleus geometry takes  $\tilde{k}_{\text{nucl}}^*$  as an input and finds the stationary points of the energy. Surface Evolver, on the other hand, is a numerical tool that uses gradient descent to find the minimum of the energy, and it was run with  $\tilde{V}_{\text{nucl}}^{S*}$  as the input for stability. Hence, the high-energy branch between the yellow and orange dots in Figure 4-3 (c) [and the corresponding portions of the plots in panels (b) and (d)] would not be accessible with SE. However, we will see in section 4.5.1.1 that this branch cannot be a part of the nucleation path anyway.

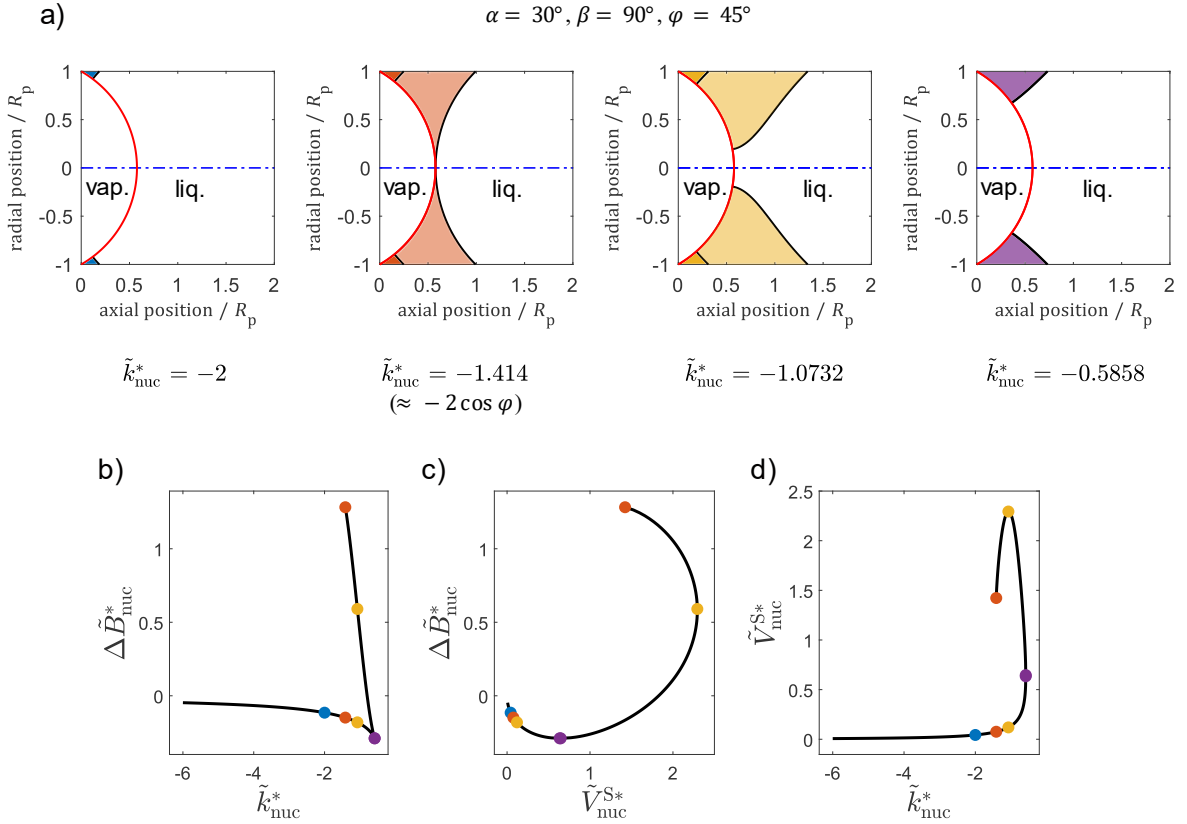


Figure 4-3. Examples of the symmetric nuclei at the meniscus. (a) 2D views of some symmetric nuclei solutions. (b) Energy vs. curvature plot. (c) Energy vs. volume plot. (d) Volume vs. curvature plot. All calculations are for  $\alpha = 30^\circ, \beta = 90^\circ$ , and  $\varphi = 45^\circ$ . In panel (a), the vapor meniscus is shown in red, and the solid nuclei are shown with the colored areas. The colored points on the plots in the bottom panels correspond to the nuclei shapes shown in panel (a).

#### 4.4.1.2 Type-1 asymmetric nucleus

When  $\alpha + \beta + \varphi > 180^\circ$  and  $\beta + \varphi - \alpha < 180^\circ$ , the nucleus forms on one side of the pore, and it contains a portion of the meniscus–pore wall intersection circle (*i.e.*, there is no gap between the solid nucleus and the meniscus–pore wall intersection line). The nucleus shapes in this case are calculated numerically using SE. Example 3D nuclei profiles for this case, calculated with SE for  $\alpha = 30^\circ, \beta = 90^\circ$ , and  $\varphi = 90^\circ$ , are given in Figure 4-4 (a). Furthermore, in panels (b), (c), and (d) of Figure 4-4, like in Figure 4-3, we plot the energy vs. curvature, energy vs. volume, and volume vs. curvature, respectively. It is seen that, unlike in the symmetric case, these plots are simpler in the sense that they are single-valued functions. For all combinations of angles satisfying the criterion  $\alpha + \beta + \varphi > 180^\circ$  and  $\beta + \varphi - \alpha < 180^\circ$ , qualitatively similar results were obtained. Note that in Figure 4-4 (b), (c), and (d), each

point corresponds to a different value of  $\tilde{k}_{\text{nuc}}^*$ , and therefore, corresponds to finding an equilibrium state for a different system, so relative free-energy values do not have a stability meaning.

$\tilde{k}_{\text{nuc,max}}^*$  is not defined for the present case because the nucleus can be made arbitrarily small increasing  $\tilde{k}_{\text{nuc}}^*$  indefinitely. However, there exists  $\tilde{V}_{\text{nuc,max}}^S$ , which is defined as the maximum volume of the nucleus calculated with SE. These values are listed in Table 4-1. If the set volume of the nucleus is larger than  $\tilde{V}_{\text{nuc,max}}^S$ , then the solid–liquid interface of the solid nucleus forms a spherical cap (concave, convex, or flat disk, depending on  $\varphi$ ), with the solid covering the entire meniscus on the other end [see Figure 4-4 (a), last illustration]. Note that we use a volume increment of  $\Delta\tilde{V}_{\text{nuc}}^{S*} = 0.05$  when computing asymmetric geometries. Therefore, the maximum volumes listed in Table 4-1 for the present case are only accurate to 0.05.

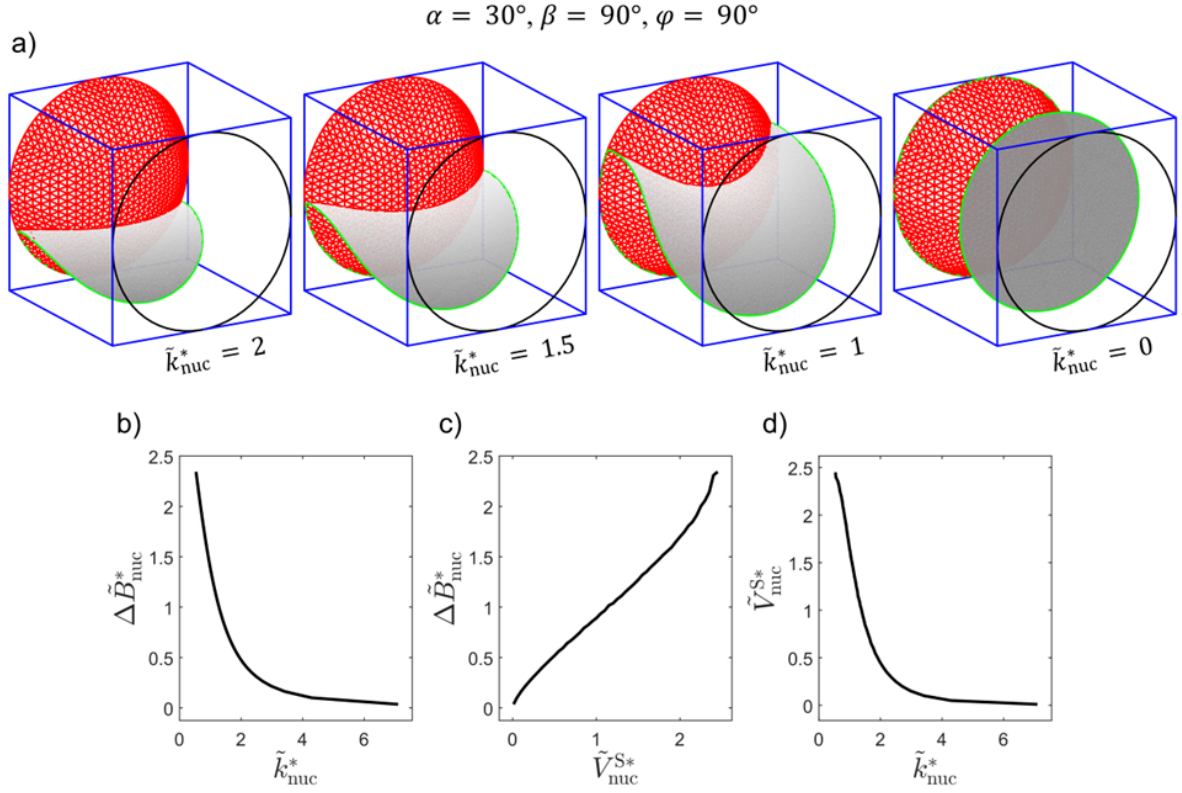


Figure 4-4. Example of type-1 asymmetric solid nuclei at the vapor meniscus. (a) The first three panels: 3D views of the type-1 asymmetric nuclei; the last panel: an example where  $\tilde{V}_{\text{nuc}}^{S*} = 3 > \tilde{V}_{\text{nuc,max}}^S$ . The meniscus is shown by the red mesh, and the solid–liquid interface of the nucleus is shown in transparent grey. The contact line of the shape with the pore wall is shown in green. (b) Energy vs. curvature plot. (c) Energy vs. volume plot. (d) Volume vs. curvature plot. All calculations are for  $\alpha = 30^\circ$ ,  $\beta = 90^\circ$ , and  $\varphi = 90^\circ$ . The plots in panels (b), (c), and (d) are up to  $\tilde{V}_{\text{nuc,max}}^S$ .

#### 4.4.1.3 Type-2 asymmetric nucleus

Finally, when  $\alpha + \beta + \varphi > 180^\circ$  and  $\beta + \varphi - \alpha > 180^\circ$ , the nucleus forms on one side of the pore, but it does not contain any portion of the meniscus–pore wall three-phase contact line (*i.e.*, there is a gap between the solid nucleus and the meniscus–pore wall intersection circle). The nucleus shapes in this case are calculated numerically using SE. Example 3D nuclei profiles for this case calculated with SE for  $\alpha = 30^\circ$ ,  $\beta = 135^\circ$ , and  $\varphi = 135^\circ$  are given in Figure 4-5 (a). Again, in panels (b), (c), and (d), we plot the energy vs. curvature, energy vs. volume, and volume vs. curvature, respectively. It is seen that these plots are similar to the plots for the type-1 asymmetric nuclei. For all combinations of angles satisfying the criterion  $\alpha + \beta + \varphi > 180^\circ$  and  $\beta + \varphi - \alpha > 180^\circ$ , qualitatively similar results were obtained. Note that, in panels (b), (c), and (d), each point corresponds to a different value

of  $\tilde{k}_{\text{nuc}}^*$ , and therefore, corresponds to finding an equilibrium state for a different system, so relative free-energy values do not have a stability meaning.

Similar to the type-1 asymmetric nucleus case,  $\tilde{k}_{\text{nuc,max}}^*$  is not defined for the present case because the nucleus can be made arbitrarily small increasing  $\tilde{k}_{\text{nuc}}^*$  indefinitely. However, again, there exists  $\tilde{V}_{\text{nuc,max}}^S$ , which is defined as the maximum volume of the nucleus calculated with SE. If the set volume of the nucleus is larger than this value, then the shape forms as a spherical cap on one end (convex or flat disk, depending on  $\varphi$ ) covering a circular middle portion of the meniscus on the other end with a gap between the nucleus and the meniscus–pore wall intersection line [see Figure 4-5 (a), last illustration]. The values of  $\tilde{V}_{\text{nuc,max}}^S$  for the type-2 asymmetric nuclei are also listed in Table 4-1. Like the type-1 asymmetric case, we use a nondimensional volume increment of  $\Delta\tilde{V}_{\text{nuc}}^S = 0.05$  when computing type-2 asymmetric nucleus geometries. Hence, the maximum nondimensional volumes listed in Table 4-1 for the present case are only accurate to 0.05.

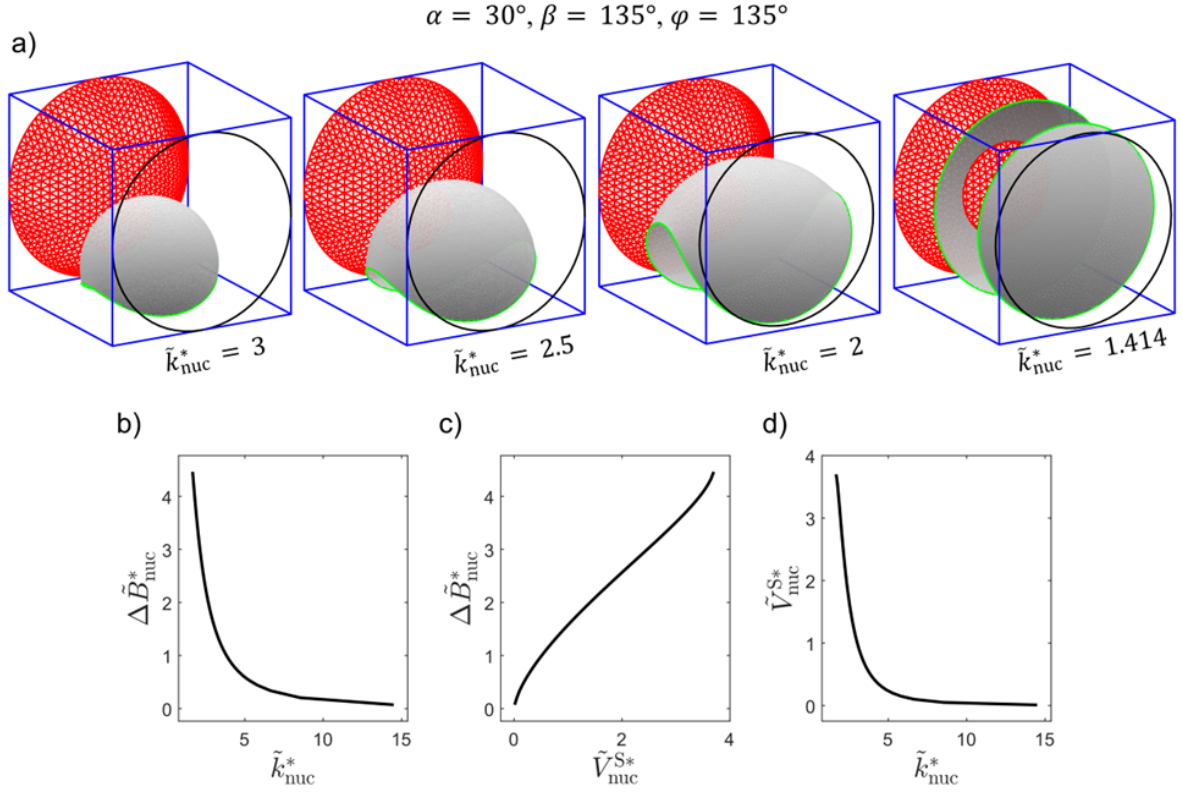


Figure 4-5. Example of type-2 asymmetric nuclei at the meniscus. (a) the first three panels: 3D views of the type-2 asymmetric nuclei; the last panel: an example where  $\tilde{V}_{\text{nuc}}^{S*} = 4 > \tilde{V}_{\text{nuc,max}}^S$ . The meniscus is shown by the red mesh, and the solid–liquid interface of the nucleus is shown in transparent grey. The contact line of the shape with the pore wall is shown in green. (b) Energy vs. curvature plot. (c) Energy vs. volume plot. (d) Volume vs. curvature plot. All calculations are for  $\alpha = 30^\circ, \beta = 135^\circ$ , and  $\varphi = 135^\circ$ . The plots in panels (b), (c), and (d) are up to  $\tilde{V}_{\text{nuc,max}}^S$ .

#### 4.4.2 Geometry of bridges

To calculate the bridge geometries, we use SE, the details of which are given in Appendix B. For bridging of the pores, we consider two or three pores:  $n = 2$  or  $3$ , three contact angles:  $\theta = 45, 90$ , or  $135^\circ$ , and two different nondimensional distances between the two adjacent pores:  $\tilde{l} = 8/3$  or  $10/3$ . The summary of all cases considered in this work is given in Table 4-2. The remaining columns of Table 4-2 will be discussed later in the chapter.

Table 4-2. Summary of all cases studied for bridging of pores.

$n$	$\tilde{l}$	$\theta$ ( $^\circ$ )	Transition type	$\tilde{V}_{\text{bri,min}}^S$	$\tilde{V}_{\text{bri,tran}}^S$	Notes
2	8/3	45	pinned	1.2	1.2850	



2	8/3	90	pinned	2.3	2.8255	Figure 4-6 Figure 4-10
2	8/3	135	pinned	3.3	4.1649	Figure B-2
2	10/3	45	unpinned	1.5	1.7130	
2	10/3	90	pinned	3.2	4.0375	
2	10/3	135	pinned	4.7	6.6995	
3	8/3	45	pinned	1.3	1.7055	
3	8/3	90	pinned	2.6	3.5516	Figure 4-6
3	8/3	135	pinned	3.6	5.1216	
3	10/3	45	unpinned	1.8	2.3346	
3	10/3	90	pinned	3.8	5.2818	Figure B-3
3	10/3	135	pinned	5.5	8.2798	

Three-dimensional examples of geometries for the bridging of two pores are shown in Figure 4-6 (a), and examples of geometries for the bridging of three pores are shown in Figure 4-6 (b), all for  $\theta = 90^\circ$  and  $\tilde{l} = 8/3$ . The shapes are pinned at the pore mouths (red, blue, and green circular curves) but are required to meet the flat portion of the surface at the angle  $\theta$  (yellow curves). We found that, in all bridging scenarios, there exists a minimum bridge volume,  $\tilde{V}_{\text{bri,min}}^S$ , below which the shape is not stable with SE, and the solid–vapor interface becomes disconnected pinned caps at the pore mouths. The  $\Delta\tilde{V}_{\text{bri}}^{S*}$  values are listed in Table 4-2, and they are accurate to 0.1 because we use a nondimensional volume increment of  $\Delta\tilde{V}_{\text{bri}}^{S*} = 0.1$  for SE calculations of bridges.

In Figure 4-6 (a) and (b), the top shapes roughly correspond to the minimum-volume bridges for two pores and three pores, respectively. The bottom shapes have equal volumes of  $\tilde{V}_{\text{bri}}^{S*} = 4$ , and they are given for illustration purposes. In Figure 4-6 (c), (d), and (e), we plot the energy *vs.* curvature, energy *vs.* volume, and volume *vs.* curvature of equilibrium bridges, respectively. From Figure 4-6 (e), it is seen that the curvature of the shape varies nonlinearly with the volume, and it is not single-valued for  $n = 3$ , resulting in sharp change in the energy plot in panel (c). Note that in these plots each point corresponds to a different value of  $\tilde{k}_{\text{bri}}^*$ , and therefore, corresponds to finding an equilibrium state for a different system, so relative free-energy values do not have a stability meaning. We also note that, as the bridge grows, it

becomes more spherical, eventually becoming a large spherical cap encapsulating all pore mouths. We define the bridge in each case only up to this volume.

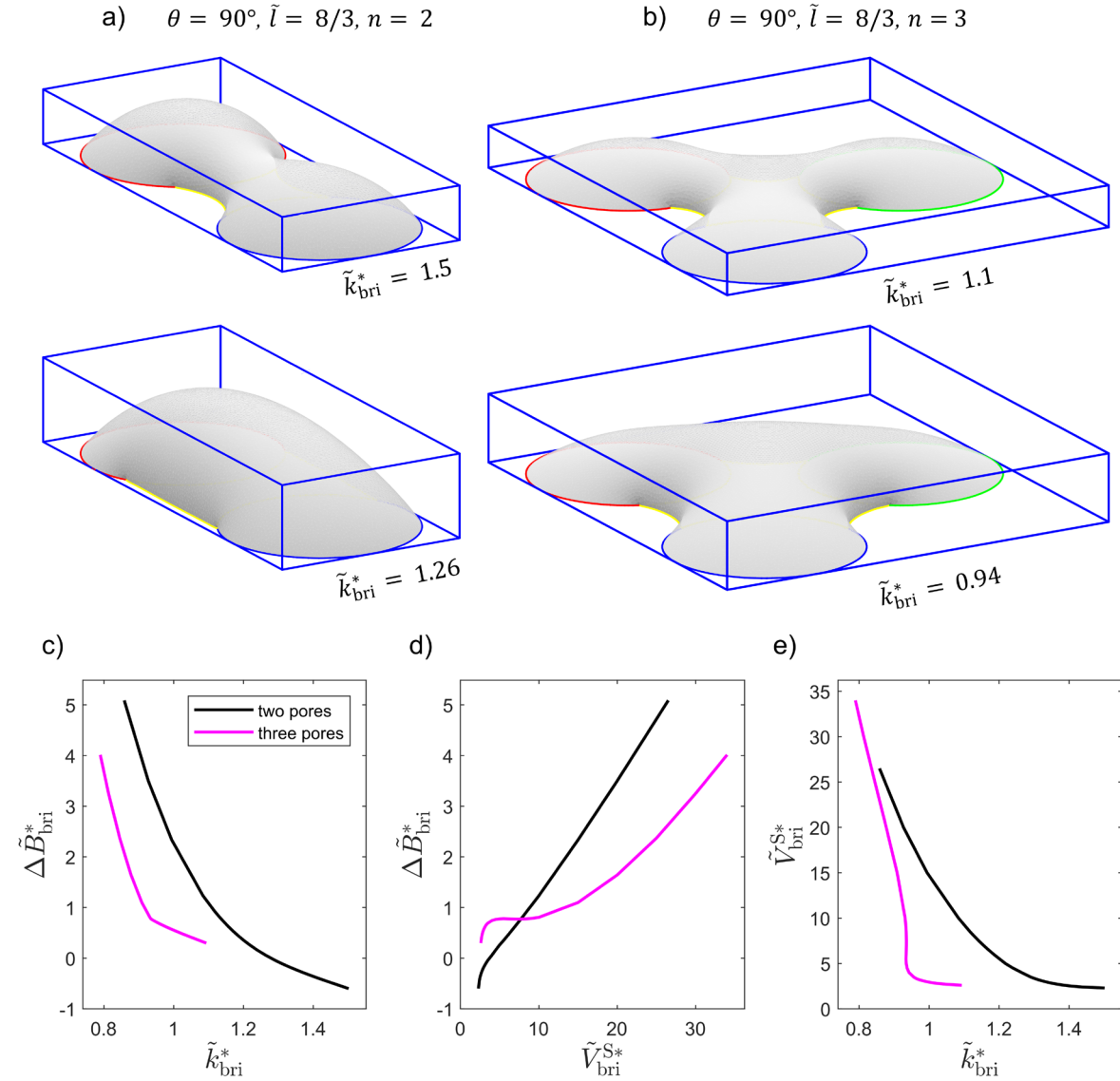


Figure 4-6. Examples of bridging of pores. (a) 3D geometries for the bridging of two pores. (b) 3D geometries for the bridging of three pores. (c) Energy vs. curvature plots. (d) Energy vs. volume plots. (e) Volume vs. curvature plots. In panels (a) and (b), the shapes are highlighted in red, blue, and green where they are pinned at the pore mouths and highlighted in yellow where they meet the flat surface at the angle  $\theta$ . All calculations are for  $\theta = 90^\circ$  and  $\tilde{l} = 8/3$ .

## 4.5 Results: Free-energy analysis and energy barriers

In this section, we perform free-energy analysis and calculate the energy barriers for the solid nucleation inside a single pore based on Equation (4-2) using the calculated nucleus

geometries. We then perform free-energy analysis and calculate the energy barriers for the bridging of neighboring pores based on Equation (4-5) using the calculated bridge geometries.

#### ***4.5.1 Free-energy analysis for nucleation at the meniscus***

##### ***4.5.1.1 Free energy of symmetric nucleation***

Upon investigating the calculated solutions of the symmetric nuclei, we found that not all solutions correspond to a nucleation path. This is because, after the symmetric nucleus reaches a certain size, a nucleus of the same volume encapsulating the entire meniscus and having a spherical solid–liquid interface becomes energetically more favorable. In all cases studied in this work, this volume was slightly lower than  $\tilde{V}_{\text{nuc,max}}^S$ , and we denote this transition volume by  $\tilde{V}_{\text{nuc,tran}}^S$ . The numerically determined values are listed in Table 4-1 for all cases studied.

In Figure 4-7, we show examples of free-energy profiles plotted at fixed values of  $\tilde{k}_{\text{nuc}}^*$  vs.  $\tilde{V}_{\text{nuc}}^S$  corresponding to the case discussed in section 4.4.1.1 (*i.e.*, for angles  $\alpha = 30^\circ$ ,  $\beta = 90^\circ$ , and  $\varphi = 45$ ). In panel (a), the solid lines are the free-energy profiles of the symmetric nuclei, and the dashed lines of the same color are the free-energy profiles for the nuclei with a spherical solid–liquid interface, both plotted vs. the nucleus volume,  $\tilde{V}_{\text{nuc}}^S$ . Following the principle of minimum-free-energy-path, the transition volume from the symmetric nucleus to the spherical-cap geometry,  $\tilde{V}_{\text{nuc,tran}}^S$ , is determined by the intersection of the paths where the lower free energy switches from one geometry to the other (shown by the vertical dashed line). The portions of the free-energy plots that lie above the minimum-free-energy path are deemed not physical and excluded. In Figure 4-7 (b), we plot the free energy vs. the distance of the solid–liquid–vapor contact line of the symmetric nucleus from the pore wall (*i.e.*,  $1 - x_0$  in Figure 4-2) to better visualize the free-energy landscape. Note that, however, unlike the nucleus volume, this distance does not have the meaning of “reaction coordinate”, so not all minima and maxima on this panel represent equilibrium. Specifically, the kinks in the free-energy plots in Figure 4-7 (a) where their derivatives with respect to the nucleus volume are not defined, also appear as extremum points in the excluded region in Figure 4-7 (b). In Figure 4-7 (c), we show a schematic sequence for the expected path of nucleation. Note that illustrations in the schematic are not to scale and they do not necessarily represent equilibrium states.

Considering the piecewise free-energy path described above, when  $\tilde{k}_{\text{nuc}}^* < -2 \cos \varphi$  [dark red lines in Figure 4-7 (a) and (b)], there is only one stable equilibrium state at the small volume of the nucleus.  $\tilde{k}_{\text{nuc}}^* = -2 \cos \varphi$  [light blue lines in Figure 4-7 (a) and (b)] represents the case where the transition to the spherical-cap geometry has the same energy as the spherical cap itself, irrespective of the volume of the cap [note the horizontal dashed line in Figure 4-7 (a)]. When  $-2 \cos \varphi < \tilde{k}_{\text{nuc}}^* < \tilde{k}_{\text{nuc,max}}^*$  [green, purple, and yellow lines in Figure 4-7 (a) and (b)] the plots have energy barriers besides the local minima at the small volume, meaning that the pore can solidify if these barriers can be crossed. For the present example, when  $\tilde{k}_{\text{nuc}}^* = -1.2$  [green lines in Figure 4-7 (a) and (b)], the energy barrier corresponds to  $\tilde{V}_{\text{nuc,tran}}^S$ , and when  $\tilde{k}_{\text{nuc}}^* = -0.75$  (yellow lines), the energy barrier corresponds to a volume smaller than  $\tilde{V}_{\text{nuc,tran}}^S$ .  $\tilde{k}_{\text{nuc}}^* = -0.9$  [purple lines in Figure 4-7 (a) and (b)] marks the point where the free-energy plot of the symmetric nucleus becomes flat at the transition volume  $\tilde{V}_{\text{nuc,tran}}^S$ . Finally, when  $\tilde{k}_{\text{nuc}}^* \geq \tilde{k}_{\text{nuc,max}}^*$  [orange and blue lines in Figure 4-7 (a) and (b)] the energy barrier and the local minimum disappear, meaning that the pore is expected to solidify spontaneously at these conditions.

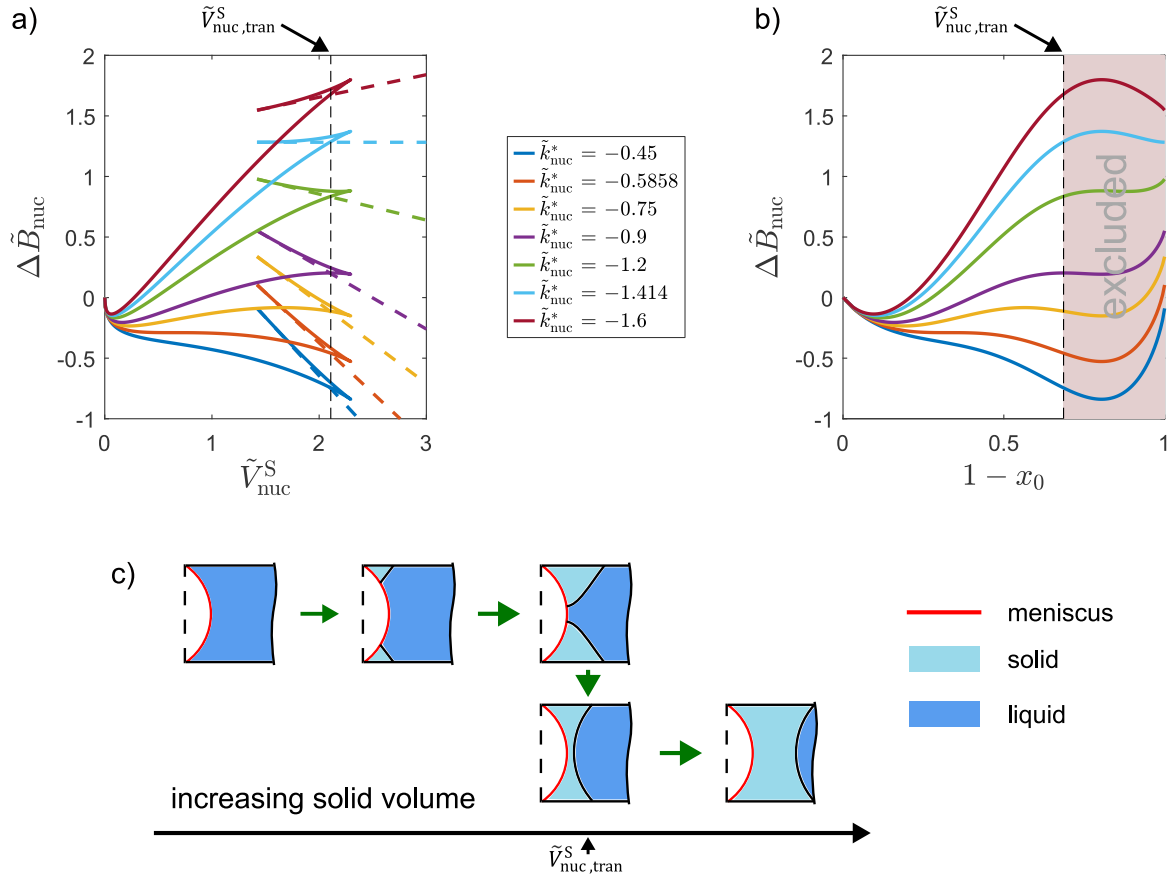


Figure 4-7. Symmetric nucleation at the meniscus. (a) Example free-energy plots for symmetric nuclei for  $\alpha = 30^\circ$ ,  $\beta = 90^\circ$ , and  $\varphi = 45^\circ$  (solid lines), and the corresponding spherical-cap geometries (dashed lines of the same color). (b) The free energy vs. the distance of the solid–liquid–vapor contact line of the symmetric nucleus from the pore wall. In panels (a) and (b), the vertical dashed lines represent the transition volume. (c) Schematic of the expected nucleation path for symmetric nucleation.

#### 4.5.1.2 Free energy of asymmetric nucleation

We found similar transitions for both types of the asymmetric nucleus as well. In Figure 4-8 (a), we show the free-energy profiles plotted at fixed values of  $\tilde{k}_{\text{nuc}}^*$  vs.  $\tilde{V}_{\text{nuc}}^S$  for the type-1 asymmetric nuclei corresponding to the case discussed in section 4.4.1.2 (*i.e.*, for angles  $\alpha = 30^\circ$ ,  $\beta = 90^\circ$ , and  $\varphi = 90^\circ$ ). Furthermore, in Figure 4-8 (b), we show the free-energy profiles for the type-2 asymmetric nuclei with angles  $\alpha = 30^\circ$ ,  $\beta = 135^\circ$ , and  $\varphi = 135^\circ$ . In both panels, the solid lines are for the asymmetric nuclei calculated with SE and the dashed lines are for the corresponding spherical-cap geometries (note that for  $\varphi = 90^\circ$  the cap is a flat disk).

Similar to the symmetric case, we see that there exists a transition volume,  $\tilde{V}_{\text{nuc,tran}}^S$ , above which the nucleus with a spherical cap has smaller free energy. In all cases studied, this

volume was always smaller than the maximum volume calculated with SE. This was the case for all the different combinations of angles studied in this work if  $\alpha + \beta + \varphi > 180^\circ$ . That is, both type-1 and type-2 asymmetric cases had qualitatively similar free-energy profiles, the only difference being their geometry as discussed in section 4.4.1. Therefore, based on the principle of minimum-free-energy path, as the nucleus grows past this point, it is expected to transform into a shape with a spherical cap on one end and the entire meniscus on the other end. The numerically determined transition volumes are given in Table 4-1. We show schematics of the expected nucleation paths for type-1 and type-2 asymmetric nuclei in Figure 4-8, in panels (c) and (d), respectively. Note that these schematics are not to-scale and they do not necessarily represent equilibrium states.

The general feature of the free-energy plots for the asymmetric nuclei is that there are no metastable states unlike for the symmetric case. Considering the type-1 asymmetric nuclei example, when  $\tilde{k}_{\text{nuc}}^* < -2 \cos \varphi$  [blue lines in Figure 4-8 (a)], the liquid is stable in the pore as there is no finite energy barrier. At  $\tilde{k}_{\text{nuc}}^* = -2 \cos \varphi$  [orange lines in Figure 4-8 (a)], the transition to the spherical-cap geometry has the same energy as the spherical cap itself, irrespective of the volume of the cap (note the horizontal dashed line). When  $\tilde{k}_{\text{nuc}}^* > -2 \cos \varphi$ , there always exists a free-energy barrier for the nucleation of the solid. Note that this contrasts with the symmetric case where the barrier ceases to exist for  $\tilde{k}_{\text{nuc}}^* \geq \tilde{k}_{\text{nuc,max}}^*$ . In this example, the barrier corresponds to the transition volume when  $-2 \cos \varphi < \tilde{k}_{\text{nuc}}^* < 0.95$  [yellow lines in Figure 4-8 (a)], and a smaller volume of the asymmetric nucleus when  $\tilde{k}_{\text{nuc}}^* > 0.95$  [green and light blue lines in Figure 4-8 (a)]. If  $\tilde{k}_{\text{nuc}}^* = 0.95$  [purple lines in Figure 4-8 (a)], the free energy of the asymmetric nucleus becomes flat at the transition volume.

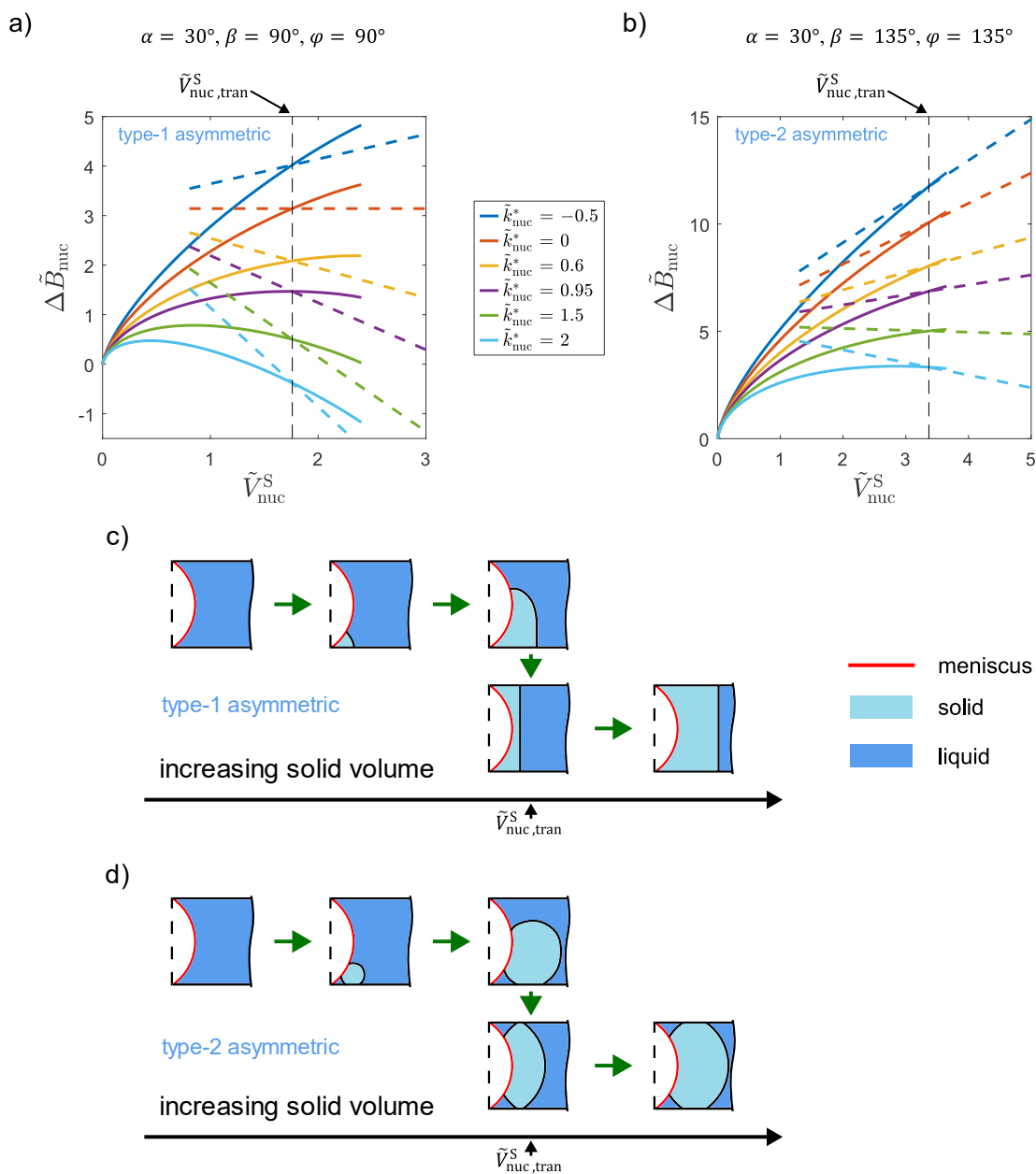


Figure 4-8. Asymmetric nucleation at the meniscus. (a) Example free-energy plots for the type-1 asymmetric nuclei for  $\alpha = 30^\circ$ ,  $\beta = 90^\circ$ , and  $\varphi = 90^\circ$  (solid lines), and the corresponding spherical-cap geometries (dashed lines of the same color). (b) Example free-energy plots for type-2 asymmetric nuclei for  $\alpha = 30^\circ$ ,  $\beta = 135^\circ$ , and  $\varphi = 135^\circ$  (solid lines), and the corresponding spherical-cap geometries (dashed lines of the same color). The vertical dashed lines represents the transition volume. (c) Schematic of the expected nucleation path for the type-1 asymmetric case. (d) Schematic of the expected nucleation path for the type-2 asymmetric case.

### 4.5.1.3 Comparison of the energy barriers for nucleation

In Figure 4-9, we plot the energy barriers,  $\Delta\tilde{B}_{\text{nuc}}^\dagger$ , for nucleation at the meniscus for all angle combinations considered in this work. For the symmetric cases,  $\Delta\tilde{B}_{\text{nuc}}^\dagger$  is calculated as the difference between the local maximum and the local minimum at the small volume considering the path illustrated in Figure 4-7. For the asymmetric cases, it is simply the height of the local maximum following the path described in Figure 4-8. It is seen that all curves start at a minimum curvature ( $-2\cos\varphi$ ) below which the liquid is stable in the pore. In all cases, as the curvature increases, the energy barrier decreases as expected. However, as mentioned, the barrier for the symmetric cases ceases to exist if  $\tilde{k}_{\text{nuc}}^* \geq \tilde{k}_{\text{nuc,max}}^*$ .

Based on Figure 4-9, the effects of  $\alpha$  on the nucleation barriers can be summarized as follows: If by decreasing  $\alpha$  the value of  $\alpha + \beta + \varphi$  can be made less than  $180^\circ$  resulting in symmetric nuclei instead of asymmetric, then the energy barrier can be significantly reduced or completely eliminated. Clearly, both  $\beta$  and  $\varphi$  need to be less than  $90^\circ$  for this to be possible. Otherwise,  $\alpha$  can slightly reduce (see the middle panel of Figure 4-9), slightly increase (see the top two panels on the right of Figure 4-9), or can have no practical effect on the barrier (see the bottom panel on the right of Figure 4-9), depending on  $\beta$  and  $\varphi$ . Note that, in most cases, the amount by which  $\alpha$  reduces the barrier for nucleation also depends on  $\tilde{k}_{\text{nuc}}^*$ .

Comparing the plots in Figure 4-9 across the rows and columns and noting the different y-axis scales, we see that the energy barriers have much stronger dependence on both  $\beta$  and  $\varphi$ . The barriers significantly increase with increasing  $\beta$  and  $\varphi$ .



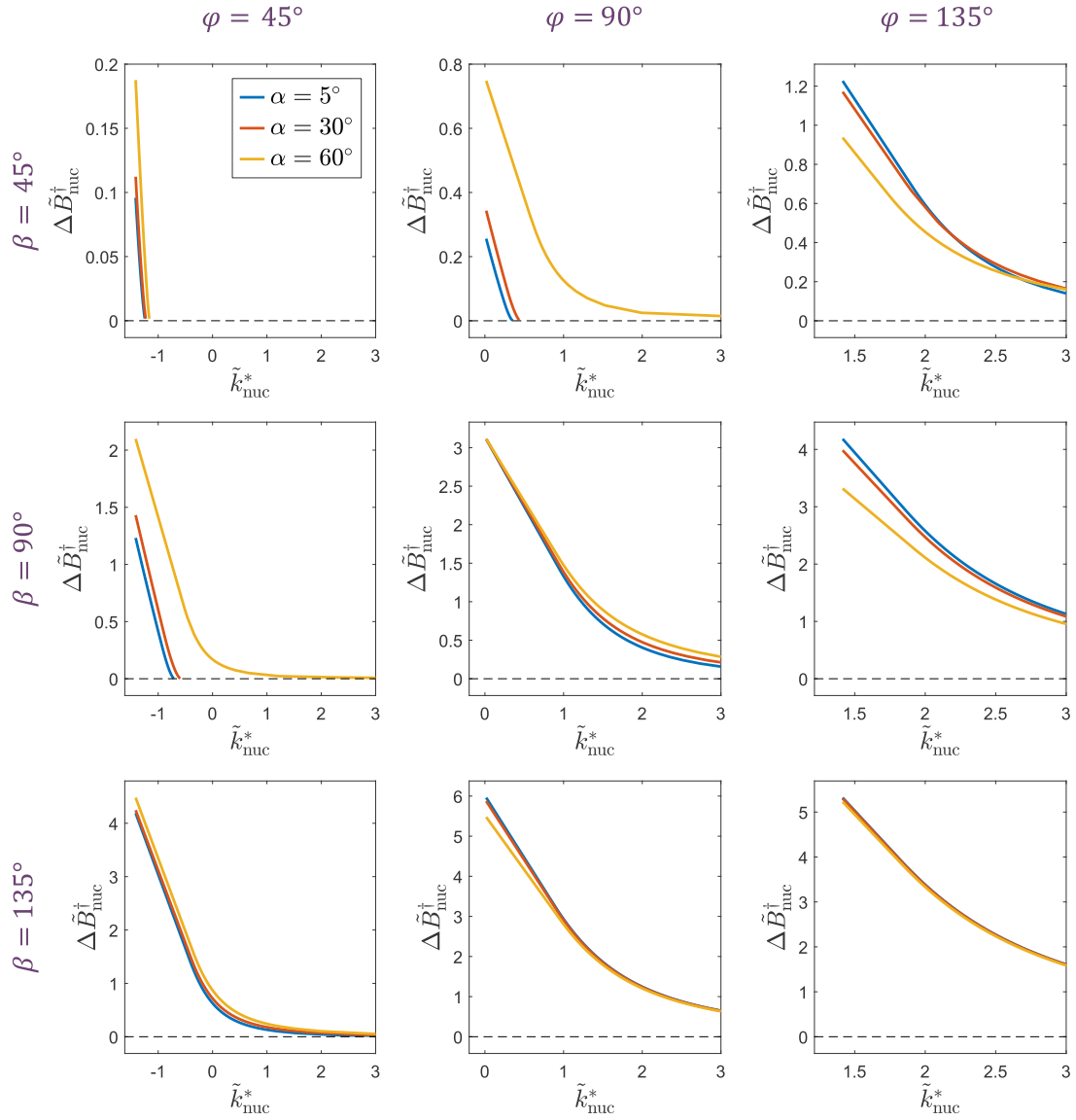


Figure 4-9. Comparison of energy barriers for nucleation at the vapor meniscus as a function of solid nucleus curvature. Each row corresponds to a different  $\beta$ , and each column corresponds to a different  $\varphi$ . Colors in each panel correspond to a different  $\alpha$ , as indicated in the first panel.

#### 4.5.2 Free energy of bridging

In Figure 4-10, we show example free-energy profiles plotted at fixed values of  $\tilde{k}_{\text{bri}}^*$  vs.  $\tilde{V}_{\text{bri}}^S$  for bridging of two pores ( $n = 2$ ) with  $\theta = 90^\circ$  and  $\tilde{l} = 8/3$ . The solid lines correspond to the bridge shapes calculated with SE, the dotted lines correspond to the growth of two pinned spherical caps simultaneously (*i.e.*, the volume, areas, and energy are twice those for a single cap), and the dashed lines correspond to the growth after the caps unpin. The caps

unpin when the pore mouth can no longer accommodate the cap because it would require contact angle larger than  $\theta$ . We see that there exists a transition volume,  $\tilde{V}_{\text{bri,tran}}^S$ , larger than the minimum stable volume calculated with SE, and the bridging of the pores past the transition volume is energetically more favorable. Therefore, following the principle of minimum-free-energy path, the shapes are expected to start as separate spherical caps and eventually form a bridge and grow. In this example, the transition volume is smaller than what is required for the caps to unpin. In two of the cases studied in this work, when  $n = 2$  or  $n = 3$  for  $\tilde{l} = 10/3$ , and  $\theta = 45^\circ$ , this transition to the bridge happens after the caps unpin and grow a small amount in the unpinned state. The transition volumes for bridges are listed in Table 4-2.

In Figure 4-10, the local minima of the free-energy paths correspond to metastable pinned caps at the pore mouths. There exists a  $\tilde{k}_{\text{bri}}^*$  where the minimum in the free energy corresponds to the transition volume ( $\tilde{k}_{\text{bri}}^* = 1.92$  in this example; purple lines in Figure 4-10). If the curvature is higher than this value, the solid is expected to grow spontaneously without a barrier. For all the other positive curvature values, there always exists a free-energy barrier (not all visible in Figure 4-10). If the required size of the nucleus is large, the barrier corresponds to a single large spherical cap encapsulating all the pore mouths instead of the bridge [see the last illustration in Figure 4-10 (b)]. At negative curvature values ( $-2 < \tilde{k}_{\text{bri}}^* < 0$ ), pinned concave caps at the pore mouths would be stable.

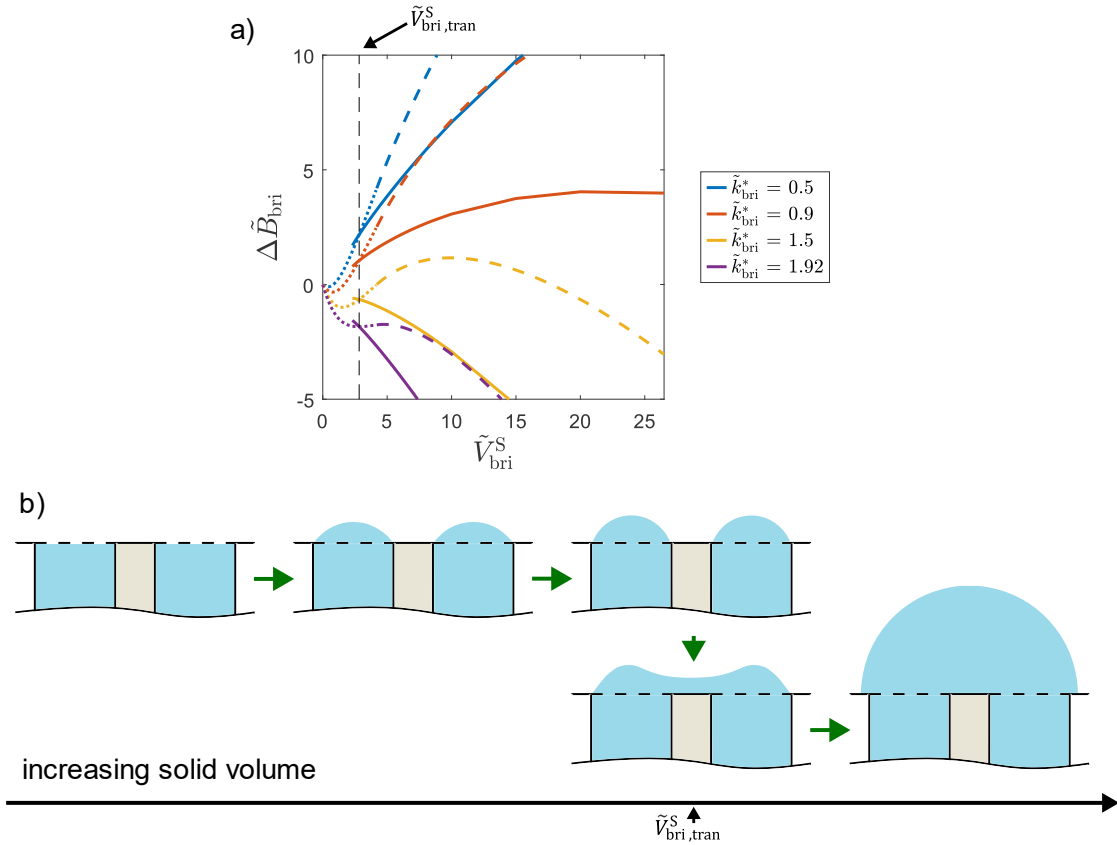


Figure 4-10. Bridging of pores. (a) Example free-energy plots for the bridging of the pores for  $n = 2$ ,  $\theta = 90^\circ$ , and  $\tilde{l} = 8/3$  (solid lines), and the corresponding profiles calculated for the growth of  $n$  number of spherical caps (dotted lines pinned; dashed lines not pinned). The vertical dashed line represents the transition volume. (b) Schematic of the expected bridging path.

#### 4.5.2.1 Comparison of the energy barriers for bridging

Assuming the growth path described above, we plot the energy barriers for bridging,  $\Delta \tilde{B}_{\text{bri}}^\dagger$ , in Figure 4-11. The barriers are calculated as the difference between the local maximum and the local minimum of free-energy profiles. The solid lines represent the cases where the maximum of the free energy is at some volume of the bridge. The dashed lines are where the required volume is large, so the maximum of the free energy is instead at some volume of a large spherical cap encapsulating the pore mouths [see the last illustration in Figure 4-10 (b)]. For comparison, we also show, by dotted lines of the same color, the barriers calculated for the growth of a cap from a single isolated pore.

From Figure 4-11, we see that the bridging of pores often provides a significantly lower free-energy barrier compared to growth from a single pore at the same conditions. In general,

the difference in the barriers increases with more pores and closer pore proximity. If the pores are far apart and/or there are not many pores in the close vicinity of each other, at large  $\tilde{k}_{\text{bri}}^*$ , single-pore growth might be more favorable (*e.g.*, see the yellow lines in the right panels of Figure 4-11). Comparing the plots in the same panel by color, smaller contact angle also reduces the barriers significantly. If  $\tilde{k}_{\text{bri}}^*$  is larger than the intersection points of the plots with the  $\Delta\tilde{B}_{\text{bri}}^\dagger = 0$  line, then the solid is expected to grow spontaneously without a barrier.

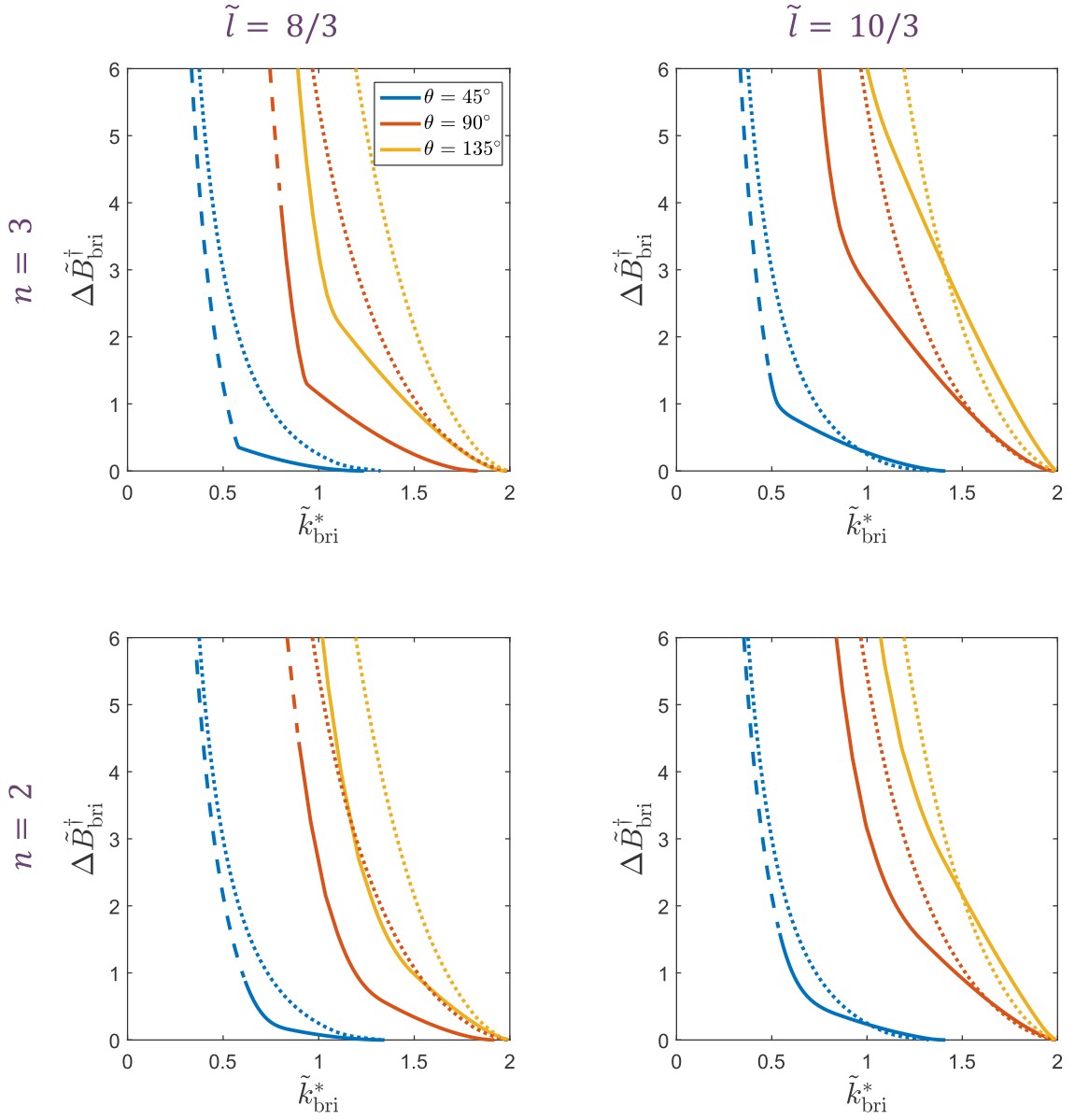


Figure 4-11. Comparison of free-energy barriers for bridging of pores (solid and dashed lines) as well as growth of a cap from a single isolated pore as a function of curvature (dotted lines). Each row corresponds to a different number of pores  $n$ , and each column corresponds to a different pore spacing  $\tilde{l}$ . Colors in each panel corresponds to different contact angle  $\theta$  as indicated in the first panel. Note that the dotted lines are the same in all panels since the growth from a single pore does not depend on  $n$  or  $\tilde{l}$ .

## 4.6 Conclusion

In this chapter, we investigated two of the limiting steps in pore condensation and solidification in a model porous particle with cylindrical pores: (i) solid nucleation inside a single pore at the liquid–vapor meniscus, and (ii) solid bridging of multiple pores above the

particle surface. We approached these problems from the thermodynamic-free-energy perspective with the main goal of computing the free-energy barriers for nucleation and then for bridging. By considering many cases of geometrical parameters—the internal angles of the solid ( $\alpha$ ,  $\beta$ , and  $\varphi$ ) for nucleation and the distance, number of pores, and contact angle ( $\tilde{l}$ ,  $n$ ,  $\theta$ ) for bridging—we compared the energy barriers. One of the challenges was the calculation of nontrivial equilibrium geometries of the nuclei and bridges that arise in these systems. We employed the Surface Evolver code in all cases, except for the symmetric nuclei for which an analytical solution could be developed. We showed that the correct calculation of the interface shapes (both for the nuclei and bridges) can be a key factor in sorting the equilibrium states as well as calculating their energies. Additionally, based on the analysis of the free-energy profiles, we determined the volumes where the transition from one type of shape to another happens, which was important for properly computing the barriers. We formulated the problems in a nondimensional framework to highlight the general features of these systems rather than focusing on the specifics, such as the liquid or solid properties, pore size, *etc.*

The findings of this study regarding the nucleation at the meniscus suggest that geometry in confinement can influence the liquid-to-solid transition by facilitating low-energy sites where the onset of phase-change is expected to take place. Specifically, besides the effects of the competition among the interfacial tensions of various interfaces (represented by angles  $\beta$  and  $\varphi$ ), the presence of sharp corners, (represented by the meniscus and its angle  $\alpha$ ) can play a role in reducing the energy barriers for nucleation in cylindrical pores. However, significant reduction is only predicted if the corner is such that the condition  $\alpha + \beta + \varphi < 180^\circ$  is met. If this is the case, not only can the barriers be reduced but also, the barriers can be completely eliminated meaning that the solid can spontaneously fill the entire pore. Furthermore, such corners can hold a small amount of solid in a metastable or stable equilibrium, because it would have lower free energy than the liquid at the same conditions. We found that, in some cases, somewhat counterintuitively, decreasing the meniscus angle results in slightly higher energy barriers. This is ultimately related to the complex relationships among all solid angles, the volume and areas of solid, and the curvature of the solid–liquid interface.

When it comes to the bridging of the pores, we found that besides the well-known effect of the affinity of the new phase to the particle surface (represented by  $\theta$ ), the presence of multiple pores in the vicinity of each other and their relative proximity determine the height of

the barrier that prevents the formation of bulk solid. Increasing the number of pores and decreasing the inter-pore distance resulted in significant reduction in the energy barriers compared to those for growth from a single, isolated pore. For example, putting a second pore next to a single pore  $8/3R_p$  distance apart reduced the energy barriers by about as much as if the contact angle was decreased from  $135^\circ$  to  $90^\circ$  for an isolated pore (see the solid yellow and dotted red lines in the lower left panel in Figure 4-11). If the pores are not close enough, the single-pore growth might still be favorable at high supersaturations. At large pore separations, we expect no bridging, and the bulk solid should form following the growth from a single pore, regardless of supersaturation.

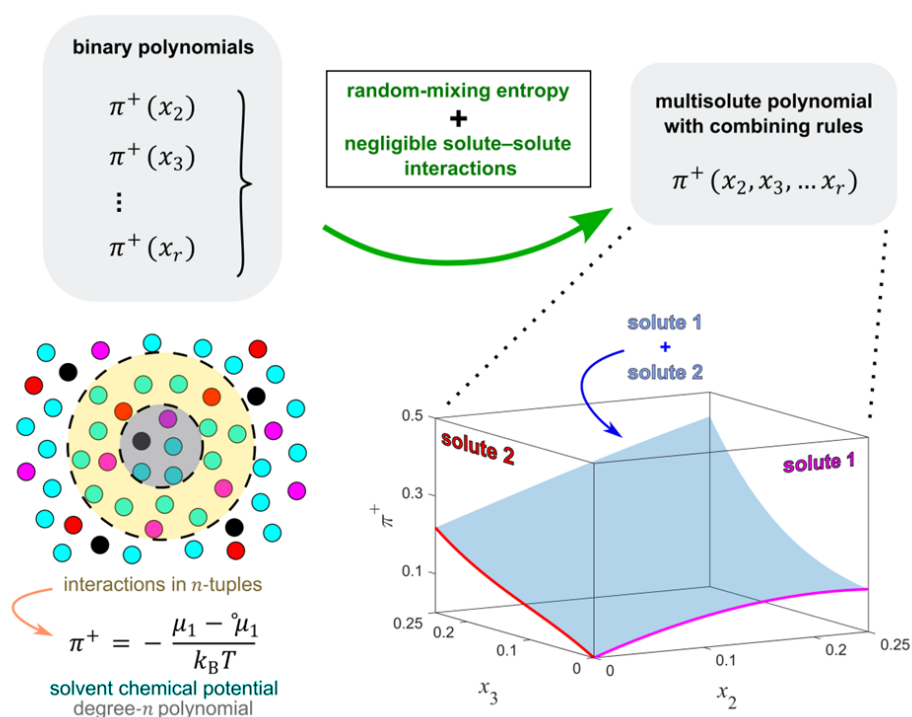
We emphasize that, although we presented our results in the framework of the pore condensation and solidification process, this chapter highlights the importance of both confinement geometry as well as the geometry of the interfaces in all related systems. The general features of the shapes analyzed in this work remain valid for other types of phase transitions. For example, the results for the solid nucleation at the meniscus can equally be interpreted for a vapor-to-liquid transition in a cylindrical pore ended by a hard sphere instead of the meniscus. Similarly, the properties of the bridges and the corresponding reduction in the energy barriers should be the same for a vapor-to-liquid (when studying bulk liquid formation from a porous particle) or liquid-to-solid transition (in the case the porous particle is surrounded by a liquid instead of a vapor). Additionally, bridging would be the same if the cylindrical pores were to be replaced by, for example, spherical pores with circular openings.

## **Part II: Multicomponent solutions**



## Chapter 5

# Multicomponent Solutions: Combining Rules for Multisolute Osmotic Virial Coefficients<sup>1</sup>



## Chapter summary

This chapter presents an exploration of a specific type of a generalized multicomponent solution model, which appears to be first given by Saulov in the current explicit form. The assumptions of the underlying theory and a brief derivation of the main equation was provided preliminarily for completeness and notational consistency. The resulting formulae for the Gibbs free energy of mixing and the chemical potentials are multivariate polynomials with

<sup>1</sup>Reproduced (including Appendix C), with minor changes, with permission from H. Binyaminov and J. A. W. Elliott. *Multicomponent Solutions: Combining Rules for Multisolute Osmotic Virial Coefficients*, J. Chem. Phys. **159**, 164116 (2023). <https://doi.org/10.1063/5.0166482> © 2023 American Institute of Physics.

physically meaningful coefficients and the mole fractions of the components as variables. With one additional assumption about the relative magnitudes of the solvent–solute and solute–solute interaction exchange energies, combining rules were obtained that express the mixed coefficients of the polynomial in terms of its pure coefficients. This was done by exploiting the mathematical structure of the asymmetric form of the solvent chemical potential equation. The combining rules allow one to calculate the thermodynamic properties of the solvent with multiple solutes from binary mixture data only (*i.e.*, each solute with the solvent), and hence, are of practical importance. Furthermore, a connection was established between the osmotic virial coefficients derived in this chapter and the original osmotic virial coefficients of Hill found by employing a different procedure, illustrating the equivalency of what appears to be two different theories. A validation of the combining rules derived here has been provided in Chapter 6 where they were successfully used to predict the freezing points of ternary salt solutions of water.

## 5.1 Introduction

There exist numerous nonideal solution theories in literature. We will not attempt a review here but rather list a few that are essential for providing a context for the approach presented in this chapter. Regular solution theory [69] is the most widely used nonideal solution theory mainly because of its simplicity. It considers only pairwise interactions and assumes random mixing. The quasi-chemical treatment [69] improves on regular solution theory by considering pairwise additive interactions without assuming random mixing (we restrict the usage of the term “regular” to the former case; Guggenheim’s definition includes the quasi-chemical treatment as part of regular solution theory). The quasi-chemical approach provides a good balance of accuracy and simplicity. It is also commonly used, especially to capture the phase-change behavior of solutions more accurately. By accounting for complex interactions in larger particle groups, formally exact theories [82,83,140] avoid all approximations, but they are rarely used in practice due to their complexity and/or for being computationally expensive.

Most solution models have been originally developed for binary mixtures and then extended to multicomponent mixtures. This extension is straight forward in the context of simple theories, such as regular solution theory, but it is challenging in more accurate

frameworks since they are complicated by nature. Hence, it is not surprising that explicit multicomponent formulae are usually not provided even when the existence of such an extension is obvious. Consequently, in practice, while the properties of a binary mixture can be calculated with any theory depending on the required accuracy, only the simple models can be effectively used for multicomponent solutions. In contrast, it is rare for mixtures in nature as well as in industrial processes to only contain two components. Consider, for example, solutions studied in biology [107,117,170], geology [151], oil processing [137,176], metallurgy [40,80,97,104], and atmospheric physics [5,35,106,109,159,182]. Therefore, it is desirable to have an accurate multicomponent solution model with manageable complexity so that practically useful equations can be developed.

In this chapter, we look at a solution made of an arbitrary number of components by considering interactions in groups consisting of an arbitrary number of particles, but nevertheless, we assume random mixing. This approach can be viewed as an extension of regular solution theory in a specific way: while the quasi-chemical treatment addresses the nonrandomness of mixing in a system with pairwise additive interactions, the method employed herein accounts for multi-body interactions with random mixing. The objectives of this chapter are twofold: (i) to give a theoretical basis for the virial equation for the change in the chemical potential of the solvent (*i.e.*, multisolute osmotic virial equation) and derive its coefficients from first principles, and (ii) to provide a method of estimating the chemical potential of a solvent in the presence of multiple solutes by deriving combining rules for the mixed coefficients.

In the first part of this chapter, we list the assumptions of the present model and rederive the corresponding equation for the Gibbs free energy of mixing. Except for the structure of the arguments, some nuances in the assumptions, and notational differences, our formulation and the resulting equation are the same as what was obtained before by Saulov [179] (and by Kakuda *et al.* [102] for special cases). We give a brief, equivalent derivation here for the sake of completeness and consistency of notation with what follows.

It should be noted that the idea of combining rules for the multisolute osmotic virial equation is not new. To our knowledge, the first such concept was put forward by Elliott *et al.* [42] who derived the arithmetic-average combining rule for the second-order mixed coefficient in the regular solution theory framework. A geometric-average combining rule was

also proposed for the cubic mixed coefficient in the same work. These combining rules were then used to predict the osmolality of solutions of interest in biology [42,164,225,226]. Later, a modified version of the multisolute osmotic virial equation with the same combining rules were applied to solutions containing salts as well [163,225,226]. In all cases, a good agreement was achieved between the predictions of the model and independent experimental measurements. This chapter aims to derive generalized combining rules in a specific solution theory framework.

This chapter is intended as a standalone work on the theoretical exploration of the multisolute osmotic virial equation and corresponding combining rules. We note that, however, we have applied an extension of this model to dissociating solutes in Chapter 6. There, the predictions of the present model for freezing points of 11 ternary inorganic salt solutions of water were found to be in excellent agreement with independent experimental measurements (root-mean-square error of 0.45 K and close to zero mean bias for a total of 371 data points).

## 5.2 The model

### 5.2.1 Assumptions of the model

We consider a single-phase multicomponent mixture theory that accounts for interactions in arbitrarily large particle groups. The goal here is to find an explicit formula for the thermodynamic potential (or free energy) of the system in terms of the energies of the particle groups. We are interested in solutions formed at constant temperature and pressure with fixed amounts of each component, hence, the Gibbs free energy,  $G$ , is the thermodynamic potential of the system. The assumptions of the model are listed below:

- (i) The total nonconfigurational Gibbs free energy of the system can be written as the sum of the interaction energies of all particle groups of a chosen size. The selection of this cutoff size is based on assumption (ii).
- (ii) For each particle, there exists a neighborhood, and the interactions of this particle with particles outside of this neighborhood can be neglected. The neighborhood is defined by the smallest spherical volume encapsulating a given number of particles. Note that negligible interaction outside of this sphere does not mean zero interaction, but instead, implies that the difference in the long-range interactions

between the pure substance and the mixture is negligible such that the associated energy remains unchanged upon mixing.

- (iii) Each particle is directly surrounded by a certain constant number of other particles, which is called the coordination number. The coordination number is well defined for a solid lattice but should be thought of as an average of many possible arrangements for liquids. The fluctuations around this average can be shown to have insignificant effect on the local geometry in liquids. No assignment of this constant is needed in our calculations.
- (iv) All particles are of similar size so that, when a particle at a site is replaced by a different type of particle, the coordination number can be assumed to be unchanged.
- (v) The particles are randomly distributed even though the exchange interaction energies are not zero. In other words, all particles have an equal probability of occupying any given site, which is also the same for all sites, independent of the occupancy of the neighboring sites.

Assumption (v) is also known as the Braggs–Williams approximation [82], and it is the main simplification made in the present treatment.

### 5.2.2 *Nonconfigurational Gibbs free energy of random mixing*

Here, it is convenient to work with a modified Gibbs free-energy function that excludes the terms due to configurational entropy. This contribution can be separately calculated and added later. Consider  $n$ -tuples as the interacting particle groups (*i.e.*, groups of  $n$  particles; smaller or larger groups are not used in the formulation) at constant pressure and temperature. Then, based on assumptions (i) and (ii), the nonconfigurational Gibbs free energy,  $G^{\text{nc}}$ , of a system made by mixing  $r$  types of components can be expressed as the sum of energies of all particle groups:

$$G^{\text{nc}} = \sum_{\ell} g_{\mathbf{A}_{\ell}} N_{\mathbf{A}_{\ell}} \quad (5-1)$$

where  $g_{\mathbf{A}_{\ell}}$  and  $N_{\mathbf{A}_{\ell}}$  are the nonconfigurational Gibbs free energy and the number of a certain type of fixed composition  $n$ -tuples denoted by the index  $\mathbf{A}_{\ell}$ , respectively. The subscript  $\ell$  is an incrementing label pointing to each unique element of  $\mathbf{A}_{\ell}$  (see the next paragraph). Each  $g_{\mathbf{A}_{\ell}}$  is assumed to be averaged over all possible spatial configurations of particle groups having

the same composition. The main idea of the present treatment is to not search for a decomposition of  $g_{\mathbf{A}_\ell}$  in terms of the energies of smaller particle groups if not necessary, and instead, treat it as a fundamental quantity. This approach reduces mathematical complexity and avoids needless approximations that may be present in other approaches, such as the quasi-chemical treatment, where the pairwise additivity of interaction energies had to be assumed. Note that this does not mean that the method presented here is superior to others. The choice is rather a matter of what one wishes to calculate/achieve using the model. For the purposes of this article, viewing the  $n$ -tuple energy as irreducible will suffice.

In Equation (5-1),  $\mathbf{A}$  denotes the set of all multisets of length  $n$ , chosen from  $r$  types (*i.e.*, all the different  $n$ -tuples that can be made of  $n$  particles chosen from  $r$  particle types or components), and  $\ell$  is used to label its elements. One such element represents a unique  $n$ -tuple type (and *vice versa*) in terms of its composition, and each  $\mathbf{A}_\ell$  is permutation-invariant (*i.e.*, no ordering is assumed). From basic combinatorics, the number of such multisets (*i.e.*, the number of elements of  $\mathbf{A}$ ) can be found to be [52]

$$|\mathbf{A}| = \binom{n+r-1}{n} = \frac{(n+r-1)!}{n!(r-1)!} \quad (5-2)$$

meaning that  $\ell \in [1, |\mathbf{A}|]$  (note that  $0! = 1$ ). We use natural numbers from 1 to  $r$  to label the components. For example, for  $n = 2$  and  $r = 3$  we have

$$G^{\text{nc}} = g_{11}N_{11} + g_{22}N_{22} + g_{33}N_{33} + g_{12}N_{12} + g_{13}N_{13} + g_{23}N_{23} \quad (5-3)$$

for  $n = 3$  and  $r = 2$  we have

$$G^{\text{nc}} = g_{111}N_{111} + g_{222}N_{222} + g_{112}N_{112} + g_{122}N_{122} \quad (5-4)$$

and so on, as desired. The complicated index notation we adopt here may seem unnecessary, however, its use has the benefit of making certain formulae in the following derivation much shorter and easier to comprehend.

Using assumptions (iii) and (iv) and taking  $z_n$  as the number of  $n$ -tuples sharing each particle, which only depends on  $n$  and the coordination number, the number of particles of type  $j$  and the number of  $n$ -tuples can be related by simple counting as follows:

$$N_j = \frac{1}{z_n} \sum_{\ell} \xi_{j|\mathbf{A}_\ell} N_{\mathbf{A}_\ell} \quad (5-5)$$

where  $0 \leq \xi_{j|\mathbf{A}_\ell} \leq n$  is the multiplicity of component  $j$  in the multiset  $\mathbf{A}_\ell$ . Noting that  $\sum_{j=1}^r \xi_{j|\mathbf{A}_\ell} = n$  for any  $\mathbf{A}_\ell$ , we can sum the left- and right-hand sides of Equation (5-5) over  $j$  and obtain

$$\sum_{\ell} N_{\mathbf{A}_\ell} = \frac{z_n}{n} \sum_{j=1}^r N_j \quad (5-6)$$

which relates the total number of  $n$ -tuples to the total number of particles of individual species. As it can be inferred from equation (5-6), the factor  $z_n/n$  is the number of times we overcount each particle when counting the particle groups. If we multiply both sides of Equation (5-5) by the pure  $n$ -tuple energy,  $g_{j\dots j}$ , before summing its left- and right-hand sides over  $j$ , we instead get

$$\frac{z_n}{n} \sum_{j=1}^r g_{j\dots j} N_j - \sum_{\ell} \left( \frac{1}{n} \sum_{j=1}^r \xi_{j|\mathbf{A}_\ell} g_{j\dots j} \right) N_{\mathbf{A}_\ell} = 0 \quad (5-7)$$

Equation (5-7) can be added to Equation (5-1) and the result can be rearranged to give

$$G^{\text{nc}} = \frac{z_n}{n} \sum_{j=1}^r g_{j\dots j} N_j + \sum_{\ell} \left( g_{\mathbf{A}_\ell} - \frac{1}{n} \sum_{j=1}^r \xi_{j|\mathbf{A}_\ell} g_{j\dots j} \right) N_{\mathbf{A}_\ell} \quad (5-8)$$

Notice that the first term on the right-hand side of Equation (5-8) is the nonconfigurational Gibbs free energy of the system when only the like particles interact. It has the same value as if we calculated the total system energy with each pure-component subsystem existing far apart.

From the second term on the right-hand side of Equation (5-8), we can naturally define the nonconfigurational Gibbs free-energy change of formation of a particle group by viewing the mixing process as the creation of a particular  $n$ -tuple from the “disassembly” and “reassembly” of the appropriate pure-component  $n$ -tuples:

$$w_{\mathbf{A}_\ell} = g_{\mathbf{A}_\ell} - \frac{1}{n} \sum_{j=1}^r \xi_{j|\mathbf{A}_\ell} g_{j\dots j} \quad (5-9)$$

Clearly,  $w_{j\dots j} = 0$  for all  $j$ , however, we will not make this substitution in some cases to preserve the symmetry of certain expressions. With this notation, the nonconfigurational Gibbs free energy of the system can be expressed as

$$G^{\text{nc}} = \frac{z_n}{n} \sum_{j=1}^r g_{j\dots j} N_j + \sum_{\ell} w_{\mathbf{A}_\ell} N_{\mathbf{A}_\ell} \quad (5-10)$$

Based on the random-mixing assumption, (v), the probability of a randomly chosen  $n$ -tuple to have the composition  $\mathbf{A}_\ell$  can be found with the help of combinatorics:

$$\mathcal{P}_{\mathbf{A}_\ell} = \frac{n!}{(\sum_{j=1}^r N_j)^n} \prod_{j=1}^r \frac{(N_j)^{\xi_{j|\mathbf{A}_\ell}}}{\xi_{j|\mathbf{A}_\ell}!} \quad (5-11)$$

which is the probability mass function of the multinomial distribution [52]. Here, it is assumed that each  $N_j$  is much larger than  $n$  so that the probability of each consecutive inclusion of a certain type of species in the group is independent of its existing fraction in that group. Using Equations (5-6) and (5-11), we can calculate the expected or average number of  $n$ -tuples of a given composition in the mixture as

$$\langle N_{\mathbf{A}_\ell} \rangle = \mathcal{P}_{\mathbf{A}_\ell} \sum_{\ell} N_{\mathbf{A}_\ell} = \frac{z_n n!}{n(\sum_{j=1}^r N_j)^{n-1}} \prod_{j=1}^r \frac{(N_j)^{\xi_{j|\mathbf{A}_\ell}}}{\xi_{j|\mathbf{A}_\ell}!} \quad (5-12)$$

Substituting Equation (5-12) into Equation (5-10), we can find the expected nonconfigurational Gibbs free energy of the entire system:

$$\langle G^{\text{nc}} \rangle = \frac{z_n}{n} \sum_{j=1}^r g_{j\dots j} N_j + \frac{z_n}{n(\sum_{j=1}^r N_j)^{n-1}} \sum_{\ell} w_{\mathbf{A}_\ell} n! \prod_{j=1}^r \frac{(N_j)^{\xi_{j|\mathbf{A}_\ell}}}{\xi_{j|\mathbf{A}_\ell}!} \quad (5-13)$$

Used here to distinguish the exact value from the expected value, we drop the angle brackets in the remainder of the text. Applying the multinomial theorem to Equation (5-13), we can notationally simplify and rewrite it as

$$G^{\text{nc}} = \frac{z_n}{n} \sum_{j=1}^r g_{j\dots j} N_j + \frac{z_n}{n(\sum_{j=1}^r N_j)^{n-1}} \sum_{i_1, i_2, \dots, i_n=1}^r w_{i_1 i_2 \dots i_n} N_{i_1} N_{i_2} \dots N_{i_n} \quad (5-14)$$

where we use a single sum notation for a series of sums repeated  $n$  times for each element (*i.e.*, each index) from the set of variables  $\{i_1, i_2 \dots i_n\}$ , each starting from 1 going up to  $r$ . Since the individual indices appear explicitly and the second sum is symmetric in Equation (5-14), this explicit notation will prove more useful in next sections compared to the notation used in Equations (5-1) to (5-13). Note that the choice to label the variable indices in an increasing order is a convention we make here and follow throughout the text.



Equation (5-13) has been previously obtained by Saulov [179] for the general case and by Kakuda *et al.* [102] for up to  $n = 4$  and  $r = 4$  using similar arguments and assumptions. Both articles have received minimal attention in the solution thermodynamics literature and are not particularly well known.

### 5.2.3 Chemical potential

To find the chemical potential of component  $j$ ,  $\mu_j$ , we take the derivative of the total Gibbs free energy with respect to the number of that component,  $N_j$ , at constant temperature,  $T$ , pressure,  $P$ , and the fixed numbers of the remaining species:

$$\begin{aligned}\mu_j &= \left( \frac{\partial G}{\partial N_j} \right)_{T,P,N_i \neq N_j} = \left( \frac{\partial G^{\text{nc}}}{\partial N_j} \right)_{T,P,N_i \neq N_j} + \left( \frac{\partial G^{\text{c}}}{\partial N_j} \right)_{T,P,N_i \neq N_j} \\ &= \mu_j^\circ + \mu_j^{\text{ex}} + k_{\text{B}}T \ln x_j\end{aligned}\quad (5-15)$$

where  $G^{\text{c}}$  is the configurational part of the Gibbs free energy ( $G = G^{\text{nc}} + G^{\text{c}}$ ),  $\mu_j^\circ = z_n g_{j\dots j}/n$  is the chemical potential of the pure substance (by the definition of chemical potential),  $k_{\text{B}}$  is the Boltzmann constant, and  $x_j$  is the mole fraction of component  $j$  in the solution. Termed the excess chemical potential of species  $j$ ,  $\mu_j^{\text{ex}}$  is the derivative of the second term on the right-hand side of Equation (5-14). The term  $k_{\text{B}}T \ln x_j$  in Equation (5-15) is the derivative of  $G^{\text{c}}$  under the random-mixing assumption and its derivation can be found in any standard textbook on the topic (*e.g.*, see Guggenheim [69]).

Next, we explicitly evaluate  $\mu_j^{\text{ex}}$  in Equation (5-15) using the expression through which it is defined:

$$\begin{aligned}\mu_j^{\text{ex}} &= \frac{\partial}{\partial N_j} \left[ \frac{z_n}{n(\sum_{k=1}^r N_k)^{n-1}} \sum_{i_1, i_2, \dots, i_n=1}^r w_{i_1 i_2 \dots i_n} N_{i_1} N_{i_2} \dots N_{i_n} \right] \\ &= \frac{z_n}{n N_j (\sum_{k=1}^r N_k)^{n-1}} \sum_{i_1, i_2, \dots, i_n=1}^r \left( \sum_{k=1}^n \delta_{j i_k} \right) w_{i_1 i_2 \dots i_n} N_{i_1} N_{i_2} \dots N_{i_n} \\ &\quad - \frac{z_n (n-1)}{n (\sum_{k=1}^r N_k)^n} \sum_{i_1, i_2, \dots, i_n=1}^r w_{i_1 i_2 \dots i_n} N_{i_1} N_{i_2} \dots N_{i_n}\end{aligned}\quad (5-16)$$

where  $\delta_{ij}$  is the Kronecker delta ( $\delta_{ij} = 1$ , if  $i = j$ ;  $\delta_{ij} = 0$ , otherwise). We can expand the innermost sum in Equation (5-16), reindex each resulting term, and recollect the terms to get

$$\mu_j^{\text{ex}} = \frac{z_n}{nN_j(\sum_{k=1}^r N_k)^{n-1}} \left( n \sum_{i_1, i_2, \dots, i_n=1}^r \delta_{ji_1} w_{i_1 i_2 \dots i_n} N_{i_1} N_{i_2} \dots N_{i_n} \right) - \frac{z_n(n-1)}{n(\sum_{k=1}^r N_k)^n} \sum_{i_1, i_2, \dots, i_n=1}^r w_{i_1 i_2 \dots i_n} N_{i_1} N_{i_2} \dots N_{i_n} \quad (5-17)$$

Cancelling out the terms in Equation (5-17) and writing it in mole fraction units, we have

$$\mu_j^{\text{ex}} = z_n \sum_{i_2, i_3, \dots, i_n=1}^r w_{ji_2 \dots i_n} x_{i_2} x_{i_3} \dots x_{i_n} - \frac{z_n(n-1)}{n} \sum_{i_1, i_2, \dots, i_n=1}^r w_{i_1 i_2 \dots i_n} x_{i_1} x_{i_2} \dots x_{i_n} \quad (5-18)$$

Equation (5-18) is the most general form of the excess chemical potential given the current assumptions. It can be substituted into Equation (5-15) giving the equation for the full chemical potential. However, in the next few steps of the derivation, it will be more convenient to work with the excess chemical potential, thus we choose to make this substitution later.

## 5.3 Solvent-dominant mixtures

In many practical applications, multicomponent mixtures are often those consisting of a solvent as the main medium with added solutes in small amounts (not necessarily dilute). Therefore, it is valuable to have a method of estimating the chemical potential of the solvent from binary solution data only. Here, with one additional assumption about the exchange interaction energies of the components, we provide a derivation of such a method based on Equation (5-18). In the remainder of this chapter, we will denote the solvent by 1 and the solutes by 2, 3 ...  $r$ .

### 5.3.1 Asymmetric form of Equation (5-18) for the solvent

Here, we work with Equation (5-18) written for the solvent (*i.e.*,  $j = 1$ ). It is useful to write this equation in terms of the mole fractions of the solutes only. This can be done by repeatedly substituting  $x_1 = 1 - \sum_{j=2}^r x_j$  in the expansion over each  $i_j$  and simplifying the results by combining the like terms. Below we give the details of substitution for  $x_1$  in the expansion over  $i_1$ :

Step (1) Separate the term containing  $x_1$  in the sum over  $i_1$  in Equation (5-18) from the rest and substitute for  $x_1$  to get

$$\begin{aligned} \mu_1^{\text{ex}} = z_n & \sum_{i_2, i_3, \dots, i_n=1}^r w_{1i_2 \dots i_n} x_{i_2} x_{i_3} \dots x_{i_n} \\ & - \frac{z_n(n-1)}{n} \sum_{i_2, i_3, \dots, i_n=1}^r w_{1i_2 \dots i_n} \left( 1 - \sum_{j=2}^r x_j \right) x_{i_2} x_{i_3} \dots x_{i_n} \quad (5-19) \\ & - \frac{z_n(n-1)}{n} \sum_{\substack{i_2, i_3, \dots, i_n=1 \\ i_1=2}}^r w_{1i_2 \dots i_n} x_{i_1} x_{i_2} \dots x_{i_n} \end{aligned}$$

Step (2) Split the expression  $(1 - \sum_{j=2}^r x_j)$  in Equation (5-19) into two terms to get

$$\begin{aligned} \mu_1^{\text{ex}} = z_n & \sum_{i_2, i_3, \dots, i_n=1}^r w_{1i_2 \dots i_n} x_{i_2} x_{i_3} \dots x_{i_n} \\ & - \frac{z_n(n-1)}{n} \sum_{i_2, i_3, \dots, i_n=1}^r w_{1i_2 \dots i_n} x_{i_2} x_{i_3} \dots x_{i_n} \\ & + \frac{z_n(n-1)}{n} \sum_{\substack{i_2, i_3, \dots, i_n=1 \\ i_1=2}}^r w_{1i_2 \dots i_n} x_{i_1} x_{i_2} \dots x_{i_n} \quad (5-20) \\ & - \frac{z_n(n-1)}{n} \sum_{\substack{i_2, i_3, \dots, i_n=1 \\ i_1=2}}^r w_{1i_2 \dots i_n} x_{i_1} x_{i_3} \dots x_{i_n} \end{aligned}$$

Step (3) Collect the terms over the same sums to get

$$\begin{aligned} \mu_1^{\text{ex}} = \frac{z_n}{n} & \sum_{i_2, i_3, \dots, i_n=1}^r w_{1i_2 \dots i_n} x_{i_2} x_{i_3} \dots x_{i_n} \\ & - \frac{z_n(n-1)}{n} \sum_{\substack{i_2, i_3, \dots, i_n=1 \\ i_1=2}}^r (w_{1i_2 \dots i_n} - w_{1i_2 \dots i_n}) x_{i_1} x_{i_2} \dots x_{i_n} \quad (5-21) \end{aligned}$$

If we now substitute  $x_1 = 1 - \sum_{j=2}^r x_j$  in the expansion over  $i_2$  in Equation (5-21) and follow the same steps (see Appendix C), we get

$$\begin{aligned}
\mu_1^{\text{ex}} &= \frac{z_n}{n} \sum_{i_3, i_4, \dots, i_n=1}^r w_{11i_3 \dots i_n} x_{i_3} x_{i_4} \dots x_{i_n} \\
&\quad - \frac{z_n(n-2)}{n} \sum_{\substack{i_3 \dots i_n=1 \\ i_2=2}}^r (w_{1i_2 \dots i_n} - w_{11i_3 \dots i_n}) x_{i_2} x_{i_3} \dots x_{i_n} \\
&\quad - \frac{z_n(n-1)}{n} \sum_{\substack{i_3, i_4, \dots, i_n=1 \\ i_1, i_2=2}}^r (w_{i_1 i_2 \dots i_n} - 2w_{1i_2 \dots i_n} \\
&\quad + w_{11i_3 \dots i_n}) x_{i_1} x_{i_2} \dots x_{i_n}
\end{aligned} \tag{5-22}$$

Similarly, if substitute  $x_1 = 1 - \sum_{j=2}^r x_j$  in the expansion over  $i_3$  in Equation (5-22) (see Appendix C), we get

$$\begin{aligned}
\mu_1^{\text{ex}} &= \frac{z_n}{n} \sum_{i_4, i_5, \dots, i_n=1}^r w_{111i_4 \dots i_n} x_{i_4} x_{i_5} \dots x_{i_n} \\
&\quad - \frac{z_n(n-3)}{n} \sum_{\substack{i_4 \dots i_n=1 \\ i_3=2}}^r (w_{11i_3 \dots i_n} - w_{111i_4 \dots i_n}) x_{i_3} x_{i_4} \dots x_{i_n} \\
&\quad - \frac{z_n(2n-3)}{n} \sum_{\substack{i_4, i_5, \dots, i_n=1 \\ i_2, i_3=2}}^r (w_{1i_2 \dots i_n} - 2w_{11i_3 \dots i_n} \\
&\quad + w_{111i_4 \dots i_n}) x_{i_2} x_{i_3} \dots x_{i_n} \\
&\quad - \frac{z_n(n-1)}{n} \sum_{\substack{i_4, i_5, \dots, i_n=1 \\ i_1, i_2, i_3=2}}^r (w_{i_1 i_2 \dots i_n} - 3w_{1i_2 \dots i_n} + 3w_{11i_3 \dots i_n} \\
&\quad - w_{111i_4 \dots i_n}) x_{i_1} x_{i_2} \dots x_{i_n}
\end{aligned} \tag{5-23}$$

Noticing the emerging pattern in this series, the result after  $n$  steps can be cast into the following compact expression:

$$\begin{aligned}
&\mu_1^{\text{ex}} \\
&= \sum_{m=2}^n \frac{z_n(1-m)}{n} \binom{n}{m} \sum_{i_1, i_2, \dots, i_m=2}^r \left[ \sum_{k=0}^m (-1)^k \binom{m}{k} w_{1 \dots 1 i_{k+1} \dots i_m} \right] x_{i_1} x_{i_2} \dots x_{i_m}
\end{aligned} \tag{5-24}$$

where  $\binom{n}{m} = \frac{n!}{m!(n-m)!}$  and  $\binom{m}{k} = \frac{m!}{k!(m-k)!}$  are the binomial coefficients. The number of 1's in the subscript of  $w$  is equal to  $n - m + k$  while the remaining  $m - k$  number of indices stay free. Note that more than one choice exists to label these free indices when  $k \geq 1$ ; the choice from  $k + 1$  up to  $m$  is arbitrary. Equation (5-24) is an asymmetric version of Equation (5-18) for the excess chemical potential of the solvent. It is a multivariate polynomial containing all possible configurations of powers from 2 to  $n$  of solute mole fractions only ( $r - 1$  variables), compared to powers of  $n - 1$  and  $n$  in Equation (5-18), which also includes the solvent mole fraction as a variable ( $r$  variables). Below we give examples of each element in the main sum in Equation (5-24) for  $n = 4$ :

for  $n = 4$  and  $m = 4$ , we have

$$\begin{aligned} & -\frac{3z_n}{4} \sum_{i_1, i_2, i_3, i_4=2}^r \left[ \sum_{k=0}^4 (-1)^k \binom{4}{k} w_{1\dots 1i_{k+1}\dots i_4} \right] x_{i_1} x_{i_2} x_{i_3} x_{i_4} \\ & = -\frac{3z_n}{4} \sum_{i_1, i_2, i_3, i_4=2}^r (w_{i_1 i_2 i_3 i_4} - 4w_{1i_2 i_3 i_4} + 6w_{11i_3 i_4} \\ & \quad - 4w_{111i_4} + w_{1111}) x_{i_1} x_{i_2} x_{i_3} x_{i_4} \end{aligned} \quad (5-25)$$

for  $n = 4$  and  $m = 3$ , we have

$$\begin{aligned} & -2z_n \sum_{i_1, i_2, i_3=2}^r \left[ \sum_{k=0}^3 (-1)^k \binom{3}{k} w_{1\dots 1i_{k+1}\dots i_3} \right] x_{i_1} x_{i_2} x_{i_3} \\ & = -2z_n \sum_{i_1, i_2, i_3=2}^r (w_{1i_1 i_2 i_3} - 3w_{11i_2 i_3} + 3w_{111i_3} \\ & \quad - w_{1111}) x_{i_1} x_{i_2} x_{i_3} \end{aligned} \quad (5-26)$$

for  $n = 4$  and  $m = 2$ , we have

$$\begin{aligned} & -\frac{3z_n}{2} \sum_{i_1, i_2=2}^r \left[ \sum_{k=0}^2 (-1)^k \binom{2}{k} w_{1\dots 1i_{k+1}\dots i_2} \right] x_{i_1} x_{i_2} \\ & = -\frac{3z_n}{2} \sum_{i_1, i_2=2}^r (w_{11i_1 i_2} - 2w_{111i_2} + w_{1111}) x_{i_1} x_{i_2} \end{aligned} \quad (5-27)$$

### 5.3.2 Derivation of combining rules

If we hope to obtain any type of combining rules (*i.e.*, a model for a multisolute mixture that uses only single-solute–solvent binary information), we need to express the coefficients of the mixed terms (*i.e.*, the terms containing the powers of more than one of  $\{x_2, x_3 \dots x_r\}$ ) of any order in terms of the coefficients of the pure terms (*i.e.*, the terms containing the powers of only one of  $\{x_2, x_3 \dots x_r\}$ ).

Note that Equation (5-24), written for a multicomponent mixture, inevitably contains terms with coefficients corresponding to purely solute–solute interactions (*e.g.*, terms with  $w_{223}$ ,  $w_{2345}$ , *etc.*). Clearly, these coefficients are not expressible in terms of the solvent–solute binary coefficients, even with any additional (physically meaningful) approximations. Therefore, to continue further, we make the following simplifying assumption:

- (vi) The interaction exchange energies of the solute species with one another are negligible compared to the interaction exchange energies of the solute species and the solvent species. That is, the nonconfigurational Gibbs free-energy change of formation of a particle group made purely from solutes is zero. This is equivalent of assuming that a mixture made of any combination of the solute components only behaves ideally.

Under assumption (vi), if one type of solute species is replaced by another type of solute species in a certain particle group, the change of the interaction energy of this group does not depend on the types of the other solute species present in the group: it only depends on the number of solvent particles in the group and the types of particles being exchanged. It is important to note that no restriction is imposed on the concentrations of the species.

We can arrive at the mathematical implications of assumption (vi) with the following thought experiment: Consider some number of copies of the same  $n$ -tuple containing at least one solvent particle, that is, consider all copies having the same composition as one system. If we swap one solute particle of a certain type from one of the  $n$ -tuples in this system with another solute particle of a different type from a different  $n$ -tuple in this system, then the nonconfigurational Gibbs free energy of the entire system will not change because of assumption (vi). Clearly, we can repeat this particle swapping any number of times without affecting the total (nonconfigurational) energy of the system. Now, to ensure that we can reduce this system of copies to a sum of  $n$ -tuples each containing the same number of solvent

particles and only one type of solute particles (*i.e.*, binary groups), we can make the initial system such that the number of the copies is equal to the number of the solute particles in one  $n$ -tuple. Consistent with the notation in Equation (5-24), we can mathematically summarize this realization as a decomposition of  $g$  in the following way:

$$g_{1\dots 1i_{k+1}\dots i_m} = \frac{1}{m-k} \sum_{j=k+1}^m g_{1\dots 1i_j\dots i_j} \quad (5-28)$$

where the number of 1's and the number of the variable indices in the subscript of  $w$  are preserved from the left side of the equation to the right side of the equation. Like in Equation (5-24), each variable index here can only represent a solute:  $i_j \in [2, r]$ . The case  $m = k$  corresponds to the pure  $n$ -tuple energy, so no decomposition exists in this case, and we do not need to worry about the division by zero.

Using Equation (5-9), it can be checked that this representation of  $g$  in terms of the binary group energies implies the same decomposition for  $w$  (see Appendix C). That is, we can write

$$w_{1\dots 1i_{k+1}\dots i_m} = \frac{1}{m-k} \sum_{j=k+1}^m w_{1\dots 1i_j\dots i_j} \quad (5-29)$$

As an example, the following series of equalities holds for  $n = 4$ ,  $m = 4$ , and  $k = 2$ :

$$\begin{cases} w_{1123} = \frac{1}{2}(w_{1122} + w_{1133}) \\ w_{1134} = \frac{1}{2}(w_{1133} + w_{1144}) \\ w_{1124} = \frac{1}{2}(w_{1122} + w_{1144}) \\ w_{1125} = \frac{1}{2}(w_{1122} + w_{1155}) \\ \vdots \end{cases} \quad (5-30)$$

Substituting Equation (5-29) into Equation (5-24), after some reindexing and regrouping (see Appendix C), the equation for the excess chemical potential can be expressed as

$$\mu_1^{\text{ex}} = \sum_{m=1}^n \sum_{i_1, i_2, \dots, i_m=2}^r \frac{1}{m} \left( \sum_{j=1}^m Q_{i_j}^{n,m} \right) x_{i_1} x_{i_2} \dots x_{i_m} \quad (5-31)$$

where

$$Q_j^{n,m} = \frac{z_n(1-m)}{n} \binom{n}{m} \sum_{k=0}^m (-1)^k \binom{m}{k} w_{1\dots 1j\dots j} \quad (5-32)$$

$Q_j^{n,m}$  is the  $m$ th order pure coefficient of the excess chemical potential expression of solute  $j$  in a degree- $n$  expansion, and it can be obtained by setting  $x_i = 0$  for all  $i$  except  $i = j$  in Equation (5-24). Note that the lower bound of the main sum in Equation (5-31) is switched from  $m = 2$  to  $m = 1$  without affecting the result because the first-order pure coefficients are zero by definition (*i.e.*,  $Q_j^{n,1} = 0$  for any  $n$ ).

In Equation (5-32), the number of 1's and  $j$ 's in the subscript of  $w$  changes from one term of the sum to another as  $k$  varies. For instance, the fourth- and third-order pure coefficients of component 2 in a degree-4 expansion are

$$Q_2^{4,4} = -\frac{3z_n}{4} w_{2222} + 3z_n w_{1222} - \frac{9z_n}{2} w_{1122} + 3z_n w_{1112} - \frac{3z_n}{4} w_{1111} \quad (5-33)$$

and

$$Q_2^{4,3} = -2z_n w_{1222} + 6z_n w_{1122} - 6z_n w_{1112} + 2z_n w_{1111} \quad (5-34)$$

respectively.

Substituting the expression for  $\mu_1^{\text{ex}}$  given by Equation (5-31) into Equation (5-15) (written for the solvent), we can calculate  $\mu_1$ . However, if we want to have a polynomial expression for  $\mu_1$  as well, we need to approximate  $\ln(x_1)$  [which will be present in Equation (5-15) when it is written for the solvent] by a suitable polynomial expression first. This can be done by substituting  $x_1 = 1 - \sum_{j=2}^r x_j$  into  $\ln(x_1)$  and writing its Taylor series expansion around  $\sum_{j=2}^r x_j = 0$  up to the  $n$ th term:



$$\begin{aligned}
\ln(x_1) &= \ln\left(1 - \sum_{j=2}^r x_j\right) \\
&\approx -\sum_{j=2}^r x_j - \frac{1}{2}\left(\sum_{j=2}^r x_j\right)^2 - \frac{1}{3}\left(\sum_{j=2}^r x_j\right)^3 - \dots \\
&\quad - \frac{1}{n}\left(\sum_{j=2}^r x_j\right)^n \\
&= -\sum_{i_1=2}^r x_{i_1} - \sum_{i_1, i_2=2}^r \frac{1}{2}x_{i_1}x_{i_2} - \sum_{i_1, i_2, i_3=2}^r \frac{1}{3}x_{i_1}x_{i_2}x_{i_3} - \dots \\
&\quad - \sum_{i_1, i_2, \dots, i_n=2}^r \frac{1}{n}x_{i_1}x_{i_2} \dots x_{i_n} \\
&= -\sum_{m=1}^n \sum_{i_1, i_2, \dots, i_m=2}^r \frac{1}{m}x_{i_1}x_{i_2} \dots x_{i_m}
\end{aligned} \tag{5-35}$$

Chemical potential is more useful in practice when it is calculated with respect to a reference state. For a solvent with added solutes, one convenient reference state is the pure solvent system at the same temperature and pressure for which the chemical potential is  $\mu_1^\circ$ . It is also convenient to express this change in chemical potential in units of  $k_B T$  to have a nondimensional equation. Thus, substituting the results from Equation (5-31) and Equation (5-35) into Equation (5-15) (written for the solvent) and rearranging, we write the following:

$$\frac{\mu_1 - \mu_1^\circ}{k_B T} = -\sum_{m=1}^n \sum_{i_1, i_2, \dots, i_m=2}^r \frac{1}{m} \left[ 1 - \frac{1}{k_B T} \left( \sum_{j=1}^m Q_{i_j}^{n,m} \right) \right] x_{i_1} x_{i_2} \dots x_{i_m} \tag{5-36}$$

Because the quantity  $(\mu_1 - \mu_1^\circ)/k_B T$  appears frequently in calculations, it has been given different names in various forms. Some notable ones are the relative activity [69] of the solvent, defined as

$$a_1 = \exp\left(\frac{\mu_1 - \mu_1^\circ}{k_B T}\right) \tag{5-37}$$

and the osmolality [45,226] of the solvent, defined as

$$\pi = -\frac{\mu_1 - \mu_1^\circ}{k_B T M_1} \tag{5-38}$$

where  $M_1$  is the solvent's molar mass. A more directly related quantity is given as

$$\pi^+ = -\frac{\mu_1 - \mu_1^\circ}{k_B T} \quad (5-39)$$

which is usually referred to as the osmole fraction [45,226] of the solvent. Because of this simple relationship, we choose to express the change in chemical potential as osmole fraction. Thus, after distributing the 1 inside the brackets evenly into  $m$  terms and introducing nondimensional coefficients, we can rewrite Equation (5-36) as

$$\pi^+ = \sum_{m=1}^n \sum_{i_1, i_2, \dots, i_m=2}^r \frac{1}{m} \left( \sum_{j=1}^m \hat{Q}_{i_j}^{n,m} \right) x_{i_1} x_{i_2} \dots x_{i_m} \quad (5-40)$$

where  $\hat{Q}_j^{n,m}$  is defined in terms of  $Q_j^{n,m}$  through the relation

$$\hat{Q}_j^{n,m} = \frac{1}{m} - \frac{Q_j^{n,m}}{k_B T} = \frac{1}{m} + \frac{z_n(m-1)}{nk_B T} \binom{n}{m} \sum_{k=0}^m (-1)^k \binom{m}{k} w_{1\dots 1j\dots j} \quad (5-41)$$

and it can be described as the mole-fraction-based  $m^{\text{th}}$  order pure osmotic virial coefficient of component  $j$  in a degree- $n$  expansion. Equation (5-40) is a multivariate polynomial in  $r - 1$  variables for the change of the chemical potential of the solvent in the presence of solutes. It is a form of the multisolute osmotic virial equation derived using assumptions (i) through (vi). The physical meaning of each coefficient of the polynomial can be inferred with the help of Equations (5-41) and (5-9). One can also obtain [82,83] other thermodynamic properties of the solvent, such as its molar volume, heat content, *etc.*, by suitable differentiations of  $\pi^+$ , which are not discussed here.

The arithmetic-average combining rules for the mixed-term coefficients follow naturally from the structure of Equation (5-40). The usefulness of such mixing rules is obvious: if one has data for the chemical potential change of the solvent as a function of solute concentration with each solute separately, then the chemical potential of the solvent in the presence of any combination of these solutes can be predicted. In practice, this can be done by fitting a polynomial to each binary solution dataset and taking the arithmetic average of the appropriate coefficients to get the coefficients of the cross terms. Alternatively, if no experimental data are available for certain binaries, the pure osmotic virial coefficients can be found from a more sophisticated model or molecular dynamics simulations.

The combining rules derived above based on assumption (vi) neglect effects expected when the solutes are ions (*e.g.*, solute dissociation, charge screening). However, previous versions of the multisolute osmotic virial equation have been successfully adapted for use with salt solutes by incorporation of a single additional parameter,  $(k_d)_j$  for each salt  $j$ , that is obtained empirically from fitting to experimental data (for each salt, replace  $x_j$  with  $(k_d)_j x_j$  in the virial equation) [163]. The parameter  $(k_d)_j$  is called the “dissociation constant of solute  $j$ ” even though it empirically accounts for more electrolyte effects than just dissociation. As noted earlier, in Chapter 6 we have empirically incorporated the dissociation constant into the solution theory presented in this chapter and investigated whether the multisolute osmotic virial equation with the new combining rules derived here can describe salt solutions [18]. There it was found that the predictions of the extended multisolute osmotic virial equation were accurate for 11 ternary aqueous salt solutions and that the new combining rules had superior performance to those developed previously by our group. In Chapter 6, the data for most single salt–water solutions were fitted well by only quadratic or cubic polynomials [*i.e.*, requiring only  $(k_d)_j$ ,  $\hat{Q}_j^{n,2}$ , and sometimes  $\hat{Q}_j^{n,3}$  for each salt; see section 5.4 for interpretation of  $n$ ].

## 5.4 Discussion

In this section, we only discuss the derived polynomial model written for a single-solute–solvent system and its coefficients. Therefore, the validity of assumption (vi) and the resulting combining rules presented in section 5.3.2 are not required here.

### 5.4.1 Connection to the original single-solute osmotic virial coefficients

The single-solute osmotic virial equation was first derived by McMillan and Mayer [140] from first principles, which expresses the osmolality of a solution in terms of the molar concentration of a solute. Later, Hill [83] obtained the same result in molality and mole fraction units by choosing different sets of independent variables (*i.e.*, different ensembles). Both methods are formally exact and necessarily equivalent through a suitable change of variables (only true if the virial expansions are kept as infinite sums; not true when they are truncated). Here, we show that one can obtain the pure osmotic virial coefficients derived in this work by applying the random-mixing assumption to an exact model.

Let us look at the quadratic and cubic coefficients of a two-component system, since these are the coefficients provided in Hill's original paper. The extension of the argument to higher-order coefficients is straight forward and will be omitted here. For a single-solute solution, the polynomial expression is simply

$$\pi^+ = x_2 + C_2 x_2^2 + C_3 x_2^3 \dots \quad (5-42)$$

and the corresponding second- and third-order coefficients from the work of Hill are

$$C_2 = N \left[ \frac{1}{2} - \exp\left(-\frac{\omega_2}{k_B T}\right) \right] \quad (5-43)$$

and

$$C_3 = 4N^2 \left[ \frac{1}{2} - \exp\left(-\frac{\omega_2}{k_B T}\right) \right]^2 - 2N^2 \left[ \frac{1}{3} - \exp\left(-\frac{\omega_2}{k_B T}\right) + \exp\left(-\frac{\omega_3}{k_B T}\right) \right] \quad (5-44)$$

respectively, where  $N = N_1 + N_2$  is the total number of particles in the system. We use here  $C$ 's (as in the paper of Hill) instead of  $\hat{Q}$ 's since they refer to coefficients derived within different theories. The quantity  $\omega_i$  in Equations (5-43) and (5-44) is defined as the total Gibbs free-energy change for the following process:  $i$  number of systems, each made of  $N - 1$  solvent molecules and 1 solute molecule, being rearranged into 1 system made of  $N - i$  solvent molecules with  $i$  number of solute molecules, plus  $i - 1$  number of pure solvent systems each with  $N$  solvent molecules. Approximating the entropy term that is present in  $\omega_i$  with a random-mixing entropy term, the exact configurational entropy change for this process can be written explicitly, and  $\omega_i$  can be expressed as

$$\omega_i = \omega_i^{\text{nc}} - k_B T \left[ \ln \binom{N}{i} - i \ln \binom{N}{1} \right] \quad (5-45)$$

where  $\omega_i^{\text{nc}}$  is the nonconfigurational part of Gibbs free-energy change, and the second term is due to the configurational entropy change for the process described above. Substituting Equation (5-45) into Equations (5-43) and (5-44), we get

$$C_2 = N \left[ \frac{1}{2} - \left( \frac{1}{2} - \frac{1}{2N} \right) \exp\left(-\frac{\omega_2^{\text{nc}}}{k_B T}\right) \right] \quad (5-46)$$

and

$$\begin{aligned}
C_3 = 4N^2 & \left[ \frac{1}{2} - \left( \frac{1}{2} - \frac{1}{2N} \right) \exp \left( -\frac{\omega_2^{\text{nc}}}{k_B T} \right) \right]^2 \\
& - 2N^2 \left[ \frac{1}{3} - \left( \frac{1}{2} - \frac{1}{2N} \right) \exp \left( -\frac{\omega_2^{\text{nc}}}{k_B T} \right) \right. \\
& \left. + \left( \frac{1}{6} - \frac{1}{2N} + \frac{1}{3N^2} \right) \exp \left( -\frac{\omega_3^{\text{nc}}}{k_B T} \right) \right]
\end{aligned} \tag{5-47}$$

Retaining only the constant and linear terms in the Taylor series expansion for the exponentials, these equations reduce to

$$C_2 = \frac{1}{2} + \frac{1}{Nk_B T} \binom{N}{2} \omega_2^{\text{nc}} \tag{5-48}$$

and

$$C_3 = \frac{1}{3} + \frac{2}{Nk_B T} \binom{N}{3} (\omega_3^{\text{nc}} - 3\omega_2^{\text{nc}}) \tag{5-49}$$

respectively. We can express the  $\omega_i^{\text{nc}}$ 's in terms of the alternative parameters defined in this work,  $w_{1\dots 12\dots 2}$ 's, using their respective definitions. Doing so, with some algebraic manipulation (see Appendix C), we find

$$C_2 = \frac{1}{2} + \frac{1}{Nk_B T} \binom{N}{2} (w_{1\dots 122} - 2w_{1\dots 12}) = \hat{Q}_2^{N,2} \tag{5-50}$$

and

$$C_3 = \frac{1}{3} + \frac{2}{Nk_B T} \binom{N}{3} (w_{1\dots 1222} - 3w_{1\dots 122} + 3w_{1\dots 12}) = \hat{Q}_2^{N,3} \tag{5-51}$$

As indicated, Equations (5-50) and (5-51) are precisely what we can obtain from Equation (5-41) by taking  $n = N$ , which translates to setting  $z_n = 1$  (each particle is shared by a single  $N$ -tuple, which is the entire system). At first, it may seem problematic to set  $n = N_1 + N_2$  because we had to assume that  $n$  is much smaller than both  $N_1$  and  $N_2$  to be able to write Equation (5-11). However, this is allowed due to the different system definitions employed: While we fix both  $N_1$  and  $N_2$  and seek the chemical potentials, Hill fixes the total number of sites,  $N$ , and the chemical potential difference,  $\mu_2 - \mu_1$ , to arrive at his osmotic virial coefficients. In other words, we look at a large but finite closed system that can only exchange heat and volume with a reservoir (a piston–cylinder device), and Hill considers an open system with a fixed number of sites in equilibrium with an infinite reservoir, while effectively treating the system as a single interacting  $N$ -tuple.

### 5.4.2 On the size of $n$

Based on the connection established above, a natural question arises: How big is the error due to the linear approximations of the exponentials in the osmotic virial coefficients of Hill? To answer this, let us consider a macroscopic system corresponding to  $N \rightarrow \infty$  limit in Equations (5-46) and (5-47). Since we expect the osmotic virial coefficients to stay finite at this limit for any physical system far from criticality, we deduce from Equations (5-46) and (5-47) that  $\lim_{N \rightarrow \infty} \omega_2^{nc} = \lim_{N \rightarrow \infty} \omega_3^{nc} = 0$ . This means that the larger the system the more accurate are the linear approximations. That is, with increasing  $n$ , the present treatment becomes asymptotically close to the exact treatment with a random-mixing entropy term, applied to a macroscopic system. This is because, even if one does not assume random mixing when calculating the nonconfigurational Gibbs free energy of the system (like in the exact treatment), the larger the particle groups the more closely their number density will follow the multinomial distribution. In other words, provided that the system's size is much larger than the range of interactions between particles, by choosing a large  $n$  the errors introduced due to Equation (5-11) can be made vanishingly small. This realization is not surprising because the assumption of a single-phase system is the same as the homogeneity of the system on large size scales (compared to the range of interactions of particles). Therefore, when compared to the exact treatment, the only significant approximation in the present model with a large  $n$  is due to the use of the random-mixing entropy term.

Another valuable consequence to consider when  $n$  is large is the potential for relaxation of assumptions (iii) and (iv). Consider, for example, a two-component solution of protein in water, where the sizes of the molecules, and hence, their coordination numbers differ greatly. Naturally, the present approach would not be applicable in the case of a small  $n$  because  $z_n$  would not be constant between the two types of molecules. However, by choosing a large  $n$  such that each  $n$ -tuple occupies a much bigger space than the protein molecule, the discrepancy in  $z_n$  can be made small. Also, note that when  $n = N$ , the formulation is independent of  $z_n$  as demonstrated in section 5.4.1. Therefore, we expect the present model with sufficiently large  $n$  would be a good approximation even for solutions containing particles of different sizes.

In practice, if polynomials are fitted to binary experimental data, the obtained coefficients would represent full interactions as well as nonrandom entropy of mixing, as given in the framework of the exact formulation [e.g., Equations (5-43) and (5-44)], which would

also include empirical corrections due to the truncation of the polynomials. Therefore, no deliberate selection of  $n$  is required in this scenario (assume  $n = N$  if interpreting the coefficients in our framework with a random-mixing entropy term). Notice that the full model contains terms up to  $N$ th degree, however, truncating the polynomial after the quadratic or cubic term typically describes the data well [18,226]. It is important to note that this truncation does not imply that only small particle groups are considered, rather it implies that the higher order terms of the polynomial are numerically negligible.

There might be situations, however, where it is desirable to pick a value of  $n$  that is as small as possible while still capturing the nonideal behavior of the system accurately (for example, due to computational cost when calculating the virial coefficients from molecular dynamics simulations). This is the same as finding the smallest system from which the osmotic virial coefficients of the macroscopic system can be inferred to within a desired accuracy. The decision of picking a suitable  $n$  should be guided by the nature and range of the interactions in a given system while considering factors such as the desired accuracy and cost of computation. In general, a solvent with salts would require a larger  $n$  compared to the same solvent with nonionic solutes because of the presence of long-range forces in the former.

## 5.5 Conclusion

In this chapter, we considered a general multicomponent solution model that assumes random mixing of the components at constant pressure and temperature, but accounts for complex interactions in arbitrarily large particle groups. Based on the model, the chemical potential of the mixture components could be expressed as a multivariate polynomial with mole fractions of the solutes as variables. It was demonstrated that, for a macroscopic system, the present model with  $n = N$  can be alternatively derived from the formally exact approach of Hill if the random-mixing entropy term is used. This was done to highlight the equivalency of two seemingly different theoretical approaches. It was also concluded that, if the model is implemented with large particle groups, it does not require some of the restrictive assumptions needed when considering small particle groups.

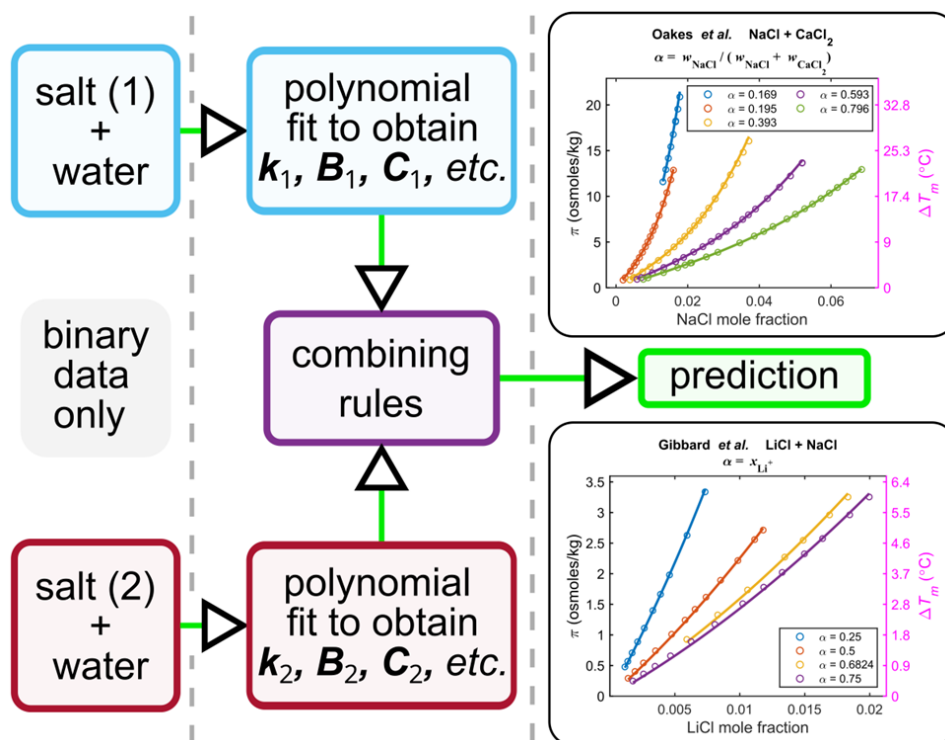
Furthermore, using the developed equations, we provided a theoretical basis for multisolute osmotic virial equation combining rules. That is, assuming negligible solute–solute interactions, the mixed-term coefficients of the polynomial could be written as the arithmetic

average of suitable pure-term coefficients. These rules are practically useful for estimating the chemical potential of a solvent in the presence of multiple solutes when no multicomponent solution data are available. The model with the combining rules, in some sense, provides the best estimate of the solvent chemical potential within the context of the present theory when no multicomponent data are available. Of course, a better estimate would be possible if one has information about the interaction exchange energies of the solutes with one another and/or any multicomponent solution data. It is important to note that the noninteracting solutes assumption [*i.e.*, assumption (vi)] and the use of the random-mixing entropy term were sufficient to arrive at the proposed combining rules, but we do not have a proof of their necessity. Comparison of the predictions of the combining-rules approach to experimental data from different kinds of multicomponent mixtures (*e.g.*, electrolyte solutions, polymer solutions, hydrocarbon solutions, their combinations, *etc.*) might shed light on the extent of the applicability of the combining rules and help researchers decide whether it is worth looking for their generalizations.



## Chapter 6

# Predicting Freezing Points of Ternary Salt Solutions with the Multisolute Osmotic Virial Equation<sup>1</sup>



### Chapter summary

Previously, the multisolute osmotic virial equation with the combining rules of Elliott *et al.* has been shown to make accurate predictions for multisolute solutions with only single-solute osmotic virial coefficients as inputs. The original combining rules take the form of an arithmetic average for the second-order mixed coefficients and a geometric average for the third-order mixed coefficients. In Chapter 5, we derived generalized combining rules from a

<sup>1</sup> Reproduced (including Appendix D), with minor changes, with permission from H. Binyaminov, H. Sun, and J. A. W. Elliott. *Predicting Freezing Points of Ternary Salt Solutions with the Multisolute Osmotic Virial Equation*, *J. Chem. Phys.* **159**, 244502 (2023). <https://doi.org/10.1063/5.0169047> © 2023 American Institute of Physics.

first principles solution theory, where all mixed coefficients could be expressed as arithmetic averages of suitable binary coefficients. In this chapter, we empirically extended the new model to account for electrolyte effects including solute dissociation and demonstrate its usefulness for calculating the properties of multielectrolyte solutions. First, the osmotic virial coefficients of 31 commonsalts in water were tabulated based on the available freezing point depression (FPD) data. This was achieved by polynomial fitting, where the degree of the polynomial was determined using a special criterion that accounts for the confidence intervals of the coefficients. Then, the multisolute model was used to predict the FPD of 11 ternary electrolyte solutions. Furthermore, models with the new combining rules and the original combining rules of Elliott *et al.* were compared using both mole fraction and molality as concentration units. We find that the mole-fraction-based model with the new combining rules performs the best, and that the results agree well with independent experimental measurements with all-system root-mean-square error of 0.24 osmoles/kg (0.45 °C) and close to zero mean bias for the entire dataset (371 data points).

## 6.1 Introduction

Thermodynamic properties of aqueous salt solutions play a crucial role in many areas of natural, biological, and industrial processes. For example, the characteristics of freezing of the most abundant electrolyte solution on the planet—seawater—are controlled by the salt concentration [135]. Because the concentration and types of the salts in seawater vary, one of the crucial aspects of an accurate ocean model is the reliability of the thermodynamic method used to determine the phase behavior of multicomponent aqueous solutions [99,135]. In another example, when water vapor condenses on the cloud condensation nuclei in the atmosphere, it dissolves some of the salts from these particles and forms a droplet of an aqueous solution. The path this droplet takes (*e.g.*, whether it evaporates or grows) in the later stages of cloud development is greatly impacted by the types of solutes and their concentrations [109,165]. Ultimately, the precipitative properties of a cloud are often determined by the microphysical processes that involve aqueous multisolute salt solutions [165]. Furthermore, as aqueous energy storage devices (*e.g.*, aqueous Li-ion, Sn-ion, Na-ion batteries) evolve and become more practical for commercial use [9,32,91,92,142,152, 207,208,221], there is a growing need for a simple and reliable multielectrolyte solution model.

One of the main concerns about aqueous batteries is their operability at extreme conditions, such as at temperatures below  $-20\text{ }^{\circ}\text{C}$ .

There exist many solution theories for nonideal, concentrated multisolute solutions, in-depth discussion of some of which can be found in references [161] and [44]. Although maybe accurate, many of these approaches rely on fitting to multisolute solution data, while some require a lot of input model parameters. These characteristics make these models not suitable for general modeling purposes for many engineering applications because of the possibility of many solutes, their different combinations, and a wide range of concentrations. Furthermore, accurate solution theories are usually complicated by nature, hence, their implementation as part of engineering design can be challenging. The desirable qualities of any predictive model are that it should require a minimum number of fitting parameters, be mathematically simple and computationally cheap, and not rely on multisolute data.

Over the past fifteen years, a form of the osmotic virial equation for multisolute solutions (multisolute osmotic virial equation or MSOVE) has been developed by Elliott *et al.* (the Elliott *et al.* MSOVE or E-MSOVE) that requires only binary solution data (*i.e.*, each solute with the solvent) to predict the chemical potential of a solution with a mixture of solutes. [42,163,223,226] The original single-solute osmotic virial equation is a polynomial equation derived from first principles that expresses osmolality of a single-solute solution as a function of the concentration of the solute [83,84,140]. Later, Elliott *et al.* [42] proposed combining rules for osmotic virial coefficients in the regular solution theory framework, which enabled osmotic-virial-equation predictions for multisolute solutions without the need for fitting to multisolute data. By comparing predictions with experimental data, our group has previously demonstrated the accuracy of the molality-based form of the E-MSOVE for solutions of interest in cryobiology, including aqueous mixtures of cryoprotectants and aqueous mixtures of proteins [225,226]. It was rigorously shown that the molality-based form of the E-MSOVE can be applied to a “grouped solute” representing all solutes when the properties of individual solutes cannot be enumerated [223], which allows the approach to be applied to complicated intracellular solutions [55,162,172,224]. Additionally, a solute chemical potential equation that is consistent with the molality-based E-MSOVE was derived [47,219,223]. Furthermore, Prickett *et al.* [163] extended the E-MSOVE to solutions containing electrolytes by introducing an additional single-solute fitting parameter to capture

dissociation and other electrolyte effects and showed that this equation could make predictions for aqueous solutions containing NaCl plus another nonelectrolyte solute as accurately as if the NaCl contributions had been calculated by the Pitzer–Debye–Hückel model—a more sophisticated electrolyte theory with more fitting parameters. The E-MSOVE was shown to make accurate predictions for many aqueous solutions containing NaCl and one or two other nonelectrolyte solutes [225,226]. Liu *et al.* [124] used the mole-fraction-based E-MOSVE to make predictions of the freezing points of multielectrolyte solutions of interest to zinc–air batteries, but without comparison to experimental data. While the previous work suggests that multielectrolyte solution osmolalities could be predicted with the E-MSOVE, this proposition has not been tested.

In Chapter 5, we further explored the theoretical aspects of the MSOVE and developed generalized combining rules for coefficients of arbitrary order in a specific solution theory framework. All newly derived combining rules take the form of an arithmetic-average of suitable pure-term coefficients, which contrasts with the geometric-average combining rule used for the cubic terms in the E-MSOVE implementation. In the previous applications of the E-MSOVE (mainly in cryobiology), most solutions were described sufficiently well by only the first- and second-order terms, and predictions using the geometric-average combining rule for the cubic-order terms were accurate enough for the application. Here, we find that some ternary salt solutions require a third-order combining rule for accurate predictions, and that there are enough accurate multielectrolyte solution data to compare different combining rules quantitatively.

The main goal of this chapter is to demonstrate the viability of the MSOVE with new combining rules (the new MSOVE) for predicting thermodynamic properties of multicomponent salt solutions. The chapter is organized as follows: We start by introducing the necessary formalism, describing the models, and detailing the fitting procedure. Then, we tabulate the mole-fraction- and molality-based osmotic virial coefficients of 31 aqueous binary mixtures of common salts by fitting to binary FPD data taken from the literature. Using the obtained mole-fraction-based binary coefficients in the new MSOVE, we make predictions for 11 ternary combinations (*i.e.*, two salts plus water) of the listed salts for which experimental data are available in the literature for comparison. We conclude by comparing the prediction

accuracy of the E-MSOVE and the new MSOVE in molality and mole fraction concentration units.

## 6.2 Methods

### 6.2.1 Virial expansion and the original combining rules

Osmolality is a measure of change in chemical potential of the solvent in the presence of solutes, mathematically defined as [42]

$$\pi = -\frac{\mu_1 - \mu_1^\circ}{\bar{R}TM_1} \quad (6-1)$$

where  $\pi$  is the osmolality (with units of osmoles/kg),  $\mu_1$  is the chemical potential of the solvent in solution (in this chapter, the only solvent is water),  $\mu_1^\circ$  is the chemical potential of the pure solvent,  $\bar{R}$  is the universal gas constant,  $T$  is absolute temperature, and  $M_1$  is the molar mass of the solvent. Osmolality can be related to other thermodynamic properties of the solution, such as its FPD and osmotic pressure. Needed for the purposes of the present study, the following expression establishes the relationship between the osmolality and the FPD of a solution [226]:

$$\pi = \frac{T_m^\circ - T_m}{\bar{R}T_m \left( \frac{M_1}{\Delta S_f^\circ} \right)} = \frac{\Delta T_m \Delta S_f^\circ}{\bar{R}M_1(T_m^\circ - \Delta T_m)} \quad (6-2)$$

where  $\Delta T_m$  represents the FPD with  $T_m$  and  $T_m^\circ$  being the freezing point of the solution, and the freezing point of the pure solvent, respectively, and  $\Delta S_f^\circ$  is the standard molar entropy change of fusion of the solvent at the freezing point of the pure solvent. We emphasize that, since the reference state in Equation (6-2) is pure water, Equation (6-2) should only be used for solutions where the concentration of the solute is below the eutectic composition.

The single-solute osmotic virial equation is a polynomial equation for the osmolality of a binary solution expressed in terms of the concentration of the solute [42]. Originally developed in terms of molarity (moles of solute per liter of solution) by McMillan and Mayer [140] and later modified to use molality (moles of solute per kilogram of solvent) and mole fraction by Hill [83,84], this polynomial expansion can be written as a function in different concentration units with underlying self-consistent solution theories in different sets of independent variables. For a single solute, one form of this expansion in terms of the

molality of the solute is given below, which follows the solution theory of Landau and Lifshitz [114]:

$$\pi = m_i + B_i m_i^2 + C_i m_i^3 + \dots \quad (6-3)$$

where  $B_i$  and  $C_i$  are the second and the third osmotic virial coefficients of solute  $i$ , respectively (conventionally,  $i$  starts from  $i = 2$ , and subscript “1” is used to refer to the solvent). Physically,  $B_i$  and  $C_i$  correspond to interactions between two and three solute molecules in the solution, respectively.  $m_i$  represents the molality of solute  $i$ . This expression was phenomenologically extended by Prickett *et al.* [163] to electrolyte solutions by modifying the osmolality equation as

$$\pi = k_i m_i + B_i (k_i m_i)^2 + C_i (k_i m_i)^3 + \dots \quad (6-4)$$

where  $k_i$  is a fitting parameter, conventionally referred to as the dissociation constant of electrolyte  $i$ , although it empirically accounts for various electrolyte effects (*e.g.*, ionic dissociation, charge screening, *etc.*) and might not indicate the actual degree of dissociation of the solute when obtained from fitting to data [45,163]. For nonelectrolytes,  $k_i = 1$  can be used, recovering the original form of the polynomial. Often, the polynomial can be truncated after the second-order term, or sometimes after the third-order term, while still accurately describing the behavior of the solution. For example, Equation (6-4) truncated to the second-order term, with only two fitting parameters ( $k_i$  and  $B_i$ ), can describe the NaCl + H<sub>2</sub>O data as accurately as the Pitzer–Debye–Hückel model, which is a sophisticated model requiring six parameters [163].

Suggested by Elliott *et al.* [42] and Prickett *et al.* [163], combining rules for the osmotic virial coefficients can be used to predict the osmolality of a solution with more than one solute. Truncated to the third-order terms, for  $r - 1$  solutes (together with the solvent there are  $r$  components), the molality-based E-MSOVE has the following general form [42]:

$$\begin{aligned} \pi = & \sum_{i=2}^r k_i m_i + \sum_{i=2}^r \sum_{j=2}^r B_{ij} k_i m_i k_j m_j \\ & + \sum_{i=2}^r \sum_{j=2}^r \sum_{k=2}^r C_{ijk} k_i m_i k_j m_j k_k m_k \end{aligned} \quad (6-5)$$

for which the following combining rules for the mixed osmotic virial coefficients were proposed [42]:

$$B_{ij} = \frac{B_i + B_j}{2} \quad (6-6)$$

for the second-order term, which accounts for interactions between two solutes  $i$  and  $j$ , and [42]

$$C_{ijk} = (C_i C_j C_k)^{1/3} \quad (6-7)$$

for the third-order term, which accounts for interactions among the three solutes  $i$ ,  $j$ , and  $k$ . The importance of Equation (6-5) (together with the combining rules) is that it can be used to predict osmolality of a multisolute solution with parameters obtained from the fits to binary solution data only (*i.e.*, two-component solutions of each solute with the solvent). However, care should be taken when extrapolating Equation (6-5) beyond the regression range (*i.e.*, the data range from which the pure coefficients were obtained) because the combining rules given by Equation (6-6) and Equation (6-7) may not account for various effects, such as the ionic strength dependence in the case of electrolyte solutions [45,163].

### 6.2.2 New combining rules for the third- and higher-order coefficients

In Chapter 5, we theoretically explored a generalized multicomponent solution model and obtained combining rules for any-order coefficients of the mole-fraction-based MSOVE in the form of arithmetic-averages of suitable pure coefficients. That is, with the mole-fraction-based formulation, we obtained an equivalent of Equation (6-6), but the equivalent of the third-order combining rule in Equation (6-7) is different, in that, it is also an arithmetic-average of suitable third-order pure coefficients. The new model allows for arbitrary-order polynomials to be combined in a similar fashion, unlike the original combining rules, which are limited to quadratic and cubic polynomials.

In the present work, we find that every binary electrolyte mixture is described well by at most a cubic polynomial. Therefore, we only need the second- and third-order mixed coefficients from the new model and they take the following forms:

$$B_{ij}^+ = \frac{B_i^+ + B_j^+}{2} \quad (6-8)$$

and

$$C_{ijk}^+ = \frac{C_i^+ + C_j^+ + C_k^+}{3} \quad (6-9)$$

respectively. Since the new model was derived with mole fractions of the solutes as variables, we use the superscript “+” to distinguish the mole-fraction-based coefficients from the

molality-based coefficients. The corresponding mole-fraction-based MSOVE, truncated to the third-order terms, takes the following form:

$$\begin{aligned} \pi^+ = & \sum_{i=2}^r k_i^+ x_i + \sum_{i=2}^r \sum_{j=2}^r B_{ij}^+ k_i^+ x_i k_j^+ x_j \\ & + \sum_{i=2}^r \sum_{j=2}^r \sum_{k=2}^r C_{ijk}^+ k_i^+ x_i k_j^+ x_j k_k^+ x_k \end{aligned} \quad (6-10)$$

where  $x_i$  is the mole fraction of species  $i$  in the solution, and  $\pi^+ = \pi M_1$  is referred to as the osmole fraction of the solvent [45,226]. Note that, similar to the modification presented in reference [163] and used in Equation (6-5), we introduce the mole-fraction-based dissociation constants,  $k_i^+$ 's, empirically in Equation (6-10) to account for the dissociation of the salts. In our theoretical work (Chapter 5), we only considered nondissociating solutes (*i.e.*,  $k_i^+ = 1$  for all  $i$ ). We will not attempt a justification here, hence, like  $k_i$ 's in Equation (6-5),  $k_i^+$ 's should be viewed as empirical fitting parameters only.

Equation (6-10) has been previously used [226] as the mole-fraction-based counterpart of Equation (6-5), however, not with the arithmetic-average combining rule for  $C_{ijk}^+$  [*i.e.*, Equation (6-9)]. Notice that the two models truncated to the third-order terms and written for the same concentration units only differ in the combining rule for the third-order mixed coefficients.

For most calculations in this chapter, conversion from molality to mole fraction or *vice versa* is needed. For component  $i$  in an aqueous solution, the relationship between the mole fraction and the molality is given as

$$x_i = \frac{M_1 m_i}{1 + M_1 \sum_{i=2}^r m_i} \quad (6-11)$$

The numerical values of the constants used for calculations in this chapter are given in Appendix D.

Throughout the text, we present the results in osmolality units and refer to osmolalities obtained from the FPD data *via* Equation (6-2) as “experimental data” for brevity. Alternatively, we could invert Equation (6-2) and use it to convert osmolality (osmole fraction) calculated from Equation (6-5) [Equation (6-10)] to FPD and compare the predictions directly



to the true experimental FPD data. Clearly, both methods are equivalent for the purposes of evaluating the models.

### 6.2.3 Determination of the osmotic virial coefficients

As detailed by our group's previous work [226], (multiple linear) regression through the origin (RTO) is implemented on the binary data in MATLAB (v. 2023a, Natick, MA, USA) to obtain the binary osmotic virial coefficients. The method is essentially polynomial fitting of a chosen degree with a matrix method, where the constant term of the polynomial is set to zero. The general form of the matrix regression model is expressed as

$$\mathbf{y} = \mathbf{F}\boldsymbol{\beta} + \boldsymbol{\epsilon} \quad (6-12)$$

where  $\mathbf{y}$  is the vector of calculated osmolalities (or osmole fractions),  $\mathbf{F}$  is the matrix of regressors, and  $\boldsymbol{\epsilon}$  is the vector of model prediction errors.  $\boldsymbol{\beta}$  is the vector of regression coefficients and it is calculated as

$$\boldsymbol{\beta} = (\mathbf{F}^T\mathbf{F})^{-1}\mathbf{F}^T\mathbf{y} \quad (6-13)$$

The estimated model variance is calculated as

$$\sigma^2 = \frac{\sum_{i=1}^n (y_i - \bar{y}_i)^2}{n - p} \quad (6-14)$$

where  $y_i$  represents the  $i$ th data point,  $\bar{y}_i$  is the model prediction at that data point,  $n$  is the number of data points used in the fit, and  $p$  is the degree of the polynomial.

With the covariance matrix being  $\mathbf{S} = (\mathbf{F}^T\mathbf{F})^{-1}$ , the 95% confidence intervals (CI) are calculated as:

$$\beta_i \pm t_{\frac{\alpha}{2}, n-p} \sqrt{\sigma^2 S_{ii}} \quad (6-15)$$

where  $\beta_i$  is the  $i$ th element of  $\boldsymbol{\beta}$ , and  $t_{\frac{\alpha}{2}, n-p}$  is the  $\alpha$ th percentile of Student's  $t$ -distribution for  $n - p$  degrees of freedom.  $S_{ii}$  is the  $i$ th diagonal element of the covariance matrix.

As the metrics to determine the degree of the polynomial fit, we use the RTO-adjusted R-squared value, defined as [226]

$$R_{\text{RTO,adj}}^2 = 1 - \frac{\sum_{i=1}^n (y_i - \bar{y}_i)^2 / (n - p)}{\sum_{i=1}^n (y_i^2 / n)} \quad (6-16)$$

combined with the relative width of the 95% CIs of the coefficients as described directly below.

For each given dataset, the  $R_{\text{RTO,adj}}^2$  and the 95% CIs of the coefficients are linearly combined into a single criterion. The combined criterion is deemed necessary because using only the value of  $R_{\text{RTO,adj}}^2$  to justify the degree of the polynomial may result in large CIs for some datasets (*i.e.*, overfitting). On the other hand, only using the CIs of the coefficients (*i.e.*, looking for the narrowest CIs) to determine the degree of polynomial is not desirable (*i.e.*, underfitting) because sometimes a much better fit (in terms of  $R_{\text{RTO,adj}}^2$ ) can be obtained while still having reasonable CIs. The proposed formula for the combined criterion is expressed as

$$\zeta = 100\eta R_{\text{RTO,adj}}^2 + (1 - \eta) \frac{\bar{y}_{\text{max}}}{\bar{y}_{95^+, \text{max}}} \quad (6-17)$$

where  $\bar{y}_{\text{max}}$  denotes the model prediction at the highest experimental concentration,  $\bar{y}_{95^+, \text{max}}$  denotes the model prediction at the highest experimental concentration corresponding to the upper bound of the 95% CIs on the coefficients. As a continuous function of concentration,  $\bar{y}_{95^+}$  is constructed by taking all coefficients at the upper bounds of their 95% CIs. Notice that this method is different than the typical way of calculating the 95% CI of a fit in statistical analysis, which generally improves (*i.e.*, gets more confident) with increasing the degree of the polynomial, and therefore, is not suitable for our purposes. In Equation (6-17),  $\eta$  is an adjustable parameter between zero and one that determines the balance between a purely confidence-based fit ( $\eta = 0$ ) and a purely  $R_{\text{RTO,adj}}^2$ -based fit ( $\eta = 1$ ). When performing the fits, for each given binary mixture dataset, a series of polynomial models are generated up to  $p = 5$  at fixed  $\eta$  out of which the one with the highest  $\zeta$  value is picked as the best fit.

The first term on the right-hand side of Equation (6-17) is multiplied by one hundred to assign appropriate weights to each term. For example, the changes of  $\Delta R_{\text{RTO,adj}}^2 = 0.001$  and  $\Delta \left( \frac{\bar{y}_{\text{max}}}{\bar{y}_{95^+, \text{max}}} \right) = 0.1$  have the same weights for the value of  $\eta = 0.5$ . In other words,  $\zeta$  is made one hundred times more sensitive to a change in  $R_{\text{RTO,adj}}^2$  compared to the change in the relative width of the CI,  $\frac{\bar{y}_{\text{max}}}{\bar{y}_{95^+, \text{max}}}$ . This is because, without scaling,  $\Delta R_{\text{RTO,adj}}^2$  is not particularly sensitive to the goodness of the fit, often changing by less than 1% when increasing the degree of the polynomial. Clearly, other choices can be made regarding the functional form of the combined criterion. The idea is to reward for goodness of the fit (in terms of  $R_{\text{RTO,adj}}^2$ ) while penalizing for large CIs of the coefficients.

## 6.3 Results

### 6.3.1 Tabulation of osmotic virial coefficients

Most of the binary FPD data were collected from the CRC Handbook of Chemistry and Physics [230] (CRC or CRC handbook hereafter). The exceptions are: the binary data for  $\text{ZnCl}_2$  and  $\text{ZnBr}_2$  (obtained from Haghghi *et al.* [74]) and  $\text{MgCl}_2$  (obtained from Gibbard and Gossmann [62]) because the CRC does not list these salts. Additionally, we also use the  $\text{CaCl}_2$  binary data of Oakes *et al.* [154] instead of the CRC data because the Oakes *et al.* [154] dataset has significantly more data points (55 vs. 27) and the fit confidence is significantly higher (when comparing the same-degree fits). The data in the CRC [230] are given as FPD vs. molality. The data in Gibbard and Gossmann [62] are given as FPD vs. equivalent concentration, and the data in Haghghi *et al.* [74] are given as FPD vs. mass percent of the solutes. All datasets from Gibbard and Gossmann [62] and Haghghi *et al.* [74] were converted to molality (then to mole fraction, where needed) using suitable equations. These unit-conversion equations are detailed in Appendix D.

After iteratively adjusting  $\eta$ , we found that  $\eta = 0.3$  gives a good balance of accuracy and relatively narrow CIs for coefficients of all binary-mixture polynomials needed in this study. When we made the mole-fraction-based fitting significantly more sensitive to  $R_{\text{RTO,adj}}^2$  by increasing  $\eta$  from 0.3 up to 0.6, it did not affect the degree of fits of most salts except for  $\text{ZnBr}_2$ ,  $\text{ZnCl}_2$ ,  $\text{Na}_2\text{S}_2\text{O}_3$ ,  $\text{ZnSO}_4$ , and  $\text{MgSO}_4$ . With  $\eta = 0.6$ : (i) for  $\text{ZnCl}_2$ , the fit confidence was unacceptably low due to the lack of number of experimental data points; (ii) for  $\text{MgSO}_4$  and  $\text{ZnBr}_2$ , the fit confidences were considerably lower, although they may be usable in some settings; (iii) for  $\text{Na}_2\text{S}_2\text{O}_3$  and  $\text{ZnSO}_4$ , the fit confidences were still high, although the data were sufficiently well described by the lower-degree fits as well. Since none of these salts are used in this study to make predictions, the value of  $\eta$  in a reasonable range does not affect the prediction results, and we decided to pick a more conservative value of  $\eta = 0.3$ . The only salt for which this value of  $\eta$  results in the fitted polynomial having a different degree for the molality-based fit is  $\text{ZnBr}_2$ , which changes from being a linear function in the mole-fraction-based case to a quadratic function in the molality-based case.

The resulting mole-fraction-based fit parameters are listed in Table 6-1, and the molality-based fit parameters are listed in Table 6-2, with each table containing additional

columns for the number of data points used for the fitting, the data limit for each dataset, the value of  $R_{\text{RTO,adj}}^2$ , and the degree of the polynomial fit. For the method of estimation of uncertainties in the coefficients and the graphical representations of the fits, see Appendix D.

Table 6-1. Mole-fraction-based binary fit coefficients and related data. The coefficients were obtained by fitting to data after converting molality to mole fraction and FPD to osmole fraction. The data used for fitting are mainly from the CRC handbook [230] except where indicated by a superscript letter, in which case the data are obtained from: (a) Oakes *et al.* [154]; (b) Gibbard and Gossmann [62]; (c) Haghghi *et al.* [74].

Salt	$k^+ \pm 95\% \text{ CI}$	$B^+ \pm 95\% \text{ CI}$	$C^+ \pm 95\% \text{ CI}$	$n$	Data limit (mole fraction)	$R_{\text{RTO,adj}}^2$	$p$
CaCl <sub>2</sub> <sup>a</sup>	$3.0464 \pm 0.1607$	$-0.8134 \pm 0.7336$	$51.5453 \pm 8.5203$	55	0.0664	1.0000	3
FeCl <sub>3</sub>	$3.3444 \pm 0.4780$	$1.5734 \pm 2.9214$	$79.9373 \pm 36.7256$	19	0.0497	0.9997	3
K <sub>2</sub> CO <sub>3</sub>	$2.3384 \pm 0.0513$	$0.2501 \pm 0.3986$	$35.2213 \pm 2.8489$	21	0.08	1.0000	3
NaCl	$1.8348 \pm 0.0048$	$0.2853 \pm 0.0533$	$14.8930 \pm 0.2823$	32	0.0843	1.0000	3
MgCl <sub>2</sub> <sup>b</sup>	$2.5265 \pm 0.0389$	$5.2909 \pm 0.5892$	$84.8666 \pm 6.1064$	30	0.0352	1.0000	3
LiCl	$1.5655 \pm 0.0452$	$11.5691 \pm 0.7648$	—	13	0.0647	0.9999	2
KI	$1.7730 \pm 0.0078$	$1.5885 \pm 0.0495$	—	25	0.0675	1.0000	2
KBr	$1.7547 \pm 0.0077$	$1.0952 \pm 0.0515$	—	27	0.0665	1.0000	2
ZnBr <sub>2</sub> <sup>c</sup>	$0.7874 \pm 0.0886$	$3.6988 \pm 1.1404$	—	5	0.2106	0.9998	2
SrCl <sub>2</sub>	$2.1184 \pm 0.0633$	$14.6683 \pm 1.0209$	—	18	0.0346	0.9999	2
NaNO <sub>3</sub>	$1.6950 \pm 0.0220$	$-0.9503 \pm 0.1334$	—	17	0.0761	0.9999	2
NH <sub>4</sub> Cl	$1.7336 \pm 0.0146$	$1.6858 \pm 0.1298$	—	14	0.0479	1.0000	2
ZnCl <sub>2</sub> <sup>c</sup>	$1.4260 \pm 0.2031$	—	—	4	0.1213	0.9920	1
NaBr	$1.8654 \pm 0.0085$	$-0.0311 \pm 0.2142$	$30.8505 \pm 2.4431$	18	0.0346	1.0000	3
CsCl	$1.7036 \pm 0.0067$	—	—	30	0.0261	0.9999	1
KCl	$1.8176 \pm 0.0063$	—	—	14	0.0348	1.0000	1
Na <sub>2</sub> S <sub>2</sub> O <sub>3</sub>	$1.9556 \pm 0.0368$	—	—	16	0.0277	0.9988	1
MnSO <sub>4</sub>	$0.9304 \pm 0.0468$	$13.3605 \pm 2.7310$	—	20	0.0290	0.9995	2
(NH <sub>4</sub> ) <sub>2</sub> SO <sub>4</sub>	$2.0757 \pm 0.0492$	$-2.4553 \pm 0.5976$	—	14	0.0253	0.9998	2
BaCl <sub>2</sub>	$2.3985 \pm 0.0378$	$4.7370 \pm 0.5468$	—	14	0.0162	0.9999	2
MgSO <sub>4</sub>	$0.9363 \pm 0.0801$	$13.2531 \pm 4.8420$	—	14	0.0277	0.9987	2
NaC <sub>2</sub> H <sub>3</sub> O <sub>2</sub>	$1.8381 \pm 0.0142$	$3.8493 \pm 0.2510$	—	10	0.0213	1.0000	2
AgNO <sub>3</sub>	$1.7860 \pm 0.0115$	$-5.9317 \pm 0.2486$	—	14	0.0198	1.0000	2
ZnSO <sub>4</sub>	$1.0390 \pm 0.0168$	—	—	17	0.0208	0.9990	1
KNO <sub>3</sub>	$1.7459 \pm 0.0241$	$-6.1918 \pm 0.5320$	—	11	0.0194	1.0000	2
CuSO <sub>4</sub>	$0.9377 \pm 0.0111$	—	—	15	0.0180	0.9995	1
Na <sub>2</sub> CO <sub>3</sub>	$1.9626 \pm 0.0666$	—	—	7	0.0107	0.9987	1

Na <sub>2</sub> SO <sub>4</sub>	2.4642 ± 0.0627	-11.7675 ± 1.6586	—	7	0.0080	0.9999	2
K <sub>2</sub> SO <sub>4</sub>	2.4229 ± 0.0579	-10.3976 ± 2.2870	—	9	0.0054	0.9999	2
Na <sub>3</sub> PO <sub>4</sub>	3.5327 ± 0.1045	-22.6001 ± 3.7881	—	5	0.0028	1.0000	2
KMnO <sub>4</sub>	1.8128 ± 0.0327	—	—	4	0.0023	0.9999	1

Table 6-2. Molality-based binary fit coefficients and related data. The coefficients were obtained by fitting to data after converting all concentration units to molality and FPD to osmolality. The data used for fitting are mainly from the CRC handbook [230] except where indicated by a superscript letter, in which case the data are obtained from: (a) Oakes *et al.* [154]; (b) Gibbard and Gossmann [62]; (c) Haghghi *et al.* [74].

Salt	$k \pm 95\% \text{ CI}$	$B \pm 95\% \text{ CI}$ (kg/osmoles)	$C \pm 95\% \text{ CI}$ (kg <sup>2</sup> /osmoles <sup>2</sup> )	$n$	Data limit (molality)	$R_{\text{RTO,adj}}^2$	$p$
CaCl <sub>2</sub> <sup>a</sup>	2.8116 ± 0.1172	0.0209 ± 0.0107	0.0142 ± 0.0019	55	3.9465	1.0000	3
FeCl <sub>3</sub>	3.2165 ± 0.4169	0.0568 ± 0.0490	0.0218 ± 0.0093	19	2.9010	0.9997	3
K <sub>2</sub> CO <sub>3</sub>	2.2362 ± 0.0718	0.0236 ± 0.0101	0.0079 ± 0.0010	21	4.8240	1.0000	3
NaCl	1.8092 ± 0.0047	0.0046 ± 0.0009	0.0030 ± 0.0001	32	5.111	1.0000	3
MgCl <sub>2</sub> <sup>b</sup>	2.5045 ± 0.0354	0.1021 ± 0.0096	0.0220 ± 0.0016	30	2.0225	1.0000	3
LiCl	1.6571 ± 0.0265	0.1454 ± 0.0057	—	13	3.8400	1.0000	2
KI	1.7861 ± 0.0059	0.0143 ± 0.0006	—	25	4.0160	1.0000	2
KBr	1.7620 ± 0.0061	0.0071 ± 0.0007	—	27	3.9540	1.0000	2
ZnBr <sub>2</sub> <sup>c</sup>	0.9796 ± 0.0593	—	—	5	14.8081	0.9976	1
SrCl <sub>2</sub>	2.1730 ± 0.0472	0.2214 ± 0.0116	—	18	1.9920	0.9999	2
NaNO <sub>3</sub>	1.6793 ± 0.0244	-0.0238 ± 0.0026	—	17	4.5750	0.9999	2
NH <sub>4</sub> Cl	1.7410 ± 0.0119	0.0167 ± 0.0018	—	14	2.7930	1.0000	2
ZnCl <sub>2</sub> <sup>c</sup>	1.2791 ± 0.1206	—	—	4	7.6619	0.9965	1
NaBr	1.8610 ± 0.0079	-0.0064 ± 0.0035	0.0083 ± 0.0007	18	1.9910	1.0000	3
CsCl	1.6714 ± 0.01	—	—	30	1.4850	0.9997	1
KCl	1.7685 ± 0.0042	—	—	14	2.0040	1.0000	1
Na <sub>2</sub> S <sub>2</sub> O <sub>3</sub>	1.9150 ± 0.0421	—	—	16	1.5810	0.9983	1
MnSO <sub>4</sub>	0.9367 ± 0.0439	0.2019 ± 0.0430	—	20	1.6560	0.9995	2
(NH <sub>4</sub> ) <sub>2</sub> SO <sub>4</sub>	2.0690 ± 0.0496	-0.0498 ± 0.0107	—	14	1.4410	0.9998	2
BaCl <sub>2</sub>	2.4036 ± 0.0367	0.0740 ± 0.0093	—	14	0.9150	0.9999	2
MgSO <sub>4</sub>	0.9415 ± 0.0762	0.2019 ± 0.0777	—	14	1.5820	0.9988	2
NaC <sub>2</sub> H <sub>3</sub> O <sub>2</sub>	1.8427 ± 0.0130	0.0556 ± 0.0040	—	10	1.2060	1.0000	2
AgNO <sub>3</sub>	1.7798 ± 0.0125	-0.1118 ± 0.0048	—	14	1.1210	1.0000	2
ZnSO <sub>4</sub>	1.0225 ± 0.0159	—	—	17	1.1800	0.9991	1
KNO <sub>3</sub>	1.7392 ± 0.0256	-0.1165 ± 0.0101	—	11	1.0990	1.0000	2
CuSO <sub>4</sub>	0.9246 ± 0.0117	—	—	15	1.0200	0.9995	1

Na <sub>2</sub> CO <sub>3</sub>	1.9455 ± 0.0694	—	—	7	0.6020	0.9985	1
Na <sub>2</sub> SO <sub>4</sub>	2.4600 ± 0.0632	-0.2152 ± 0.0301	—	7	0.4490	0.9999	2
K <sub>2</sub> SO <sub>4</sub>	2.4210 ± 0.0581	-0.1920 ± 0.0412	—	9	0.3020	0.9999	2
Na <sub>3</sub> PO <sub>4</sub>	3.5306 ± 0.1027	-0.4095 ± 0.0670	—	5	0.1560	1.0000	2
KMnO <sub>4</sub>	1.8092 ± 0.0335	—	—	4	0.1280	0.9999	1

With  $\eta = 0.3$ , it is apparent that aqueous solutions of most salts can be accurately modeled with only a linear and a quadratic term with only six binaries requiring a cubic term. Naturally, in all cases, the degree and/or the confidence of the fits can be improved by including more high-quality experimental data points. Additionally, since the fitted polynomials are forced to pass through the origin, they have varying sensitivity to the accuracy of experimental data at different concentrations. Therefore, it is important to have more high-quality data points covering the entire concentration range to obtain smaller CIs.

When it comes to the physical meaning of the coefficients, if we assume that the empirical extension due to the electrolyte effects is correct in its functional form (*i.e.*, the modification by a multiplicative constant from  $m_i$  to  $k_i m_i$  or from  $x_i$  to  $k_i^+ x_i$ ), the  $B_i$ 's and  $C_i$ 's (or the  $B_i^+$ 's and  $C_i^+$ 's) can be interpreted as the second and third osmotic virial coefficients of the salt (see reference [16]) with the numerical values of these parameters fitted to experimental data also being affected by the truncation of the polynomial. Although it is understood that the values of the  $k_i$ 's (or the  $k_i^+$ 's) reflect the collective effects of solute dissociation (*i.e.*, stoichiometric coefficients of the salt), ion charge, ion size, *etc.*, their interpretation is not straight forward since various electrolyte effects are not explicitly accounted for in the model.

Nevertheless, analyzing the numerical values of the  $k_i^+$ 's in Table 6-1, they show clear dependence on the salt's stoichiometric coefficients and the charge of the ions (the  $k_i$ 's in Table 6-2 have similar values):

1. All 1:1 salts with monovalent ions (NaCl, LiCl, KI, KBr, NaNO<sub>3</sub>, NH<sub>4</sub>Cl, NaBr, CsCl, KCl, NaC<sub>2</sub>H<sub>3</sub>O<sub>2</sub>, AgNO<sub>3</sub>, KNO<sub>3</sub>, KMnO<sub>4</sub>) have dissociation constants between 1.5 and 2, whereas for 1:1 salts with bivalent ions (MnSO<sub>4</sub>, MgSO<sub>4</sub>, ZnSO<sub>4</sub>, CuSO<sub>4</sub>) the dissociation constants are close to unity.
2. All 2:1 salts with monovalent cations and bivalent anions [K<sub>2</sub>CO<sub>3</sub>, Na<sub>2</sub>S<sub>2</sub>O<sub>3</sub>, (NH<sub>4</sub>)<sub>2</sub>SO<sub>4</sub>, Na<sub>2</sub>CO<sub>3</sub>, Na<sub>2</sub>SO<sub>4</sub>, K<sub>2</sub>SO<sub>4</sub>] have dissociation constants between 2 and 2.5.

3. The data for 1:2 salts with bivalent cations and monovalent anions (CaCl<sub>2</sub>, MgCl<sub>2</sub>, ZnBr<sub>2</sub>, SrCl<sub>2</sub>, ZnCl<sub>2</sub>, BaCl<sub>2</sub>) have a large range in the values of the dissociation constants from 0.8 for ZnBr<sub>2</sub> to 3.1 for CaCl<sub>2</sub>. If we exclude ZnBr<sub>2</sub> and ZnCl<sub>2</sub> from the analysis due to the limited number of experimental data points to which the polynomials were fitted, this range becomes 2–3.1.
4. FeCl<sub>3</sub> and Na<sub>3</sub>PO<sub>4</sub>—the only salts with trivalent ions in the present study—have dissociation constants of about 3.5.

We were not able to find any other consistent features in the results when we looked for patterns in the variation of the dissociation constants with the ion size, hydration number, or overall ionic strength of the solution. Tabulating and analyzing these parameters for more compounds (*e.g.*, organic salts) while also including other types of experimental data might provide insight in the future.

### 6.3.2 Predictions using the mole-fraction-based new MSOVE

In this section, we compare the predictions of the mole-fraction-based new MSOVE to experimental data from the literature [60–62,74,77,105,147,154,197–199] (total 371 data points) for 11 different ternary systems. The studied solutions are mostly mixtures of chloride salts, in which case the anion is common between the two salts, except for NaBr + KBr and NaCl + NaNO<sub>3</sub> systems, which share a bromide anion and a sodium cation, respectively. We choose to present the results as the osmolality of the solvent by converting the reported FPD data. The data and results in terms of the root-mean-square error (RMSE) are summarized in Table 6-3. Root-mean-square errors were calculated using the following formula:

$$\text{RMSE} = \sqrt{\frac{\sum_{i=1}^n (y_i - \bar{y}_i)^2}{n}} \quad (6-18)$$

Root-mean-square errors were calculated for each subsystem separately as well as for all data points (all-system RMSE,  $n = 371$ ), which is shown at the end of Table 6-3 in blue. The data sources are indicated in the second column of Table 6-3 with the number of data points from each source shown in the third column. In all cases, there are one or more isopleths meaning the dataset can be connected by a common feature, depending on the original authors' choice. For example, nine data points from Vilcu and Stanciu [198] for NaBr + KBr are all equimolar mixtures ( $m_{\text{NaBr}} = m_{\text{KBr}}$ ), while 62 data points measured by Hall *et al.* [77] for

NaCl + KCl can be combined into four isopleths, each at a certain constant value of the weight ratio of the salts. The number of isopleths for each dataset and the connecting feature of each isopleth are given in the fourth and fifth columns of Table 6-3, respectively. Additionally, across all data sources, different units of concentration are used, which are shown in the sixth column of Table 6-3. The conversion of these units to molality is discussed in Appendix D. The reported FPD values were converted to osmolality using Equation (6-2). As mentioned before, the resulting numbers are referred to as experimental data points.

Table 6-3. Summary of ternary experimental data from the literature and RMSEs for each subsystem of prediction of the mole-fraction-based new MSOVE. The RMSEs are colored from green (lowest) to red (highest). The all-system RMSE was calculated by considering all data points as one system (total 371 data points).

System	Data source	Number of data points	Number of isopleths	Connecting feature	Original units	RMSE [osmoles /kg (°C)]
NaBr + KBr	Vilcu <i>et al.</i> [198]	9	1	equimolality	FPD vs. molality	0.018 (0.034)
LiCl + NaCl	Gibbard <i>et al.</i> [60]	42	4	equivalent fraction wrt Li <sup>+</sup>	FPD vs. equivalent concentration	0.030 (0.056)
	Vilcu <i>et al.</i> [197]	5	1	equimolality	FPD vs. molality	0.020 (0.037)
NaCl + MgCl <sub>2</sub>	Gibbard <i>et al.</i> [62]	23	3	equivalent fraction wrt Na <sup>+</sup>	FPD vs. equivalent concentration	0.050 (0.093)
	Haghighi <i>et al.</i> [74]	5	1	wt % of NaCl	FPD vs. mass percent of MgCl <sub>2</sub>	0.391 (0.726)
	Mun <i>et al.</i> [147]	12	3	total molality	FPD vs. molality	0.077 (0.143)
NaCl + BaCl <sub>2</sub>	Gibbard <i>et al.</i> [61]	21	3	equivalent fraction wrt Na <sup>+</sup>	FPD vs. equivalent concentration	0.018 (0.034)
LiCl + KCl	Vilcu <i>et al.</i> [197]	5	1	equimolality	FPD vs. molality	0.224 (0.417)
LiCl + CsCl	Vilcu <i>et al.</i> [197]	5	1	equimolality	FPD vs. molality	0.216 (0.402)
NaCl + KCl	Hall <i>et al.</i> [77]	62	4	weight ratio of salts	FPD vs. total salinity	0.108 (0.201)
	Vilcu <i>et al.</i> [197–199]	13	1	equimolality	FPD vs. molality	0.197 (0.366)
	Haghighi <i>et al.</i> [74]	5	1	wt % of KCl	FPD vs. mass percent of NaCl	0.242 (0.450)



NaCl + CaCl <sub>2</sub>	Gibbard <i>et al.</i> [61]	11	1	equivalent fraction wrt Na <sup>+</sup>	FPD vs. equivalent concentration	0.045 (0.084)
	Oakes <i>et al.</i> [154]	94	5	weight ratio of salts	FPD vs. total salinity	0.144 (0.268)
	Haghighi <i>et al.</i> [74]	5	1	wt % of CaCl <sub>2</sub>	FPD vs. mass percent of NaCl	0.732 (1.356)
CaCl <sub>2</sub> + KCl	Haghighi <i>et al.</i> [74]	5	1	wt % of KCl	FPD vs. mass percent of CaCl <sub>2</sub>	1.224 (2.260)
NaCl + NaNO <sub>3</sub>	Khitrova [105]	15	5	wt % of NaCl in the initial binary	FPD vs. wt % of salts	0.437 (0.811)
	Khitrova [105]	22	5	wt % of NaNO <sub>3</sub> in the initial binary	FPD vs. wt % of salts	0.366 (0.680)
KCl + MgCl <sub>2</sub>	Mun <i>et al.</i> [147]	12	3	total molality	FPD vs. mole %	0.211 (0.392)
	Total	371	45		All-system RMSE	0.240 (0.446)

The fact that all data can be separated into isopleths allows us to efficiently present the goodness of the predictions graphically in 2D. The results are given in Figure 6-1 and Figure 6-2 for each ternary solution of each source plotted as osmolality vs. mole fraction. The data are grouped so that Figure 6-1 contains comparisons with data from all references listed in Table 6-3, except for data from Haghighi *et al.* [74] and Vilcu *et al.* [197–199], which are given in Figure 6-2. In Figure 6-1 and Figure 6-2, the open circles (○) represent the experimental data (original FPD data converted to osmolality). The solid lines of the matching color correspond to the predictions of the mole-fraction-based new MSOVE in the entire data range following the same isopleth connecting feature, as defined in the title and in the legend of each panel.

As evident by the small RMSE values listed in Table 6-3, as well as from Figure 6-1 and Figure 6-2, in most cases, the predictions of the model agree well with the experimental data. Notable exceptions with above-average RMSE values are: (i) all datasets from Haghighi *et al.* [74] and (ii) both datasets from Khitrova [105] (see Appendix D for a discussion). The all-system RMSE value of 0.24 osmoles/kg (corresponding to FPD error of 0.45 °C) was calculated by summing the squares of errors for all data points, dividing the results by the

number of points (371) and taking the square root of it [see Equation (6-18)]. It is small, indicating that the model can predict the FPD of ternary electrolyte solutions well. A more detailed analysis of the errors is given in section 6.4.

When using the MSOVE with combining rules for predictions, the apparent mismatch with experimental data or relatively large residuals can occur from three main sources: (i) inherent errors due to the simplifying assumptions of the model [16] (*e.g.*, the assumption of noninteracting solutes); (ii) the multisolute experimental data not being accurate; and/or (iii) the binary data used for fitting either not being accurate or not having enough data points for high fit confidence. Additionally, errors in both binary data and multisolute data can add up to result in higher apparent discrepancy, or they can cancel out to result in better apparent prediction, depending on the relative signs of the deviations. The comparison of the binary data from the sources from which the ternary data were obtained and the fitted curves that were used for predictions is given in Appendix D.

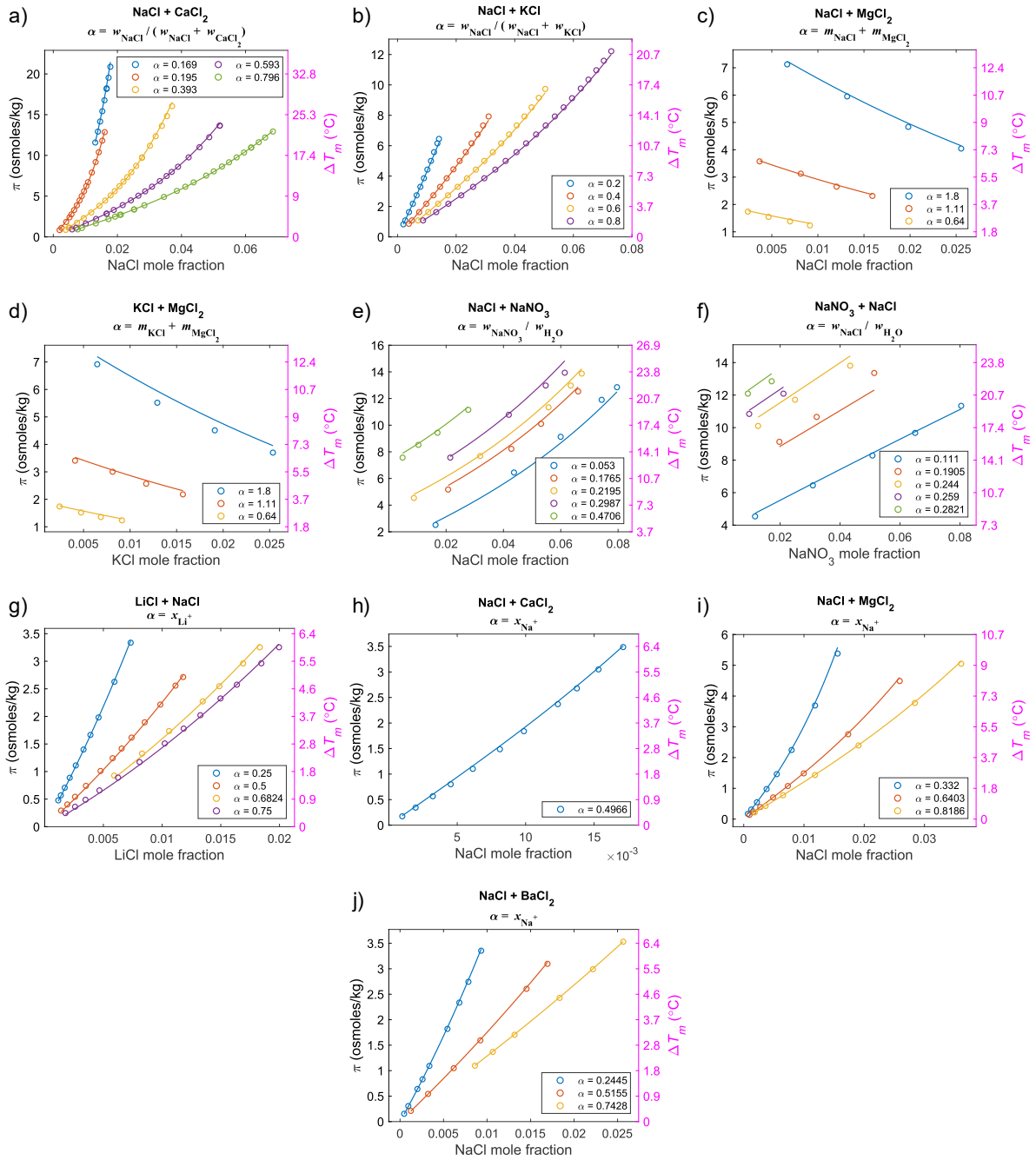


Figure 6-1. Comparison of experimental data (○) with the predictions of the mole-fraction-based new MSOVE for aqueous ternary electrolyte solutions from the following sources: (a) Oakes *et al.* [154]; (b) Hall *et al.* [77]; (c) and (d) Mun and Darer [147]; (e) and (f) Khitrova [105]; and (g)–(j) three papers by Gibbard *et al.* [60–62]. In the title of each panel,  $\alpha$  indicates the connecting feature of each isopleth in that panel. Note that the  $\pi$  axes are linear but the  $\Delta T_m$  axes are slightly nonlinear due to the nonlinearity of Equation (6-2).

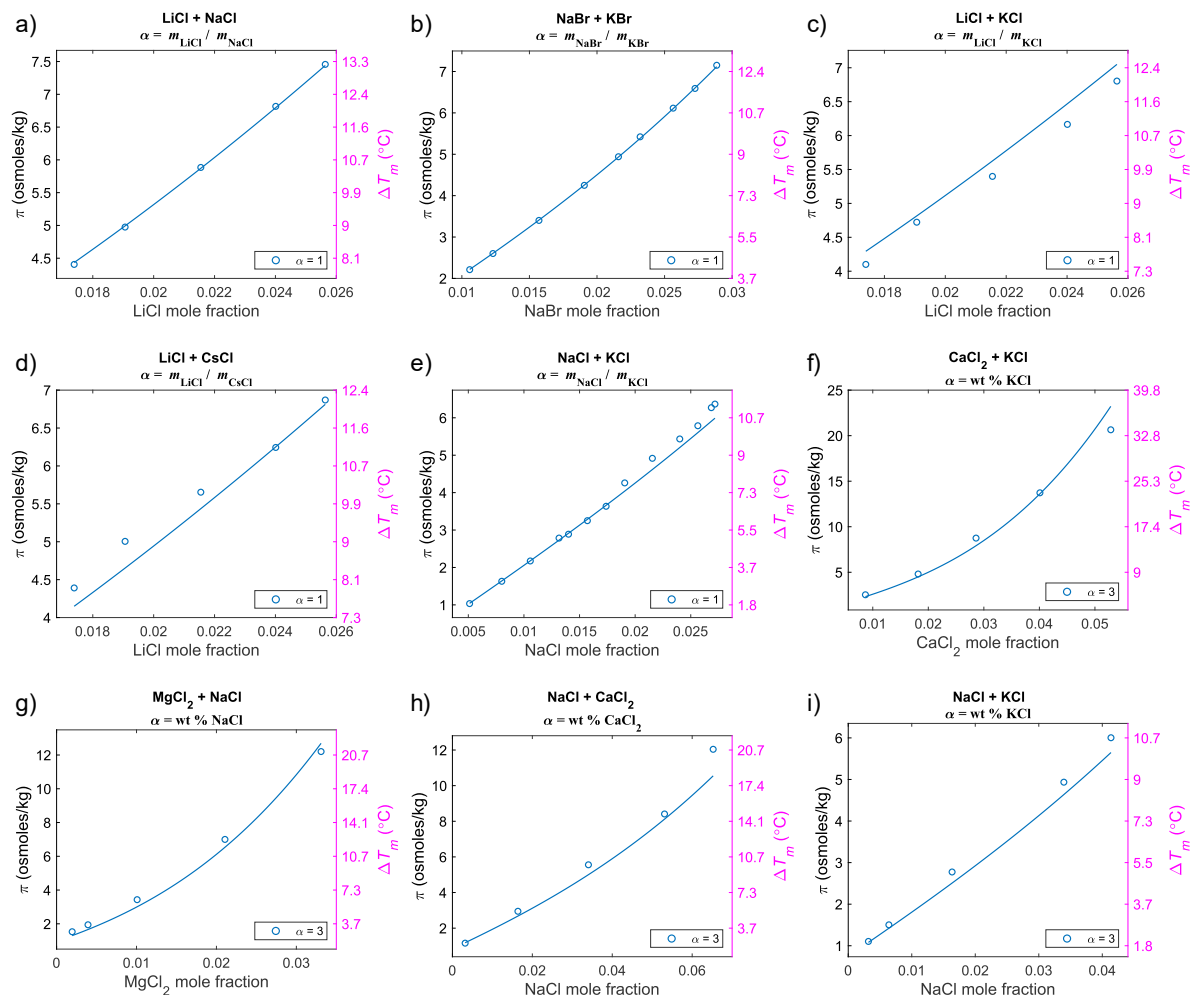


Figure 6-2. Comparison of experimental data ( $\circ$ ) from the given reference with the predictions of the mole-fraction-based new MSOVE for aqueous ternary electrolyte solutions from the following sources: (a)–(e) three papers by Vilcu *et al.* [197–199]; and (f)–(i) Haghghi *et al.* [74]. In the title of each panel,  $\alpha$  indicates the connecting feature of each isopleth in that panel. Note that the  $\pi$  axes are linear but the  $\Delta T_m$  axes are slightly nonlinear due to the nonlinearity of Equation (6-2).

## 6.4 Comparison of the new and original combining rules

In this section, we compare the prediction accuracies of the original and the new combining rules using the same dataset used in section 6.3.2 for validation. Previously, it has been argued that the E-MSOVE can be derived both in terms of molality and mole fraction, depending on the underlying assumptions of the theory [223]. Here, merely for comparison purposes, we assume that the same holds for the new MSOVE. As a result, we have four models that can be compared in terms of their predictive accuracy: (i) molality-based E-MSOVE

[Equations (6-5) to (6-7)]; (ii) mole-fraction-based E-MSOVE [Equation (6-10) with combining rules analogous to Equations (6-6) and (6-7)]; (iii) molality-based new MSOVE [Equation (6-5) with combining rules analogous to Equations (6-8) and (6-9)]; and (iv) mole-fraction-based new MSOVE [Equations (6-8) to (6-10)], which is the model tested in section 6.3.2.

The RMSEs of all four models are presented in Figure 6-3, which are grouped on a subsystem basis (see the third column of Table 6-3). Based on this figure alone, it seems that some data are better predicted with the new MSOVE, and some data are better predicted with the E-MSOVE. However, comparing RMSEs is not enough to assess the relative performance of the models conclusively because biases may be present within each model. Furthermore, the number of experimental data points varies significantly from one subsystem to another. For example, the NaCl + KCl dataset from Hall *et al.* [77] contains 62 data points, whereas the dataset for the same system from Haghghi *et al.* [74] has only five data points. The systems where the RMSEs are significantly higher for the new MSOVE (both mole fraction and molality-based versions) are the CaCl<sub>2</sub> + KCl system from Haghghi *et al.* [74] with five data points and the KCl + MgCl<sub>2</sub> system from Mun and Darer [147] with 12 data points.

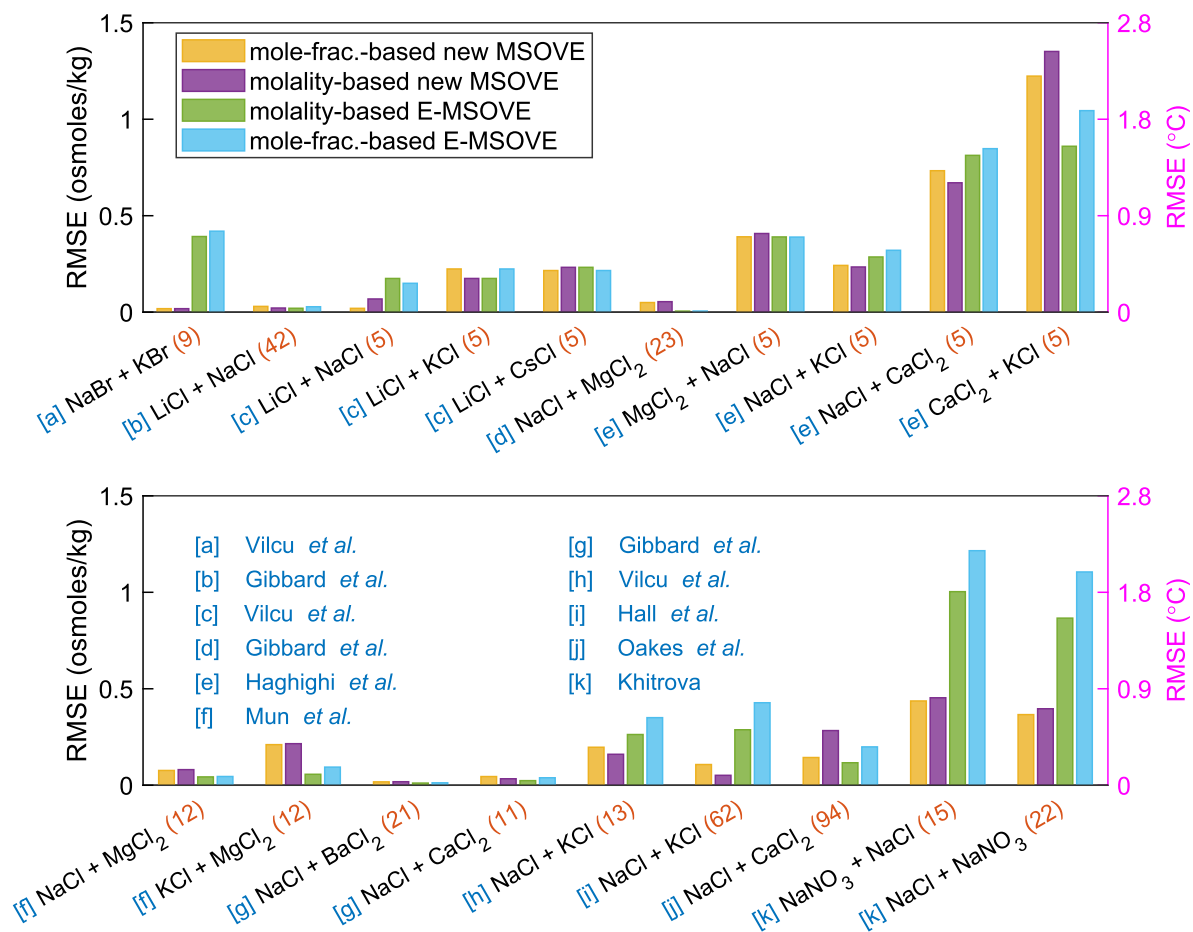


Figure 6-3. RMSE values of predictions for every ternary system (separated based on the source) obtained using four versions of the MSOVE. The letters in square brackets are for the references given in blue in the legend: (a) [198]; (b) [60]; (c) [197]; (d) [62]; (e) [74]; (f) [147]; (g) [61]; (h) [197–199]; (i) [77]; (j) [154]; (k) [105]. Notice that the data from the same source are grouped so that they appear sequentially. The numbers in parentheses in red at the end of each  $x$ -axis label are the numbers of experimental data points for each system.

For a more thorough comparison, we additionally performed residual analyses, the summaries of which are shown graphically in Figure 6-4 and Figure 6-5 for the mole-fraction-based and the molality-based models, respectively. In these figures, the top panels correspond to the new MSOVE, and the bottom panels correspond to the E-MSOVE. On the left panels, the predictions are plotted *vs.* the measurements, and on the right panels, the residuals are plotted *vs.* the total solute concentration. The histograms to the right of the plots show the distributions of errors, given on a log scale.

To quantitatively compare the models, we calculate all-system mean absolute error (MAE) and all-system mean bias (MB). They are defined as

$$\text{MAE} = \frac{\sum_{i=1}^n |y_i - \bar{y}_i|}{n} \quad (6-19)$$

and

$$\text{MB} = \frac{\sum_{i=1}^n (y_i - \bar{y}_i)}{n} \quad (6-20)$$

respectively. A numerical summary of the performance of these four models in terms of RMSEs, MAEs, and MBs is presented in Table 6-4.

Based on Figure 6-4, Figure 6-5, and Table 6-4, it is seen that the mole-fraction-based new MSOVE performs better in terms of RMSEs and MAEs, but more importantly, the MB is close to zero, as evident by the distribution of the errors. Both versions of the E-MSOVE have negative biases, meaning that they tend to underpredict on average. Note that, although the absolute values of the MBs for the E-MSOVE predictions may still look small, they are significant because most of the experimental data points lie in the first half of the data spread (lower concentration region), where the deviations are not as pronounced. The tendency of the E-MSOVE to underpredict is the direct result of using the geometric-average combining rule for the third-order mixed coefficients. When this combining rule is used, if one of the pure coefficients is equal to zero (*e.g.*, when combining a second-degree fit with a third-degree fit), the entire term (which is positive since all third-order pure coefficients are positive in this study; see Table 6-1 and Table 6-2) is eliminated, whereas for the arithmetic-average combining rule this is not the case. In general, the arithmetic mean of nonnegative numbers is never smaller than their geometric mean (AM–GM inequality), so one would expect relative underprediction from the E-MSOVE even in the case of combining two third-order fits. However, the resulting discrepancy between the predictions of the models for NaCl + CaCl<sub>2</sub> and NaCl + MgCl<sub>2</sub> mixtures—the only cases where both salts have nonzero cubic coefficients—was negligible (see Figure 6-3). As an example, taking the pure cubic osmotic virial coefficient values from Table 6-1 for NaCl and CaCl<sub>2</sub>, a quick calculation shows that the arithmetic average *vs.* geometric average combining rule only results in 0.1 osmoles/kg difference at high salt concentration of  $x_2 = x_3 = 0.05$ .

### Mole-fraction-based models

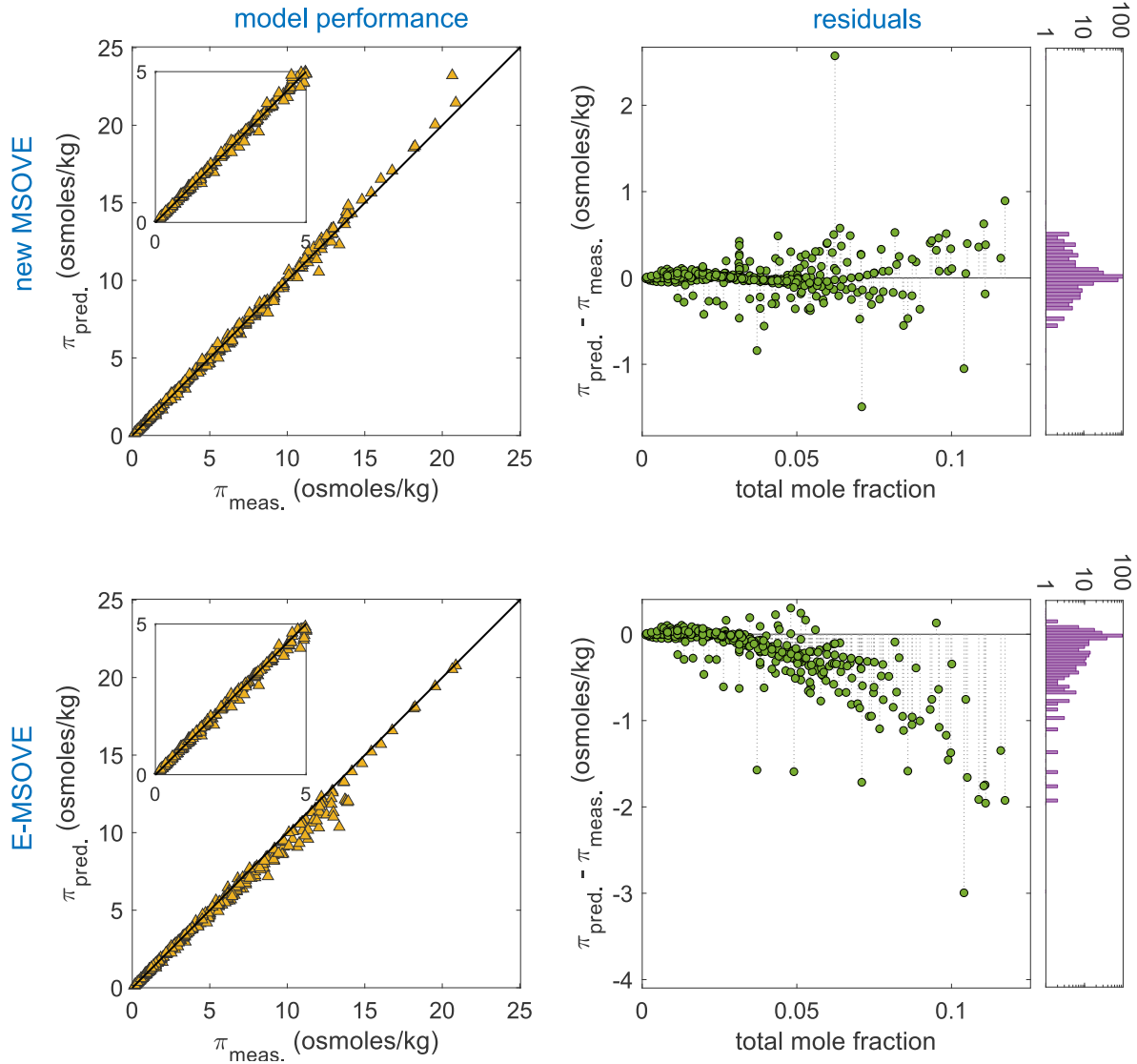


Figure 6-4. Graphical representation of the performance and residuals of the mole-fraction-based models. The top panels are for the mole-fraction-based new M-SOVE, and the bottom panels are for the mole-fraction-based E-M-SOVE. On the left panels, the predictions are plotted against the measurements with solid black lines representing perfect prediction. In the panels on the right, the residuals are plotted against the total concentration for each model with a histogram to the right of the panel showing the frequency distribution of the errors. Note that the histograms are given on a log scale.



## Molality-based models

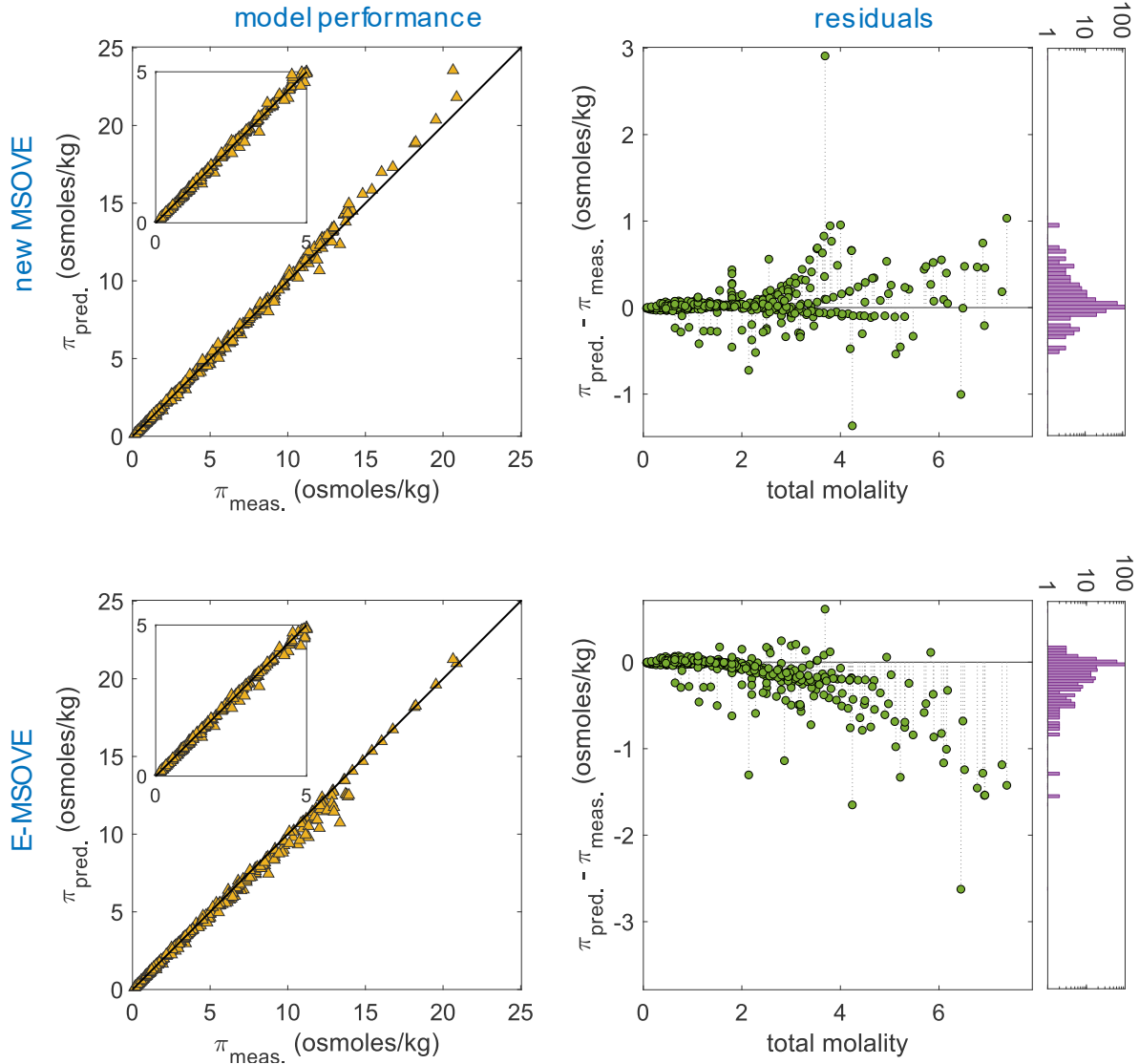


Figure 6-5. Graphical representation of the performance and residuals of the molality-based models. The top panels are for the molality-based new MSOVE, and the bottom panels are for the molality-based E-MSOVE. On the left panels, the predictions are plotted against the measurements with solid black lines representing perfect prediction. In the panels on the right, the residuals are plotted against the total concentration for each model with a histogram to the right of the panel showing the frequency distribution of the errors. Note that the histograms are given on a log scale.

Table 6-4. Numerical summary of the performance of the models in terms of all-system RMSEs, MAEs, and MBs. All measures were calculated by considering all data points as one system (total of 371 data points). Each column is separately colored from green (lowest absolute value) to red (highest absolute value).

Model	RMSE (osmoles/kg)	MAE (osmoles/kg)	MB (osmoles/kg)
Mole-fraction-based new MSOVE	0.2403	0.1176	0.0145
Mole-fraction-based E-MSOVE	0.4597	0.2429	-0.2204
Molality-based new MSOVE	0.2760	0.1336	0.0519
Molality-based E-MSOVE	0.3639	0.1831	-0.1585

## 6.5 Conclusion

In this chapter, we demonstrated that the mole-fraction-based MSOVE with arithmetic-average combining rules, developed in Chapter 5, can accurately predict the FPD of concentrated, ternary salt solutions of water. To do this, we first empirically extended our model to account for salt dissociation by including an extra fitting parameter (the dissociation constant) for each salt in the virial expansion. Then, we fitted polynomials to single-salt–water binary FPD data found in the literature, which are the only required inputs to the model. To determine the degree of each fitted polynomial, we proposed a unified criterion that allows the balance between the RTO-adjusted R-squared value and the CIs of the fitted coefficients to be set with a single user-adjustable parameter. Using the proposed fitting criterion, we tabulated both the mole-fraction-based and the molality-based osmotic virial coefficients of 31 salts in water (plus the dissociation constants). Next, using the tabulated coefficients, we predicted osmolalities of 11 different aqueous solutions containing two salts. Comparison with experimental data from various sources showed that the model can predict the FPD of ternary electrolyte solutions accurately. Finally, we compared two different combining rules and concentration units and found that the mole-fraction-based model with arithmetic-average combining rules works the best for aqueous electrolytes.

We note that this article serves as a proof-of-concept since it only predicts a small set of a specific type of multisolute data from the experimental literature (*i.e.*, FPD of water). The MSOVE with the arithmetic-average combining rules is a virial expansion for the concentration dependence of the chemical potential of the solvent, therefore, it can be used to

predict a plethora of other related thermodynamic properties of multicomponent solutions (*e.g.*, activity, fugacity, osmotic pressure, vapor pressure, *etc.*) for which a lot of experimental data are available in the literature for comparison. Additionally, the model's predictive capability can be tested for more complex solutions containing many species and/or different types of species (*e.g.*, salts and proteins in the same solution).

The main benefit of the method of combining rules is that equilibrium properties of multicomponent solutions can be predicted with a minimum number of fitting parameters obtained from binary data only. The model is simple, accurate, and computationally inexpensive. However, reliable binary data are required to determine the binary polynomials to high accuracies since the errors may propagate and result in poor predictions, which would be exacerbated with increasing number of solutes. When no or limited data are available, the binary coefficients can be alternatively calculated using a more sophisticated model or inferred from molecular dynamics simulations. These coefficients can be used in suitable combining rules to obtain the mixed coefficients. Then, the MSOVE can be constructed based on these parameters and used to make predictions.

We are not aware of any model that is as simple and is able to predict the properties of multicomponent electrolyte solutions as accurately from binary data alone. Although the MSOVE and its combining rules for nonelectrolyte solutions can be derived rigorously from the theory, its extension to electrolyte solutions is purely empirical. Consequently, the good agreement between the model predictions and the experimental measurements is somewhat surprising.

# Chapter 7

## Conclusions

This work provided theoretical insights into the behavior of confined fluid phases and multicomponent solutions, valuable for many technological applications as well as for fundamental understanding of relevant systems. Based on these insights, two relatively simple models were proposed and applied: (i) a model for calculating the drying pressure of nanopores filled with liquid–gas solutions (derived and applied in Chapter 3) and (ii) a polynomial model for calculating the chemical potential of a solvent with multiple solutes (derived in Chapter 5, applied in Chapter 6). This thesis consists of two parts, and its main outcomes are summarized below.

In Part I of this thesis, three problems were considered in the framework of Gibbsian composite-system thermodynamics where the geometry of interfaces and the geometry of confinement dictate the equilibrium properties of a system.

Specifically, in Chapter 2, the interactions of drop–drop and drop–bubble systems were investigated, and their equilibrium configurations were identified. Using free-energy analysis, the stability of different configurations was explored, their energies were quantified, and stability diagrams were constructed. It was shown that the concept of spreading coefficient can equally be applied to liquid–gas systems, and it holds true for nanoscale systems as well. In addition, the effects of volumes and interfacial tensions of the phases on the free energies of the configurations were quantified. Finally, the importance of additional terms in the free-energy equation due to the compressibility of the gas phase was highlighted. It was shown that neglecting these extra terms for a nanoscale drop–bubble system results in not only incorrect free-energy calculation, but also qualitatively wrong conclusions in certain cases.

In Chapter 3, a predictive model was developed for quantifying the influence of a dissolved gas on the ease of drying of hydrophobic nanopores (emptying of liquid-filled pores). At the core of this model is an equation relating the curvature of the liquid–vapor interface of

the nucleus to the nonideal liquid–vapor equilibrium. This equilibrium was solved using the nonrandom two-liquid model for the liquid, and the Peng–Robinson equation of state for the vapor. At the pressures of interest, it was found that the typically made ideality assumption may result in considerable errors. The equilibrium vapor nucleus shape was found to be influenced by cylindrical confinement, which had to be computed numerically. The curvature of the liquid–vapor interface of the nucleus in turn dictates the equilibrium behavior of the system. The analysis showed that gases dissolved in water, such as nitrogen or carbon dioxide, can significantly reduce the pressure required for drying of the pores. The required gas concentration was much higher than the solubilities of these gases in atmospheric conditions. However, such concentrations can be reached at high pressures needed for liquid intrusion into the pores. For quantitative predictions, the small radius of the pores investigated (1–5 nm) necessitated that line tension effects be included. By combining the developed equation with classical nucleation theory, a single fitted line tension value—in the range of reported values for pure water systems in the literature—was sufficient for the model to satisfactorily describe independent experimental measurements.

In Chapter 4, the ideas from Chapter 3 were extended to the problem of pore condensation and freezing. Namely, solid nucleation from a confined liquid near the liquid–vapor meniscus in a nanopore and then bridging of neighboring solid-filled pores on the porous particle were considered. By computing the equilibrium nucleus and bridge geometries for many cases, a comparative free-energy analysis was performed allowing the determination of minimum-free-energy routes. For the nucleation inside the pore, depending on the internal angles of the solid nucleus, three qualitatively different geometry classes were identified. The analysis showed that sharp corners, such as the one created by the meniscus, can be efficient nucleation sites, or even reduce the energy barrier to zero (depending on the conditions) by making the sum of internal angles of the solid nucleus less than  $180^\circ$ . When it comes to the growth of the solid out of the pores, it was shown that having multiple pores in the vicinity of each other can lower the energy barriers by bridging, and hence, facilitate the bulk solid growth. In some cases, this bridging resulted in an order of magnitude decrease in the energy barrier compared to the growth from a single pore.

In Part II of this thesis, a practically important model for the chemical potential of a solvent with multiple solutes was rigorously derived using elements from combinatorics and statistical mechanics and then validated.

The derivation of the model was provided in Chapter 5, which takes into account full interactions in a particle group of an arbitrary size and assumes random mixing of the species. The resulting equation is a multivariate polynomial in mole fractions of the components with physically meaningful coefficients. Moreover, the equivalency between the derived model and the exact solution theories was demonstrated in the large-particle-group limit. With one additional assumption about the relative strengths of the interaction between the solute particles and the interaction between the solute and solvent particles, combining rules were obtained. These combining rules allow the mixed coefficients of the polynomial to be expressed as arithmetic averages of appropriate binary coefficients (coefficients obtained from binary solvent–single solute mixture data), and therefore, multicomponent predictions to be made using only binary data.

In Chapter 6, the derived model was extended to dissociating solutes by following a previous approach of introducing a single empirical fitting parameter (a constant) for each solute, and a new fitting criterion was described to truncate the binary polynomials when fitting to data. Using the extended model and the new fitting criterion, the binary coefficients of 31 common salts were tabulated based on literature data. Then, predictions were made for freezing points of 11 different ternary aqueous mixtures (two salts + water) and the results were compared to a dataset consisting of 371 data points collected from the literature. The predictive ability of the model was found to be excellent with an all-system root-mean-square error of 0.45 °C and negligible mean bias. Furthermore, a comparison to a similar model from the literature proved the new model to be more accurate.

In the future, it would be interesting to compare the findings of Part I of this thesis to experiments or simulation studies. This will allow researchers to assess the validity of assumptions and the accuracy of calculations, identify the limits, and propose possible modifications. For example: What would be the impact of relaxing the immiscibility assumption of interacting drops and bubbles? What would be the impact of including the influence of dissolved gas on the interfacial tensions for vapor nucleation in a nanopore? How relevant is the lattice structure of a solid in a nanopore for computing the nucleation paths and

energy barriers? For Part II of this thesis, it would be interesting to check whether it is possible to derive the extra fitting parameters for dissociating solutes in the multisolute osmotic virial equation from theory instead of empirically introducing them. Additionally, the model could be used to make predictions for as many datasets as possible, including different types of solvents and solutes, to understand its validity region.

Although the model from Part II was not applied to similar systems studied in Part I, its value for such systems is obvious. If, for example, a nanopore were to be filled with a solvent containing a high concentration of multiple solutes—an important case in the studies of liquid behavior in confinement—a nonideal chemical potential equation would need to be used. The model from Part II would be well suited for such a scenario. Overall, the insights and models provided in this thesis help further our understanding of interface-dominated multiphase systems in confinement and of multicomponent solutions.

## References

- [1] C. Alba-Simionesco, B. Coasne, G. Dosseh, G. Dudziak, K. E. Gubbins, R. Radhakrishnan, and M. Sliwinska-Bartkowiak, *Effects of Confinement on Freezing and Melting*, J. Phys. Condens. Matter **18**, R15 (2006).
- [2] G. Algara-Siller, O. Lehtinen, F. C. Wang, R. R. Nair, U. Kaiser, H. A. Wu, A. K. Geim, and I. V. Grigorieva, *Square Ice in Graphene Nanocapillaries*, Nature **519**, 443 (2015).
- [3] A. B. Almeida, S. V. Buldyrev, A. M. Alencar, and N. Giovambattista, *How Small Is Too Small for the Capillarity Theory?*, J. Phys. Chem. C **125**, 5335 (2021).
- [4] A. Amirfazli and A. W. Neumann, *Status of the Three-Phase Line Tension*, Adv. Colloid Interface Sci. **110**, 121 (2004).
- [5] A. S. Ansari and S. N. Pandis, *Prediction of Multicomponent Inorganic Atmospheric Aerosol Behavior*, Atmos. Environ. **33**, 745 (1999).
- [6] O. Arjmandi-Tash, N. M. Kovalchuk, A. Trybala, I. V. Kuchin, and V. Starov, *Kinetics of Wetting and Spreading of Droplets over Various Substrates*, Langmuir **33**, 4367 (2017).
- [7] G. Bai, D. Gao, Z. Liu, X. Zhou, and J. Wang, *Probing the Critical Nucleus Size for Ice Formation with Graphene Oxide Nanosheets*, Nature **576**, 437 (2019).
- [8] M. Barisik and A. Beskok, *Wetting Characterisation of Silicon (1,0,0) Surface*, Mol. Simul. **39**, 700 (2013).
- [9] F. Beck and P. Rüetschi, *Rechargeable Batteries with Aqueous Electrolytes*, Electrochim. Acta **45**, 2467 (2000).
- [10] J. S. Beck et al., *A New Family of Mesoporous Molecular Sieves Prepared with Liquid Crystal Templates*, J. Am. Chem. Soc. **114**, 10834 (1992).
- [11] O. Beckstein and M. S. P. Sansom, *Liquid–Vapor Oscillations of Water in Hydrophobic*



- Nanopores*, Proc. Natl. Acad. Sci. U. S. A. **100**, 7063 (2003).
- [12] R. Bey, B. Coasne, and C. Picard, *Carbon Dioxide as a Line Active Agent: Its Impact on Line Tension and Nucleation Rate*, Proc. Natl. Acad. Sci. U. S. A. **118**, e2102449118 (2021).
- [13] Y. Bi, B. Cao, and T. Li, *Enhanced Heterogeneous Ice Nucleation by Special Surface Geometry*, Nat. Commun. **8**, 15372 (2017).
- [14] P. K. Bikkina, O. Shoham, and R. Uppaluri, *Equilibrated Interfacial Tension Data of the CO<sub>2</sub>–Water System at High Pressures and Moderate Temperatures*, J. Chem. Eng. Data **56**, 3725 (2011).
- [15] H. Binyaminov, F. Abdullah, L. Zargarzadeh, and J. A. W. Elliott, *Thermodynamic Investigation of Droplet–Droplet and Bubble–Droplet Equilibrium in an Immiscible Medium*, J. Phys. Chem. B **125**, 8636 (2021).
- [16] H. Binyaminov and J. A. W. Elliott, *Multicomponent Solutions: Combining Rules for Multisolute Osmotic Virial Coefficients*, J. Chem. Phys. **159**, 164116 (2023).
- [17] H. Binyaminov and J. A. W. Elliott, *Quantifying the Effects of Dissolved Nitrogen and Carbon Dioxide on Drying Pressure of Hydrophobic Nanopores*, J. Chem. Phys. **158**, 204710 (2023).
- [18] H. Binyaminov, H. Sun, and J. A. W. Elliott, *Predicting Freezing Points of Ternary Salt Solutions with the Multisolute Osmotic Virial Equation*, J. Chem. Phys. **159**, 244502 (2023).
- [19] D. Bonn, J. Eggers, J. Indekeu, J. Meunier, and E. Rolley, *Wetting and Spreading*, Rev. Mod. Phys. **81**, 739 (2009).
- [20] P. Boonme, K. Krauel, A. Graf, T. Rades, and V. B. Junyaprasert, *Characterization of Microemulsion Structures in the Pseudoternary Phase Diagram of Isopropyl Palmitate/Water/Brij 97:1-Butanol*, AAPS PharmSciTech **7**, E1 (2006).
- [21] K. A. Brakke, *The Surface Evolver*, Exp. Math. **1**, 141 (1992).
- [22] K. A. Brakke, *Surface Evolver Manual*, <https://kenbrakke.com/evolver/downloads/manual270.pdf>.

- [23] D. Bratko and A. Luzar, *Attractive Surface Force in the Presence of Dissolved Gas: A Molecular Approach*, *Langmuir* **24**, 1247 (2008).
- [24] J. C. Burton, F. M. Huisman, P. Alison, D. Rogerson, and P. Taborek, *Experimental and Numerical Investigation of the Equilibrium Geometry of Liquid Lenses*, *Langmuir* **26**, 15316 (2010).
- [25] H. B. Callen, *Thermodynamics and an Introduction to Thermostatistics*, 2nd ed. (John Wiley & Sons, 1985).
- [26] G. Camisasca, A. Tinti, and A. Giacomello, *Gas-Induced Drying of Nanopores*, *J. Phys. Chem. Lett.* **11**, 9171 (2020).
- [27] J. M. Campbell and H. K. Christenson, *Nucleation- and Emergence-Limited Growth of Ice from Pores*, *Phys. Rev. Lett.* **120**, 165701 (2018).
- [28] J. M. Campbell, F. C. Meldrum, and H. K. Christenson, *Observing the Formation of Ice and Organic Crystals in Active Sites*, *Proc. Natl. Acad. Sci. U. S. A.* **114**, 810 (2017).
- [29] J. Canivet, A. Fateeva, Y. Guo, B. Coasne, and D. Farrusseng, *Water Adsorption in MOFs: Fundamentals and Applications*, *Chem. Soc. Rev.* **43**, 5594 (2014).
- [30] B. Cao, E. Xu, and T. Li, *Anomalous Stability of Two-Dimensional Ice Confined in Hydrophobic Nanopores*, *ACS Nano* **13**, 4712 (2019).
- [31] J. J. Carroll, *Henry's Law Revisited*, *Chem. Eng. Prog.* **95**, 49 (1999).
- [32] D. Chao, W. Zhou, F. Xie, C. Ye, H. Li, M. Jaroniec, and S.-Z. Qiao, *Roadmap for Advanced Aqueous Batteries: From Design of Materials to Applications*, *Sci. Adv.* **6**, eaba4098 (2020).
- [33] A. Checco, P. Guenoun, and J. Daillant, *Nonlinear Dependence of the Contact Angle of Nanodroplets on Contact Line Curvature*, *Phys. Rev. Lett.* **91**, 186101 (2003).
- [34] H. K. Christenson, *Confinement Effects on Freezing and Melting*, *J. Phys. Condens. Matter* **13**, R95 (2001).
- [35] S. L. Clegg, J. H. Seinfeld, and P. Brimblecombe, *Thermodynamic Modelling of Aqueous Aerosols Containing Electrolytes and Dissolved Organic Compounds*, *J. Aerosol Sci.* **32**, 713 (2001).

- [36] L. Coiffard and V. Eroshenko, *Temperature Effect on Water Intrusion/Expulsion in Grafted Silica Gels*, *J. Colloid Interface Sci.* **300**, 304 (2006).
- [37] R. O. David, J. Fahrni, C. Marcolli, F. Mahrt, D. Brühwiler, and Z. A. Kanji, *The Role of Contact Angle and Pore Width on Pore Condensation and Freezing*, *Atmos. Chem. Phys.* **20**, 9419 (2020).
- [38] R. O. David, C. Marcolli, J. Fahrni, Y. Qiu, Y. A. Perez Sirkin, V. Molinero, F. Mahrt, D. Brühwiler, U. Lohmann, and Z. A. Kanji, *Pore Condensation and Freezing Is Responsible for Ice Formation below Water Saturation for Porous Particles*, *Proc. Natl. Acad. Sci. U. S. A.* **116**, 8184 (2019).
- [39] A. Le Donne, A. Tinti, E. Amayuelas, H. K. Kashyap, G. Camisasca, R. C. Remsing, R. Roth, Y. Grosu, and S. Meloni, *Intrusion and Extrusion of Liquids in Highly Confining Media: Bridging Fundamental Research to Applications*, *Adv. Phys. X* **7**, 2052353 (2022).
- [40] J. Eiken, B. Böttger, and I. Steinbach, *Multiphase-Field Approach for Multicomponent Alloys with Extrapolation Scheme for Numerical Application*, *Phys. Rev. E* **73**, 066122 (2006).
- [41] J. A. W. Elliott, *On the Complete Kelvin Equation*, *Chem. Eng. Educ.* **35**, 274 (2001).
- [42] J. A. W. Elliott, R. C. Prickett, H. Y. Elmoazzen, K. R. Porter, and L. E. McGann, *A Multisolute Osmotic Virial Equation for Solutions of Interest in Biology*, *J. Phys. Chem. B* **111**, 1775 (2007).
- [43] J. A. W. Elliott and O. Voitcu, *On the Thermodynamic Stability of Liquid Capillary Bridges*, *Can. J. Chem. Eng.* **85**, 692 (2007).
- [44] J. R. Elliott and C. T. Lira, *Introductory Chemical Engineering Thermodynamics*, 2nd ed. (Prentice-Hall Inc, 2012).
- [45] J. A. W. Elliott, *Gibbsian Surface Thermodynamics*, *J. Phys. Chem. B* **124**, 10859 (2020).
- [46] J. A. W. Elliott, *Surface Thermodynamics at the Nanoscale*, *J. Chem. Phys.* **154**, 190901 (2021).

- [47] H. Y. Elmoazzen, J. A. W. Elliott, and L. E. McGann, *Osmotic Transport across Cell Membranes in Nondilute Solutions: A New Nondilute Solute Transport Equation*, *Biophys. J.* **96**, 2559 (2009).
- [48] V. Eroshenko, R.-C. Regis, M. Soulard, and J. Patarin, *Energetics: A New Field of Applications for Hydrophobic Zeolites*, *J. Am. Chem. Soc.* **123**, 8129 (2001).
- [49] F. Eslami and J. A. W. Elliott, *Thermodynamic Investigation of the Barrier for Heterogeneous Nucleation on a Fluid Surface in Comparison with a Rigid Surface*, *J. Phys. Chem. B* **115**, 10646 (2011).
- [50] M. H. Factorovich, V. Molinero, and D. A. Scherlis, *Vapor Pressure of Water Nanodroplets*, *J. Am. Chem. Soc.* **136**, 4508 (2014).
- [51] R. Farajzadeh, A. Andrianov, R. Krastev, G. J. Hirasaki, and W. R. Rossen, *Foam–Oil Interaction in Porous Media: Implications for Foam Assisted Enhanced Oil Recovery*, *Adv. Colloid Interface Sci.* **183–184**, 1 (2012).
- [52] W. Feller, *An Introduction to Probability Theory and Its Applications*, 2nd ed. (John Wiley & Sons, 1968).
- [53] Q. Feng, J. Li, X. Zhou, and H. Lu, *Effect of an Electric Field on Dewetting Transition of Nitrogen–Water System*, *Chinese Phys. B* **31**, 036801 (2022).
- [54] T. W. Forest and C. A. Ward, *Effect of a Dissolved Gas on the Homogeneous Nucleation Pressure of a Liquid*, *J. Chem. Phys.* **66**, 2322 (1977).
- [55] L. A. Gabler Pizarro, L. E. McGann, and J. A. W. Elliott, *Permeability and Osmotic Parameters of Human Umbilical Vein Endothelial Cells and H9C2 Cells under Non-Ideal Thermodynamic Assumptions: A Novel Iterative Fitting Method*, *J. Phys. Chem. B* **125**, 12934 (2021).
- [56] C. F. Gauss, *Principia Generalia Theoriae Figurae Fluidorum in Statu Aequilibrii* (Dieterichs, 1830).
- [57] X.-H. Ge, J.-P. Huang, J.-H. Xu, J. Chen, and G.-S. Luo, *Water–Oil Janus Emulsions: Microfluidic Synthesis and Morphology Design*, *Soft Matter* **12**, 3425 (2016).
- [58] L. D. Gelb, K. E. Gubbins, R. Radhakrishnan, and M. Sliwiska-Bartkowiak, *Phase*

*Separation in Confined Systems*, Reports Prog. Phys. **62**, 1573 (1999).

- [59] A. Giacomello, C. M. Casciola, Y. Grosu, and S. Meloni, *Liquid Intrusion in and Extrusion from Non-Wettable Nanopores for Technological Applications*, Eur. Phys. J. B **94**, 1 (2021).
- [60] H. F. Gibbard and A. Fawaz, *Freezing Points and Related Properties of Electrolyte Solutions. II. Mixtures of Lithium Chloride and Sodium Chloride in Water*, J. Solution Chem. **3**, 745 (1974).
- [61] H. F. Gibbard and S.-L. Fong, *Freezing Points and Related Properties of Electrolyte Solutions. III. The Systems NaCl-CaCl<sub>2</sub>-H<sub>2</sub>O and NaCl-BaCl<sub>2</sub>-H<sub>2</sub>O*, J. Solution Chem. **4**, 863 (1975).
- [62] H. F. Gibbard and A. F. Gossmann, *Freezing of Electrolyte Mixtures. I. Mixtures of Sodium Chloride and Magnesium Chloride in Water*, J. Solution Chem. **3**, 385 (1974).
- [63] J. W. Gibbs, *On the Equilibrium of Heterogeneous Substances*. Trans. Conn. Acad. **3**, 108 (1876) and **3**, 343 (1878). Republished in *The Scientific Papers of J. Willard Gibbs: Vol. 1* (Ox Bow Press, 1993).
- [64] R. Giro, P. W. Bryant, M. Engel, R. F. Neumann, and M. B. Steiner, *Adsorption Energy as a Metric for Wettability at the Nanoscale*, Sci. Rep. **7**, 46317 (2017).
- [65] A. Goebel and K. Lunkenheimer, *Interfacial Tension of the Water/n-Alkane Interface*, Langmuir **13**, 369 (1997).
- [66] E. González Solveyra, E. de la Llave, D. A. Scherlis, and V. Molinero, *Melting and Crystallization of Ice in Partially Filled Nanopores*, J. Phys. Chem. B **115**, 14196 (2011).
- [67] Y. Grosu, O. Ievtushenko, V. Eroshenko, J. M. Nedelec, and J. P. E. Grolier, *Water Intrusion/Extrusion in Hydrophobized Mesoporous Silica Gel in a Wide Temperature Range: Capillarity, Bubble Nucleation and Line Tension Effects*, Colloids Surfaces A Physicochem. Eng. Asp. **441**, 549 (2014).
- [68] Y. Grosu, M. Mierzwa, V. A. Eroshenko, S. Pawlus, M. Chorażewski, J.-M. Nedelec, and J.-P. E. Grolier, *Mechanical, Thermal, and Electrical Energy Storage in a Single*

- Working Body: Electrification and Thermal Effects upon Pressure-Induced Water Intrusion–Extrusion in Nanoporous Solids*, ACS Appl. Mater. Interfaces **9**, 7044 (2017).
- [69] E. A. Guggenheim, *Mixtures: The Theory of the Equilibrium Properties of Some Simple Classes of Mixtures Solutions and Alloys* (Clarendon Press, 1952).
- [70] E. A. Guggenheim, *The Statistical Mechanics of Regular Solutions*, Proc. R. Soc. A Math. Phys. Eng. Sci. **148**, 304 (1935).
- [71] L. Guillemot, T. Biben, A. Galarneau, G. Vigier, and É. Charlaix, *Activated Drying in Hydrophobic Nanopores and the Line Tension of Water*, Proc. Natl. Acad. Sci. U. S. A. **109**, 19557 (2012).
- [72] L. Guillemot, A. Galarneau, G. Vigier, T. Abensur, and É. Charlaix, *New Device to Measure Dynamic Intrusion/Extrusion Cycles of Lyophobic Heterogeneous Systems*, Rev. Sci. Instrum. **83**, 105105 (2012).
- [73] J. Guzowski, P. M. Korczyk, S. Jakiela, and P. Garstecki, *The Structure and Stability of Multiple Micro-Droplets*, Soft Matter **8**, 7269 (2012).
- [74] H. Haghighi, A. Chapoy, and B. Tohidi, *Freezing Point Depression of Electrolyte Solutions: Experimental Measurements and Modeling Using the Cubic-Plus-Association Equation of State*, Ind. Eng. Chem. Res. **47**, 3983 (2008).
- [75] A. Haji-Akbari and P. G. Debenedetti, *Computational Investigation of Surface Freezing in a Molecular Model of Water*, Proc. Natl. Acad. Sci. U. S. A. **114**, 3316 (2017).
- [76] A. Haji-Akbari, R. S. DeFever, S. Sarupria, and P. G. Debenedetti, *Suppression of Sub-Surface Freezing in Free-Standing Thin Films of a Coarse-Grained Model of Water*, Phys. Chem. Chem. Phys. **16**, 25916 (2014).
- [77] D. L. Hall, S. Michael Sterner, and R. J. Bodnar, *Freezing Point Depression of NaCl-KCl-H<sub>2</sub>O Solutions*, Econ. Geol. **83**, 197 (1988).
- [78] W. D. Harkins and A. Feldman, *Films. The Spreading of Liquids and the Spreading Coefficient*, J. Am. Chem. Soc. **44**, 2665 (1922).
- [79] J. Haywood and O. Boucher, *Estimates of the Direct and Indirect Radiative Forcing Due to Tropospheric Aerosols: A Review*, Rev. Geophys. **38**, 513 (2000).

- [80] U. Hecht et al., *Multiphase Solidification in Multicomponent Alloys*, Mater. Sci. Eng. R Reports **46**, 1 (2004).
- [81] R. Helmy, Y. Kazakevich, C. Ni, and A. Y. Fadeev, *Wetting in Hydrophobic Nanochannels: A Challenge of Classical Capillarity*, J. Am. Chem. Soc. **127**, 12446 (2005).
- [82] T. L. Hill, *An Introduction to Statistical Thermodynamics* (Dover Publications, 1986).
- [83] T. L. Hill, *Theory of Solutions. I*, J. Chem. Phys. **79**, 4885 (1957).
- [84] T. L. Hill, *Theory of Solutions. II. Osmotic Pressure Virial Expansion and Light Scattering in Two Component Solutions*, J. Chem. Phys. **30**, 93 (1959).
- [85] T. Hiratsuka, H. Tanaka, and M. T. Miyahara, *Comprehensive Modeling of Capillary Condensation in Open-Ended Nanopores: Equilibrium, Metastability, and Spinodal*, J. Phys. Chem. C **121**, 26877 (2017).
- [86] L. N. Ho, S. Clauzier, Y. Schuurman, D. Farrusseng, and B. Coasne, *Gas Uptake in Solvents Confined in Mesopores: Adsorption versus Enhanced Solubility*, J. Phys. Chem. Lett. **4**, 2274 (2013).
- [87] L. N. Ho, J. Perez Pellitero, F. Porcheron, and R. J.-M. Pellenq, *Enhanced CO<sub>2</sub> Solubility in Hybrid MCM-41: Molecular Simulations and Experiments*, Langmuir **27**, 8187 (2011).
- [88] L. N. Ho, Y. Schuurman, D. Farrusseng, and B. Coasne, *Solubility of Gases in Water Confined in Nanoporous Materials: ZSM-5, MCM-41, and MIL-100*, J. Phys. Chem. C **119**, 21547 (2015).
- [89] N. L. Ho, F. Porcheron, and R. J.-M. Pellenq, *Experimental and Molecular Simulation Investigation of Enhanced CO<sub>2</sub> Solubility in Hybrid Adsorbents*, Langmuir **26**, 13287 (2010).
- [90] Y. Hu, L. Huang, S. Zhao, H. Liu, and K. E. Gubbins, *Effect of Confinement in Nanoporous Materials on the Solubility of a Supercritical Gas*, Mol. Phys. **114**, 3294 (2016).
- [91] J. Huang, Z. Guo, Y. Ma, D. Bin, Y. Wang, and Y. Xia, *Recent Progress of Rechargeable Batteries Using Mild Aqueous Electrolytes*, Small Methods **3**, 1800272

- (2019).
- [92] S. Huang, J. Zhu, J. Tian, and Z. Niu, *Recent Progress in the Electrolytes of Aqueous Zinc-Ion Batteries*, Chem. A Eur. J. **25**, 14480 (2019).
- [93] A. Hudait and V. Molinero, *Ice Crystallization in Ultrafine Water-Salt Aerosols: Nucleation, Ice-Solution Equilibrium, and Internal Structure*, J. Am. Chem. Soc. **136**, 8081 (2014).
- [94] G. Hummer, J. C. Rasaiah, and J. P. Noworyta, *Water Conduction through the Hydrophobic Channel of a Carbon Nanotube*, Nature **414**, 188 (2001).
- [95] S. Hussain and A. Haji-Akbari, *Role of Nanoscale Interfacial Proximity in Contact Freezing in Water*, J. Am. Chem. Soc. **143**, 2272 (2021).
- [96] S. Hyde, S. Andersson, K. Larsson, Z. Blum, T. Landh, S. Lidin, and B. W. Ninham, *The Language of Shape* (Elsevier B.V., 1997).
- [97] Y. Ikeda, B. Grabowski, and F. Körmann, *Ab Initio Phase Stabilities and Mechanical Properties of Multicomponent Alloys: A Comprehensive Review for High Entropy Alloys and Compositionally Complex Alloys*, Mater. Charact. **147**, 464 (2019).
- [98] J. N. Israelachvili, *Intermolecular and Surface Forces*, 3rd ed. (Academic Press, 2011).
- [99] D. R. Jackett, T. J. McDougall, R. Feistel, D. G. Wright, and S. M. Griffies, *Algorithms for Density, Potential Temperature, Conservative Temperature, and the Freezing Temperature of Seawater*, J. Atmos. Ocean. Technol. **23**, 1709 (2006).
- [100] K. B. Jinesh and J. W. M. Frenken, *Experimental Evidence for Ice Formation at Room Temperature*, Phys. Rev. Lett. **101**, 036101 (2008).
- [101] J. C. Johnston and V. Molinero, *Crystallization, Melting, and Structure of Water Nanoparticles at Atmospherically Relevant Temperatures*, J. Am. Chem. Soc. **134**, 6650 (2012).
- [102] Y. Kakuda, E. Uchida, and N. Imai, *A New Model of the Excess Gibbs Energy of Mixing for a Regular Solution*, Proc. Japan Acad. Ser B Phys. Biol. Sci. **70**, 163 (1994).
- [103] D. Kashchiev, *Nucleation: Basic Theory with Applications* (Butterworth Heinemann, 2000).



- [104] S. N. Khan, J. B. Staunton, and G. M. Stocks, *Statistical Physics of Multicomponent Alloys Using KKR-CPA*, Phys. Rev. B **93**, 054206 (2016).
- [105] N. N. Khitrova, *Polytherms of the Ternary  $\text{NaNO}_3\text{-NaCl-H}_2\text{O}$* , Zhurnal Prikl. Khimii **27**, 1281 (1954).
- [106] Y. P. Kim, J. H. Seinfeld, and P. Saxena, *Atmospheric Gas-Aerosol Equilibrium I. Thermodynamic Model*, Aerosol Sci. Technol. **19**, 157 (1993).
- [107] R. S. King, H. W. Blanch, and J. M. Prausnitz, *Molecular Thermodynamics of Aqueous Two-phase Systems for Bioseparations*, AIChE J. **34**, 1585 (1988).
- [108] M. Kolle and S. Lee, *Progress and Opportunities in Soft Photonics and Biologically Inspired Optics*, Adv. Mater. **30**, 1702669 (2018).
- [109] T. Koop, B. Luo, A. Tsias, and T. Peter, *Water Activity as the Determinant for Homogeneous Ice Nucleation in Aqueous Solutions*, Lett. to Nat. **406**, 611 (2000).
- [110] A. K. Kota, G. Kwon, W. Choi, J. M. Mabry, and A. Tuteja, *Hygro-Responsive Membranes for Effective Oil–Water Separation*, Nat. Commun. **3**, 1025 (2012).
- [111] C. T. Kresge, M. E. Leonowicz, W. J. Roth, J. C. Vartuli, and J. S. Beck, *Ordered Mesoporous Molecular Sieves Synthesized by a Liquid-Crystal Template Mechanism*, Nature **359**, 710 (1992).
- [112] M. Kruk, M. Jaroniec, and A. Sayari, *Application of Large Pore MCM-41 Molecular Sieves to Improve Pore Size Analysis Using Nitrogen Adsorption Measurements*, Langmuir **13**, 6267 (1997).
- [113] R. Kumar, S. Kumar, and V. R. Sinha, *Evaluation and Optimization of Water-in-Oil Microemulsion Using Ternary Phase Diagram and Central Composite Design*, J. Dispers. Sci. Technol. **37**, 166 (2016).
- [114] L. D. Landau and E. M. Lifshitz, *Course of Theoretical Physics: Vol. 5: Statistical Physics* (Pergamon Press, 1980).
- [115] P.-S. Laplace, *Supplément Au Dixième Livre Du Traité de Mécanique Céleste*, in *Traité de Mécanique Céleste: Vol. 4* (Courcier, 1805), pp. 1–79.
- [116] M. Lattuada and T. A. Hatton, *Synthesis, Properties and Applications of Janus*

*Nanoparticles*, Nano Today **6**, 286 (2011).

- [117] T. C. Laurent, B. N. Preston, and L.-O. Sundelöf, *Transport of Molecules in Concentrated Systems*, Nature **279**, 60 (1979).
- [118] B. Lefevre, A. Saugey, J. L. Barrat, L. Bocquet, E. Charlaix, P. F. Gobin, and G. Vigier, *Intrusion and Extrusion of Water in Hydrophobic Mesopores*, J. Chem. Phys. **120**, 4927 (2004).
- [119] B. Lefevre, A. Saugey, J. L. Barrat, L. Bocquet, E. Charlaix, P. F. Gobin, and G. Vigier, *Intrusion and Extrusion of Water in Highly Hydrophobic Mesoporous Materials: Effect of the Pore Texture*, Colloids Surfaces A Physicochem. Eng. Asp. **241**, 265 (2004).
- [120] K. Leung, A. Luzar, and D. Bratko, *Dynamics of Capillary Drying in Water*, Phys. Rev. Lett. **90**, 065502 (2003).
- [121] M. Li, L. Xu, and W. Lu, *Effect of Extra Gas Amount on Liquid Outflow from Hydrophobic Nanochannels: Enhanced Liquid–Gas Interaction and Bubble Nucleation*, Langmuir **36**, 4682 (2020).
- [122] M. Li, C. Zhan, and W. Lu, *Spontaneous Liquid Outflow from Hydrophobic Nanopores: Competing Liquid–Solid and Liquid–Gas Interactions*, Appl. Phys. Lett. **119**, 181603 (2021).
- [123] W. Li, X. Zuo, X. Zhou, and H. Lu, *Effect of Aggregated Gas Molecules on Dewetting Transition of Water between Nanoscale Hydrophobic Plates*, J. Chem. Phys. **150**, 104702 (2019).
- [124] F. Liu, H. J. Chung, and J. A. W. Elliott, *Freezing of Aqueous Electrolytes in Zinc–Air Batteries: Effect of Composition and Nanoscale Confinement*, ACS Appl. Energy Mater. **1**, 1489 (2018).
- [125] F. Liu, L. Zargarzadeh, H. J. Chung, and J. A. W. Elliott, *Thermodynamic Investigation of the Effect of Interface Curvature on the Solid-Liquid Equilibrium and Eutectic Point of Binary Mixtures*, J. Phys. Chem. B **121**, 9452 (2017).
- [126] A. K. Lugli, C. S. Yost, and C. H. Kindler, *Anaesthetic Mechanisms: Update on the Challenge of Unravelling the Mystery of Anaesthesia*, Eur. J. Anaesthesiol. **26**, 807

(2009).

- [127] C. C. M. Luijten and M. E. H. Van Dongen, *Nucleation at High Pressure. I. Theoretical Considerations*, J. Chem. Phys. **111**, 8524 (1999).
- [128] L. Lupi and V. Molinero, *Does Hydrophilicity of Carbon Particles Improve Their Ice Nucleation Ability?*, J. Phys. Chem. A **118**, 7330 (2014).
- [129] A. Luzar and D. Bratko, *Gas Solubility in Hydrophobic Confinement*, J. Phys. Chem. B **109**, 22545 (2005).
- [130] C. I. Lynch, S. Rao, and M. S. P. Sansom, *Water in Nanopores and Biological Channels: A Molecular Simulation Perspective*, Chem. Rev. **120**, 10298 (2020).
- [131] S. M. A. Malek, P. H. Poole, and I. Saika-Voivod, *Surface Tension of Supercooled Water Nanodroplets from Computer Simulations*, J. Chem. Phys. **150**, 234507 (2019).
- [132] V. Mani and K. K. Mohanty, *Effect of the Spreading Coefficient on Three-Phase Flow in Porous Media*, J. Colloid Interface Sci. **187**, 45 (1997).
- [133] C. Marangoni, *Sul Principio Della Viscosita' Superficiale Dei Liquidi Stabilito Dalsig. J. Plateau*, Nuovo Cim. **5–6**, 239 (1871).
- [134] C. Marangoni, *Ueber Die Ausbreitung Der Tropfen Einer Flüssigkeit Auf Der Oberfläche Einer Anderen*, Ann. Phys. **219**, 337 (1871).
- [135] G. M. Marion, R. E. Farren, and A. J. Komrowski, *Alternative Pathways for Seawater Freezing*, Cold Reg. Sci. Technol. **29**, 259 (1999).
- [136] V. Martínez-Gómez, R. Pérez-Garibay, and J. Rubio, *Factors Involving the Solids-Carrying Flotation Capacity of Microbubbles*, Miner. Eng. **53**, 160 (2013).
- [137] E. McCarthy, E. S. Fraga, and J. W. Ponton, *An Automated Procedure for Multicomponent Product Separation Synthesis*, Comput. Chem. Eng. **22**, S77 (1998).
- [138] D. T. McCoy, S. M. Burrows, R. Wood, D. P. Grosvenor, S. M. Elliott, P.-L. Ma, P. J. Rasch, and D. L. Hartmann, *Natural Aerosols Explain Seasonal and Spatial Patterns of Southern Ocean Cloud Albedo*, Sci. Adv. **1**, e1500157 (2015).
- [139] R. McGraw, *Dynamics of Barrier Crossing in Classical Nucleation Theory*, J. Phys.

- Chem. B **105**, 11838 (2001).
- [140] W. G. McMillan and J. E. Mayer, *The Statistical Thermodynamics of Multicomponent Systems*, J. Chem. Phys. **13**, 276 (1945).
- [141] M. Miyahara, H. Kanda, T. Yoshioka, and M. Okazaki, *Modeling Capillary Condensation in Cylindrical Nanopores: A Molecular Dynamics Study*, Langmuir **16**, 4293 (2000).
- [142] F. Mo, G. Liang, Q. Meng, Z. Liu, H. Li, J. Fan, and C. Zhi, *A Flexible Rechargeable Aqueous Zinc Manganese-Dioxide Battery Working at  $-20$  °C*, Energy Environ. Sci. **12**, 706 (2019).
- [143] E. B. Moore, E. de la Llave, K. Welke, D. A. Scherlis, and V. Molinero, *Freezing, Melting and Structure of Ice in a Hydrophilic Nanopore*, Phys. Chem. Chem. Phys. **12**, 4124 (2010).
- [144] Y. H. Mori, *Classification of Configurations of Two-Phase Vapor/Liquid Bubbles in an Immiscible Liquid in Relation to Direct-Contact Evaporation and Condensation Processes*, Int. J. Multiph. Flow **11**, 571 (1985).
- [145] Y. H. Mori, *Configurations of Gas-Liquid Two-Phase Bubbles in Immiscible Liquid Media*, Int. J. Multiph. Flow **4**, 383 (1978).
- [146] Y. H. Mori, N. Tsui, and M. Klyomlya, *Surface and Interfacial Tensions and Their Combined Properties in Seven Binary, Immiscible Liquid-Liquid-Vapor Systems*, J. Chem. Eng. Data **29**, 407 (1984).
- [147] A. N. Mun and R. S. Darer, *Cryoscopy of Aqueous Salt Solutions. II. Systems NaCl-MgCl<sub>2</sub>-H<sub>2</sub>O and KCl-MgCl<sub>2</sub>-H<sub>2</sub>O*, Zhurnal Neorg. Khimii **2**, 1658 (1957).
- [148] S. Nagelberg et al., *Reconfigurable and Responsive Droplet-Based Compound Micro-Lenses*, Nat. Commun. **8**, 14673 (2017).
- [149] G. Navascués and P. Tarazona, *Line Tension Effects in Heterogeneous Nucleation Theory*, J. Chem. Phys. **75**, 2441 (1981).
- [150] M. J. Neeson, R. F. Tabor, F. Grieser, R. R. Dagastine, and D. Y. C. Chan, *Compound Sessile Drops*, Soft Matter **8**, 11042 (2012).

- [151] C. E. Neuzil, *Osmotic Generation of “anomalous” Fluid Pressures in Geological Environments*, *Nature* **403**, 182 (2000).
- [152] Q. Nian, J. Wang, S. Liu, T. Sun, S. Zheng, Y. Zhang, Z. Tao, and J. Chen, *Aqueous Batteries Operated at  $-50\text{ }^{\circ}\text{C}$* , *Angew. Chemie Int. Ed.* **58**, 16994 (2019).
- [153] T. Nosoko and Y. H. Mori, *An Improved Method for Determining Equilibrium Spreading Coefficient of Oils on Water*, *J. Colloid Interface Sci.* **140**, 326 (1990).
- [154] C. S. Oakes, R. J. Bodnar, and J. M. Simonson, *The System NaCl-CaCl<sub>2</sub>-H<sub>2</sub>O: I. The Ice Liquidus at 1 Atm Total Pressure*, *Geochim. Cosmochim. Acta* **54**, 603 (1990).
- [155] G. Ortiz, H. Nouali, C. Marichal, G. Chaplais, and J. Patarin, *Versatile Energetic Behavior of ZIF-8 upon High Pressure Intrusion–Extrusion of Aqueous Electrolyte Solutions*, *J. Phys. Chem. C* **118**, 7321 (2014).
- [156] A. J. Page and R. P. Sear, *Heterogeneous Nucleation in and out of Pores*, *Phys. Rev. Lett.* **97**, 065701 (2006).
- [157] D. Peng and D. B. Robinson, *A New Two-Constant Equation of State*, *Ind. Eng. Chem. Fundam.* **15**, 59 (1976).
- [158] M. Pera-Titus, R. El-Chahal, V. Rakotovo, C. Daniel, S. Miachon, and J.-A. Dalmon, *Direct Volumetric Measurement of Gas Oversolubility in Nanoliquids: Beyond Henry’s Law*, *ChemPhysChem* **10**, 2082 (2009).
- [159] M. D. Petters and S. M. Kreidenweis, *A Single Parameter Representation of Hygroscopic Growth and Cloud Condensation Nucleus Activity*, *Atmos. Chem. Phys.* **7**, 1961 (2007).
- [160] G. G. Poon, *Extending Classical Nucleation Theory: Understanding the Effects of Trace Additives and Inhomogeneous Concentration Distributions* (PhD Thesis), University of California Santa Barbara, 2018.
- [161] J. M. Prausnitz, R. N. Lichtenthaler, and E. G. de Azevedo, *Molecular Thermodynamics of Fluid-Phase Equilibria*, 3rd ed. (Prantice Hall PTR, 1999).
- [162] R. C. Prickett, J. A. W. Elliott, S. Hakda, and L. E. McGann, *A Non-Ideal Replacement for the Boyle van’t Hoff Equation*, *Cryobiology* **57**, 130 (2008).

- [163] R. C. Prickett, J. A. W. Elliott, and L. E. McGann, *Application of the Multisolute Osmotic Virial Equation to Solutions Containing Electrolytes*, *J. Phys. Chem. B* **115**, 14531 (2011).
- [164] R. C. Prickett, J. A. W. Elliott, and L. E. McGann, *Application of the Osmotic Virial Equation in Cryobiology*, *Cryobiology* **60**, 30 (2010).
- [165] H. R. Pruppacher and J. D. Klett, *Microphysics of Clouds and Precipitation*, 2nd ed. (Kluwer Academic Publishers, 2004).
- [166] Y. Qiao, G. Cao, and X. Chen, *Effects of Gas Molecules on Nanofluidic Behaviors*, *J. Am. Chem. Soc.* **129**, 2355 (2007).
- [167] Y. Qiu and V. Molinero, *Morphology of Liquid–Liquid Phase Separated Aerosols*, *J. Am. Chem. Soc.* **137**, 10642 (2015).
- [168] S. Rao, C. I. Lynch, G. Klesse, G. E. Oakley, P. J. Stansfeld, S. J. Tucker, and M. S. P. Sansom, *Water and Hydrophobic Gates in Ion Channels and Nanopores*, *Faraday Discuss.* **209**, 231 (2018).
- [169] H. Renon and J. M. Prausnitz, *Local Compositions in Thermodynamic Excess Functions for Liquid Mixtures*, *AIChE J.* **14**, 135 (1968).
- [170] J. Reščič, V. Vlachy, A. Jamnik, and O. Glatter, *Osmotic Pressure, Small-Angle X-Ray, and Dynamic Light Scattering Studies of Human Serum Albumin in Aqueous Solutions*, *J. Colloid Interface Sci.* **239**, 49 (2001).
- [171] E. Rosky, W. Cantrell, T. Li, I. Nakamura, and R. A. Shaw, *Molecular Simulations Reveal That Heterogeneous Ice Nucleation Occurs at Higher Temperatures in Water under Capillary Tension*, *Atmos. Chem. Phys.* **23**, 10625 (2023).
- [172] L. U. Ross-Rodriguez, J. A. W. Elliott, and L. E. McGann, *Non-Ideal Solution Thermodynamics of Cytoplasm*, *Biopreserv. Biobank.* **10**, 462 (2012).
- [173] S. Ross and P. Becher, *The History of the Spreading Coefficient*, *J. Colloid Interface Sci.* **149**, 575 (1992).
- [174] R. Roth, D. Gillespie, W. Nonner, and R. E. Eisenberg, *Bubbles, Gating, and Anesthetics in Ion Channels*, *Biophys. J.* **94**, 4282 (2008).

- [175] G. Roudsari, O. H. Pakarinen, B. Reischl, and H. Vehkamäki, *Atomistic and Coarse-Grained Simulations Reveal Increased Ice Nucleation Activity on Silver Iodide Surfaces in Slit and Wedge Geometries*, *Atmos. Chem. Phys.* **22**, 10099 (2022).
- [176] A. D. Ryabtsev, N. P. Kotsupalo, A. A. Kurakov, N. M. Nemkov, and A. G. Vakhromeev, *Rational Use of Multicomponent Brines Extracted Together with Oil*, *Theor. Found. Chem. Eng.* **54**, 756 (2020).
- [177] S. A. Safran and L. A. Turkevich, *Phase Diagrams for Microemulsions*, *Phys. Rev. Lett.* **50**, 1930 (1983).
- [178] M. Sagir, M. Mushtaq, M. S. Tahir, M. B. Tahir, and A. R. Shaik, *Surfactant in Petroleum Industry*, in *Surfactants for Enhanced Oil Recovery Applications* (Springer, 2020).
- [179] D. Saulov, *On the Multicomponent Polynomial Solution Models*, *Calphad* **30**, 405 (2006).
- [180] L. L. Schramm, E. N. Stasiuk, and M. MacKinnon, *Surfactants in Athabasca Oil Sands Slurry Conditioning, Flotation Recovery, and Tailings Processes*, in *Surfactants: Fundamentals and Applications in the Petroleum Industry* (Cambridge University Press, 2000).
- [181] R. P. Sear, *Nucleation at Contact Lines Where Fluid-Fluid Interfaces Meet Solid Surfaces*, *J. Phys. Condens. Matter* **19**, 466106 (2007).
- [182] K. Semeniuk and A. Dastoor, *Current State of Atmospheric Aerosol Thermodynamics and Mass Transfer Modeling: A Review*, *Atmosphere (Basel)*. **11**, 156 (2020).
- [183] N. Shardt and J. A. W. Elliott, *Isobaric Vapor-Liquid Phase Diagrams for Multicomponent Systems with Nanoscale Radii of Curvature*, *J. Phys. Chem. B* **122**, 2434 (2018).
- [184] N. Shardt and J. A. W. Elliott, *Gibbsian Thermodynamics of Wenzel Wetting (Was Wenzel Wrong? Revisited)*, *Langmuir* **36**, 435 (2020).
- [185] N. Shardt and J. A. W. Elliott, *Gibbsian Thermodynamics of Cassie–Baxter Wetting (Were Cassie and Baxter Wrong? Revisited)*, *Langmuir* **34**, 12191 (2018).

- [186] N. Shardt and J. A. W. Elliott, *Thermodynamic Study of the Role of Interface Curvature on Multicomponent Vapor–liquid Phase Equilibrium*, *J. Phys. Chem. A* **120**, 2194 (2016).
- [187] D. Shin, J. Hwang, and W. Jhe, *Ice-VII-like Molecular Structure of Ambient Water Nanomeniscus*, *Nat. Commun.* **10**, 286 (2019).
- [188] F. L. Smith and A. H. Harvey, *Avoid Common Pitfalls When Using Henry’s Law*, *Chem. Eng. Prog.* **103**, 33 (2007).
- [189] R. Soltanpour, M. Irannajad, and F. Nakhaei, *Investigation of Effective Operating Parameters on Carrying Capacity in Column Flotation of Copper Sulfide Minerals*, *Part. Sci. Technol.* **37**, 677 (2019).
- [190] F. Staniscia and M. Kanduč, *Apparent Line Tension Induced by Surface-Active Impurities*, *J. Chem. Phys.* **157**, 184707 (2022).
- [191] D. Stoddart, A. J. Heron, E. Mikhailova, G. Maglia, and H. Bayley, *Single-Nucleotide Discrimination in Immobilized DNA Oligonucleotides with a Biological Nanopore*, *Proc. Natl. Acad. Sci. U. S. A.* **106**, 7702 (2009).
- [192] H. Su, C. A. Hurd Price, L. Jing, Q. Tian, J. Liu, and K. Qian, *Janus Particles: Design, Preparation, and Biomedical Applications*, *Mater. Today Bio* **4**, 100033 (2019).
- [193] V. Talanquer and D. W. Oxtoby, *Nucleation in a Slit Pore*, *J. Chem. Phys.* **114**, 2793 (2001).
- [194] H. Tan, S. Guo, N.-D. Dinh, R. Luo, L. Jin, and C.-H. Chen, *Heterogeneous Multi-Compartmental Hydrogel Particles as Synthetic Cells for Incompatible Tandem Reactions*, *Nat. Commun.* **8**, 663 (2017).
- [195] A. Tinti, A. Giacomello, Y. Grosu, and C. M. Casciola, *Intrusion and Extrusion of Water in Hydrophobic Nanopores*, *Proc. Natl. Acad. Sci. U. S. A.* **114**, E10266 (2017).
- [196] S. Torza and S. G. Mason, *Coalescence of Two Immiscible Liquid Drops*, *Science*. **163**, 813 (1969).
- [197] R. Vilcu, F. Irinei, and V. Isverceanu, *Thermodynamics of Multicomponent Electrolyte Solution. IV: Individual Activities in Electrolyte Solutions*, *Bull. Des Soc. Chim. Belges*



93, 261 (1984).

- [198] R. Vilcu and F. Stanciu, *Thermodynamic Properties of Aqueous Electrolyte Solutions II: Differential Cryoscopy of Sodium Chloride-Potassium Chloride and Potassium Bromide-Sodium Bromide Systems*, Rev. Roum. Chim. **13**, 253 (1968).
- [199] R. Vilcu and F. Stanciu, *Differential Cryoscopy in Ternary System*, Rev. Roum. Chim. **10**, 499 (1965).
- [200] B. Wang, D. A. Knopf, S. China, B. W. Arey, T. H. Harder, M. K. Gilles, and A. Laskin, *Direct Observation of Ice Nucleation Events on Individual Atmospheric Particles*, Phys. Chem. Chem. Phys. **18**, 29721 (2016).
- [201] C. A. Ward, A. Balakrishnan, and F. C. Hooper, *On the Thermodynamics of Nucleation in Weak Gas-Liquid Solutions*, J. Basic Eng. **92**, 695 (1970).
- [202] C. A. Ward, W. R. Johnson, R. D. Venter, S. Ho, T. W. Forest, and W. D. Fraser, *Heterogeneous Bubble Nucleation and Conditions for Growth in a Liquid-Gas System of Constant Mass and Volume*, J. Appl. Phys. **54**, 1833 (1983).
- [203] C. A. Ward and E. Levart, *Conditions for Stability of Bubble Nuclei in Solid Surfaces Contacting a Liquid-Gas Solution*, J. Appl. Phys. **56**, 491 (1984).
- [204] C. A. Ward and J. Wu, *Effect of Contact Line Curvature on Solid-Fluid Surface Tensions without Line Tension*, Phys. Rev. Lett. **100**, 256103 (2008).
- [205] T. Werder, J. H. Walther, R. L. Jaffe, T. Halicioglu, and P. Koumoutsakos, *On the Water-Carbon Interaction for Use in Molecular Dynamics Simulations of Graphite and Carbon Nanotubes*, J. Phys. Chem. B **107**, 1345 (2003).
- [206] L. Xu, M. Li, and W. Lu, *Time- and Pressure-Dependent Gas Diffusion in a Nanoconfined Liquid Phase*, J. Phys. Chem. C **125**, 5596 (2021).
- [207] N. Yabuuchi, K. Kubota, M. Dahbi, and S. Komaba, *Research Development on Sodium-Ion Batteries*, Chem. Rev. **114**, 11636 (2014).
- [208] Y. Yamada, K. Usui, K. Sodeyama, S. Ko, Y. Tateyama, and A. Yamada, *Hydrate-Melt Electrolytes for High-Energy-Density Aqueous Batteries*, Nat. Energy **1**, 16129 (2016).
- [209] K. Yamashita and H. Daiguji, *Molecular Dynamics Simulations of Water Uptake into a*

- Silica Nanopore*, J. Phys. Chem. C **119**, 3012 (2015).
- [210] S. Yan, X. Yang, Z. Bai, X. Xu, and H. Wang, *Drop Attachment Behavior of Oil Droplet-Gas Bubble Interactions during Flotation*, Chem. Eng. Sci. **223**, 115740 (2020).
- [211] G. Yang, D. Chai, Z. Fan, and X. Li, *Capillary Condensation of Single- And Multicomponent Fluids in Nanopores*, Ind. Eng. Chem. Res. **58**, 19302 (2019).
- [212] T. Young, *An Essay on the Cohesion of Fluids*, Philos. Trans. **95**, (1805).
- [213] C. Yu, J. Fan, B. Tian, D. Zhao, and G. D. Stucky, *High-Yield Synthesis of Periodic Mesoporous Silica Rods and Their Replication to Mesoporous Carbon Rods*, Adv. Mater. **14**, 1742 (2002).
- [214] H. Yu et al., *A Review of Measurement-Based Assessments of the Aerosol Direct Radiative Effect and Forcing*, Atmos. Chem. Phys. **6**, 613 (2006).
- [215] L. Zargarzadeh and J. A. W. Elliott, *Comparative Surface Thermodynamic Analysis of New Fluid Phase Formation between a Sphere and a Flat Plate*, Langmuir **29**, 3610 (2013).
- [216] L. Zargarzadeh and J. A. W. Elliott, *Surface Thermodynamic Analysis of Fluid Confined in a Cone and Comparison with the Sphere–Plate and Plate–Plate Geometries*, Langmuir **29**, 12950 (2013).
- [217] L. Zargarzadeh and J. A. W. Elliott, *Bubble Formation in a Finite Cone: More Pieces to the Puzzle*, Langmuir **35**, 13216 (2019).
- [218] L. Zargarzadeh and J. A. W. Elliott, *Thermodynamics of Surface Nanobubbles*, Langmuir **32**, 11309 (2016).
- [219] L. Zargarzadeh and J. A. W. Elliott, *Comparison of the Osmotic Virial Equation with the Margules Activity Model for Solid–Liquid Equilibrium*, J. Phys. Chem. B **123**, 1099 (2019).
- [220] L. D. Zarzar, V. Sresht, E. M. Sletten, J. A. Kalow, D. Blankschtein, and T. M. Swager, *Dynamically Reconfigurable Complex Emulsions via Tunable Interfacial Tensions*, Nature **518**, 520 (2015).

- [221] Q. Zhang, Y. Ma, Y. Lu, L. Li, F. Wan, K. Zhang, and J. Chen, *Modulating Electrolyte Structure for Ultralow Temperature Aqueous Zinc Batteries*, *Nat. Commun.* **11**, 4463 (2020).
- [222] Y. Zhang, A. Shitta, J. C. Meredith, and S. H. Behrens, *Bubble Meets Droplet: Particle-Assisted Reconfiguration of Wetting Morphologies in Colloidal Multiphase Systems*, *Small* **12**, 3309 (2016).
- [223] M. W. Zielinski, L. E. McGann, J. A. Nychka, and J. A. W. Elliott, *Nonideal Solute Chemical Potential Equation and the Validity of the Grouped Solute Approach for Intracellular Solution Thermodynamics*, *J. Phys. Chem. B* **121**, 10443 (2017).
- [224] M. W. Zielinski, L. E. McGann, J. A. Nychka, and J. A. W. Elliott, *Measurement of Grouped Intracellular Solute Osmotic Virial Coefficients*, *Cryobiology* **97**, 198 (2020).
- [225] M. W. Zielinski, L. E. McGann, J. A. Nychka, and J. A. W. Elliott, *Comment on "Determination of the Quaternary Phase Diagram of the Water–Ethylene Glycol–Sucrose–NaCl System and a Comparison between Two Theoretical Methods for Synthetic Phase Diagrams" *Cryobiology* 61 (2010) 52-57*, *Cryobiology* **70**, 287 (2015).
- [226] M. W. Zielinski, L. E. McGann, J. A. Nychka, and J. A. W. Elliott, *Comparison of Non-Ideal Solution Theories for Multi-Solute Solutions in Cryobiology and Tabulation of Required Coefficients*, *Cryobiology* **69**, 305 (2014).
- [227] M. W. Zielinski, L. E. McGann, J. A. Nychka, and J. A. W. Elliott, *Cryobiology Comparison of Non-Ideal Solution Theories for Multi-Solute Solutions in Cryobiology and Tabulation of Required Coefficients*, *Cryobiology* **69**, 305 (2014).
- [228] A. Zuend and J. H. Seinfeld, *Modeling the Gas-Particle Partitioning of Secondary Organic Aerosol: The Importance of Liquid-Liquid Phase Separation*, *Atmos. Chem. Phys.* **12**, 3857 (2012).
- [229] W. M. Haynes, editor, *Vapor Pressure and Other Saturation Properties of Water*, in *CRC Handbook of Chemistry and Physics*, 95th ed. (CRC Press, 2015).
- [230] W. M. Haynes, editor, *Concentrative Properties of Aqueous Solutions: Density, Refractive Index, Freezing Point Depression, and Viscosity*, in *CRC Handbook of Chemistry and Physics*, 95th ed. (CRC Press, 2015).

# Appendices

# Appendix A

## Supplementary Information for Chapter 3

### A.1 Description of the thermodynamic model

#### A.1.1 NRTL activity model

In the nonrandom two-liquid (NRTL) model [32], the activity coefficients are related to the concentration of species through the following equations:

$$\ln \gamma_1 = x_2^2 \left[ \tau_{21} \left( \frac{G_{21}}{x_1 + x_2 G_{21}} \right)^2 + \frac{\tau_{12} G_{12}}{(x_2 + x_1 G_{12})^2} \right] \quad (\text{A-1})$$

$$\ln \gamma_2^* = x_1^2 \left[ \tau_{12} \left( \frac{G_{12}}{x_2 + x_1 G_{12}} \right)^2 + \frac{\tau_{21} G_{21}}{(x_1 + x_2 G_{21})^2} \right] - (\tau_{12} + \tau_{21} G_{21}) \quad (\text{A-2})$$

with

$$G_{12} = \exp(-\alpha_{12} \tau_{12}) \quad (\text{A-3})$$

$$G_{21} = \exp(-\alpha_{21} \tau_{21}) \quad (\text{A-4})$$

where  $\alpha_{12}$  and  $\alpha_{21}$  are the nonrandomness parameters. The NRTL interaction parameters,  $\tau_{12}(T)$  and  $\tau_{21}(T)$ , are adjustable parameters in practice that are only functions of temperature.

For carbon dioxide in water, we take  $\alpha_{12} = \alpha_{21} = 0.3$  since it is a polar–nonpolar mixture and use the interaction parameters from Hou *et al.* [20]:

$$\tau_{12} = 3.720 - \frac{803.18}{T} + 21.13 \left( \frac{T_0 - T}{T} + \ln \frac{T}{T_0} \right) \quad (\text{A-5})$$

$$\tau_{21} = 18.664 - \frac{5549.77}{T} - 112.67 \left( \frac{T_0 - T}{T} + \ln \frac{T}{T_0} \right) \quad (\text{A-6})$$

where  $T$  (K) is the temperature and  $T_0 = 298.15$  K. Due to its low solubility even at high pressures, for nitrogen in water we use  $\tau_{21} = \tau_{12} = 0$ , which means  $\gamma_1 = \gamma_2^* = 1$ .

#### A.1.2 Peng–Robinson EOS

To calculate the fugacity coefficients in the vapor phase, we use the Peng–Robinson cubic equation of state (P–R EOS) [30]. For the vapor phase of a pure component, it is written as

$$P^V = \frac{\bar{R}T}{v^{\text{PR}} - b^{\text{PR}}} - \frac{a^{\text{PR}}(T)}{v^{\text{PR}}(v^{\text{PR}} + b^{\text{PR}}) + b^{\text{PR}}(v^{\text{PR}} - b^{\text{PR}})} \quad (\text{A-7})$$

where  $v^{\text{PR}}$  is the molar volume, and  $a^{\text{PR}}$  and  $b^{\text{PR}}$  are the energy and co-volume parameters defined below:

$$a^{\text{PR}} = \frac{0.457235(\bar{R}T_c)^2 \alpha(T)}{P_c} \quad (\text{A-8})$$

where  $T_c$  (K) and  $P_c$  (Pa) are the critical temperature and pressure, respectively, and

$$\alpha(T) = \left[ 1 + (0.37464 + 1.54226\omega - 0.26992\omega^2) \left( 1 - \sqrt{\frac{T}{T_c}} \right) \right]^2 \quad (\text{A-9})$$

where  $\omega$  is the acentric factor.  $b^{\text{PR}}$  is defined as

$$b^{\text{PR}} = \frac{0.077796\bar{R}T_c}{P_c} \quad (\text{A-10})$$

Using mixing rules, the P–R EOS can be extended to mixtures. The classical mixing rules are (written for the vapor phase) [30,31]:

$$a^{\text{PR}} = \sum_i \sum_j y_i y_j a_{ij}^{\text{PR}} \quad (\text{A-11})$$

$$a_{ij}^{\text{PR}} = (1 - k_{ij}) \sqrt{a_i a_j} \quad (\text{A-12})$$

$$b^{\text{PR}} = \sum_i \sum_j \frac{y_i y_j (b_i + b_j)}{2} \quad (\text{A-13})$$

where  $k_{ij}$  is the binary interaction parameter.  $a_i$  and  $b_i$  are the energy and co-volume parameters for pure components, as given by Equations (A-8) and (A-10). By substituting Equations (A-11) and (A-13) into Equation (A-7), it describes the vapor phase of a mixture.

Equation (A-7) is equivalent to solving the following cubic equation [30]

$$\begin{aligned} Z^3 - (1 - B^{\text{PR}})Z^2 + [A^{\text{PR}} - 3(B^{\text{PR}})^2 - 2B^{\text{PR}}]Z \\ - [A^{\text{PR}}B^{\text{PR}} - (B^{\text{PR}})^2 - (B^{\text{PR}})^3] = 0 \end{aligned} \quad (\text{A-14})$$

where  $Z$  is the vapor phase compressibility factor defined as

$$Z = \frac{P^V v^{PR}}{\bar{R}T} \quad (\text{A-15})$$

and the parameters  $A^{PR}$  and  $B^{PR}$  are defined as

$$A^{PR} = \frac{a^{PR} P^V}{(\bar{R}T)^2} \quad (\text{A-16})$$

$$B^{PR} = \frac{b^{PR} P^V}{\bar{R}T} \quad (\text{A-17})$$

Finally, the fugacity coefficients are related to the compressibility and the concentration through the following relation [30]

$$\ln \hat{\phi}_i^V = \frac{b_i^{PR}}{b^{PR}} (Z - 1) - \ln(Z - B^{PR}) - \frac{A^{PR}}{2\sqrt{2}B^{PR}} \left( \frac{2 \sum_k y_k a_{ki}^{PR}}{a^{PR}} - \frac{b_i^{PR}}{b^{PR}} \right) \ln \left[ \frac{Z + (1 + \sqrt{2})B^{PR}}{Z + (1 - \sqrt{2})B^{PR}} \right] \quad (\text{A-18})$$

where  $\hat{\phi}_i^V$  is the fugacity coefficient of component  $i$  in the vapor phase. The required parameters for the systems of interest in this work are given in Table A-1 [25].

Table A-1. Parameters for P–R EOS calculations [25].

Component	$T_c$ (K)	$P_c$ (MPa)	$\omega$
water	647.10	22.064	0.3443
nitrogen	126.19	3.3958	0.0372
carbon dioxide	304.13	7.3773	0.2239

We use constant (temperature-independent) interaction parameters from Søreide *et al.* [37] for both systems:  $k_{\text{H}_2\text{O}-\text{N}_2} = 0.4778$  and  $k_{\text{H}_2\text{O}-\text{CO}_2} = 0.1896$ .

### A.1.3 Calculating $\phi_{1,\text{sat}}$ , $H_{12}$ , $\bar{v}_{2,\infty}^L$ , $P_{1,\text{sat}}$ , and $v_{1,\text{sat}}^L$

To calculate the fugacity coefficient of the vapor of pure water at saturation,  $\phi_{1,\text{sat}}$ , we use the correlation from Hass [19]:

$$\phi_{1,\text{sat}} = \exp \left( \frac{10P_{1,\text{sat}}p_0 + 5P_{1,\text{sat}}^2\bar{T}^6p_1 + 2P_{1,\text{sat}}^5\bar{T}^{24}p_2}{46.151T} \right) \quad (\text{A-19})$$

with

$$p_0 = 0.512004 - 1.191807\bar{T} + 2.599832\bar{T}^2 - 21.433083\bar{T}^3 + 15.281761\bar{T}^4 - 2.527165\bar{T}^5 - 2.454047\bar{T}^6 \quad (\text{A-20})$$

$$p_1 = 0.661366 - 3.258346\bar{T} + 6.393115\bar{T}^2 - 6.447504\bar{T}^3 + 3.202128\bar{T}^4 - 0.514945\bar{T}^5 - 0.120192\bar{T}^6 \quad (\text{A-21})$$

$$p_3 = (8.44104 + 28.86344\bar{T} - 270.10366\bar{T}^2 + 624.08835\bar{T}^3 - 675.70455\bar{T}^4 + 363.16788\bar{T}^5 - 79.26405\bar{T}^6) \times 10^{-6} \quad (\text{A-22})$$

where  $T$  (K) is the temperature and  $\bar{T} = T/500$ .

We calculate Henry's law constant,  $H_{12}$ , for nitrogen in water from the correlation of Harvey [18] using the improved parameters of Prini *et al.* [11] (given in units of Pa):

$$H_{12} = P_{1,\text{sat}} \exp \left[ -\frac{9.67578}{T_r} + 4.72162 \frac{(1 - T_r)^{0.355}}{T_r} + 11.70585 T_r^{-0.41} \exp(1 - T_r) \right] \quad (\text{A-23})$$

where  $T$  (K) is the temperature,  $P_{1,\text{sat}}$  (Pa) is the saturation vapor pressure of pure water at  $T$ , and  $T_r = T/647.1$ .

We calculate Henry's law constant,  $H_{12}$ , for carbon dioxide in water using the correlation of Hou *et al.* [20] (given in units of Pa):

$$H_{12} = 10^6 \exp \left[ -6.1384 + 42.842 \left( \frac{T_0}{T} \right) - 44.358 \left( \frac{T_0}{T} \right)^2 + 12.786 \left( \frac{T_0}{T} \right)^3 \right] \quad (\text{A-24})$$

where  $T$  (K) is the temperature and  $T_0 = 298.15$  K.

We find the infinite dilution partial molar volume of nitrogen in water,  $\bar{v}_{2,\infty}^L$ , from the correlation of Sun [39] (given in units of  $\text{m}^3/\text{mol}$ ):

$$\bar{v}_{2,\infty}^L = \bar{R} \left( 2.3546047 \times 10^{-5} - 1.04544 \times 10^{-14} P^L - 4.3078 \times 10^{-7} T - 8.09187 \times 10^{-7} \frac{T}{680 - T} + 6.474123 \times 10^{-8} T \ln T \right) \quad (\text{A-25})$$

where  $T$  (K) is the temperature and  $P^L$  (Pa) is the liquid pressure.

For carbon dioxide in water, we calculate the infinite dilution partial molar volume of the gas using the correlation of Sedlbauer *et al.* [36] (given in units of  $\text{m}^3/\text{mol}$ ):



$$\begin{aligned}
\bar{v}_{2,\infty}^L = & \kappa_{T,1} \bar{R}T + 0.5558(v_1^L - \kappa_{T,1} \bar{R}T) \\
& + \kappa_{T,1} \bar{R}T \rho_1 \left\{ 3.3921 \times 10^{-3} \right. \\
& - 1.3880 \times 10^{-5} \exp\left(\frac{1500}{T}\right) \\
& + 1.4801 \times 10^{-4} [\exp(0.005\rho_1) - 1] \\
& \left. + 1.2 \times 10^{-3} [\exp(-0.01\rho_1) - 1] \right\}
\end{aligned} \tag{A-26}$$

where  $\kappa_{T,1}$  ( $\text{Pa}^{-1}$ ) is the isothermal compressibility,  $v_1^L$  ( $\text{m}^3/\text{mol}$ ) is the molar volume, and  $\rho_1$  ( $\text{kg}/\text{m}^3$ ) is the mass density of pure liquid water at  $T$  (K) and  $P^L$  (Pa). The values of  $\kappa_{T,1}$ ,  $v_1^L$ , and  $\rho_1$  as well as the saturation properties,  $P_{1,\text{sat}}$  and  $v_{1,\text{sat}}^L$ , for water are taken from REFPROP 10 [25]. Note that, for ease of reference, we generated look-up tables using REFPROP 10 [25] for the properties of interest at each temperature used in our work. In these tables, we set the pressure increment to 0.1 MPa and used linear interpolation for in-between values.

The plots of molar volumes as functions of pressure at three different temperatures are given in Figure A-1. In all cases, the linear (or close to linear) dependence on pressure allows us to evaluate the molar volume integrals in the phase equilibrium equations [Equations (3-13) and (3-22)] by the trapezoidal rule,  $\int_{c_1}^{c_2} f(x) dx \approx [f(c_1) + f(c_2)](c_2 - c_1)/2$ , without loss of accuracy.

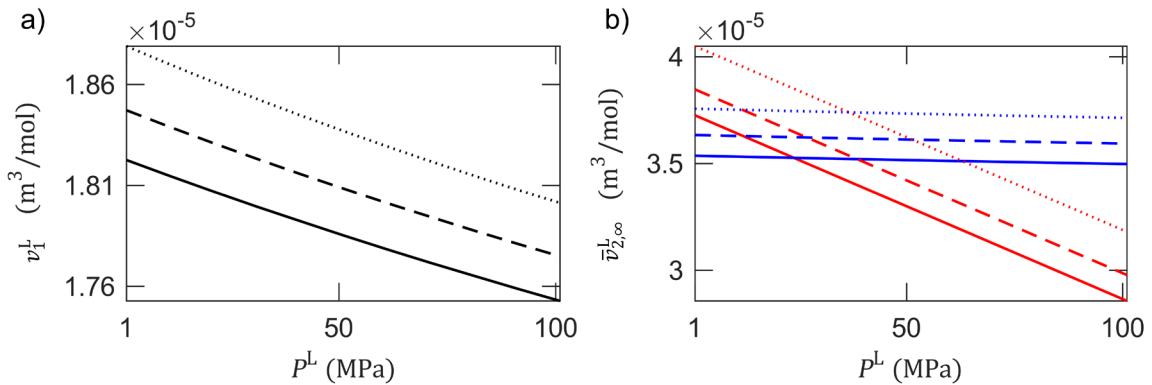


Figure A-1. Plots of molar volumes as functions of pressure at three different temperatures:  $T = 323.15$  K (solid lines),  $T = 348.15$  K (dashed lines), and  $T = 373.15$  K (dotted lines). Panel (a) shows the plots of pure liquid water molar volume,  $v_1^L$ , and panel (b) shows the plots of infinite dilution partial molar volume,  $\bar{v}_{2,\infty}^L$ , for nitrogen in water (red lines) and for carbon dioxide in water (blue lines).

### A.1.4 Validation of the thermodynamic model

We plot the mutual solubilities of nitrogen–water and carbon dioxide–water systems at three different temperatures and at high pressures (up to 100 MPa) in Figure A-2 and Figure A-3, respectively, as calculated from the (nonideal) model described in this work. Some experimental data points from the literature are also shown for comparison. Overall, although it is relatively simple, the model captures the behavior of both systems in the entire pressure range accurately enough for our purposes.

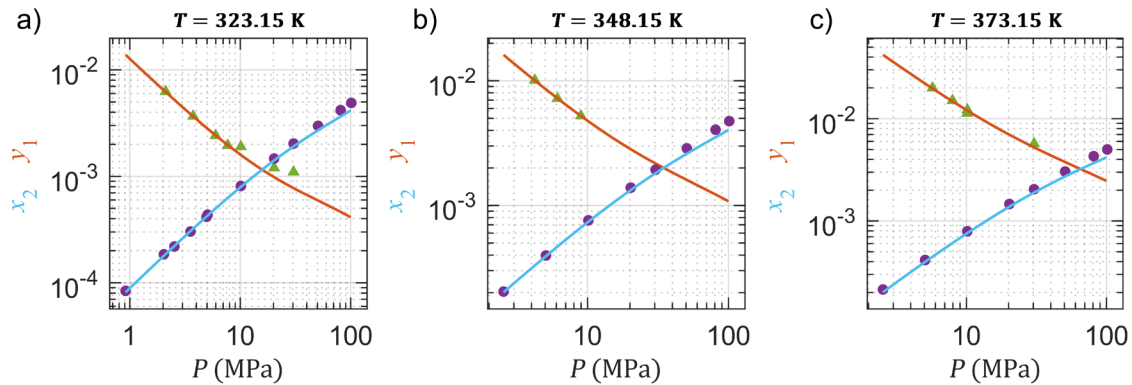


Figure A-2. Mutual solubilities of nitrogen and water as functions of pressure at three different temperatures: (a)  $T = 323.15$  K, (b)  $T = 348.15$  K, and (c)  $T = 373.15$  K. The orange lines show the mole fraction of water in vapor phase,  $y_1$ , and light blue lines show the mole fraction of nitrogen in the liquid phase,  $x_2$ , as calculated from the model described in this work. The green markers are the experimental data points for the water concentration in the vapor phase and violet markers are the experimental data points for the gas concentration in the liquid phase from the literature [6,33,34,46] as compiled in reference [1].

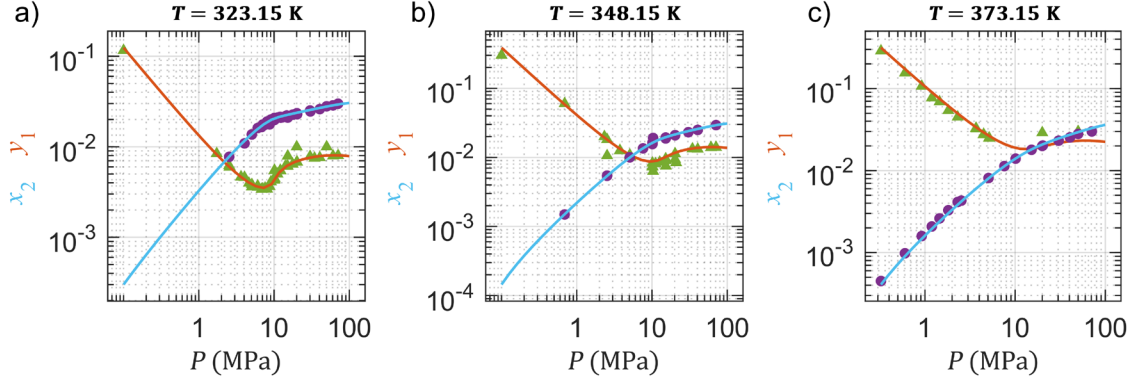


Figure A-3. Mutual solubilities of carbon dioxide and water as functions of pressure at three different temperatures: (a)  $T = 323.15$  K, (b)  $T = 348.15$  K, and (c)  $T = 373.15$  K. The orange lines show the mole fraction of water in the vapor phase,  $y_1$ , and the light blue lines show the mole fraction of carbon dioxide in the liquid phase,  $x_2$ , as calculated from the model described in this work. The green markers are the experimental data points for the water concentration in the vapor phase and the violet markers are the experimental data points for the gas concentration in the liquid phase from the literature [2,5,7–9,15,21,27,35,40,44,45] as compiled in reference [38].

## A.2 Solution procedure for the system of equations

In general, at a fixed temperature, there are eleven equations that need to be solved simultaneously for thermodynamic equilibrium:

$$\left\{ \begin{array}{l} \text{Equation (3-12)} \\ \text{Equation (3-21)} \\ \text{Equation (A-14)} \\ x_1 + x_2 = 1 \\ y_1 + y_2 = 1 \\ \gamma_1 = \gamma_1(x_1, x_2) \\ \gamma_2^* = \gamma_2^*(x_1, x_2) \\ \hat{\phi}_1^V = \hat{\phi}_1^V(P^V, Z, y_1, y_2) \\ \hat{\phi}_2^V = \hat{\phi}_2^V(P^V, Z, y_1, y_2) \\ v_1^L = v_1^L(P^L) \\ \bar{v}_{2,\infty}^L = \bar{v}_{2,\infty}^L(P^L) \end{array} \right. \quad (\text{A-27})$$

However, there are thirteen unknowns:  $P^L$ ,  $P^V$ ,  $Z$ ,  $x_1$ ,  $x_2$ ,  $y_1$ ,  $y_2$ ,  $\hat{\phi}_1^V$ ,  $\hat{\phi}_2^V$ ,  $\gamma_1$ ,  $\gamma_2^*$ ,  $v_1^L$ , and  $\bar{v}_{2,\infty}^L$ . This means that two more equations are required to close the system of equations. We have four cases that are relevant in this work:

- (i) to solve for saturation across a flat interface

- Step 1. fix the system pressure at  $P^L = P^V = \text{constant}$  (when pressure is known) or fix the gas concentration at  $x_2 = \text{constant}$  and set  $P^L = P^V$  (when concentration is known)
- Step 2. solve the system of Equations (A-27)
- (ii) to find the free-energy barrier for the given pore size at fixed gas concentration and liquid pressure
- Step 1. fix the gas concentration at  $x_2 = \text{constant}$  and the liquid pressure at  $P^L = \text{constant}$
- Step 2. find the vapor pressure,  $P^V$ , by solving the system of Equations (A-27)
- Step 3. find the curvature,  $k_c$ , of the corresponding shape using Equation (3-7) [or Equation (3-23)]
- Step 4. find the shape and its energy,  $\Delta B_c$ , for the prescribed curvature and pore radius by interpolating in the geometry data from Surface Evolver
- (iii) to find the extrusion pressure for the given pore size at fixed gas concentration
- Step 1. fix the gas concentration at  $x_2 = \text{constant}$  and take the free-energy barrier to be  $\Delta B_c = 35k_B T$
- Step 2. find the corresponding nucleus curvature,  $k_c$ , by interpolating in the geometry data from Surface Evolver for the specified pore radius
- Step 3. use Equation (3-7) to find  $P^V - P^L = \text{constant}$
- Step 4. solve the system of Equations (A-27) to find  $P_{\text{ext}} = P^L$
- (iv) to find the required gas concentration to empty a given pore at fixed liquid pressure
- Step 1. fix the liquid pressure  $P^L = P_{\text{ext}} = \text{constant}$  and take the free-energy barrier to be  $\Delta B_c = 35k_B T$
- Step 2. find the corresponding nucleus curvature,  $k_c$ , by interpolating in the geometry data from Surface Evolver for the specified pore radius
- Step 3. use Equation (3-7) to determine the vapor pressure,  $P^V$
- Step 4. solve the system of Equations (A-27) to find the gas concentration,  $x_2$

The system of Equations (A-27) is solved numerically with MATLAB (v. 2021a, Natick, MA, USA) using the built-in solver *vpasolve()* by providing physically appropriate ranges for the variables. The pressure dependence of the molar volume of pure water and the partial molar volume of carbon dioxide is implicit and complicated. However, they are much

weaker functions of pressure compared to the partial molar volume of nitrogen (see Figure A-1). If the liquid pressure is an unknown that is to be found by solving the system of equations [*e.g.*, extrusion pressure calculations; see (iii) above], the molar volume of water and the partial molar volume of carbon dioxide are fixed at  $P_{1,\text{sat}}$  as constants. For the nitrogen–water system, since  $\bar{v}_{2,\infty}^L$  is explicitly given as a linear function of pressure, only water molar volume is fixed at  $P_{1,\text{sat}}$ .

### A.3 Analytical solution of the symmetric nucleus profile

It is possible to develop an analytical solution for the shape of the critical nucleus by requiring it to have rotational symmetry with the axis of symmetry being the cylinder axis and solving the variational problem (*i.e.*, the Euler–Lagrange equation). This solution is given by Lefevre *et al.* [24], and the final equation for the profile is (translated to our notation)

$$d(r) = \pm \int_c^r \frac{2\cos\theta_{\text{eq}} + R_p k_c (x^2 - 1)}{\sqrt{4x^2 - [2\cos\theta_{\text{eq}} + R_p k_c (x^2 - 1)]^2}} dx \quad (\text{A-28})$$

where the magnitude of  $d(r)$  is the distance to the liquid–vapor interface from a circle of radius  $r$  on the radial plane whose center is on the cylinder axis.  $x$  is an integration variable, and the lower bound of integration,  $c$ , is given as

$$c = \frac{\sqrt{1 - R_p k_c (\cos\theta_{\text{eq}} - R_p k_c)} - 1}{R_p k_c} \quad (\text{A-29})$$

Equation (A-28) is integrated numerically. Example profiles calculated using Equation (A-28) are shown in Figure 3-3 (c).

### A.4 Pore size distribution data from Li *et al.* [26]

The normalized pore volume distribution data from Li *et al.* [26] is given in Figure A-4 (a) (manually digitized) for which the reported volume-based mean is 6 nm. We converted this data to a number distribution by dividing each data point by  $\pi R_p^2 l_p$  where  $l_p$  is the pore length assumed to be a constant (independent of  $R_p$ ). This distribution data is for the raw hydrophilic material as received. To make the pores hydrophobic, the pore surfaces were coated with a thin

layer of chloro(dimethyl)octylsilane. Although the authors do not mention the pore size distribution after this step, we could estimate the thickness of the applied layer using the method of Fadeev *et al.* [10]. Due to the structural differences in the arrangement of the molecules in this layer, the layer thickness is about one third of the radius for pores smaller than  $\sim 2.5$  nm in radius and  $\sim 1$  nm for larger pores. In order to have a continuous variation, we chose a slightly higher cut-off value at  $R_p = 3$  nm and subtracted the layer thickness from the pore radii.

After transforming the data, we fitted a continuous distribution curve to this data using MATLAB's (v. 2021a, Natick, MA, USA) built-in distribution fitter *fitdist()*. This function fits a chosen distribution to data using maximum likelihood estimation. Among many common distribution types tried, the Weibull distribution fitted the data best (*i.e.*, the lowest root-mean-square deviation) with the number-based mean of  $2.5 \times 10^{-9}$  m and the variance of  $3.1 \times 10^{-18}$  m<sup>2</sup>. The fitted curve is shown in Figure A-4 (b) (black line) together with the transformed data. Using the fitted distribution, we could generate a collection of pores mimicking the samples in the experiments and simulate the intrusion–extrusion curves.

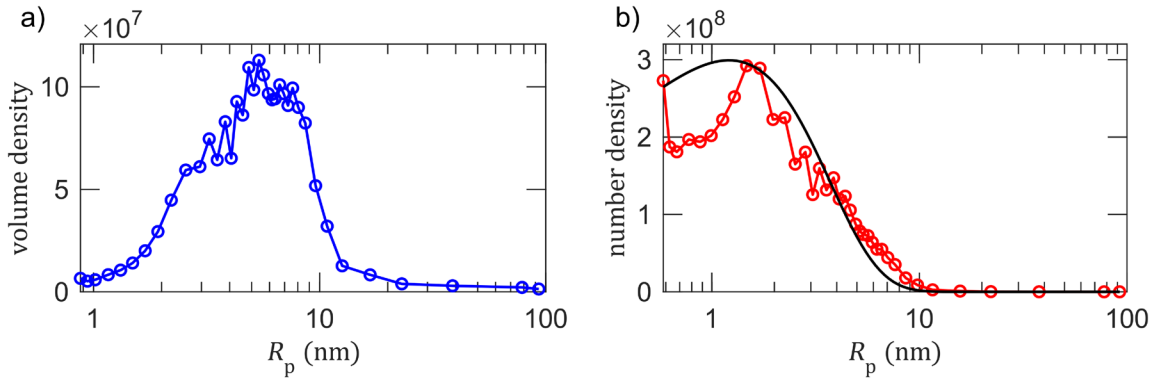


Figure A-4. Pore size distribution data from the work of Li *et al.* [26]. (a) Volume density data as originally reported but normalized. (b) Transformed number density data with hydrophobic layer thickness subtracted (red) and fitted with a continuous distribution curve (black line). All curves (both data curves and the fitted curve) are normalized in the data range to unity.

# Appendix B

## Supplementary Information for Chapter 4

### B.1 Surface Evolver calculation details

We use the Surface Evolver (SE) code [3] to calculate the nontrivial shapes of the asymmetric nucleus and bridge geometries. Surface Evolver is a special software package designed for complex variational problems involving surface forces. The surface is represented as a simplicial complex using triangles, which are moved towards the equilibrium shape with the built-in gradient descent or conjugate gradient methods. The basic elements of geometry are the vertices, edges, and triangle facets. Additionally, level set constraints with prescribed contact angles can be included. For stability and speed, the facets on the constraints are not included and their areas are calculated using appropriate line integrals along the edges on the constraints using Stokes's theorem (see below). Furthermore, the volumes are calculated by evaluating surface integrals according to the Divergence theorem, which are also converted to line integrals on the constraints. For numerical stability, it is better to evolve the shape with a prescribed volume and obtain the curvature, than prescribing the curvature to obtain the volume.

Below we give a brief summary of the main ideas from the SE manual [4] relevant to our work. For more details, see the manual [4].

In general, the volume of a body  $B$  is

$$V = \iiint_B 1 dx dy dz \quad (\text{B-1})$$

Surface Evolver replaces this integral with a double integral around the body boundary  $\partial B$  using the Divergence theorem:

$$V = \iint_{\partial B} z \vec{k} \cdot \vec{N} dA \quad (\text{B-2})$$

since  $\nabla \cdot z\vec{k} = 1$ . We denote the unit vectors with  $\vec{i}$ ,  $\vec{j}$ , and  $\vec{k}$  in the  $x$ ,  $y$ , and  $z$  directions, respectively. Taking the upward pointing normal, SE actually calculates

$$V = \iint_{\partial B} z dx dy \quad (\text{B-3})$$

The volume contributions of explicitly given facets are automatically handled by SE. Since the facets on the constraints are omitted, compensating integrals should be specified, which are evaluated as line integrals over the oriented edges on constraints using Stokes's theorem.

Let  $S$  be a portion of  $\partial B$  that lies on the level set constraint  $F(x, y, z) = 0$  with  $\partial S$  being its oriented boundary, oriented counterclockwise with respect to the unit normal vector  $\vec{N}$ . Because  $\nabla \cdot z\vec{k} \neq 0$ , there does not exist a vector field whose curl is equal to  $z\vec{k}$  [because  $\nabla \cdot (\nabla \times \vec{w}) = 0$  should hold for any  $\vec{w}$ ]. To be able to use Stokes's theorem, the implicit equation of the constraint should be solved explicitly for  $z = f(x, y)$ . Then the volume contribution can be calculated as

$$\iint_S f\vec{k} \cdot \vec{N} dA = \int_{\partial S} \vec{w} \cdot d\vec{l} \quad (\text{B-4})$$

for some vector field  $\vec{w}$  with  $f\vec{k} = \nabla \times \vec{w}$ . It remains to solve this equation for  $\vec{w}$ , which has many solutions all differing by a gradient of some scalar function. One convenient solution is to take  $\vec{w} = \langle M(x, y), N(x, y), 0 \rangle$  with  $f(x, y) = \frac{\partial N}{\partial x} - \frac{\partial M}{\partial y}$ . This still does not have a unique solution. For rotationally symmetric problems around the  $z$ -axis, one convenient solution is to take [4]

$$\vec{w} = g(t)(-y\vec{i} + x\vec{j}) \quad (\text{B-5})$$

where  $t = x^2 + y^2$ . Then, using the chain rule on  $t$  and denoting  $h(t) = f(x, y)$ , we can obtain [4]

$$g(t) = \frac{1}{2t} \int h(t) dt \quad (\text{B-6})$$

Once  $g(t)$  is found, the definition of  $t$  can be substituted back in, and using  $F(x, y, z) = 0$ , it can be further simplified, if needed, obtaining  $\vec{w}$ . The integration constant can be determined from the knowledge of the expected behavior of the vector field at certain points (e.g., the integral of  $\vec{w}$  vanishes at  $z = 0$ ).



Similarly, SE takes care of the areas of explicitly given facets. For areas on the constraints, we again want to use Stokes's theorem [4]:

$$A = \iint_S 1 dA = \iint_S \vec{v} \cdot \vec{N} dA = \int_{\partial S} \vec{w} \cdot d\vec{l} \quad (\text{B-7})$$

with  $\vec{v} \cdot \vec{N} = 1$ ,  $\nabla \cdot \vec{v} = 0$ , and  $\vec{v} = \nabla \times \vec{w}$ . Using  $z = f(x, y)$  and

$$\vec{v} = \sqrt{1 + \left(\frac{\partial f}{\partial x}\right)^2 + \left(\frac{\partial f}{\partial y}\right)^2} \vec{k} \quad (\text{B-8})$$

rotationally symmetric  $\vec{w}$  can be found by integrating in the same way as the volume calculation. The vector field solutions to the above problems for volume and areas are directly used in the SE datafile.

### ***B.1.1 Calculating the asymmetric nucleus shape***

In the top row of Figure B-1, different views of the initial geometry of the shape for the asymmetric nucleus are shown. The cylinder (*i.e.*, pore) axis is the  $z$ -axis and its radius is 1. The radius of the meniscus sphere is  $R_s = 1/\cos \alpha$ . The center of the sphere is placed at  $x = 0$ ,  $y = 0$ , and  $z = R_s$  so that its lowest point in the  $z$  direction is at  $x = 0$ ,  $y = 0$ , and  $z = 0$ . With this setup, the above-described method for the volume integrand on the sphere yields

$$\vec{w} = \left[ \frac{R_s^2}{3(2R_s - z)} - \frac{R_s}{2} - z \right] (-y\vec{i} + x\vec{j}) \quad (\text{B-9})$$

and for the area integrand on the sphere, it yields

$$\vec{w} = -\frac{R_s}{2R_s - z} (-y\vec{i} + x\vec{j}) \quad (\text{B-10})$$

The volume contribution of the cylinder is zero because it is parallel to the  $z$ -axis. The area integrand for the cylinder is found as

$$\vec{w} = z(-y\vec{i} + x\vec{j}) \quad (\text{B-11})$$

An example evolved shape is shown in the bottom row of Figure B-1.

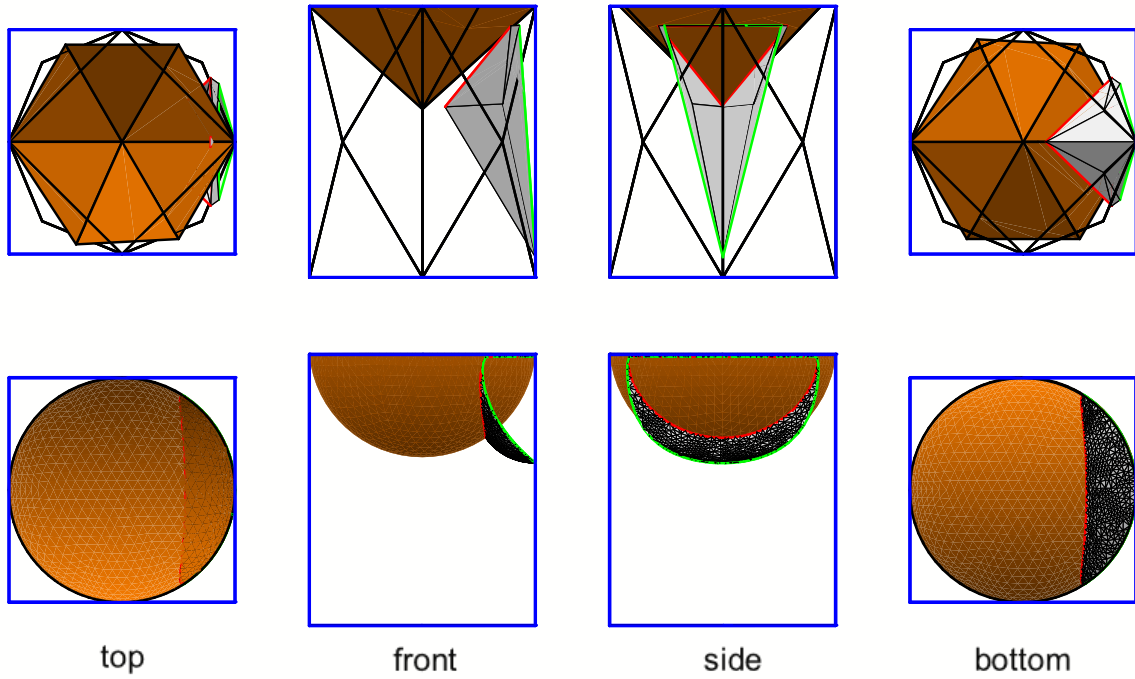


Figure B-1. Different views of an example asymmetric nucleus geometry at the meniscus before (top row) and after (bottom row) the evolution with SE. The cylinder wall and the edges on the meniscus are not shown after the evolution for clarity. The radius of the cylinder is  $R_p = 1$  and the volume of the nucleus was set to  $\tilde{V}_{\text{nuc}}^{S^*} = 0.2$ . The meniscus–nucleus contact angle is  $\beta = 90^\circ$  and the contact line is highlighted in red. The cylinder–nucleus contact angle is also  $\varphi = 90^\circ$  and the contact line is highlighted in green. The meniscus angle is  $\alpha = 5^\circ$ . Note that the initial shape is not required to have the correct, prescribed volume.

### B.1.2 Calculating the bridge geometries

Different views of the initial geometry of the shapes for the bridging of two pores and three pores are shown in the top rows of Figure B-2 and Figure B-3, respectively. In both cases, the surface of the porous particle was placed at the  $z = 0$  plane. The shapes were pinned at the pore mouths and only the portions of the shapes between the pores were required to meet with the particle surface at the angle  $\theta$ . The pores centers are  $\tilde{l}$  apart and the pores have radii of 1. Since the constraint is at  $z = 0$ , it has no volume contribution. The area integrand for this constraint is

$$\vec{w} = -y\vec{t} \tag{B-12}$$

which is integrated along appropriate edges (shown in yellow in Figure B-2 and Figure B-3). Example evolved shapes for two pores and three pores are shown in the bottom rows of Figure B-2 and Figure B-3, respectively.

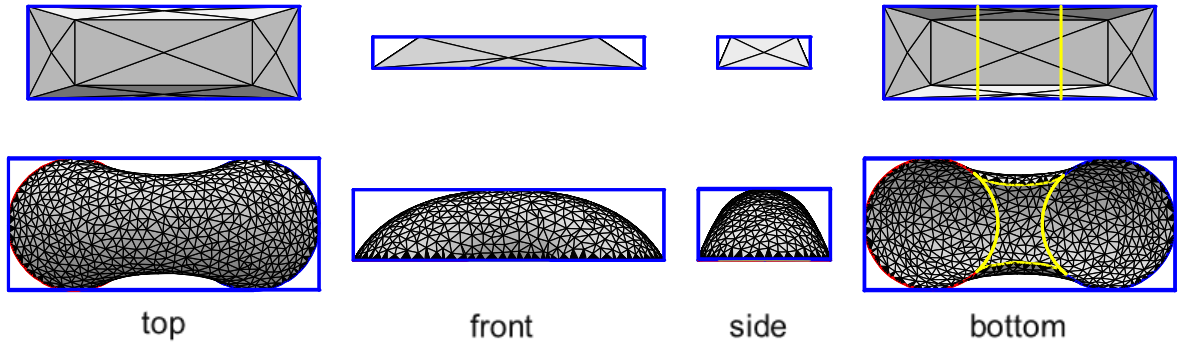


Figure B-2. Different views of an example bridge geometry connecting two pores before (top row) and after (bottom row) the evolution in SE. The shape is pinned at the pore mouths (circles) but makes  $\theta = 135^\circ$  angle with the flat surface between the pores (the portions of the yellow lines connecting the circles). The radii of the circles are  $R_p = 1$  and the distance between the centers of the circles is  $\tilde{l} = 8/3$ . The volume of the shape is  $\tilde{V}_{\text{bri}}^{S^*} = 5$ . Note that the initial shape is not required to have the correct, prescribed volume.

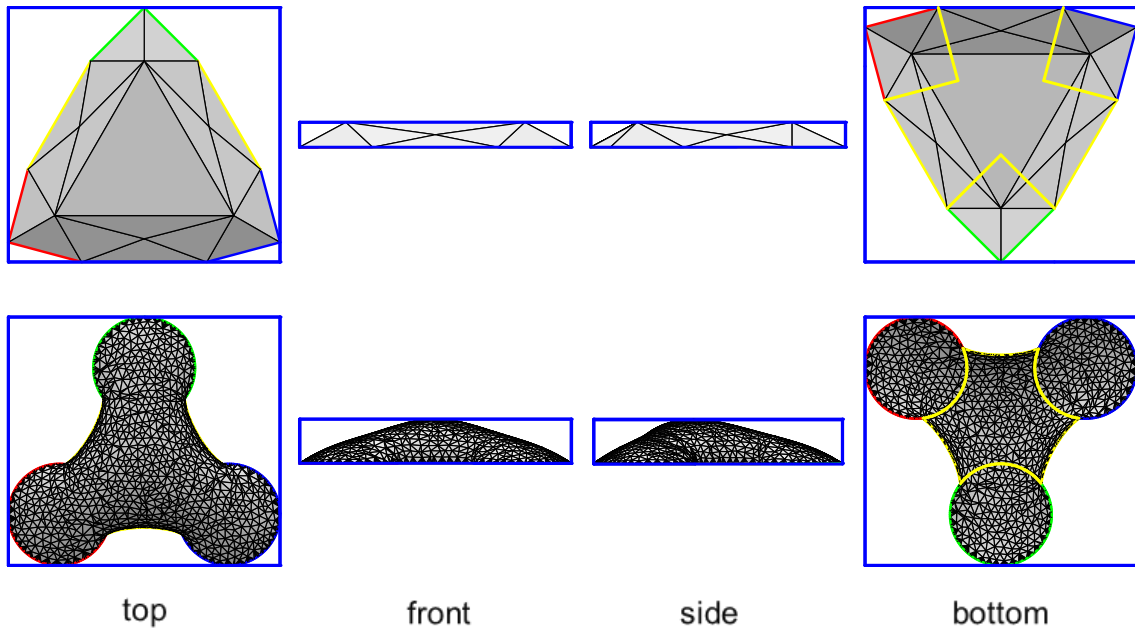


Figure B-3. Different views of an example bridge geometry connecting three pores before (top row) and after (bottom row) the evolution with SE. The shape is pinned at the pore mouths (circles) but makes  $\theta = 90^\circ$  angle with the flat surface between the pores (the portions of the yellow lines connecting the circles). The radii of the circles are  $R_p = 1$  and the distance between the centers of the circles is  $\tilde{l} = 10/3$ . The volume of the shape is  $\tilde{V}_{\text{bri}}^{S^*} = 6$ . Note that the initial shape is not required to have the correct, prescribed volume.

As the convergence criterion, in all applicable SE calculations in Chapter 4, we stopped the evolution if the energy change for a given triangulation was at least less than  $10^{-4}$  and the scale factor (see the SE manual [4]) was roughly stable in the expected range after 50 conjugate

gradient iterations. Note that finer meshes have been used for the final calculations reported in Chapter 4 than for the evolved surfaces shown in Figure B-1, Figure B-2, and Figure B-3.

# Appendix C

## Supplementary Information for Chapter 5

### C.1 Detailed steps between Equations (5-21) and (5-22) and Equations (5-22) and (5-23)

From the main text, Equation (5-21) is

$$\begin{aligned} \mu_1^{\text{ex}} = & \frac{z_n}{n} \sum_{i_2, i_3, \dots, i_n=1}^r w_{1i_2 \dots i_n} x_{i_2} x_{i_3} \dots x_{i_n} \\ & - \frac{z_n(n-1)}{n} \sum_{\substack{i_2, i_3, \dots, i_n=1 \\ i_1=2}}^r (w_{i_1 i_2 \dots i_n} - w_{1i_2 \dots i_n}) x_{i_1} x_{i_2} \dots x_{i_n} \end{aligned} \quad (\text{C-1})$$

To get Equation (5-22), the omitted steps are:

Step (1) Separate the term containing  $x_1$  in the sum over  $i_2$  in Equation (C-1) from the rest and substitute  $1 - \sum_{j=2}^r x_j$  for  $x_1$  to get

$$\begin{aligned}
\mu_1^{\text{ex}} &= \frac{z_n}{n} \sum_{i_3, i_4, \dots, i_n=1}^r w_{11i_3 \dots i_n} \left( 1 - \sum_{j=2}^r x_j \right) x_{i_3} \dots x_{i_n} \\
&\quad + \frac{z_n}{n} \sum_{\substack{i_3, i_4, \dots, i_n=1 \\ i_2=2}}^r w_{1i_2 \dots i_n} x_{i_2} x_{i_3} \dots x_{i_n} \\
&\quad - \frac{z_n(n-1)}{n} \sum_{\substack{i_3, i_4, \dots, i_n=1 \\ i_1=2}}^r (w_{i_1 1 i_3 \dots i_n} - w_{11 i_3 \dots i_n}) x_{i_1} \left( 1 \right. \\
&\quad \left. - \sum_{j=2}^r x_j \right) x_{i_3} \dots x_{i_n} \\
&\quad - \frac{z_n(n-1)}{n} \sum_{\substack{i_3, i_4, \dots, i_n=1 \\ i_1, i_2=2}}^r (w_{i_1 i_2 \dots i_n} - w_{1 i_2 \dots i_n}) x_{i_1} x_{i_2} \dots x_{i_n}
\end{aligned} \tag{C-2}$$

Step (2) Where present in Equation (C-2), split the expression  $(1 - \sum_{j=2}^r x_j)$  into two terms and recover the consecutive labels by reindexing the sum over  $i_1 = 2$  and  $i_3, i_4 \dots i_n = 1$  as the sum over  $i_2 = 2$  and  $i_3, i_4 \dots i_n = 1$  to get

$$\begin{aligned}
\mu_1^{\text{ex}} &= \frac{z_n}{n} \sum_{i_3, i_4, \dots, i_n=1}^r w_{11i_3 \dots i_n} x_{i_3} x_{i_4} \dots x_{i_n} \\
&\quad - \frac{z_n}{n} \sum_{\substack{i_3, i_4, \dots, i_n=1 \\ i_2=2}}^r w_{11i_3 \dots i_n} x_{i_2} x_{i_3} \dots x_{i_n} \\
&\quad + \frac{z_n}{n} \sum_{\substack{i_3, i_4, \dots, i_n=1 \\ i_2=2}}^r w_{1i_2 \dots i_n} x_{i_2} x_{i_3} \dots x_{i_n} \\
&\quad - \frac{z_n(n-1)}{n} \sum_{\substack{i_3, i_4, \dots, i_n=1 \\ i_2=2}}^r (w_{1i_2 \dots i_n} - w_{11i_3 \dots i_n}) x_{i_2} x_{i_3} \dots x_{i_n} \\
&\quad + \frac{z_n(n-1)}{n} \sum_{\substack{i_3, i_4, \dots, i_n=1 \\ i_1, i_2=2}}^r (w_{1i_2 \dots i_n} - w_{11i_3 \dots i_n}) x_{i_1} x_{i_2} \dots x_{i_n} \\
&\quad - \frac{z_n(n-1)}{n} \sum_{\substack{i_3, i_4, \dots, i_n=1 \\ i_1, i_2=2}}^r (w_{i_1 i_2 \dots i_n} - w_{1i_2 \dots i_n}) x_{i_1} x_{i_2} \dots x_{i_n}
\end{aligned} \tag{C-3}$$

Step (3) Collect the terms over the same sums in Equation (C-3) to get

$$\begin{aligned}
\mu_1^{\text{ex}} &= \frac{z_n}{n} \sum_{i_3, i_4, \dots, i_n=1}^r w_{11i_3 \dots i_n} x_{i_3} x_{i_4} \dots x_{i_n} \\
&\quad - \frac{z_n(n-2)}{n} \sum_{\substack{i_3, \dots, i_n=1 \\ i_2=2}}^r (w_{1i_2 \dots i_n} - w_{11i_3 \dots i_n}) x_{i_2} x_{i_3} \dots x_{i_n} \\
&\quad - \frac{z_n(n-1)}{n} \sum_{\substack{i_3, i_4, \dots, i_n=1 \\ i_1, i_2=2}}^r (w_{i_1 i_2 \dots i_n} - 2w_{1i_2 \dots i_n} \\
&\quad \quad + w_{11i_3 \dots i_n}) x_{i_1} x_{i_2} \dots x_{i_n}
\end{aligned} \tag{C-4}$$

which is the same as Equation (5-22).

To get equation (23), the omitted steps are:

Step (1) Separate the term containing  $x_1$  in the sum over  $i_3$  in Equation (C-4) from the rest and substitute  $1 - \sum_{j=2}^r x_j$  for  $x_1$  to get

$$\begin{aligned}
\mu_1^{\text{ex}} = & \frac{z_n}{n} \sum_{i_4, i_5, \dots, i_n=1}^r w_{111i_4 \dots i_n} \left( 1 - \sum_{j=2}^r x_j \right) x_{i_4} x_{i_5} \dots x_{i_n} \\
& + \frac{z_n}{n} \sum_{\substack{i_4, i_5, \dots, i_n=1 \\ i_3=2}}^r w_{11i_3 \dots i_n} x_{i_3} x_{i_4} \dots x_{i_n} \\
& - \frac{z_n(n-2)}{n} \sum_{\substack{i_4, i_5, \dots, i_n=1 \\ i_2=2}}^r (w_{1i_2 1i_4 \dots i_n} - w_{111i_4 \dots i_n}) x_{i_2} \left( 1 \right. \\
& \left. - \sum_{j=2}^r x_j \right) x_{i_4} \dots x_{i_n} \\
& - \frac{z_n(n-2)}{n} \sum_{\substack{i_4, i_5, \dots, i_n=1 \\ i_2, i_3=2}}^r (w_{1i_2 \dots i_n} - w_{11i_3 \dots i_n}) x_{i_2} x_{i_3} \dots x_{i_n} \tag{C-5} \\
& - \frac{z_n(n-1)}{n} \sum_{\substack{i_4, i_5, \dots, i_n=1 \\ i_1, i_2=2}}^r (w_{i_1 i_2 1i_4 \dots i_n} - 2w_{1i_2 1i_4 \dots i_n} \\
& + w_{111i_4 \dots i_n}) x_{i_1} x_{i_2} \left( 1 - \sum_{j=2}^r x_j \right) x_{i_4} \dots x_{i_n} \\
& - \frac{z_n(n-1)}{n} \sum_{\substack{i_4, i_5, \dots, i_n=1 \\ i_1, i_2, i_3=2}}^r (w_{i_1 i_2 \dots i_n} - 2w_{1i_2 \dots i_n} \\
& + w_{11i_3 \dots i_n}) x_{i_1} x_{i_2} \dots x_{i_n}
\end{aligned}$$

Step (2) Where present in Equation (C-5), split the expression  $(1 - \sum_{j=2}^r x_j)$  into two terms and recover the consecutive labels where needed by reindexing to get



$$\begin{aligned}
\mu_1^{\text{ex}} = & \frac{z_n}{n} \sum_{i_4, i_5 \dots i_n=1}^r w_{111i_4 \dots i_n} x_{i_4} x_{i_5} \dots x_{i_n} - \frac{z_n}{n} \sum_{\substack{i_4, i_5 \dots i_n=1 \\ i_3=2}}^r w_{111i_4 \dots i_n} x_{i_3} x_{i_4} \dots x_{i_n} \\
& + \frac{z_n}{n} \sum_{\substack{i_4, i_5 \dots i_n=1 \\ i_3=2}}^r w_{11i_3 \dots i_n} x_{i_3} x_{i_4} \dots x_{i_n} \\
& - \frac{z_n(n-2)}{n} \sum_{\substack{i_4, i_5 \dots i_n=1 \\ i_3=2}}^r (w_{11i_3 i_4 \dots i_n} - w_{111i_4 \dots i_n}) x_{i_3} x_{i_4} \dots x_{i_n} \\
& + \frac{z_n(n-2)}{n} \sum_{\substack{i_4, i_5 \dots i_n=1 \\ i_2, i_3=2}}^r (w_{11i_3 i_4 \dots i_n} - w_{111i_4 \dots i_n}) x_{i_2} x_{i_3} \dots x_{i_n} \\
& - \frac{z_n(n-2)}{n} \sum_{\substack{i_4, i_5 \dots i_n=1 \\ i_2, i_3=2}}^r (w_{1i_2 \dots i_n} - w_{11i_3 \dots i_n}) x_{i_2} x_{i_3} \dots x_{i_n} \\
& - \frac{z_n(n-1)}{n} \sum_{\substack{i_4, i_5 \dots i_n=1 \\ i_2, i_3=2}}^r (w_{1i_2 \dots i_n} - 2w_{11i_3 \dots i_n} \\
& + w_{111i_4 \dots i_n}) x_{i_2} x_{i_3} \dots x_{i_n} \\
& + \frac{z_n(n-1)}{n} \sum_{\substack{i_4, i_5 \dots i_n=1 \\ i_1, i_2, i_3=2}}^r (w_{1i_2 \dots i_n} - 2w_{11i_3 \dots i_n} \\
& + w_{111i_4 \dots i_n}) x_{i_1} x_{i_2} \dots x_{i_n} \\
& - \frac{z_n(n-1)}{n} \sum_{\substack{i_4, i_5 \dots i_n=1 \\ i_1, i_2, i_3=2}}^r (w_{i_1 i_2 \dots i_n} - 2w_{1i_2 \dots i_n} \\
& + w_{11i_3 \dots i_n}) x_{i_1} x_{i_2} \dots x_{i_n}
\end{aligned} \tag{C-6}$$

Step (3) Collect the terms over the same sums in Equation (C-6) to get

$$\begin{aligned}
\mu_1^{\text{ex}} = & \frac{z_n}{n} \sum_{i_4, i_5 \dots i_n=1}^r w_{111i_4 \dots i_n} x_{i_4} x_{i_5} \dots x_{i_n} \\
& - \frac{z_n(n-3)}{n} \sum_{\substack{i_4, i_5 \dots i_n=1 \\ i_3=2}}^r (w_{111i_3 i_4 \dots i_n} \\
& - w_{111i_4 \dots i_n}) x_{i_3} x_{i_4} \dots x_{i_n} \\
& - \frac{z_n(2n-3)}{n} \sum_{\substack{i_4, i_5 \dots i_n=1 \\ i_2, i_3=2}}^r (w_{1i_2 \dots i_n} - 2w_{11i_3 \dots i_n} \\
& + w_{111i_4 \dots i_n}) x_{i_2} x_{i_3} \dots x_{i_n} \\
& - \frac{z_n(n-1)}{n} \sum_{\substack{i_4, i_5 \dots i_n=1 \\ i_1, i_2, i_3=2}}^r (w_{i_1 i_2 \dots i_n} - 3w_{1i_2 \dots i_n} + 3w_{11i_3 \dots i_n} \\
& - w_{111i_4 \dots i_n}) x_{i_1} x_{i_2} \dots x_{i_n}
\end{aligned} \tag{C-7}$$

which is the same as Equation (5-23).

## C.2 Detailed steps between Equations (5-28) and (5-29)

Using the definition of  $w$  given by Equation (5-9), in the explicit notation, we can write

$$w_{1 \dots 1 i_{k+1} \dots i_m} = g_{1 \dots 1 i_{k+1} \dots i_m} - \frac{1}{n} \left[ (n - m + k) g_{1 \dots 1} + \sum_{j=k+1}^m g_{i_j \dots i_j} \right] \tag{C-8}$$

noting that each variable index here can only represent a solute:  $i_j \in [2, r]$ . If we look at a generic binary group containing the same number of solvent particles (*i.e.*,  $n - m + k$ ) and the same number of solute particles as above (*i.e.*,  $m - k$ ), we have

$$w_{1 \dots 1 i_j \dots i_j} = g_{1 \dots 1 i_j \dots i_j} - \frac{1}{n} \left[ (n - m + k) g_{1 \dots 1} + (m - k) g_{i_j \dots i_j} \right] \tag{C-9}$$

Now, if we take the sum over the labels from  $j = k + 1$  to  $m$  of both sides of Equation (C-9) and divide both sides by  $m - k$ , we have

$$\begin{aligned}
\frac{1}{m-k} \sum_{j=k+1}^m w_{1\dots 1i_j\dots i_j} &= \frac{1}{m-k} \sum_{j=k+1}^m g_{1\dots 1i_j\dots i_j} \\
&\quad - \frac{1}{n} \left[ (n-m+k)g_{1\dots 1} + \sum_{j=k+1}^m g_{i_j\dots i_j} \right]
\end{aligned} \tag{C-10}$$

Using Equation (5-28), we can substitute for the first term on the right-hand side of Equation (C-10) and obtain

$$\begin{aligned}
\frac{1}{m-k} \sum_{j=k+1}^m w_{1\dots 1i_j\dots i_j} &= g_{1\dots 1i_{k+1}\dots i_m} - \frac{1}{n} \left[ (n-m+k)g_{1\dots 1} + \sum_{j=k+1}^m g_{i_j\dots i_j} \right]
\end{aligned} \tag{C-11}$$

Comparing Equations (C-11) and (C-8), we get

$$w_{1\dots 1i_{k+1}\dots i_m} = \frac{1}{m-k} \sum_{j=k+1}^m w_{1\dots 1i_j\dots i_j} \tag{C-12}$$

which is the same as Equation (5-29).

### C.3 Detailed steps to arrive at Equation (5-31) using Equations (5-24) and (5-29)

Given Equation (5-29), we want to show that the following holds for the sum appearing in Equation (5-24):

$$\sum_{k=0}^m (-1)^k \binom{m}{k} w_{1\dots 1i_{k+1}\dots i_m} = \frac{1}{m} \sum_{j=1}^m \sum_{k=0}^m (-1)^k \binom{m}{k} w_{1\dots 1i_j\dots i_j} \tag{C-13}$$

which would give us the sum over  $Q$ 's when multiplied by the coefficient  $\frac{z_n(1-m)}{n} \binom{n}{m}$  (omitted here).

Starting with the left-hand side of Equation (C-13), we substitute for  $w_{1\dots 1i_{k+1}\dots i_m}$  using its decomposition given by Equation (5-29):

$$\sum_{k=0}^m (-1)^k \binom{m}{k} w_{1\dots 1i_{k+1}\dots i_m} = \sum_{k=0}^m (-1)^k \binom{m}{k} \frac{1}{m-k} \sum_{j=k+1}^m w_{1\dots 1i_j\dots i_j} \quad (\text{C-14})$$

Now, we extend the sum from  $j = k + 1$  to  $m$  to  $j = 1$  to  $m$  by noting

$$\sum_{j=1}^m w_{1\dots 1i_j\dots i_j} = \sum_{j=k+1}^m w_{1\dots 1i_j\dots i_j} + \sum_{j=1}^k w_{1\dots 1i_j\dots i_j} \quad (\text{C-15})$$

Since we at most need  $m - k$  distinct labels for the indices of  $w$  on the left-hand side of Equation (C-13), and the sum from  $j = k + 1$  to  $m$  is chosen arbitrarily, we can reindex the terms in the second sum on the right-hand side of Equation (C-15) by splitting each term into a sum over index labels  $k + 1$  to  $m$ . That is, we can write

$$\begin{aligned} \sum_{j=1}^m w_{1\dots 1i_j\dots i_j} &= \sum_{j=k+1}^m w_{1\dots 1i_j\dots i_j} + \sum_{j=1}^k \frac{1}{m-k} \sum_{t=k+1}^m w_{1\dots 1i_t\dots i_t} = \\ &= \sum_{j=k+1}^m w_{1\dots 1i_j\dots i_j} + \frac{1}{m-k} \sum_{t=k+1}^m \sum_{j=1}^k w_{1\dots 1i_t\dots i_t} \\ &= \sum_{j=k+1}^m w_{1\dots 1i_j\dots i_j} + \frac{k}{m-k} \sum_{t=k+1}^m w_{1\dots 1i_t\dots i_t} \\ &= \frac{m}{m-k} \sum_{j=k+1}^m w_{1\dots 1i_j\dots i_j} \end{aligned} \quad (\text{C-16})$$

Rearranging this result and substituting it back into Equation (C-14), we obtain Equation (C-13):

$$\begin{aligned} \sum_{k=0}^m (-1)^k \binom{m}{k} w_{1\dots 1i_{k+1}\dots i_m} &= \sum_{k=0}^m (-1)^k \binom{m}{k} \frac{1}{m-k} \left( \frac{m-k}{m} \sum_{j=1}^m w_{1\dots 1i_j\dots i_j} \right) \\ &= \frac{1}{m} \sum_{j=1}^m \sum_{k=0}^m (-1)^k \binom{m}{k} w_{1\dots 1i_j\dots i_j} \end{aligned} \quad (\text{C-17})$$

## C.4 Detailed steps between Equations (5-48) and (5-50) and Equations (5-49) and (5-51)

According to the definition before Equation (5-45),  $\omega_2^{\text{nc}}$  in Equations (5-48) and (5-49) is defined as the nonconfigurational Gibbs free-energy change for the following process: 2 systems, each made of  $N - 1$  solvent molecules and 1 solute molecule, being rearranged into 1 system made of  $N - 2$  solvent molecules with 2 solute molecules, plus 1 pure solvent system with  $N$  solvent particles. Similarly,  $\omega_3^{\text{nc}}$  in Equation (5-49) is defined as the nonconfigurational Gibbs free-energy change for the following process: 3 systems, each made of  $N - 1$  solvent molecules and 1 solute molecule, being rearranged into 1 system made of  $N - 3$  solvent molecules with 3 solute molecules, plus 2 pure solvent system with  $N$  solvent particles. Based on these definitions, denoting the solute by the subscript 2, we can write

$$\omega_2^{\text{nc}} = g_{1\dots 122} + g_{1\dots 1} - 2g_{1\dots 12} \quad (\text{C-18})$$

and

$$\omega_3^{\text{nc}} = g_{1\dots 1222} + 2g_{1\dots 1} - 3g_{1\dots 12} \quad (\text{C-19})$$

where  $g$ 's denote the energies of the respective groups made of  $N$  particles each, consistent with our notation (*i.e.*,  $N$ -tuple energies). We can recast Equation (C-18) into the following form:

$$\begin{aligned} \omega_2^{\text{nc}} &= g_{1\dots 122} - \frac{1}{N} [(N - 2)g_{1\dots 1} + 2g_{2\dots 2}] \\ &\quad - 2 \left\{ g_{1\dots 12} - \frac{1}{N} [(N - 1)g_{1\dots 1} + g_{2\dots 2}] \right\} \\ &= w_{1\dots 122} - 2w_{1\dots 12} \end{aligned} \quad (\text{C-20})$$

which is the same equivalence used in Equation (5-50), and recast Equation (C-19) into the following form:

$$\begin{aligned} \omega_3^{\text{nc}} &= g_{1\dots 1222} - \frac{1}{N} [(N - 3)g_{1\dots 1} + 3g_{2\dots 2}] \\ &\quad - 3 \left\{ g_{1\dots 12} - \frac{1}{N} [(N - 1)g_{1\dots 1} + g_{2\dots 2}] \right\} \\ &= w_{1\dots 1222} - 3w_{1\dots 12} \end{aligned} \quad (\text{C-21})$$

Combining Equations (C-20) and (C-21) into the expression present in Equation (5-49), we have

$$\begin{aligned}\omega_3^{\text{nc}} - 3\omega_2^{\text{nc}} &= w_{1\dots1222} - 3w_{1\dots12} - 3(w_{1\dots122} - 2w_{1\dots12}) \\ &= w_{1\dots1222} - 3w_{1\dots122} + 3w_{1\dots12}\end{aligned}\tag{C-22}$$

which is the same equivalence used in Equation (5-51). The arguments above can be generalized to relate any order coefficients expressed in terms of  $\omega^{\text{nc}}$  to the respective coefficients expressed in terms of  $w$ 's.

## Appendix D

### Supplementary Information for Chapter 6

#### D.1 Discussion of binary data reported in the references used for ternary data

In Figure D-1, we plot some of the binary fits and compare them with the binary data found in the sources that were used to collect the ternary solution data. Note that none of the data points shown in Figure D-1 were included in the binary data used for fitting. The original binary data used to generate the fit polynomials, hence, used in predictions in section 6.3, are from Gibbard and Gossmann [14] for  $\text{MgCl}_2$ , from Oakes *et al.* [29] for  $\text{CaCl}_2$ , and from the CRC [47] for the rest. The  $\text{ZnBr}_2$  and  $\text{ZnCl}_2$  binary data from Haghghi *et al.* [16] are not required for predictions because there are no ternary solution data involving these salts. We focus on the fits that were used for the prediction of ternary data reported by Haghghi *et al.* [16] and Khitrova [22], where the predictions have relatively high, above average RMSE values (see Table 6-3 and Figure 6-3). When the fitted curves [Figure D-1 (b), (c), and (d)] are compared the reported binary data, we notice relatively large deviations for the mentioned references. Therefore, at least some of the errors in the predictions for these data sets can be attributed to the systematic mismatch of the experimental data used for binary fitting and the ternary solution data from these references. Since there were not enough binary data points in most of the ternary solution references to obtain a high-confidence fit and make predictions based on that fit, a direct comparison was not possible.

Furthermore, in Figure D-1 (a), we show the fitted curve and its extrapolation for  $\text{KCl}$ . Since some ternary data extended beyond the data limit of the binary fit, the extrapolation region was used in these cases to make the predictions. It is clear from the plot that the binary data from Vilcu *et al.* [41] and from Hall *et al.* [17] deviate significantly from the extrapolated curve. However, it is not possible to state with confidence which is closer to the true osmolality curve. When we included the binary data points from these references for  $\text{KCl}$  fitting, the

polynomial changed from linear to quadratic, and the prediction results were not better on average, so we decided not to include these points for fitting. The highest RMSE value (1.22 osmoles/kg) for the prediction of the model is for the CaCl<sub>2</sub> + KCl system data from Haghghi *et al.* [16]. Although the reported binary data for CaCl<sub>2</sub> from this reference were poorly described with the binary curve [see Figure D-1 (c)], there were no KCl binary data for comparison. Nevertheless, it seems reasonable to assume that the prediction errors for ternary solutions that contain KCl can be, at least partially, attributed to the systematic mismatch between the results of the binary data source used for fitting (with its extrapolation) and the results of the ternary data source.

One possible reason for the mismatch is the accuracy of the experimental methods and their various biases. Additionally, the measurement accuracies are important, although, they were not always reported (see the discussion of the data sources in section D.3) and even when they were reported, some are questionable. For example, Vilcu *et al.* [41–43] reported a temperature measurement accuracy of  $\pm 0.0002$  °C for all their works. However, Gibbard and Grossmann [14] found as high as 0.5 °C discrepancy when comparing their data to the Vilcu *et al.* [41] data, especially at molalities higher than 1.6 m. This is an indication of either different biases of two experimental methods and/or inaccurate measurements.



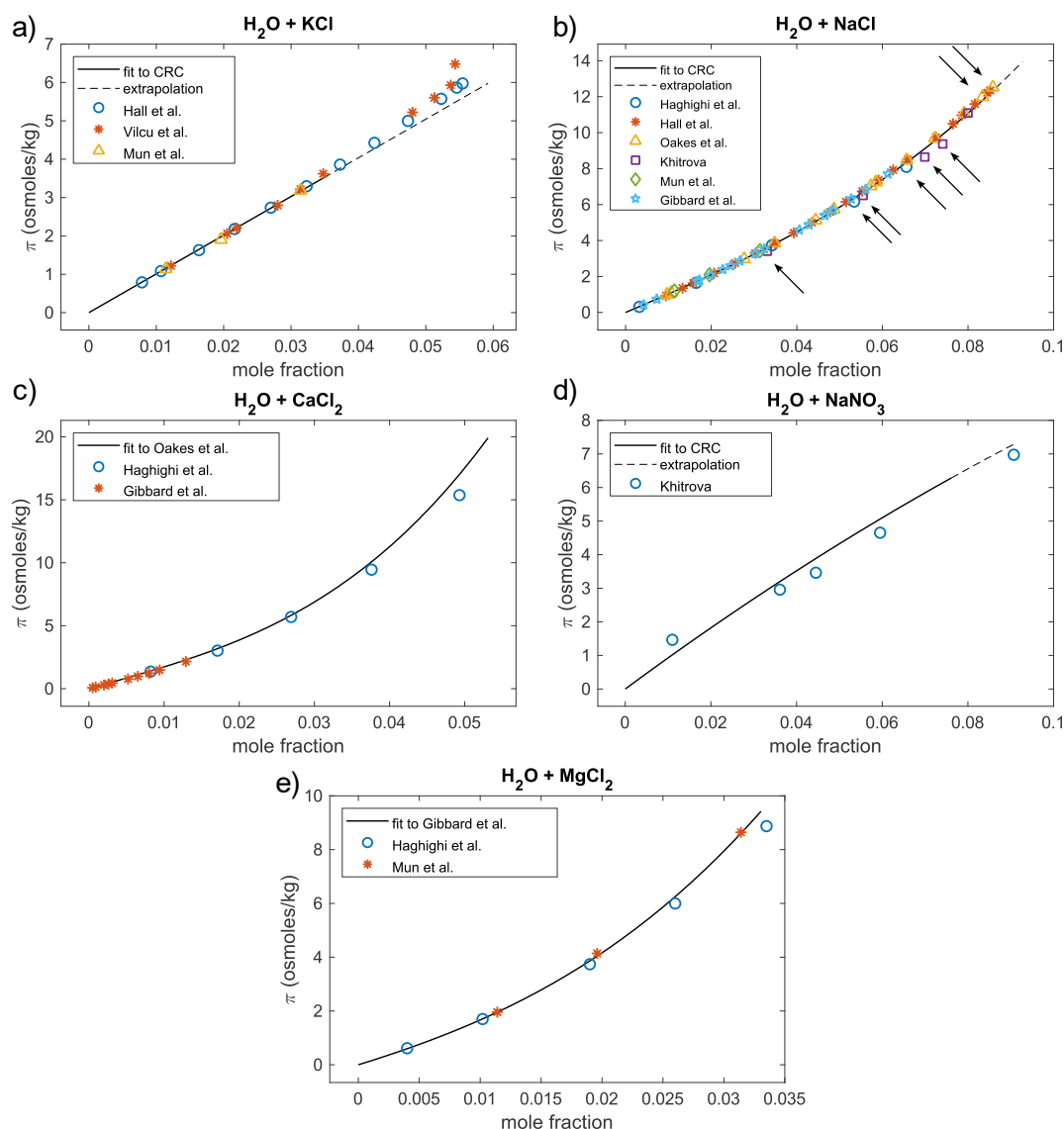


Figure D-1. Comparison of some of the mole-fraction-based binary fits [black lines; (a), (b), and (d) fit to CRC [47], (c) fit to Oakes *et al.* [29], and (e) fit to Gibbard and Gossmann [14]], used in this work to make predictions, with reported binary data from the sources from which the ternary data were obtained [Hall *et al.* [17] in panels (a) and (b); Vilcu *et al.* [41] in panel (a); Mun and Darer [28] in panels (a), (b), and (e); Haghghi *et al.* [16] in panels (b), (c), and (e); Oakes *et al.* [29] in panel (b); Khitrova [22] in panels (b) and (d); Gibbard and Gossman [14] in panel (b); Gibbard and Fong [13] in panel (c)]. Dashed lines represent extrapolation of the fitted curves. None of these data points were used for fitting in this work. In particular, note that the binary data points from Haghghi *et al.* [16] and Khitrova [22] are poorly described by the curves resulting from fitting to other data or their extrapolations [panels (b), (c), and (d)]. Additionally, note the discrepancy between the experimental data available and the extrapolated polynomial for KCl which was used for the high-concentration prediction region (panel a). Because of the high number of data points in the NaCl plot [panel (b)], black arrows are used to indicate the points that have the highest deviation from the curve.

## D.2 Graphical representations of binary fits

Visual representations of the binary data fits are given in Figure D-2 (mole-fraction-based fits) and Figure D-3 (molality-based fits). Binary fits were performed using multiple linear regression through the origin as described in the main text. The combined criterion described in the main text was used to determine the degree of the polynomials. The data are from Gibbard and Gossman [14] for  $\text{MgCl}_2$ , Oakes *et al.* [29] for  $\text{CaCl}_2$ , Haghghi *et al.* [16] for  $\text{ZnBr}_2$  and  $\text{ZnCl}_2$ , and from the CRC [47] for the rest. See the main text for more details.

### Mole-fraction-based fits

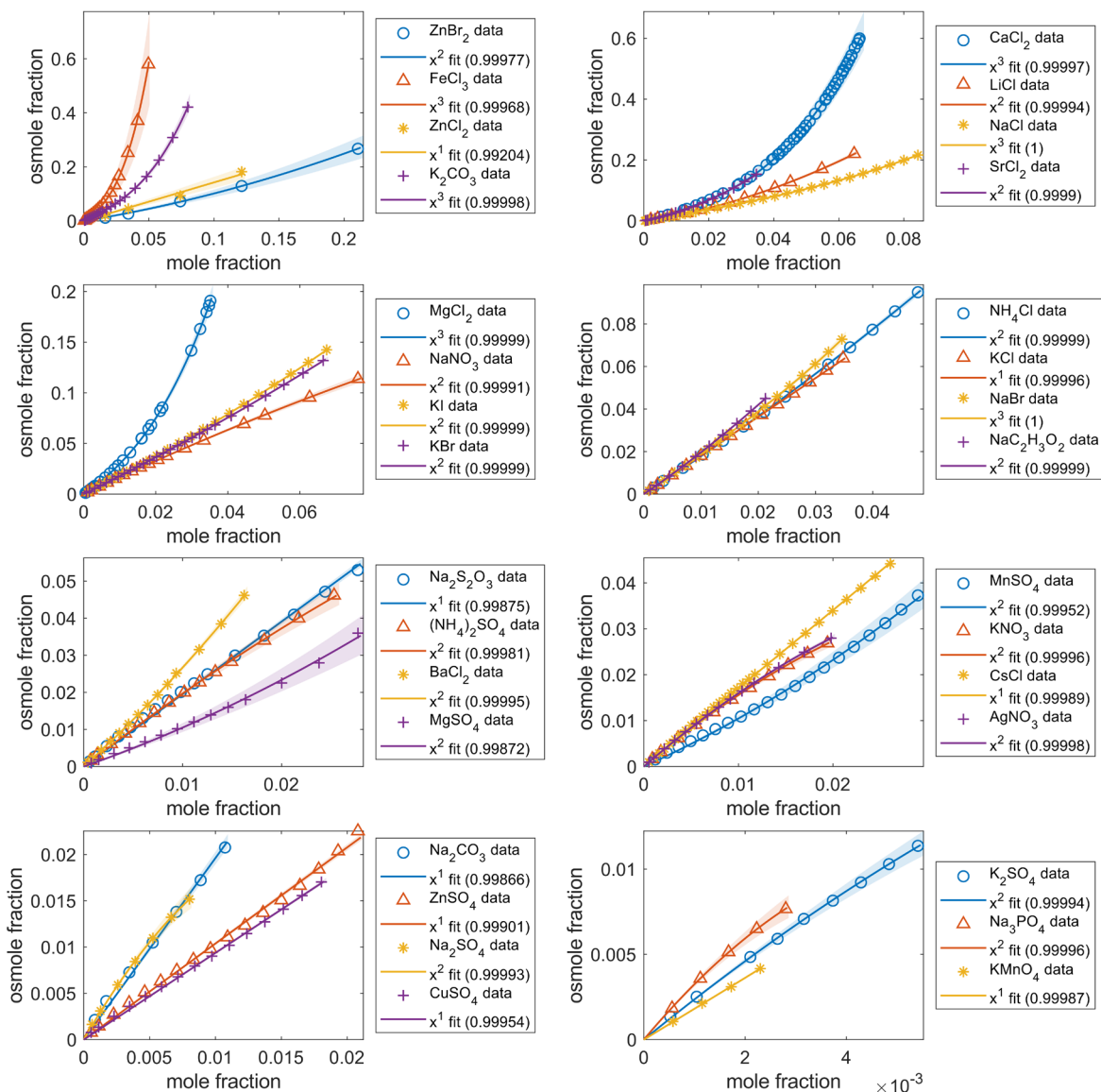


Figure D-2. Mole-fraction-based fits to binary solution data plotted as osmole fraction vs. mole fraction. Markers indicate the experimental data points, and solid lines of the same color indicate the best fit based on the mixed criterion described in the main text. The shaded region of the same color indicates the area where all coefficients are within their 95% CIs. The polynomial degree of each fit is given in the legend with the  $R^2_{RTO,adj}$  values in parentheses.

### Molality-based fits

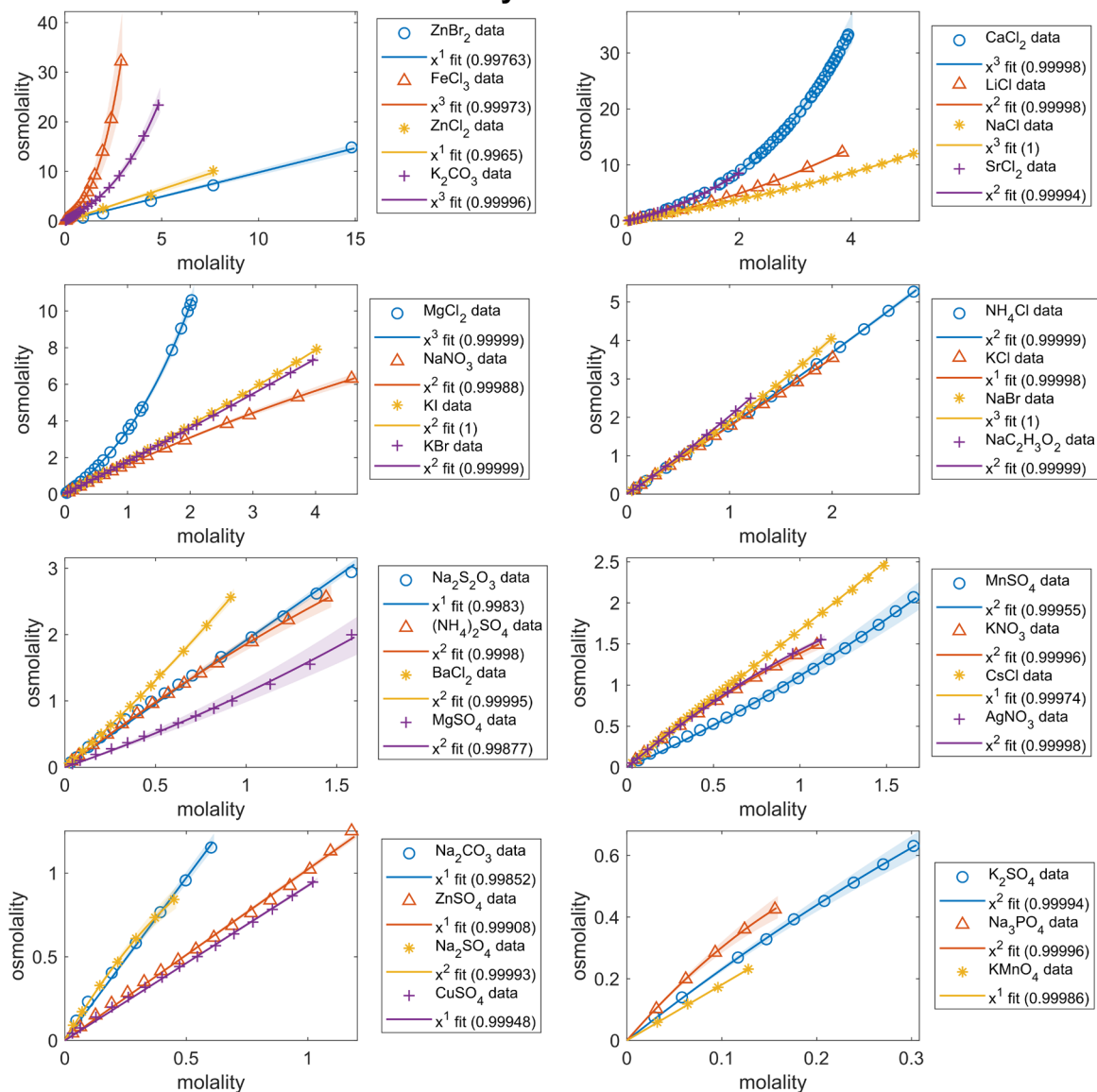


Figure D-3. Molality-based fits to binary solution data plotted as osmolality vs. molality. Markers indicate the experimental data points, and solid lines of the same color indicate the best fit based on the mixed criterion described in the main text. The shaded region of the same color indicates the area where all coefficients are within their 95% CIs. The polynomial degree of each fit is given in the legend with the  $R_{\text{RTO,adj}}^2$  values in parentheses. The units of osmolality are osmoles/kg, and the units of molality are (moles of solute)/(kg of solvent) on these plots.

### D.3 Data sources and unit conversions

Data for ternary solutions were obtained from multiple sources. Because of the different concentration units used, summaries for data sets from each source and the appropriate unit conversions are given separately below. Works from the same author(s) are grouped together.

#### D.3.1 Gibbard *et al.*

In a series of three papers [12–14], Gibbard *et al.* reported freezing point depression measurements for aqueous mixtures of: (i) NaCl + MgCl<sub>2</sub> [14], (ii) LiCl + NaCl [12], and (iii) NaCl + CaCl<sub>2</sub> and NaCl + BaCl<sub>2</sub> [13]. In all three works, the reported accuracies were  $\pm 0.001$  °C for temperature measurements and  $\pm 0.1\%$  for molality measurements.

In all three works, units of “equivalent concentration”,  $m'$ , and “equivalent fraction”,  $x'_i$ , were used. These units are represented as

$$m' = \frac{1}{2} \sum_{i=1}^{\# \text{ ion types}} m_i z_i \quad (\text{D-1})$$

$$x'_i = \frac{m_i z_i}{m'} \quad (\text{D-2})$$

where  $z_i$  is the charge of the ion species labeled with  $i$  and  $m_i$  is molality. For NaCl and LiCl, Equation (D-1) becomes (in the following equations,  $\times$  is used as a multiplication symbol in some places for clarity):

$$m' = \frac{1}{2} \sum m_i z_i = \frac{1}{2} [(m_i \times 1) + (m_i \times 1)] = m_i \quad (\text{D-3})$$

That is, for 1:1 salts, the equivalent concentration equals molality. However, for 1:2 salts (MgCl<sub>2</sub>, BaCl<sub>2</sub>, CaCl<sub>2</sub>), the following is obtained:

$$\begin{aligned} m' &= \frac{1}{2} \sum m_i z_i = \frac{1}{2} [(m_{\text{cation}} \times 2) + (m_{\text{anion}} \times 1)] \\ &= \frac{1}{2} [(m_{\text{cation}} \times 2) + (2 \times m_{\text{cation}} \times 1)] = 2m_i \end{aligned} \quad (\text{D-4})$$

In the case of 1:2 salt mixtures (*i.e.*, NaCl + BaCl<sub>2</sub>, NaCl + CaCl<sub>2</sub>, and NaCl + MgCl<sub>2</sub>),  $x'_i$ , chosen to be the equivalent fraction with regards to the sodium ion ( $x'_i = x_{\text{Na}^+}$ ), needs to be converted to the actual molality of both salts with the following conversion equations:

$$\begin{aligned} m' &= \frac{1}{2} [(m_{\text{Na}^+}) \times 1 + (m_{\text{Cl}^-}) \times 1 + (m_{\text{Mg}^{2+}}) \times 2 + 2 \times (m_{\text{Cl}^-}) \times 1] \\ &= m_{\text{NaCl}} + 2m_{\text{MgCl}_2} \end{aligned} \quad (\text{D-5})$$

$$x'_i = x_{\text{Na}^+} = \frac{m_{\text{Na}^+}}{m_{\text{NaCl}} + 2m_{\text{MgCl}_2}} \quad (\text{D-6})$$

Isolating  $m_{\text{NaCl}}$ , we have

$$m_{\text{NaCl}} = \frac{2x_{\text{Na}^+}}{1 - x_{\text{Na}^+}} m_{\text{MgCl}_2} \quad (\text{D-7})$$

and substituting into  $m'$ , we get

$$m_{\text{NaCl}} = x_{\text{Na}^+} m' \quad (\text{D-8})$$

$$m_{\text{MgCl}_2} = \frac{1 - x_{\text{Na}^+}}{2} m' \quad (\text{D-9})$$

Similarly, for 1:1 salt mixtures (*i.e.*, LiCl + NaCl), using the same algebraic method, the following are obtained:

$$m_{\text{NaCl}} = (1 - x_{\text{Li}^+}) m' \quad (\text{D-10})$$

$$m_{\text{LiCl}} = x_{\text{Li}^+} m' \quad (\text{D-11})$$

Furthermore, as noted in the main text, the binary MgCl<sub>2</sub> data were also collected from the work of Gibbard and Gossmann [14] to obtain the osmotic virial coefficients because this mixture is not found in the CRC [47].

### ***D.3.2 Haghghi et al.***

Haghghi *et al.* [16], measured the freezing point depression of four aqueous ternary mixtures: NaCl + KCl, NaCl + CaCl<sub>2</sub>, KCl + CaCl<sub>2</sub>, NaCl + MgCl<sub>2</sub>. The reported temperature measurement accuracy is  $\pm 0.1$  °C. Additionally, the reported binary data for ZnCl<sub>2</sub> and ZnBr<sub>2</sub> from Haghghi *et al.* [16] were used to obtain the osmotic virial coefficients because these salts are not found in the CRC [47]. NaCl, CaCl<sub>2</sub>, MgCl<sub>2</sub> single-solute data were only used in the prediction plots for comparison. All four ternary data sets and all data points in every set were included for prediction accuracy evaluation. Haghghi *et al.* [16] reported their measurements as mass percent in the solution, and the isopleths are the constant-mass-percent curves of the second salt (see the ordering of the salts above). The formulae below were used to convert the weight percentages to molalities:

$$m_2 = \frac{w_2}{M_2(100 - w_2 - w_3)} \quad (\text{D-12})$$

$$m_3 = \frac{w_3}{M_3(100 - w_2 - w_3)} \quad (\text{D-13})$$

where  $m_2$  and  $m_3$  are the molalities,  $M_2$  and  $M_3$  are the molar masses, and  $w_2$  and  $w_3$  are the weight percentages of solutes 2 and 3, respectively, in the solution (subscript “1” is reserved for the solvent). Note that  $w_3 = 3\%$  is constant for all ternary data sets from this reference.

### ***D.3.3 Hall et al.***

Hall *et al.* [17] measured the freezing point depression of ternary aqueous solutions of NaCl + KCl, including binary limits. All data points from this study were included in this work for comparison with MSOVE predictions. The results of Hall *et al.* [17] were reported as freezing point depression vs. weight ratio and total salinity. As reported by the authors, the measurement uncertainties of temperature and salinity are about  $\pm 0.05$  °C and  $\pm 0.02\%$  (mass percent), respectively. The weight ratios and total salinities were converted to molalities using the conversion equations given below:

$$m_{\text{NaCl}} = \frac{\bar{w}s}{M_{\text{NaCl}}(100 - s)} \quad (\text{D-14})$$

$$m_{\text{KCl}} = \frac{(1 - \bar{w})s}{M_{\text{KCl}}(100 - s)} \quad (\text{D-15})$$

where  $\bar{w} = w_{\text{NaCl}}/(w_{\text{NaCl}} + w_{\text{CaCl}_2})$  and  $s$  are the weight ratio and total salinity, respectively.

### ***D.3.4 Khitrova***

Khitrova [22] reported ternary solution data for NaNO<sub>3</sub> + NaCl in terms of freezing temperature of solution vs. the mass percent of each component in the mixture and the initial concentration of one of the salts in mass percent. They also reported other phase-transition data for this system, which we do not use in this work. No measurement accuracies were reported. The concentration units were converted to molality using the same equations as for Haghghi *et al.* [16] [Equations (D-12) and (D-13)]. All data points for freezing point depression of solution were included in this work for comparison with MSOVE predictions.

### ***D.3.5 Mun and Darer***

The work of Mun and Darer [28] contains NaCl + MgCl<sub>2</sub> and KCl + MgCl<sub>2</sub> ternary data as freezing temperature of solution vs. mole percent of the salts added and total molality of solution. No measurement accuracy was reported. To convert the total molality to the molality of each salt, we multiplied the total molality by the reported mole percent of each salt. All ternary data points from this reference were included in this work for comparison with MSOVE predictions.

### ***D.3.6 Oakes et al.***

Oakes *et al.* [29] reported freezing point depression of aqueous NaCl + CaCl<sub>2</sub> solutions using a similar experimental method to Hall *et al.* [17]. The accuracy of the temperature measurements was generally better than  $\pm 0.02$  °C, and the accuracy of the solution concentration measurements was similar to that of Hall *et al.* [17]. Additionally, we used binary CaCl<sub>2</sub> data from this reference for fitting. Following the methodology of the authors, we excluded five data points from their results in our work. Four of these points were from the binary data for CaCl<sub>2</sub>. The same conversion equations were used as for the data from Hall *et al.* [17] [Equations (D-14) and (D-15)], where the second equation was written for CaCl<sub>2</sub>.

### ***D.3.7 Vilcu et al.***

In a series of three papers by Vilcu *et al.* [41–43], the authors reported freezing point depression measurements of equimolal aqueous ternary solutions of: (i) NaCl + KCl [43]; (ii) NaCl + KCl and NaBr + KBr [42]; and (iii) LiCl + NaCl, LiCl + KCl, LiCl + CsCl, and NaCl + KCl [41]. Data were reported as freezing point depression *vs.* total molality. All data points from these works were included for comparison with MSOVE predictions. Note that no measurement accuracy was reported for the determination of concentration and the reported temperature measurement accuracy was  $\pm 0.0002$  °C. However, as noted, Gibbard and Gossmann [14] found as high as 0.5 °C discrepancy when comparing the measurements to their data. Furthermore, when comparing these three works by Vilcu *et al.* [41–43], we found inconsistencies and round-off errors in the reported data.

## **D.4 Estimation of uncertainties in MSOVE coefficients**

When fitting to binary data for electrolytes, we obtained the coefficients of the polynomial (for example, for a molality-based fit; the same holds for the mole-fraction-based fits) as  $k_i$ ,  $k_i^2 B_i$ ,  $k_i^3 C_i$ , *etc.* To obtain the uncertainties (here, uncertainty means a 95% CI; see the main text) in the coefficients of the virial equation (*i.e.*,  $B_i$ 's,  $C_i$ 's, *etc.*), the uncertainties must be appropriately propagated upon dividing by a suitable non-negative integer power of  $k_i$ . We used standard deviation-based error propagation, that is, if  $z = f(u, v)$  is a function of two independent variables  $u$  and  $v$  with uncorrelated uncertainties  $\Delta u$  and  $\Delta v$ , respectively,



then the uncertainty  $\Delta z$  of the dependent variable  $z$  can be estimated from the following formula [23]:

$$(\Delta z)^2 = \left(\frac{\partial z}{\partial u}\right)^2 (\Delta u)^2 + \left(\frac{\partial z}{\partial v}\right)^2 (\Delta v)^2 \quad (\text{D-16})$$

Substituting  $z = u/v^h$  (where  $h$  is a nonnegative integer) and simplifying, we have

$$\frac{\Delta z}{z} = \sqrt{\left(\frac{\Delta u}{u}\right)^2 + h^2 \left(\frac{\Delta v}{v}\right)^2} \quad (\text{D-17})$$

## D.5 Numerical values of constants

The numerical values of the required constants for calculations in Chapter 6 are listed in Table D-1 [48]. The molar masses of the salts were used for converting from the reported concentration units to molality and mole fraction.

Table D-1. The numerical values of the required constants for calculations [48].

Constant	Value	Units
$M_{\text{H}_2\text{O}}$	$18.015 \times 10^{-3}$	kg/mole
$M_{\text{NaCl}}$	$58.443 \times 10^{-3}$	kg/mole
$M_{\text{KCl}}$	$74.551 \times 10^{-3}$	kg/mole
$M_{\text{MgCl}_2}$	$95.211 \times 10^{-3}$	kg/mole
$M_{\text{CaCl}_2}$	$110.984 \times 10^{-3}$	kg/mole
$M_{\text{ZnCl}_2}$	$136.315 \times 10^{-3}$	kg/mole
$M_{\text{ZnBr}_2}$	$225.217 \times 10^{-3}$	kg/mole
$M_{\text{NaNO}_3}$	$84.995 \times 10^{-3}$	kg/mole
$\bar{R}$	8.3145	J/(mole $\times$ K)
$\Delta s_f^\circ$ (for water)	21.9723	J/(mole $\times$ K)
$T_m^\circ$ (for water)	273.15	K

## References

- [1] A. M. Abudour, S. A. Mohammad, and K. A. M. Gasem, *Modeling High-Pressure Phase Equilibria of Coalbed Gases/Water Mixtures with the Peng-Robinson Equation of State*, *Fluid Phase Equilib.* **319**, 77 (2012).
- [2] A. Bamberger, G. Sieder, and G. Maurer, *High-Pressure (Vapor + Liquid) Equilibrium in Binary Mixtures of (Carbon Dioxide + Water or Acetic Acid) at Temperatures from 313 to 353 K*, *J. Supercrit. Fluids* **17**, 97 (2000).
- [3] K. A. Brakke, *The Surface Evolver*, *Exp. Math.* **1**, 141 (1992).
- [4] K. A. Brakke, *Surface Evolver Manual*,  
<https://kenbrakke.com/evolver/downloads/manual270.pdf>.
- [5] J. A. Briones, J. C. Mullins, M. C. Thies, and B.-U. Kim, *Ternary Phase Equilibria for Acetic Acid-Water Mixtures with Supercritical Carbon Dioxide*, *Fluid Phase Equilib.* **36**, 235 (1987).
- [6] A. Chapoy, A. H. Mohammadi, B. Tohidi, and D. Richon, *Gas Solubility Measurement and Modeling for the Nitrogen + Water System from 274.18 K to 363.02 K*, *J. Chem. Eng. Data* **49**, 1110 (2004).
- [7] C. R. Coan and A. D. King, *Solubility of Water in Compressed Carbon Dioxide, Nitrous Oxide, and Ethane. Evidence for Hydration of Carbon Dioxide and Nitrous Oxide in the Gas Phase*, *J. Am. Chem. Soc.* **93**, 1857 (1971).
- [8] R. D'Souza, J. R. Patrick, and A. S. Teja, *High Pressure Phase Equilibria in the Carbon Dioxide–*n*-Hexadecane and Carbon Dioxide–Water Systems*, *Can. J. Chem. Eng.* **66**, 319 (1988).
- [9] R. Dohrn, A. P. Bünz, F. Devlieghere, and D. Thelen, *Experimental Measurements of Phase Equilibria for Ternary and Quaternary Systems of Glucose, Water, CO<sub>2</sub> and Ethanol with a Novel Apparatus*, *Fluid Phase Equilib.* **83**, 149 (1993).

- [10] A. Y. Fadeev and S. M. Staroverov, *Geometric Structural Properties of Bonded Layers of Chemically Modified Silicas*, J. Chromatography A **447**, 103 (1988).
- [11] R. Fernández-Prini, J. L. Alvarez, and A. H. Harvey, *Henry's Constants and Vapor–Liquid Distribution Constants for Gaseous Solutes in H<sub>2</sub>O and D<sub>2</sub>O at High Temperatures*, J. Phys. Chem. Ref. Data **32**, 903 (2003).
- [12] H. F. Gibbard and A. Fawaz, *Freezing Points and Related Properties of Electrolyte Solutions. II. Mixtures of Lithium Chloride and Sodium Chloride in Water*, J. Solution Chem. **3**, 745 (1974).
- [13] H. F. Gibbard and S.-L. Fong, *Freezing Points and Related Properties of Electrolyte Solutions. III. The Systems NaCl–CaCl<sub>2</sub>–H<sub>2</sub>O and NaCl–BaCl<sub>2</sub>–H<sub>2</sub>O*, J. Solution Chem. **4**, 863 (1975).
- [14] H. F. Gibbard and A. F. Gossman, *Freezing of Electrolyte Mixtures. I. Mixtures of Sodium Chloride and Magnesium Chloride in Water*, J. Solution Chem. **3**, 385 (1974).
- [15] P. C. Gillepsie and G. M. Wilson, *Vapor–Liquid and Liquid–Liquid Equilibria: Water–Methane, Water–Carbon Dioxide, Water–Hydrogen Sulfide, Water–n-Pentane, Water–Methane–n-Pentane*. Research Report RR-48, Gas Processors Association, 1982.
- [16] H. Haghghi, A. Chapoy, and B. Tohidi, *Freezing Point Depression of Electrolyte Solutions: Experimental Measurements and Modeling Using the Cubic-Plus-Association Equation of State*, Ind. Eng. Chem. Res. **47**, 3983 (2008).
- [17] D. L. Hall, S. Michael Sterner, and R. J. Bodnar, *Freezing Point Depression of NaCl–KCl–H<sub>2</sub>O Solutions*, Econ. Geol. **83**, 197 (1988).
- [18] A. H. Harvey, *Semiempirical Correlation for Henry's Constants over Large Temperature Ranges*, AIChE J. **42**, 1491 (1996).
- [19] J. L. Hass, *Fugacity of H<sub>2</sub>O from 0° to 350°C at the Liquid–Vapor Equilibrium and at 1 Atmosphere*, Geochim. Cosmochim. Acta **34**, 929 (1970).
- [20] S. X. Hou, G. C. Maitland, and J. P. M. Trusler, *Measurement and Modeling of the Phase Behavior of the (Carbon Dioxide + Water) Mixture at Temperatures from 298.15 K to 448.15 K*, J. Supercrit. Fluids **73**, 87 (2013).

- [21] K. Jackson, L. E. Bowman, and J. L. Fulton, *Water Solubility Measurements in Supercritical Fluids and High-Pressure Liquids Using near-Infrared Spectroscopy*, *Anal. Chem.* **67**, 2368 (1995).
- [22] N. N. Khitrova, *Polytherms of the Ternary NaNO<sub>3</sub>-NaCl-H<sub>2</sub>O*, *Zhurnal Prikl. Khimii* **27**, 1281 (1954).
- [23] H. H. Ku, *Notes on the Use of Propagation of Error Formulas*, *J. Res. Natl. Bur. Stand. Sect. C Eng. Instrum.* **70C**, 263 (1966).
- [24] B. Lefevre, A. Saugey, J. L. Barrat, L. Bocquet, E. Charlaix, P. F. Gobin, and G. Vigier, *Intrusion and Extrusion of Water in Hydrophobic Mesopores*, *J. Chem. Phys.* **120**, 4927 (2004).
- [25] E. W. Lemmon, I. H. Bell, M. L. Huber, and M. O. McLinden, *NIST Standard Reference Database 23: Reference Fluid Thermodynamic and Transport Properties-REFPROP*, v10.0.
- [26] M. Li, L. Xu, and W. Lu, *Effect of Extra Gas Amount on Liquid Outflow from Hydrophobic Nanochannels: Enhanced Liquid-Gas Interaction and Bubble Nucleation*, *Langmuir* **36**, 4682 (2020).
- [27] G. Müller, E. Bender, and G. Maurer, *Das Dampf-Flüssigkeitsgleichgewicht Des Ternären Systems Ammoniak-Kohlendioxid-Wasser Bei Hohen Wassergehalten Im Bereich Zwischen 373 Und 473 Kelvin*, *Berichte Der Bunsengesellschaft Für Phys. Chemie* **92**, 148 (1988).
- [28] A. N. Mun and R. S. Darer, *Cryoscopy of Aqueous Salt Solutions. II. Systems NaCl-MgCl<sub>2</sub>-H<sub>2</sub>O and KCl-MgCl<sub>2</sub>-H<sub>2</sub>O*, *Zhurnal Neorg. Khimii* **2**, 1658 (1957).
- [29] C. S. Oakes, R. J. Bodnar, and J. M. Simonson, *The System NaCl-CaCl<sub>2</sub>-H<sub>2</sub>O: I. The Ice Liquidus at 1 Atm Total Pressure*, *Geochim. Cosmochim. Acta* **54**, 603 (1990).
- [30] D. Peng and D. B. Robinson, *A New Two-Constant Equation of State*, *Ind. Eng. Chem. Fundam.* **15**, 59 (1976).
- [31] J. M. Prausnitz, R. N. Lichtenthaler, and E. G. de Azevedo, *Molecular Thermodynamics of Fluid-Phase Equilibria*, 3rd ed. (Prantice Hall PTR, 1999).

- [32] H. Renon and J. M. Prausnitz, *Local Compositions in Thermodynamic Excess Functions for Liquid Mixtures*, AIChE J. **14**, 135 (1968).
- [33] M. Rigby and M. Prausnitz, *Solubility of Water in Compressed Nitrogen, Argon, and Methane*, J. Phys. Chem. **72**, 330 (1968).
- [34] A. W. Saddington and N. W. Krase, *Vapor–Liquid Equilibria in the System Nitrogen–Water*, J. Am. Chem. Soc. **56**, 353 (1934).
- [35] T. Sako, T. Sugeta, N. Nakazawa, T. Okubo, M. Sato, T. Taguchi, and T. Hiaki, *Phase Equilibrium Study of Extraction and Concentration of Furfural Produced in Reactor Using Supercritical Carbon Dioxide*, J. Chem. Eng. Japan **24**, 449 (1991).
- [36] J. Sedlbauer, J. P. O’Connell, and R. H. Wood, *A New Equation of State for Correlation and Prediction of Standard Molal Thermodynamic Properties of Aqueous Species at High Temperatures and Pressures*, Chem. Geol. **163**, 43 (2000).
- [37] I. Søreide and C. H. Whitson, *Peng-Robinson Predictions for Hydrocarbons, CO<sub>2</sub>, N<sub>2</sub>, and H<sub>2</sub>S with Pure Water and NaCl Brine*, Fluid Phase Equilib. **77**, 217 (1992).
- [38] N. Spycher, K. Pruess, and J. Ennis-King, *CO<sub>2</sub>-H<sub>2</sub>O Mixtures in the Geological Sequestration of CO<sub>2</sub>. I. Assessment and Calculation of Mutual Solubilities from 12 to 100°C and up to 600 Bar*, Geochim. Cosmochim. Acta **67**, 3015 (2003).
- [39] R. Sun, W. Hu, and Z. Duan, *Prediction of Nitrogen Solubility in Pure Water and Aqueous NaCl Solutions up to High Temperature, Pressure, and Ionic Strength*, J. Solution Chem. **30**, 561 (2001).
- [40] K. Tödheide and E. U. Franck, *Das Zweiphasengebiet Und Die Kritische Kurve Im System Kohlendioxid–Wasser Bis Zu Drucken von 3500 Bar*, Zeitschrift Für Phys. Chemie **37**, 387 (1963).
- [41] R. Vilcu, F. Irinei, and V. Isverceanu, *Thermodynamics of Multicomponent Electrolyte Solution. IV: Individual Activities in Electrolyte Solutions*, Bull. Des Soc. Chim. Belges **93**, 261 (1984).
- [42] R. Vilcu and F. Stanciu, *Thermodynamic Properties of Aqueous Electrolyte Solutions II: Differential Cryoscopy of Sodium Chloride-Potassium Chloride and Potassium*

- Bromide-Sodium Bromide Systems*, Rev. Roum. Chim. **13**, 253 (1968).
- [43] R. Vilcu and F. Stanciu, *Differential Cryoscopy in Ternary System*, Rev. Roum. Chim. **10**, 499 (1965).
- [44] R. Wiebe and V. L. Gaddy, *Vapor Phase Composition of Carbon Dioxide–Water Mixtures at Various Temperatures and at Pressures to 700 Atmospheres*, J. Am. Chem. Soc. **63**, 475 (1941).
- [45] R. Wiebe and V. L. Gaddy, *The Solubility in Water of Carbon Dioxide at 50, 75, and 100°, at Pressures to 700 Atmospheres.*, J. Am. Chem. Soc. **61**, 315 (1939).
- [46] R. Wiebe, V. L. Gaddy, and C. Heins, *The Solubility of Nitrogen in Water at 50, 75, 100° from 25 to 1000 Atmospheres*, J. Am. Chem. Soc. **55**, 947 (1933).
- [47] W. M. Haynes, editor , *Concentrative Properties of Aqueous Solutions: Density, Refractive Index, Freezing Point Depression, and Viscosity*, in *CRC Handbook of Chemistry and Physics*, 95th ed. (CRC Press, 2015).
- [48] W. M. Haynes, editor , *Physical Constants of Inorganic Compounds*, in *CRC Handbook of Chemistry and Physics*, 95th ed. (CRC Press, 2015).